



HAL
open science

New Minimal Path Model for Tubular Extraction and Image Segmentation

Da Chen

► **To cite this version:**

Da Chen. New Minimal Path Model for Tubular Extraction and Image Segmentation. General Mathematics [math.GM]. Université Paris sciences et lettres, 2016. English. NNT : 2016PSLED037 . tel-01526847

HAL Id: tel-01526847

<https://theses.hal.science/tel-01526847>

Submitted on 23 May 2017

HAL is a multi-disciplinary open access archive for the deposit and dissemination of scientific research documents, whether they are published or not. The documents may come from teaching and research institutions in France or abroad, or from public or private research centers.

L'archive ouverte pluridisciplinaire **HAL**, est destinée au dépôt et à la diffusion de documents scientifiques de niveau recherche, publiés ou non, émanant des établissements d'enseignement et de recherche français ou étrangers, des laboratoires publics ou privés.

THÈSE DE DOCTORAT

de l'Université de recherche Paris Sciences et Lettres
PSL Research University

Préparée à l'Université Paris-Dauphine

Nouveaux modèles de chemins minimaux pour l'extraction
de structures tubulaires et la segmentation d'images

École Doctorale de Dauphine — ED 543

Spécialité **Sciences**

**Soutenue le 27-09-2016
par Da CHEN**

Dirigée par **Laurent D. COHEN**

COMPOSITION DU JURY :

Laurent D. COHEN
University Paris Dauphine
Directeur de thèse

Ron KIMMEL
Technion - Israel Institute of Technology
Rapporteur

Remco DUIJS
Eindhoven University of Technology
Rapporteur

Gabriel PEYRÉ
University Paris Dauphine
Président du jury

Jean-Marie MIREBEAU
Université Paris-Sud
Membre du jury

Grégoire MALANDAIN
INRIA Sophia Antipolis
Membre du jury

Roberto ARDON
Philips Research Medisys
Membre du jury

Michel PAQUES
Centre d'Investigations Cliniques,
Membre du jury

New Minimal Paths Models for Tubular Structure Extraction and Image Segmentation

by
Da CHEN

Supervisor: Prof. Laurent D. Cohen

A thesis submitted for the degree of
Doctor of Philosophy

in the

CEREMADE, CNRS, UMR 7534

Université Paris Dauphine, PSL Research University



December 2016

*L'université n'entend donner aucune approbation ni improbation
aux opinions émises dans les thèses : ces opinions doivent
être considérées comme propres à leurs auteurs*

Acknowledgement

My deepest gratitude naturally goes first to my supervisor Prof. Laurent D. Cohen, without whom this thesis would not be possible. I am extremely lucky to be his Ph. D student. His knowledge, enthusiasm, expertise and experience make me to enjoy the research work during the past four years.

I would like to express my heartfelt gratitude to Dr. Jean-Marie Mirebeau, who gave me exciting and constructive help that facilitates my entry into the field of numerical analysis. A substantial part of this work was initiated by a collaboration with Dr. Jean-Marie Mirebeau.

I would like to warmly thank all the members of my thesis committee. I would like to give my appreciation to Prof. Ron Kimmel and Prof. Remco Duits who kindly gave me some of their extremely valuable time to carefully read this manuscript and to write the reports. I am also very honoured by the presence of prof. Grégoire Malandain, Prof. Michel Paques, Prof. Gabriel Peyré, and Dr. Roberto Ardon in my defense as examiners. Particularly, I thank Prof. Michel Paques who gave some motivation for retinal vessel tree analysis at an early stage of this work.

I also would like to give my appreciation to Prof. Alfred M. Bruckstein for his fruitful discussion on my subject.

I would like to thank CEREMADE that funds me to join many international conferences (even including trips to China and America) in the past four years. I thank China ScholarShip Council for the financial support to finish this thesis.

I thank the entire team of CEREMADE, University Paris Dauphine to provide me various help for my daily work. I am also very grateful to my colleagues Fang Yang, Qi-Chong Tian, Emmanuel Cohen for their fruitful discussion on my subject. I also would like to thank my Chinese friends Ke Wang, Hua Lu, Bang-Xian Han,

Qun Wang, Qi-Long Weng, Shuo-Qing Deng and Chang-Ye Wu for their timely support.

I would like also to thank Jiong Zhang and Erik Bekkers from Eindhoven University of Technology to share me the retinal images with detailed annotations such as the vessel boundary, segmentation ground truth, and artery-vein ground truth, which gave me great help to evaluate my models.

I have a special gratitude to all my family, especially to my parents. Thank you for the unconditional support during the past four years.

Finally, let me convey my sincerest gratitude to my wife Han Li for her concommittance all the time. Whatever the situation is, you always support and believe me. My true gratitude is beyond any words description. I believe that this thesis is one of the most precious efforts we have experienced.

Abstract

In the fields of medical imaging and computer vision, segmentation plays a crucial role with the goal of separating the interesting components from one image or a sequence of image frames. It bridges the gaps between the low-level image processing and high level clinical and computer vision applications. These high level applications may include diagnosis, therapy planning, object detection and recognition and so on. Among the existing segmentation methods, minimal geodesics have important theoretical and practical advantages such as the global minimum of the geodesic energy and the well-established fast marching method for numerical solution. In this thesis, we focus on the Eikonal partial differential equation based geodesic methods to investigate accurate, fast and robust tubular structure extraction and image segmentation methods, by developing various local geodesic metrics for types of clinical and segmentation tasks.

This thesis aims to apply different geodesic metrics for the Eikonal partial differential equation framework to solve different image segmentation and boundary detection problems especially for tubularity segmentation and region-based active contours models, by making use of more information from the image feature and prior clinical knowledges. The designed geodesic metrics basically take advantages of the geodesic orientation or anisotropy, the image feature consistency, the geodesic curvature and the geodesic asymmetry property to deal with various difficulties suffered by the classical minimal geodesic models and the active contours models. This thesis eventually presents the interpretation of classical image processing models: the Euler elastica model and the active contours models by the framework of the Eikonal partial differential equation based minimal geodesics. Therefore, those classical models can share the advantages of the minimal geodesics.

Upon the mathematical models developed in this thesis, we show the power of the minimal geodesics in the challenging clinical task of retinal blood vessels extraction including both the centreline positions and the corresponding vessel width values at these positions. Combining with the novel metrics investigated in this thesis, the minimal paths inspired solution to this task thus is able to benefit from the fast numerical solver such as the fast marching method, and easy user intervention, thus very practical and flexible. These models provide the possibilities to satisfy

the requirements of real time solution and flexible and efficient interactive way, which are highly expected by the medical experts in many situations.

The main contributions of this thesis lie at the deep study of the various geodesic metrics and their applications in medical imaging and image segmentation. Experiments on medical images and nature images show the effectiveness of the presented contributions.

Keywords: Minimal path, geodesic, Eikonal partial differential equation, image segmentation, tubular structure segmentation, active contours, Euler elastica curve, Riemannian metric, Finsler metric, curvature penalty, fast marching method.

Résumé

Dans les domaines de l'imagerie médicale et de la vision par ordinateur, la segmentation joue un rôle crucial dans le but d'extraire les composantes intéressantes d'une image ou d'une séquence d'images. Elle est à l'intermédiaire entre le traitement d'images de bas niveau et les applications cliniques et celles de la vision par ordinateur de haut niveau. Ces applications de haut niveau peuvent inclure le diagnostic, la planification de la thérapie, la détection et la reconnaissance d'objet, etc. Parmi les méthodes de segmentation existantes, les courbes géodésiques minimales possèdent des avantages théoriques et pratiques importants tels que le minimum global de l'énergie géodésique et la méthode bien connue de Fast Marching pour obtenir une solution numérique. Dans cette thèse, nous nous concentrons sur les méthodes géodésiques basées sur l'équation aux dérivées partielles, l'équation Eikonale, afin d'étudier des méthodes précises, rapides et robustes, pour l'extraction de structures tubulaires et la segmentation d'image, en développant diverses métriques géodésiques locales pour des applications cliniques et la segmentation d'images en général.

Cette thèse vise à appliquer différentes métriques géodésiques dans le cadre de l'équation Eikonale, afin de résoudre différents problèmes de segmentation d'image et de détection de frontière, en particulier pour la segmentation de structures tubulaires et les modèles de contours actifs région, en faisant usage de plus d'informations issues des caractéristiques d'image et de connaissances cliniques préalables. Les métriques géodésiques introduites tirent essentiellement leurs avantages de l'orientation géodésique et de l'anisotropie, de la cohérence des caractéristiques de l'image, de la courbure géodésique et de la propriété géodésique d'asymétrie pour faire face aux diverses difficultés posées par les modèles classiques de géodésiques minimales et les modèles de contours actifs. Enfin, cette thèse présente une interprétation des modèles classiques de traitement d'image: le modèle *Elastica* d'Euler et les contours actifs, par les géodésiques minimales basées sur l'équation aux dérivées partielles Eikonale. Par conséquent, ces modèles classiques peuvent tirer profit des avantages des géodésiques minimales.

A propos des modèles mathématiques développés dans cette thèse, nous montrons la puissance des géodésiques minimales pour l'extraction des vaisseaux de la rétine, tâche clinique souvent difficile à réaliser, en indiquant à la fois la ligne médiane

et les valeurs des diamètres des vaisseaux correspondants. En combinant avec les nouvelles métriques étudiées dans cette thèse, cette solution basée sur les chemins minimaux bénéficie d'un solveur numérique rapide tel que la méthode du Fast Marching et d'une facilité d'interaction pour l'utilisateur, très pratique et flexible. Les méthodes développées dans cette thèse offrent une solution en temps réel, flexible et un moyen d'interaction efficace, regroupant ainsi des critères hautement exigés par les spécialistes du domaine médical dans différentes situations.

Cette thèse contribue principalement à l'étude approfondie des diverses métriques géodésiques et leurs applications en imagerie médicale et segmentation d'images. Des expériences ont été réalisées sur des images médicales et des images naturelles pour montrer l'efficacité des contributions présentées.

Mots-clés: Chemin minimal, géodésique, équation aux dérivées partielles, équation Eikonale, segmentation d'images, segmentation de structure tubulaire, contours actifs, courbe *Elastica* d'Euler, métrique de Riemann, métrique de Finsler, pénalité de courbure, méthode de Fast Marching.

Introduction (French)

English speakers are invited to go to Chapter 1 for the English version of this introduction.

La segmentation des images joue un rôle essentiel dans le domaine du traitement d'images, liant le traitement d'images de bas niveau, comme le débruitage d'images, la restauration et l'amélioration d'images et les tâches de haut niveau pour des applications en imagerie médicale ainsi que la vision par ordinateur. L'objectif fondamental de la segmentation d'images consiste à obtenir une partition de l'image c'est à dire une collection de régions, qui sont généralement disjointes les unes des autres. La segmentation d'images est encore un problème difficile à résoudre, puisque différents types d'images nécessitent différentes méthodes de segmentation.

Il existe un grand nombre de méthodes de segmentation, celle-ci ont été étudiées au cours des dernières décennies. Parmi elles, la classe des méthodes de seuillage qui est largement utilisée est généralement considérée comme l'étape de segmentation brute suivie de procédures de raffinement, grâce à la facilité de sa mise en oeuvre et à une faible complexité. Ces méthodes utilisent l'information des niveaux de gris ou bien l'information en couleurs de chaque pixel ou groupe de pixels (comme un patch de l'image) et attribuent la même étiquette aux pixels ayant des propriétés similaires. Cependant, sans une régularisation des pixels, ces procédés de seuillage sont le plus souvent sensibles au bruit. En outre, ces méthodes de segmentation ne sont pas capables d'intégrer des informations plus complexes et utiles, telles que la texture, la connaissance deforme préalable et l'interaction de l'utilisateur. Pour pallier ce problème, des méthodes de segmentation plus modernes ont été développées, comme les modèles basés sur les graphes et les méthodes variationnelles de modèles déformables.

Des méthodes de segmentation basées sur les graphes ont été proposées tels que le modèle de *normalized cut* proposé par (Shi and Malik, 2000), la méthode de segmentation *graph cut* (Boykov and Funka-Lea, 2006) ainsi que la méthode de segmentation par marche aléatoire (Grady, 2006). La formulation de ces modèles suppose que les images soient basées sur le domaine discret considérant une image comme un graphe composé d'arêtes et de noeuds. L'optimisation des énergies

s'appuyant sur des graphes est particulièrement efficace, comme par exemple, la méthode de minimisation de *graph cut* (Boykov and Kolmogorov, 2004; Kolmogorov and Zabini, 2004). Un autre avantage des modèles de segmentation basée sur les graphes est la facilité de la mise en oeuvre d'interactions de l'utilisateur. Le mode d'initialisation populaire pour des méthodes comme (Boykov and Funkalea, 2006) et (Grady, 2006) consiste à introduire des points sources prescrits à l'intérieur de chaque région de l'image désirée. Par ailleurs, une régularisation des frontières des régions de l'image peut être envisagée. Le terme de régularisation le plus populaire est la minimisation de la longueur Euclidienne des bords. Récemment, certaines de ces techniques mises en place par (El-Zehiry and Grady, 2010; Schoenemann et al., 2012) proposent de meilleurs résultats au niveau de la segmentation dans certains cas, comme pour les images dotées de structures à la fois longues et fines.

Les modèles de contours actifs sont conçus pour minimiser une fonctionnelle d'énergie de la courbe dans le domaine continu sur la base des équations d'Euler-Lagrange et de principes variationnels. L'idée fondamentale du modèle des contours actifs (Kass et al., 1988) est de déformer la courbe ou 'snake' convergeant vers les bords de l'objet tant par des forces internes que par des forces externes. La force interne peut assurer d'obtenir des contours actifs qui sont lisses, tandis que les forces externes, calculées en fonction de données images, peut attirer les contours actifs vers les frontières. Dans ce sens, diverses forces externes (Cohen, 1991; Cohen and Cohen, 1993; Xie and Mirmehdi, 2008; Xu and Prince, 1998) ont été proposées pour améliorer la performance du modèle des contours actifs. Les modèles des contours actifs géométriques (Caselles et al., 1993, 1997) sont basés sur le flux de mouvement par courbure Euclidienne. Dans leur formulation de base, les contours actifs sont représentés par l'ensemble de niveau zéro d'une fonction (Osher and Sethian, 1988). Ces modèles géométriques sont en mesure de faire automatiquement face aux changements topologiques grâce à l'évolution de la courbe basée sur l'ensemble de niveau. Le principal inconvénient de ces équations d'Euler-Lagrange, inspirées des modèles de contours actifs, est qu'elles tombent parfois dans des contours parasites provoqués par le bruit ou par les hétérogénéités d'intensité. Ces contours actifs ont également une énergie non-convexe. Ainsi, il est difficile de trouver les minimums globaux des énergies.

Un modèle de chemin minimal a été proposée par (Cohen and Kimmel, 1997) afin de trouver le minimum global de l'énergie géodésique en résolvant une équation aux dérivées partielles non linéaires (EDP), au lieu de l'équation linéaire d'Euler Lagrange, utilisée dans le modèle géodésique classique des contours actifs (Caselles et al., 1997). Le point crucial, dans ce modèle, est la conception de la métrique géodésique \mathcal{F} , où l'énergie de la courbe est obtenue en intégrant \mathcal{F} le long d'une courbe Γ . Une fois la métrique \mathcal{F} obtenue, les géodésiques minimales entre un point quelconque dans le domaine et le point source initial peuvent être immédiatement déterminées, après le calcul donné par la carte de distance géodésique. Le modèle

d'origine du chemin minimal de Cohen-Kimmel a été suivi par de nombreuses méthodes de segmentation d'images interactives par le biais de procédures de détection de contour fermé (Appia and Yezzi, 2011; Appleton and Talbot, 2005; Mille et al., 2014), où il est communément proposé que les contours de l'objet soient délimités par un ensemble de chemins minimaux contraints par les points sources fournis par l'utilisateur. De plus, les modèles fondés sur des chemins minimaux sont particulièrement appropriés pour l'extraction de structures tubulaires (Bemansour and Cohen, 2011; Li and Yezzi, 2007).

Dans cette thèse, diverses métriques appropriées \mathcal{F} sont conçues pour différentes tâches de détection de structures tubulaires pour l'extraction des vaisseaux rétiniens et des contours actifs pour la segmentation d'images. Les contributions techniques sont décrites dans les chapitres 3 à 6. Le chapitre 2 est notamment consacré aux modèles déformables qui constituent la base de cette thèse. La structure principale est ainsi décrite:

- Le **Chapitre 2** introduit le contexte scientifique de la thèse: les modèles déformables, y compris les modèles de contours actifs et les modèles de chemin minimal. Nous commençons ce chapitre par l'analyse de l'énergie du modèle d'origine des contours actifs proposé par Kass et al. (1988). Ensuite, les modèles de contours actifs classiques sont introduits, selon la manière dont ces modèles sont capables de résoudre les problèmes qui affectent le modèle original des contours actifs.

Dans ce chapitre, la méthode d'ensembles de niveau ainsi que la méthode de Fast Marching, constituant les outils numériques pour les modèles des contours actifs et pour les modèles de chemin minimal, sont discutées respectivement. Nous utilisons plus particulièrement les méthodes de Fast Marching anisotrope introduites dans (Mirebeau, 2014a,b) comme les solveurs Eikonal associés aux paramètres de conception, utilisés dans cette thèse. Les détails de la construction des stencils adaptatifs sont présentés dans la section 2.4.4.

- Le **Chapitre 3** illustre le rôle des chemins minimaux à la base de l'EDP Eikonale pour la tâche de segmentation de structure tubulaire, en particulier pour l'extraction des vaisseaux rétiniens. Nous abordons les problèmes consistant à trouver à la fois les lignes centrales et les bords des vaisseaux, affectant les modèles existants de chemin minimal.
 - La Section 3.2 traite du filtre de flux orienté (OOF) de manière optimale (Law and Chung, 2008), considéré dans cette thèse comme le descripteur d'anisotropie tubulaire pour l'extraction de la structure tubulaire. Ce filtre peut être utilisé pour détecter la probabilité de chaque pixel d'appartenir à un vaisseau et l'orientation optimale pour chaque point de ce vaisseau.

- La Section 3.3 présente les détails de la construction de la métrique anisotrope de Riemann, proposée par (Benmansour and Cohen, 2011) en espace+rayon. Dans la formulation de base, chaque point d'un chemin minimal de espace3D+rayon, associé à cette métrique, comprend trois composantes: les deux premières, qui sont les coordonnées, représentent la position physique et la troisième est la valeur du rayon du vaisseau correspondante.
- La Section 3.4 présente une méthode de détection de points-clés, basée sur un masque pour l'extraction automatique de l'arbre vasculaire et son application pour l'extraction de l'arbre des vaisseaux rétinien. Ce modèle, qui ne nécessite qu'un seul point source initial, permet de trouver le point-clé suivant qui est considéré comme le nouveau point source initial pour la méthode de Fast Marching. Le masque peut être calculé par un détecteur quelconque de structures vasculaires. S'appuyant sur le masque, notre méthode visant à rechercher le point-clé peut éviter les problèmes de fuites et utiliser une petite valeur du seuil de la longueur de la courbe.
- La Section 3.5 propose une nouvelle métrique dynamique anisotrope Riemannienne, pour le modèle de chemin minimal pour l'extraction interactive des vaisseaux rétinien. Cette métrique dynamique est calculée par l'utilisation de la courbe géodésique locale et des informations supplémentaire sur l'image. Notre objectif est d'extraire une géodésique le long de laquelle la fonction de l'image varie lentement, étant un indice très important pour l'extraction des vaisseaux rétinien. Nous présentons également un modèle de chemin minimal contraint dans une région, pour obtenir à la fois des lignes centrales et les bords des vaisseaux sanguins de la rétine.
- La Section 3.6 introduit un procédé automatique pour mesurer la largeur du vaisseau sur la base du modèle de chemin minimal contraint à une région. Cette méthode peut utiliser une carte binaire pré-segmentée qui fournit une collection de points sources et de régions contraignant la méthode de Fast Marching, de cette façon, les chemins minimaux extraits sont inclus à l'intérieur de cette région, ce qui peut écarter le problème de chevauchement.
- Le **Chapitre 4** propose une méthode de Fast Marching anisotrope de propagation du front pour la segmentation de l'arbre vasculaire. Dans ce chapitre, il s'agit notamment d'étudier la construction de la métrique anisotrope dynamique Riemannienne, mise en oeuvre par la méthode de Fast Marching anisotrope. L'amélioration dynamique et anisotrope permet d'éviter le problème des fuites qui affectent le modèle classique isotrope de propagation du front, reposant uniquement sur la position.

- Le **Chapitre 5** introduit un modèle de chemin minimal pénalisant la courbure avec la métrique de Finsler pour un modèle *Elastica* et en espace+orientation. Ce procédé est réalisé par l'établissement d'une relation entre l'énergie de flexion de l'*Elastica* d'Euler et l'énergie géodésique, à travers la métrique *Elastica* de Finsler. En résolvant l'EDP Eikonale associée à la métrique de Finsler *Elastica*, nous pouvons obtenir les géodésiques minimales pénalisant la courbure et globalement minimisantes, susceptibles d'être utilisées pour approcher les courbes élastiques d'Euler.

A partir de la métrique *Elastica* de Finsler, nous présentons des méthodes afin de détecter les contours fermés, le groupement perceptuel et l'extraction de structure tubulaire. Le modèle proposé de chemin minimal *Elastica* de Finsler utilise à la fois l'information sur l'orientation et la courbure, obtenant ainsi des résultats bien meilleurs que les modèles classiques de chemin minimal.

- Le **Chapitre 6** introduit une nouvelle méthode s'appuyant sur l'EDP Eikonale non linéaire pour la segmentation d'images par contours actifs basés Région. Nous transformons l'énergie des contours actifs basés Région en une énergie de courbe géodésique, par la métrique de Finsler, à travers le théorème de divergence. Par conséquent, la minimisation de l'énergie basée Région est obtenue en résolvant l'EDP Eikonale associée aux métriques de Finsler par la méthode de Fast Marching anisotrope (Mirebeau, 2014b). Le minimum correspondant est plus robuste et plus efficace. La stratégie traditionnelle de minimisation de l'énergie des contours actifs basée Région utilise la méthode de descente de gradient et l'évolution de la courbe basée sur la méthode des ensembles de niveau, étant sensible aux minima locaux et nécessitant d'un réglage attentif des paramètres. En revanche, la méthode proposée permet d'éviter les problèmes de sensibilité aux minima locaux et des paramètres. En outre, compte tenu de la simplicité d'utilisation de la méthode, il est naturel d'intégrer les informations fournies par l'utilisateur.
- Le **Chapitre 7** résume les principales contributions de cette thèse et donne les perspectives des futurs travaux.

List of Peer-Reviewed Publications

The work done during this Ph.D. lead to the following publications.

Conference Papers

1. **Da Chen**, JEAN-MARIE MIREBEAU, and LAURENT D. COHEN, *Finsler Geodesic Evolution Model for Region based Active Contours*, British Machine Vision Conference (BMVC 2016).
2. **Da Chen**, JEAN-MARIE MIREBEAU, and LAURENT D. COHEN, *A New Finsler Minimal Path Model with Curvature Penalization for Image Segmentation and Closed Contour Detection*, IEEE Conference on Computer Vision and Pattern Recognition (CVPR 2016).
3. **Da Chen** and LAURENT D. COHEN, *Vessel Tree Segmentation Via Front Propagation and Dynamic Anisotropic Riemannian Metric*, IEEE International Symposium on Biomedical Imaging (ISBI 2016).
4. **Da Chen**, JEAN-MARIE MIREBEAU, and LAURENT D. COHEN, *Global Minimum for Curvature Penalized Minimal Path Method*, British Machine Vision Conference (BMVC 2015).
5. **Da Chen** and LAURENT D. COHEN, *Piecewise Geodesics for Vessel Centreline Extraction and Boundary Delineation with application to Retina Segmentation*, International Conference on Scale Space and Variational Methods in Computer Vision (SSVM 2015).
6. **Da Chen** and LAURENT D. COHEN, *Interactive Retinal Vessel Centreline Extraction and Boundary Delineation using Anisotropic Fast Marching and*

Intensities Consistency, Annual International Conference of IEEE Engineering in Medicine and Biology Society (EMBC 2015).

7. **Da Chen** and LAURENT D. COHEN, *Automatic Tracking of Retinal Vessel Segments using Radius-Lifted Minimal Path Method*, Medical Image Understanding and Analysis Conference (MIUA 2015).
8. **Da Chen**, JEAN-MARIE MIREBEAU, and LAURENT D. COHEN, *Vessel Extraction Using Anisotropic Minimal Paths and Path Score*, IEEE International Conference on Image Processing (ICIP 2014).
9. **Da Chen** and LAURENT D. COHEN, *Automatic Vessel Tree Structure Extraction by Growing Minimal Paths and A Mask*, IEEE International Symposium on Biomedical Imaging (ISBI 2014).

Journal Papers

1. **Da Chen**, JEAN-MARIE MIREBEAU, and LAURENT D. COHEN, *Global Minimum For A Finsler Elastica Minimal Path Approach*, International Journal of Computer Vision, 2016.
2. **Da Chen**, JEAN-MARIE MIREBEAU, and LAURENT D. COHEN, *Eikonal Active Contours*, Submitted to IEEE Trans. on Pattern Analysis and Machine Intelligence (Under Review).
3. **Da Chen** and LAURENT D. COHEN, *Tubular Structure Extraction using Intensity Consistency Penalized and Region Constrained Minimal Path Model*, Submitted to IEEE Trans. Image Processing (Under Review).
4. **Da Chen**, MINGQIANG YANG, and LAURENT D. COHEN, *Global minimum for a variant Mumford–Shah model with application to medical image segmentation*, Computer Methods in Biomechanics and Biomedical Engineering: Imaging and Visualization, 2013, 1(1): 48-60. (**Best Paper Award**)
5. **Da Chen**, JEAN-MARIE MIREBEAU, and LAURENT D. COHEN, *Vessel Tree Extraction using Radius-Lifted Keypoints Searching Scheme and Anisotropic Fast Marching Method*, Journal of Algorithms and Computational Technology, 2016.

Contents

	iii
Acknowledgement	v
Abstract	vii
Résumé	ix
Introduction (French)	xi
List of Peer-Reviewed Publications	xvii
List of Figures	xxiii
List of Tables	xxvii
Notations	xxix
1 Introduction	1
2 Active Contours and Minimal Paths	7
2.1 Active Contours Models	8
2.1.1 Original Active Contours Model	8
2.1.2 Active Contours Model with Ballon Force	10
2.1.3 Active Contours with Distance Vector Flow	11
2.1.4 Active Contours with Gradient Vector Flow	11
2.2 Level Set-based Active Contours	14
2.2.1 Level Set Method	14
2.2.2 Geometric Active Contours	16
2.2.3 Geodesic Active Contours	19
2.2.4 Alignment Active Contours	20
2.3 Cohen-Kimmel Minimal Path Model and its Extensions	22
2.3.1 From Active Contours to Eikonal PDE-based Minimal Paths	22
2.3.2 Cohen-Kimmel Minimal Path Model	23
2.3.3 Minimal Paths with Isotropic Radius-Lifted Riemannian Metric	26
2.3.4 Minimal Paths with Anisotropic Riemannian Metric	28

2.3.5	Minimal Paths with Anisotropic Radius-Lifted Riemannian Metric	32
2.3.6	Minimal Paths with Isotropic Orientation-Lifted Riemannian Metric	33
2.3.7	General Minimal Path Model and Finsler Metric	34
2.4	Fast Marching Method	37
2.4.1	Overview of the Fast Marching Method	37
2.4.2	Isotropic Fast Marching Method with Sethian's Update Scheme	39
2.4.3	Hopf-Lax Update Scheme	42
2.4.4	Anisotropic Fast Marching Method	43
2.4.5	Adaptive Stencil-based Anisotropic Fast Marching Method	46
3	Retinal Vessel Segmentation via New Minimal Paths Models	51
3.1	Introduction	53
3.2	Anisotropy Descriptor: Optimally Oriented Flux Filter	56
3.3	Optimally Oriented Flux Filter-based Anisotropic radius-lifted Riemannian Metric Construction	58
3.4	Mask-based Keypoints Detection	59
3.4.1	Brief Introduction to Existing Keypoints Models	59
3.4.2	Euclidean Curve Length Calculation	60
3.4.3	Keypoints Definition with a Path Score	62
3.4.4	Numerical Experiments	67
3.4.5	Conclusion	69
3.5	Vessel Extraction using Dynamic Riemannian Metric and Region-Constrained Minimal Path Refinement Method	73
3.5.1	Introduction	73
3.5.2	Dynamic Riemannian Metric with Feature Consistency Penalty	74
3.5.3	Region-Constrained Minimal Path Model	77
3.5.4	Conclusion	82
3.6	Centerlines Extraction and Boundaries Delineation for Retinal Vessels via a Region-Constrained Minimal Path Model	83
3.6.1	Introduction	83
3.6.2	PreProcessing	83
3.6.3	Endpoints Correction	85
3.6.4	Experimental Results on Retinal Images	88
3.6.5	Conclusion	92
4	Anisotropic Front Propagation for Tubular Structure Segmentation	95
4.1	Introduction	96
4.2	Front Propagation for Image Segmentation	97
4.2.1	Flux-based Active Contours Model	97
4.2.2	Fast Marching Front Propagation Model	98
4.3	Front Propagation with Anisotropic Riemannian Metric and Fast Marching Method	99

4.4	Dynamic Riemannian Metric Construction	99
4.5	Experimental Results	102
4.6	Conclusion	104
5	Global Minimum for a Finsler Elastica Minimal Path Approach	107
5.1	Introduction	109
5.1.1	Motivation	112
5.1.2	Contributions	113
5.2	Finsler Elastica Minimal Path Model	114
5.2.1	Geodesic Energy Interpretation of the Euler Elastica Bending Energy via a Finsler Metric	115
5.2.2	λ Penalized Asymmetric Finsler Elastica Metric \mathcal{F}^λ	117
5.2.3	Numerical Implementations	119
5.2.4	Image Data-Driven Finsler Elastica Metric \mathcal{P}	122
5.3	Computation of Data-Driven Speed Functions by Steerable Filters	123
5.3.1	Steerable Edge Detector	123
5.3.2	Multi-Orientation Optimally Oriented Flux Filter	124
5.3.3	Computation of the Data-Driven Speed Function Φ	125
5.4	Closed Contour Detection and Tubular Structure Extraction	125
5.4.1	Closed Contour Detection as a Set of Piecewise Smooth Finsler Elastica Minimal Paths	127
5.4.2	Perceptual Grouping	129
5.4.3	Tubular Structure Extraction	130
5.5	Experimental Results	131
5.5.1	Riemannian Metrics Construction	131
5.5.2	Parameters Setting	133
5.5.3	Smoothness and Asymmetry of the Finsler Elastic Minimal Paths	133
5.5.4	Closed Contour Detection and Image Segmentation	135
5.5.5	Perceptual Grouping	139
5.5.6	Tubular Structure Extraction	140
5.6	Conclusion	145
6	Finsler Geodesics Evolution Model for Region-based Active Contours	147
6.1	Introduction	148
6.2	Region-based Active Contours Models	149
6.2.1	Mumford-Shah Functional Inspired Active Contours Models	149
6.2.2	Piecewise Constant Chan-Vese Active Contours Model	150
6.2.3	Locally Binary Fitting Model	151
6.2.4	Pairwise Region-based Active Contours Energy	153
6.3	Region-based Energy Minimization Problem	154
6.3.1	Linear Approximation of the Region-based Energy	154
6.3.2	Time-Dependent Gradient Descent Method for Energy Minimization	155

6.4	Finsler Geodesic Energy Interpretation of the Region-based Energy	157
6.4.1	Computation of Vector Field \mathcal{V} Over a Subdomain U	159
6.5	Tubular Neighbourhood Construction	164
6.6	Finsler Minimal Paths Extraction Strategy for the Minimization of $\tilde{\mathcal{L}}$	165
6.6.1	Contour Initialization	165
6.6.1.1	In Case $N_s = 2$	165
6.6.1.2	In Case $N_s \geq 3$	167
6.6.2	Fixed Points Initialization	168
6.6.3	Computation of f for various types of Region-based Active Contours Energies	168
6.7	Numerical Experiments	169
6.8	Conclusion	171
7	Summary of the Contributions and the Future Work	175
A	Proof of Finsler Elastica Minimal Paths Convergence	179
B	Numerical Solution to the Minimization Problem with Linear Constraint	185
	Bibliography	187

List of Figures

2.1	An example of gradient vector field	12
2.2	An example for level set function.	17
2.3	Image Segmentation by using geodesic active contours.	18
2.4	Geodesic active contours for object segmentation with concave region using a small value of the constant c	20
2.5	Minimal path extraction results using Cohen-Kimmel minimal path model on a curve image.	23
2.6	Single vessel extraction results by the Cohen-Kimmel minimal path model and the Li-Yezzi minimal path model.	27
2.7	Comparative vessel tree extraction results by Cohen-Kimmel and Li-Yezzi minimal path models.	27
2.8	Visualization for a typical 2D positive definite symmetric tensor by an ellipse.	29
2.9	Comparative minimal paths extraction results by using the isotropic and anisotropic Riemannian metrics, respectively.	30
2.10	Geodesic distance maps with different values of anisotropy ratio.	32
2.11	Stencil examples: 4-connectivity and 8-connectivity stencils on 2D cartesian grid.	37
2.12	Example for fast marching front.	40
2.13	Illustration for Bellman's optimality principle.	42
2.14	Demonstrations of the Uint balls for Riemannian Metrics and the respective stencils which are constructed using the method proposed by Mirebeau (2014a).	46
2.15	Demonstrations of the Uint balls for Finsler Metrics and the respective stencils which are constructed using the method proposed by Mirebeau (2014b).	48
2.16	Demonstrations of the Uint balls for Finsler Metrics and the respective stencils which are constructed using the method proposed by Mirebeau (2014b).	49
3.1	A Retinal vessel network image (left) and the corresponding vessel ground truth image (right).	53
3.2	An example of retinal vessel image and its vesselness map.	54
3.3	Steps of keypoints searching scheme.	64
3.4	Keypoints searching result with two path score thresholds.	66
3.5	Comparison between our algorithm and the classical KPSM.	67

3.6	Comparison of the classical KPSM and the proposed algorithm in real retinal image.	71
3.7	Keypoints searching result from our algorithm with curve length threshold 40.	72
3.8	Keypoints searching result from our algorithm with a large path score threshold.	72
3.9	Vessel extraction results by the Benmansour-Cohen model. Blue cross and yellow star indicate the initial source points and end points respectively.	74
3.10	An example for back-tracked points and the corresponding local geodesics in a patch of a retinal image.	75
3.11	An example for back-tracked points and the corresponding local geodesics in a synthetic image.	75
3.12	Steps for the proposed Retinal vessel extraction method.	80
3.13	Centreline bias correction.	80
3.14	Comparative Retinal vessel extraction results by the Benmansour-Cohen model and the proposed model.	81
3.15	Tubular structure preprocessing step.	84
3.16	Identifying the segments by removing the branch points and construct the constrained tubular neighbourhood region.	85
3.17	Comparative extraction results.	86
3.18	Illustration for the proposed algorithm step by step.	88
3.19	Segmentation of a retinal image by the proposed method.	89
3.20	Details of the segmentation results shown in Fig. 3.19.	90
3.21	Improved results by Endpoints Correction.	91
4.1	Illustration of the approximation of the flux computation.	97
4.2	Illustration for the various regions used in the proposed model in the course of the fast marching front propagation.	101
4.3	Front propagation based on the tensor field \mathcal{M}_c in (4.14) for different values of anisotropy ratio.	103
4.4	The course of the fast marching front propagation using isotropic fast marching front propagation method	104
4.5	Comparative vessel tree segmentation results from different methods.	105
5.1	Minimal path extraction results using different metrics.	112
5.2	Visualization for the metrics \mathcal{F}^∞ and \mathcal{F}^λ with $\alpha = 1$ by Tissot's indicatrix.	114
5.3	Approximating Euler elastica curves by Finsler elastica minimal paths with uniform speed.	120
5.4	Steps for the closed contour detection procedure.	126
5.5	Flexible Finsler minimal paths extraction on ellipse-like curves.	135
5.6	Comparative minimal paths extraction results on Spirals.	135
5.7	Finding the nearest orientation-lifted candidate to the orientation-lifted initial source point in terms of geodesic distance associated to data-driven Finsler elastica metric.	136

5.8	Finsler elastica minimal paths extraction results.	136
5.9	Comparative closed contour detection results obtained by using different metrics.	137
5.10	Closed contour detection results by using only two given physical positions and the corresponding orientations.	138
5.11	Contour detection results with different values of curvature penalization parameter α	139
5.12	Perceptual grouping results by the proposed method and Finsler elastica metric.	140
5.13	Perceptual grouping results by the proposed method and Finsler elastica metric.	141
5.14	Perceptual grouping results by the proposed method where three groups are identified.	142
5.15	Comparative blood vessel extraction results on retinal images.	143
5.16	Comparative blood vessel extraction results on fluoroscopy images.	143
5.17	Comparative arteries vessels extraction results on retinal images.	144
5.18	Retinal veins extraction results from different metrics.	145
5.19	Comparative blood vessel extraction results on blurred retinal image.	145
5.20	Roads extraction results by the proposed Finsler elastica metric in aerial image blurred by Gaussian noise.	146
6.1	Illustration of the Chan-Vese active contours model.	150
6.2	Illustration for the U -constrained shape evolution.	158
6.3	Tubular neighbourhood regions for $\tau = 0$, where we denote the neighbourhood regions by red shadow.	166
6.4	Shape evolution results of the proposed model with contour initialization and two sampled vertices.	169
6.5	Shape evolution results of the proposed model with contour initialization and four sampled vertices.	170
6.6	Shape evolution results of the proposed model with three fixed points initialization.	173
6.7	Comparative segmentation results by the level set based nonlocal active contours model (Jung et al., 2012) and the proposed model with contour initialization.	174
6.8	Comparative segmentation results by the level set based locally binary fitting model (Li et al., 2008) and the proposed model with fixed points initialization.	174

List of Tables

3.1	Comparison of the vessel extraction results for the Benmansour-Cohen model and the proposed minimal path model.	82
3.2	Comparison of our segmentation results with the second manual segmentation on the test set of DRIVE dataset.	92
3.3	Comparison of our segmentations Computation time (in Seconds) with Benmansour and Cohen (2011) model on retinal images from the test set of DRIVE dataset.	92
5.1	Computation time (in seconds) and average number of Hopf-Lax updates required for each grid point by fast marching method with $\alpha = 500$ and different values of λ on a $300^2 \times 108$ grid.	121
6.1	Computation time and evolution steps (ES) required by the proposed method with regional term f^{CV} under different pairs of (δ, d) in equations (6.54) and (6.56).	170

Notations

Ω	image domain, an open subset of \mathbb{R}^2 , $\Omega \subset \mathbb{R}^2$
$\hat{\Omega}$	radius-lifted domain
$\bar{\Omega}$	orientation-lifted domain
I	a gray level image, an integrable function $I : \Omega \rightarrow \mathbb{R}$
\mathbf{I}	a color image, a vector-valued function $\mathbf{I} : \Omega \rightarrow \mathbb{R}^3$
\mathbf{x}	a point in the image domain, $\mathbf{x} \in \Omega$
\mathbf{y}	a point in the image domain, $\mathbf{y} \in \Omega$
Γ	a regular curve
γ	another regular curve
$\mathcal{C}_{\mathbf{x},\mathbf{y}}$	a geodesic joining \mathbf{x} to \mathbf{y}
\mathbf{u}	vector field, usually defined in the image domain, $\mathbf{u} : \Omega \rightarrow \mathbb{R}^2$
\mathbf{v}	vector field, usually defined in the image domain, $\mathbf{v} : \Omega \rightarrow \mathbb{R}^2$
\mathcal{N}	unit normal field of a curve
\mathcal{M}	tensor field
\mathcal{F}	geodesic metric
∇	gradient operator
$\nabla \cdot$	divergence operator
Δ	Laplacian operator
$*$	convolution
G_σ	Gaussian function with variance σ

Chapter 1

Introduction

Image segmentation plays an essential role in the field of image processing, linking low level image processing procedure like image denoising, restoration and enhancement to the high level medical imaging applications and computer vision. The basic goal of image segmentation is to partition the image to a collection of components, which generally are disjoint to each other. Image segmentation is still a challenging problem, since different types of images may require different segmentation methods.

There are a large number of segmentation methods have been studied in the past decades. Among these methods, the class of thresholding methods is widely used which are usually taken as the rough segmentation step for the possible refined procedures, thanks to its easy implementation and low complexity. These methods make use of the grey level or color information of each pixel or group of pixels (like image patch) and assign the same label to these pixels with similar properties. However, without the regularization to the connectivity of pixels, these thresholding methods often suffer from the problem of sensitivity to noise. Furthermore, thresholding based segmentation methods lack of the ability to incorporate more complicated and useful information, such as texture, shape prior and user intervention. More advanced segmentation methods have been devoted to this field, such as the graph based models and the variational deformable models.

Graph-based segmentation methods such as the normalized cut model proposed by [Shi and Malik \(2000\)](#), the graph cut-based segmentation method ([Boykov and Funka-Lea, 2006](#)) and the random walk segmentation model ([Grady, 2006](#)). The formulation of these models assume that the images survive on the discrete domain and regard an image as a graph making up of edges and nodes. The optimization of the graph-based energies are particularly efficient, for instance, the graph cut minimization methods ([Boykov and Kolmogorov, 2004](#); [Kolmogorov and Zabini, 2004](#)). Another advantage of the graph-based segmentation models is the easy

implementation of user interaction. The popular initialization way for the methods like (Boykov and Funka-Lea, 2006) and (Grady, 2006) is to place a set of prescribed seeds, inside each desired image component. Moreover, regularization on the boundaries of the image components can be considered. The most popular regularization term is the minimization of Euclidean curve length of the boundaries. Recently, the curvature regularization methods (El-Zehiry and Grady, 2010; Schoenemann et al., 2012) are proved to have better segmentation results for objects with long and thin structures.

Active contours models are designed to minimize curve energy functionals survived on the continuous domain based on the Euler-Lagrange equations and variational principles. The basic idea of the active contours model (Kass et al., 1988) is to deform a curve or a snake to converge to the object boundaries, where the curve is controlled by the internal and external forces. Specifically, the internal force can ensure the active contours to be smooth, while the external force, computed in terms of image data, can attract the active contours toward to the boundaries. Various external forces (Cohen, 1991; Cohen and Cohen, 1993; Xie and Mirmehdi, 2008; Xu and Prince, 1998) have been proposed to improve the performance of the active contours model. The geometric active contours models (Caselles et al., 1993, 1997) are based on the Euclidean curvature motion flow. In their basic formulation, the active contours are represented by the zero value of a level set function (Osher and Sethian, 1988). These geometric models are able to deal with the topological changes automatically, thanks to the level set-based curve evolution scheme. However, based on the respective Euler-Lagrange equations and gradient descent flows, these active contours models sometimes fall into spurious edges resulted by noise or intensities inhomogeneity. Further, these active contours energies have strong non-convex formulas. Thus it is difficult to find the global minima of the energies.

The minimal path model was proposed by Cohen and Kimmel (1997) to find the global minimum of the geodesic energy by solving a nonlinear partial differential equation (PDE), instead of the linear Euler-Lagrange equation which is used in the classical geodesic active contours model (Caselles et al., 1997). The crucial point in this minimal path model is the design of the geodesic metric \mathcal{F} , where the curve energy is obtained by integrating \mathcal{F} along a regular curve Γ . Once one gets the metric \mathcal{F} , the minimal geodesics between any point in the domain and the initial source point can be determined immediately, following the calculation of the geodesic distance map. The original Cohen-Kimmel minimal path model (Cohen and Kimmel, 1997) has raised many interactive image segmentation methods via closed contour detection procedures (Appia and Yezzi, 2011; Appleton and Talbot, 2005; Benmansour and Cohen, 2009; Mille et al., 2014), where the common proposal is that the object boundaries are delineated by a set of minimal paths constrained by the user input seeds. Moreover, minimal paths-based models

are particularly suitable for tubular structure extraction (Benmansour and Cohen, 2011; Li and Yezzi, 2007).

Within this thesis, various suitable metrics \mathcal{F} are designed for different tasks of tubular structure extraction for retinal blood vessels extraction and active contours for image segmentation. The technical contributions are outlined in Chapters 3 to 6. In chapter 2 we give the introduction to deformable models which form the basis of this thesis. The main structure is outlined as follows:

- **Chapter 2** introduces the scientific background of this thesis: the deformable models including the active contours models and the minimal path models. We start this chapter from the analysis of the curve energy of the original active contours model proposed by Kass et al. (1988). Then the classical active contours models are introduced along the line of how these models are able to solve the problems suffered by the original active contours model.

In this chapter, the level set method and the fast marching method, which are the numerical tools for the active contours models and for the minimal path models, are also discussed respectively. Specifically, we make use of the state-of-art anisotropic fast marching methods introduced in (Mirebeau, 2014a,b) as the Eikonal solvers associated to the designed metrics that are used through this thesis. The details of the construction of the adaptive stencils are presented in Section 2.4.4.

- **Chapter 3** demonstrates the power of the Eikonal PDE-based minimal paths for the task of tubular structure segmentation, especially for retinal blood vessels extraction. We address the problems of finding both the centrelines and boundaries of the vessels simultaneously that are suffered by the existing state-of-the-art minimal path models.
 - Section 3.2 discusses the optimally oriented flux filter (Law and Chung, 2008) which is taken as the tubular anisotropy descriptor in this thesis for tubular structure extraction. This filter can be used to detect the probability of each pixel belonging to a vessel and the optimal orientation for each vessel point.
 - Section 3.3 introduces the details of the construction of the anisotropic radius-lifted Riemannian metric proposed by Benmansour and Cohen (2011). In the basic formulation, each point of a 3-D radius-lifted minimal path associated to this metric includes three components: the first two coordinates represent the physical position and the last coordinate is the value of the corresponding vessel radius value.
 - Section 3.4 introduces a mask-based keypoints detection method for automatic vessel tree extraction and its application for retinal vessel tree extraction. This model only requires one initial source point and

is able to iteratively find the successive keypoint which will be taken as a new initial source point for the fast marching front propagation scheme. The mask can be computed by any tubular structure detector. Based on the mask, our keypoint searching method can avoid leaking problem completely and use a small curve length threshold value.

- Section 3.5 proposes a novel dynamic anisotropic Riemannian metric-based minimal path model for interactive retinal vessel extraction. This dynamic Riemannian metric is computed by using the local back-tracked geodesic and the consistency of the additional image feature information. The main goal of this model is to extract a geodesic along which the image feature varies slowly. In this section, we show that this property is very helpful for interactive retinal blood vessel extraction. We introduce a region-constrained minimal path model to obtain both the centrelines and boundaries of the retinal blood vessel.
- Section 3.6 presents an automatic method for vessel width measurement based on the region-constrained minimal path model. This method can make use of the binary pre-segmented map to provide a collection of end points and constrained regions to the fast marching method, thus the extracted minimal paths are included inside the constrained region, which can avoid the overlapping extraction problem.
- **Chapter 4** proposes an anisotropic fast marching front propagation method for vessel tree segmentation. The main contribution of this chapter is the construction of dynamic anisotropic Riemannian metric implemented by the anisotropic fast marching method. The dynamic and anisotropic enhancement can avoid the leaking problem suffered by the classical isotropic front propagation model, which only relies on the positions.
- **Chapter 5** introduces a curvature-penalized minimal path model with an orientation-lifted Finsler elastica metric. This is done by establishing the relationship between the Euler elastica bending energy and the geodesic curve energy through a Finsler elastica metric. By solving the Eikonal PDE associated to the Finsler elastica metric, we can obtain the globally minimizing curvature-penalized minimal geodesics which can be used to approximate the Euler elastica curves.

Based on this Finsler elastica metric, we present the methods for closed contour detection, perceptual grouping and tubular structure extraction. The proposed Finsler elastica minimal path model make use of both the information of the orientation and the curvature, thus obtaining better results than the classical minimal path models.

- **Chapter 6** introduces a novel non-linear Eikonal-PDE based method for region-based active contours and image segmentation. We transform the

region-based active contours energy to the geodesic curve energy, by a Finsler metric, in terms of the divergence theorem. Therefore, the minimization of the region-based energy is turned to solve the Eikonal PDE associated to the Finsler metrics by the anisotropic fast marching method (Mirebeau, 2014b). The minimum of the corresponding Eikonal PDE is very robust and efficient. Traditional region-based active contours energy minimization strategy uses the gradient descent scheme and level set-based curve evolution method, which is sensitive to local minimum and needs a careful treatment to the parameters. In contrast, the proposed method can avoid the problems of sensitivity to local minimum and parameters. Moreover, the proposed method is very easy and natural to incorporate the user-provided information.

- **Chapter 7** summaries the main contributions of this thesis and gives the perspective future work.

Chapter 2

Active Contours and Minimal Paths

Abstract

In their basic formulation, deformable models are designed for the goal of driving a curve, closed or open, to converge to the object boundary according to some variational principles. The class of active contours models is one of the most successful and powerful models in the field of image segmentation. Active contours models have solid mathematical background and well established numerical tools to support various real world applications. Among these active contours models, the Eikonal equation based minimal path model has distinguished advantages, such as global minimum and fast numerical solution, which guarantee the wide use of this model in medical imaging like tubular structure extraction in medical imaging and boundary detection in computer vision.

In this chapter, we briefly discuss the existing well known active contours models, their respective gradient descent flows and the corresponding level set-based curve evolution scheme, and the Eikonal PDE-based minimal path models with different geodesic metrics as well as the respective numerical fast marching methods associated to these metrics.

2.1 Active Contours Models

2.1.1 Original Active Contours Model

Active contours models have been considerably studied and used for object segmentation and feature extraction during almost three decades, since the pioneering work of the active contours/snakes model proposed by Kass et al. (1988). The core idea behind this model is to deform a snake to converge at the interesting edges, where a snake is a regular parametrized curve $\Gamma : [0, 1] \rightarrow \Omega$ locally minimizing the curve energy:

$$E_{\text{Snake}}(\Gamma) = \int_0^1 (w_1 \|\Gamma'(t)\|^2 + w_2 \|\Gamma''(t)\|^2 + P(\Gamma(t))) dt, \quad (2.1)$$

with appropriate boundary conditions at the endpoints $t = 0$ and $t = 1$. Ω is the image domain. Γ' and Γ'' are the first- and second-order derivatives of the curve Γ , respectively. Positive constants w_1 and w_2 relate to the elasticity and rigidity of the curve Γ , hence weight its internal forces. This approach models object boundaries as curves Γ locally minimizing an objective energy functional E that consists of an internal force and an external force. The internal force terms depend on the first- and second-order derivatives of the curves or snakes, and respectively account for a prior of small length and of low curvature of the contours. The external force is derived from a potential function P , depending on image features like gradient magnitude, and designed to attracting the active contours or snakes to the image features of interest such as object boundaries. The function P has a small values around the interested image features, where a common P can be computed by

$$P(\mathbf{x}) = g(\|\nabla I(\mathbf{x})\|), \quad \forall \mathbf{x} \in \Omega, \quad (2.2)$$

where g is a non-negative decreasing function such as

$$g(a) = \eta_0 + \frac{1}{\eta_1 + a}, \quad \text{or} \quad g(a) = \eta_0 + \exp(-\eta_1 a), \quad a \in [0, \infty), \quad (2.3)$$

where η_0 and η_1 are positive constants.

The Euler-Lagrange equation of the energy functional E_{snake} with respect to the admissible curve Γ is expressed as

$$- \omega_1 \Gamma''(t) + \omega_2 \Gamma''''(t) + \nabla P(\Gamma(t)) = \mathbf{0}, \quad \forall t \in [0, 1], \quad (2.4)$$

which means that a curve Γ^* locally minimizing the active contours energy E_{snake} should obey the Euler-Lagrange equation (2.4). Γ'''' is the fourth order derivative

defined by

$$\Gamma''''(t) = \frac{\partial^4}{\partial t^4} \Gamma(t), \quad \forall t \in [0, 1].$$

In order to find the locally optimal contour Γ^* , applied the gradient descent method to iteratively minimize E_{snake} (2.4), which introduced a family of curve $\Gamma(\tau, \cdot) : [0, \infty) \times [0, 1] \rightarrow \Omega$ with respect to time τ .

The curve evolution formula associate to τ can be expressed as

$$\frac{\partial \Gamma}{\partial \tau} = \underbrace{\omega_1 \Gamma'' - \omega_2 \Gamma''''}_{\text{Regular Term}} - \underbrace{\nabla P(\Gamma)}_{\text{External Vector Field}}. \quad (2.5)$$

One expects the curve Γ to delineate the desired boundaries when $\tau \rightarrow \infty$. The regular term of (2.5) enforce the curves to be smooth, thus referred to an internal force

$$\mathbf{F}_{\text{smooth}} := \omega_1 \Gamma'' - \omega_2 \Gamma'''. \quad (2.6)$$

The terms ∇P is used to attract the active contours to the boundaries. This forms the external force of the active contours model:

$$\mathbf{F}_{\text{Ext}} := -\nabla P. \quad (2.7)$$

Generally, the external vector field ∇P , associated to the external force, has a small supported domain which is around the object boundaries which may lead the active contours model to be sensitive to initial curves.

The efforts for the improvements of classical active contours model (Kass et al., 1988) are mainly devoted to three drawbacks: 1) sensitive to initialization, 2) difficult to deal with topological changes of the active contours, and 3) strong non-convex curve functional energy.

- Regarding the initialization of this classical active contours model, it requires an initial guess close to the desired image features, and preferably enclosing them because energy minimization tends to shorten the snakes. The introduction of an expanding balloon force allows to be less demanding on the initial curve given inside the objective region (Cohen, 1991). Moreover, extended vector field approaches have been studied in (Cohen and Cohen, 1993; Li and Acton, 2007; Xie and Mirmehdi, 2008; Xu and Prince, 1998) to enlarge the supported domain of the external force \mathbf{F}_{Ext} , which will be introduced in next sections.
- The issue of topology changes led, on the other hand, to the development of active contour methods, which represent object boundaries as the zero level set (Osher and Sethian, 1988) of the solution to a PDE (Caselles et al., 1993,

1997; Malladi et al., 1994; Yezzi et al.), where inside and outside the active contours, values of the scalar level set function have opposite signs. Therefore, the curve evolution scheme (2.5) is transformed to the evolution of the level set function, where the topology changes can be handled automatically and naturally.

- Minimizing the active contours energy functional E_{Snake} relies on its Euler-Lagrange equation (2.4) meaning that only the local minimum of E_{snake} can be obtained. This may result that the minimizing curves Γ^* are sensitive to noise and spurious edges. Cohen and Kimmel (1997) suggested a way to obtain the global minimum of a variant of the energy functional E_{Snake} through the solution of the Eikonal PDE. This variant energy is the famous geodesic energy (Caselles et al., 1997) that removes the second-order derivative term Γ'' . Moreover, the geodesic energy is independent of the parameterization of the curve, a problem that is suffered by the classical active contours model (Kass et al., 1988).

2.1.2 Active Contours Model with Balloon Force

Cohen (1991) introduced a additional external force for the active contour models. This external force drives the contour to deform as a balloon in a inflation way. In the basic formulation, the new external balloon force can be expressed as

$$\mathbf{F}_{\text{Ballon}} := c \mathcal{N}, \quad (2.8)$$

where \mathcal{N} denotes the normal vector of the curve Γ .

Note that the balloon force $\mathbf{F}_{\text{Ballon}}$ (2.8) can be obtained by minimizing the following region-based functional

$$c \int_{R_i} d\mathbf{x},$$

where c is a constant and R_i is the region inside the curve Γ , i.e., $\Gamma = \partial R_i$.

Based on the balloon force $\mathbf{F}_{\text{Ballon}}$ (2.8), Cohen (1991) presented a new external force

$$\mathbf{F}_{\text{Ext}} = \mathbf{F}_{\text{Ballon}} - c_2 \frac{\nabla P}{\|\nabla P\|}, \quad (2.9)$$

where c_2 is a constant. The parameter c_2 should be a little larger than c . Hence the edge points can stop the evolution of the curve Γ under the control of \mathbf{F}_{Ext} (2.9). With the additional balloon force $\mathbf{F}_{\text{Ballon}}$, spurious edges produced by noise can be avoided. Moreover, the initial curve can be placed far from the boundaries, thus the balloon force based active contours model is insensitive to the initialization.

2.1.3 Active Contours with Distance Vector Flow

Cohen and Cohen (1993) presented a new external force making use of the pre-detected edge points to reduce the problem of sensitivity to the initializations of the classical active contours model (Kass et al., 1988). This method firstly computes a Euclidean distance map D for each point $\mathbf{x} \in \Omega$ where $D(\mathbf{x})$ denotes the Euclidean distance value of \mathbf{x} to the nearest edge points.

By the use of a decreasing function g (2.3), the external force of the distance vector field can be expressed as

$$\mathbf{F}_{\text{Ext}}(\mathbf{x}) := -g'(D(\mathbf{x})) \nabla D(\mathbf{x}), \quad \forall \mathbf{x} \in \Omega. \quad (2.10)$$

where ∇D is the gradient map of D , which points to the edge points. This gradient vector field can be considered as the distance competition such that the curve will be attracted to its nearest edge points. The edge points can be detected by using various edge detectors such as the Canny detector (Canny, 1986) or the higher order steerable edge detector (Freeman and Adelson, 1991; Jacob and Unser, 2004).

2.1.4 Active Contours with Gradient Vector Flow

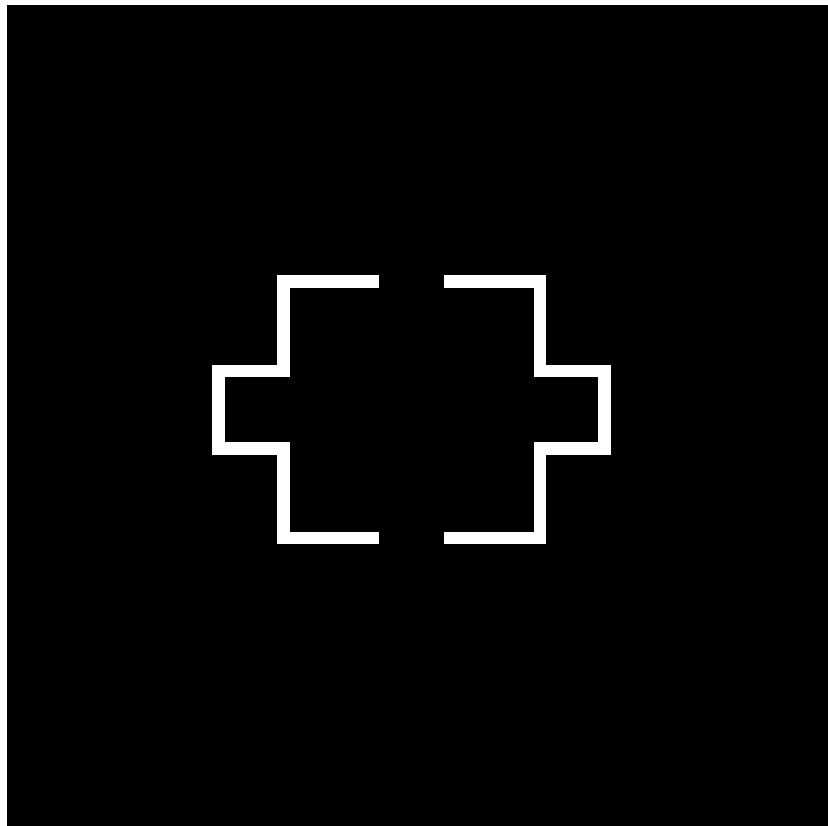
Xu and Prince (1998) proposed a new external force for active contours evolution scheme based on the diffused gradient vectors of the edge map. The basic idea is to diffuse the image gradient information to the whole image domain Ω , leading to an insensitive initialization for the active contours model.

Let $\mathbf{H} = (u, v) : \Omega \rightarrow \mathbb{R}^2$ be the expected diffused gradient vector field. \mathbf{H} can be obtained by solving the following minimization problem:

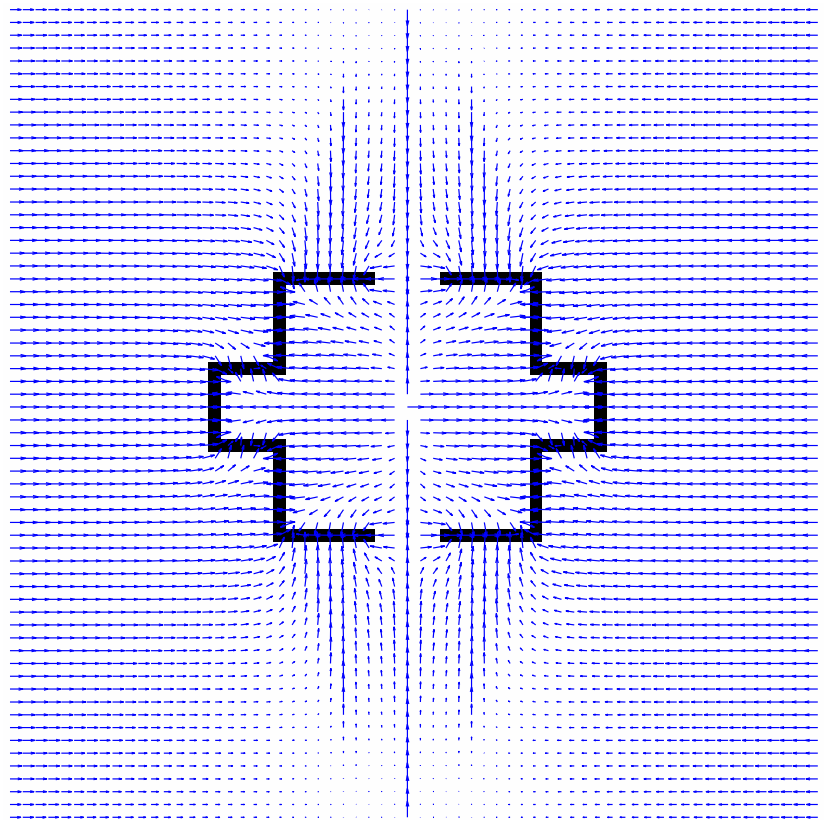
$$\min_{u,v} \left\{ \underbrace{\mu \int_{\Omega} (\|\nabla u(\mathbf{x})\|^2 + \|\nabla v(\mathbf{x})\|^2) d\mathbf{x}}_{\dagger} + \underbrace{\int_{\Omega} \|\nabla h(\mathbf{x})\|^2 \|\mathbf{H}(\mathbf{x}) - \nabla h(\mathbf{x})\|^2 d\mathbf{x}}_{\ddagger} \right\} \quad (2.11)$$

where $h(\cdot) = \|\nabla I(\cdot)\|$ is the norm of the image gradient $\nabla I(\cdot)$ and μ is a positive constant that is used to balance the importance between terms \dagger and \ddagger . The term \dagger ensures the smoothness of the vector field \mathbf{H} and \ddagger is the image data term. At the edge points, minimizing (2.11) implies that $\mathbf{H} \approx \nabla h$ since at these points the value of the norm $\|\nabla h\|$ is very large.

The gradient vector field \mathbf{H} satisfies the Euler-Lagrange equation of (2.11). Xu and Prince (1998) suggested to use the following gradient descent equation to



(a) Edge map



(b) Gradient vector field

FIGURE 2.1: An example of gradient vector field.

computed the desired vector field \mathbf{H} for any $\mathbf{x} = (x, y) \in \Omega$:

$$\frac{\partial u}{\partial \tau}(\mathbf{x}) = \mu \Delta u(\mathbf{x}) - (u(\mathbf{x}) - h_x(\mathbf{x})) \|\nabla h(\mathbf{x})\|^2, \quad (2.12)$$

$$\frac{\partial v}{\partial \tau}(\mathbf{x}) = \mu \Delta v(\mathbf{x}) - (v(\mathbf{x}) - h_y(\mathbf{x})) \|\nabla h(\mathbf{x})\|^2, \quad (2.13)$$

where $h_x = \frac{\partial h}{\partial x}$ and Δ is the Laplacian operator. If point \mathbf{x} is in homogeneous region, the norm $\|\nabla h(\mathbf{x})\| \approx 0$ and $(u(\mathbf{x}) - h_x(\mathbf{x})) \|\nabla h(\mathbf{x})\|^2$ or $(v(\mathbf{x}) - h_y(\mathbf{x})) \|\nabla h(\mathbf{x})\|^2$ will vanish. Thus in such region, the components u and v of vector field \mathbf{H} are computed by the diffusion equation which enforce the smoothness of \mathbf{H} . In contrast, if point \mathbf{x} is at the vicinity region of the image boundaries, one has

$$u(\mathbf{x}) \approx h_x(\mathbf{x}) \quad \text{and} \quad v(\mathbf{x}) \approx h_y(\mathbf{x}).$$

Then the gradient vector flow force \mathbf{F}_{GVF} can be expressed as

$$\mathbf{F}_{\text{GVF}} := \mathbf{H}, \quad (2.14)$$

or more generally, the gradient vector flow can be computed by the normalized gradient vector field of \mathbf{H}

$$\mathbf{F}_{\text{GVF}}(\mathbf{x}) := \frac{\mathbf{H}(\mathbf{x})}{\|\mathbf{H}(\mathbf{x})\|}, \quad \forall \mathbf{x} \in \Omega. \quad (2.15)$$

The gradient vector field \mathbf{H} extends the narrow band supported domain of the original image gradient vector field ∇h to the whole domain Ω , thus the active contours model controlled by the gradient vector field \mathbf{H} is insensitive to initializations. In other words, one can place the initial curve far from the object boundaries (Xu and Prince, 1998).

2.2 Level Set-based Active Contours

In this section, the level set function proposed by [Osher and Sethian \(1988\)](#) is first briefly introduced. Then based on the level set function, three typical active contours models are reviewed.

2.2.1 Level Set Method

In its basic formulation, a level set function is a scalar embedding function, the values of which have opposite signs inside and outside the closed curves. A family of time dependent curves $\Gamma : [0, \infty) \times [0, 1] \rightarrow \Omega$ is represented by the corresponding zero-level set of $\phi : [0, \infty) \times \Omega \rightarrow \mathbb{R}$:

$$\Gamma = \{\mathbf{x}; \mathbf{x} \in \Omega, \phi(\tau, \mathbf{x}) = 0\}. \quad (2.16)$$

In [Fig. 2.2](#), we show an example for a level set function. [Fig. 2.2a](#) shows a contour indicated by black curve. [Fig. 2.2b](#) shows the implicit representation of the curve in [Fig. 2.2a](#) by zero value of the level set function and [Fig. 2.2c](#) is the 3D visualization of the level set function.

Let us consider the basic curve evolution equation([Caselles et al., 1997](#); [Osher and Sethian, 1988](#)) in terms of

$$\frac{\partial \Gamma}{\partial \tau} = f \mathcal{N}, \quad (2.17)$$

where τ denotes the time, f is a given scalar function, and \mathcal{N} is the normal vector of the curve Γ . According to [\(2.16\)](#), one has

$$\phi(\tau, \Gamma) = 0, \quad (2.18)$$

which yields

$$\left\langle \nabla \phi, \frac{\partial \Gamma}{\partial \tau} \right\rangle + \frac{\partial \phi}{\partial \tau} = 0 \quad (2.19)$$

Recalling that the curve Γ is defined as the zero-level set of the scalar function ϕ , the normal vector \mathcal{N} of Γ can be interpreted by

$$\mathcal{N} = \frac{\nabla \phi}{\|\nabla \phi\|}. \quad (2.20)$$

Thus one obtains

$$\frac{\partial \phi}{\partial \tau} = - \left\langle \nabla \phi, f \frac{\nabla \phi}{\|\nabla \phi\|} \right\rangle = -f \|\nabla \phi\|, \quad (2.21)$$

which is considered as a front propagation equation with speed f .

The level set function ϕ should be reinitialized as a signed distance map in the course of the level set evolution (Osher and Sethian, 1988; Sussman et al., 1994). As discussed in (Sussman et al., 1994), at the time τ_0 , the level set reinitialization can be done by solving the following time-dependent PDE

$$\begin{cases} \frac{\partial \psi}{\partial \tau} = \text{sign}(\phi^{\tau_0})(1 - \|\nabla \psi\|), \\ \psi(0, \cdot) = \phi(\tau_0, \cdot), \end{cases} \quad (2.22)$$

where $\phi^{\tau_0}(\cdot) = \phi(\tau_0, \cdot)$ and the new level set function $\tilde{\phi}$ is equal to the solution ψ at the steady state of (2.22).

Note that the level set function can also be reinitialized by using the solution φ of the Eikonal PDE:

$$\begin{cases} \|\nabla \varphi(\mathbf{x})\| = 1, & \forall \mathbf{x} \in \Omega \setminus \Psi_0, \\ \varphi(\mathbf{x}) = 0, & \forall \mathbf{x} \in \Psi_0, \end{cases} \quad (2.23)$$

where Ψ_0 is defined as a collection

$$\Psi_0 := \{\mathbf{x} \in \Omega; \psi(\tau_0, \mathbf{x}) = 0\}.$$

The desired reinitialized level set function $\tilde{\phi}$ can be computed by

$$\tilde{\phi} = \text{sign}(\phi^{\tau_0}) \varphi.$$

The Eikonal PDE (2.23) can be solved the isotropic fast marching method (Sethian, 1996, 1999) or by the GPU-accelerated fast sweeping method proposed by (Weber et al., 2008).

Li et al. (2010) proposed a new method to avoid the level set reinitialization operation. This is done by minimizing the following term

$$\int_{\Omega} \mathcal{P}_{\text{Regu}}(\|\nabla \phi(\mathbf{x})\|) d\mathbf{x}, \quad (2.24)$$

where $\mathcal{P}_{\text{Regu}}$ is a potential function. One possible choice for this potential function, as suggested In (Li et al., 2010), can be formulated as

$$\mathcal{P}_{\text{Regu}}(x) = \frac{1}{2}(x - 1)^2. \quad (2.25)$$

Minimizing (2.24) with respect to the potential function formulated in (2.25) is used to enforce $\|\nabla \phi\| \equiv 1$, which implies that ϕ is a distance function. However, the potential function $\mathcal{P}_{\text{Regu}}$ (2.25) may suffer from the *side effect* problem (Li et al., 2010). To solve this problem, Li et al. (2010) designed a double-well potential

function

$$\mathcal{P}_{\text{Regu}}(x) = \begin{cases} \frac{1}{4\pi^2}(1 - \cos(2\pi x)), & \text{if } x \leq 1, \\ \frac{1}{2}(x - 1)^2, & \text{if } x \geq 1, \end{cases}$$

which is twice differentiable.

2.2.2 Geometric Active Contours

The geometric active contours model was proposed by [Caselles et al. \(1993\)](#) and [Malladi et al. \(1994\)](#) for object boundary detection, by driving the contours according to the following flow:

$$\frac{\partial \Gamma}{\partial \tau} = g(\kappa + c)\mathcal{N}, \quad (2.26)$$

where g is the image data function defined in (2.3), c is a positive constant and κ is the curvature of curve Γ . Actually, g plays the role of stopping function which can stop the evolution of Γ when it arrives at the real object boundaries, since at these boundaries one has $g \approx 0$.

The curve evolution flow (2.26) is actually based on the Euclidean curvature flow or Euclidean heat flow

$$\frac{\partial \Gamma}{\partial \tau} = \kappa \mathcal{N}, \quad (2.27)$$

which can shorten and smooth the curve Γ . This flow can drive the curve Γ to minimize its curve length functional

$$\int_0^1 \|\Gamma'(t)\| dt$$

in the gradient direction ([Caselles et al., 1993](#)). By incorporating the curve Γ into the level set function ϕ , we can obtain the level set evolution equation according to (2.26) as follows:

$$\frac{\partial \phi}{\partial \tau} = \left(\nabla \cdot \left(\frac{\nabla \phi}{\|\nabla \phi\|} \right) + c \right) g \|\nabla \phi\|, \quad (2.28)$$

where $\nabla \cdot \mathbf{u}$ denotes the divergence value of vector \mathbf{u} . This level set evolution equation is based on the fact that

$$\kappa = \nabla \cdot \left(\frac{\nabla \phi}{\|\nabla \phi\|} \right).$$

Corresponding to the general level set-based curve evolution flow (2.21), we have that the speed function $f = g(c + \kappa)$. When the curve Γ is far from the boundary, the stopping function g can be considered as a positive constant such that the

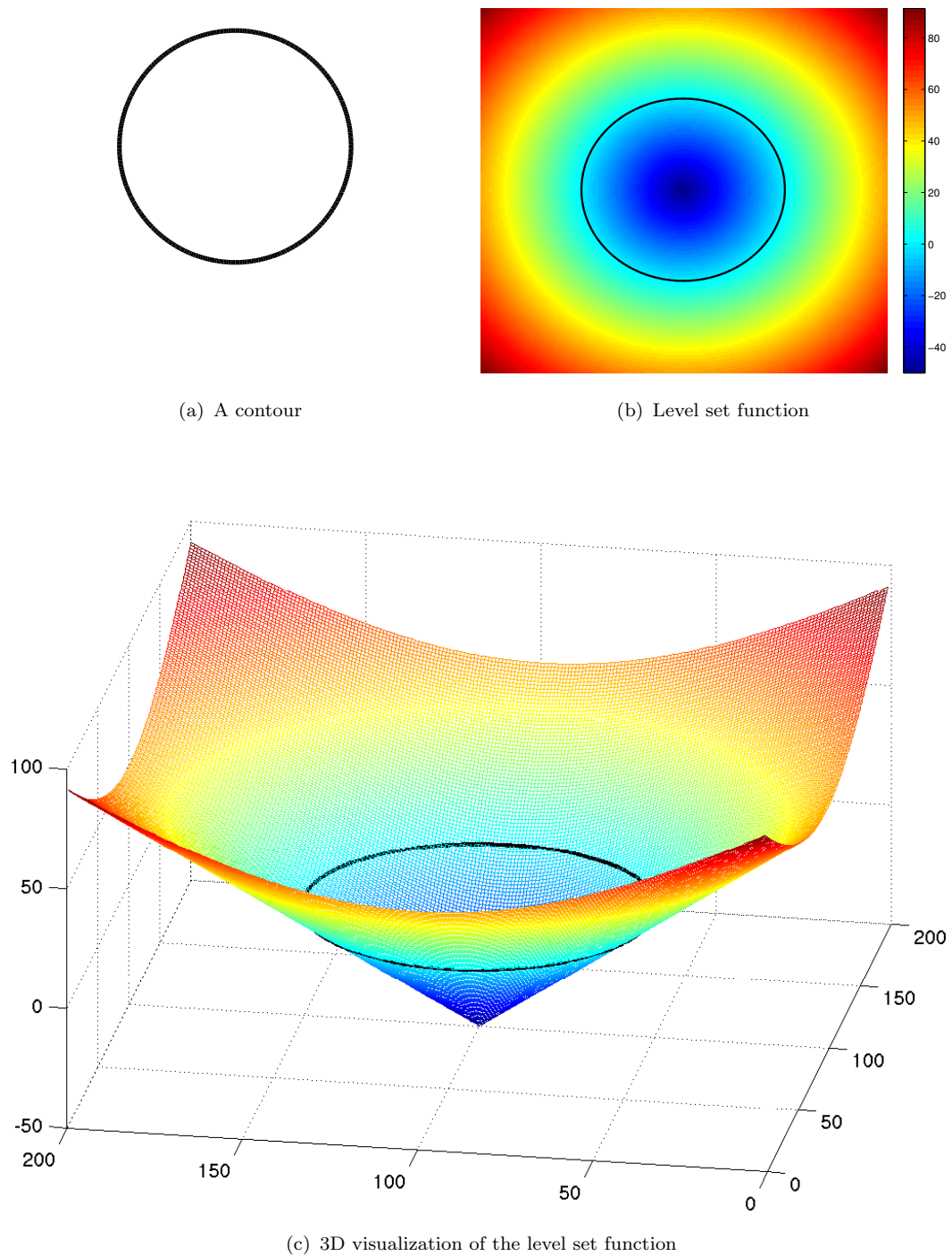


FIGURE 2.2: An example for level set function. **(a)** A contour indicated by a black closed curve. **(b)** Implicit representation for the curve demonstrated in (a) by the zero value of the level set function. **(c)** 3D visualization for the level set function shown in (b).

behaviour of the curve mainly is controlled by the Euclidean heat flow $\kappa \mathcal{N}$ and



(a) Initial contour



(b) Intermediate result



(c) Final result

FIGURE 2.3: Image Segmentation by using geodesic active contours. (a) Original image and initial contour. (b) Intermediate segmentation result. (c) Final segmentation result.

the balloon force $c\mathcal{N}$. When Γ is close to the boundaries, one has $g \approx 0$ such that the evolution of the contour will be terminated.

This level set based geometric active contours model can deal with curve topology changes automatically. The initial curve can be placed outside the object and far from its boundaries. Moreover, starting from a convex curves, one can obtain a non-convex final contours represented by the zero value of level set function ϕ .

2.2.3 Geodesic Active Contours

The famous geodesic active contours model proposed by Caselles et al. (1997) aims at finding a locally optimal curve Γ^* to (locally) minimize the geodesic energy in a Riemannian space with a isotropic Riemannian metric

$$E_{\text{GAC}}(\Gamma) = \int_0^1 P(\Gamma(t)) \|\Gamma'(t)\| dt, \quad (2.29)$$

with potential function P . This energy removed the second-order derivative term of the curve Γ from the classical snakes energy E_{Snake} in (2.1). The gradient flow of the geodesic energy E_{GAC} can be expressed as (Caselles et al., 1997; Kichenassamy et al., 1995)

$$\frac{\partial \Gamma}{\partial \tau} = (g \kappa + \langle \nabla g, \mathcal{N} \rangle) \mathcal{N}. \quad (2.30)$$

The term of $\langle \nabla g, \mathcal{N} \rangle$ can push the curve toward the valley of the stopping function g (Caselles et al., 1997). This property is very useful for purpose of detecting a boundary that passes through the regions with inhomogeneous intensities and high noise.

In order to improve the performance of the geodesic gradient flow (2.30) to deal with the detection of boundaries with high curvature, Caselles et al. (1997) give the gradient flow by adding a constant c as

$$\frac{\partial \Gamma}{\partial \tau} = \left((g + c) \kappa + \langle \nabla g, \mathcal{N} \rangle \right) \mathcal{N}. \quad (2.31)$$

The behaviour of this geodesic gradient flow can be divided to two cases:

- When the curve is close to the boundary, the stopping function g is degenerated to a constant and $\nabla g = 0$. The gradient flow (2.31) is identical to the Euclidean heat flow: the curve tends to shrink to a point.
- When the curve is close to the boundary, the stopping function g have small values and the force $\langle \nabla g, \mathcal{N} \rangle$ will push or pull the curve to the explicit boundary where each point \mathbf{x}_b at the boundary obeying that $\nabla g(\mathbf{x}_b) = \mathbf{0}$.

By combining with the level set function ϕ , we can obtain the level set evolution equation:

$$\frac{\partial \phi}{\partial \tau} = (g + c) \text{div} \left(\frac{\nabla \phi}{\|\nabla \phi\|} \right) \|\nabla \phi\| + \langle \nabla g, \nabla \phi \rangle, \quad (2.32)$$

which is a geometric front propagation approach. In Fig. 2.3 we show the segmentation result using the geodesic active contours model. Fig. 2.3a is the original image with initial contour indicated by red curve, Fig. 2.3b is the intermediate result and Fig. 2.3c is the final segmentation contour.

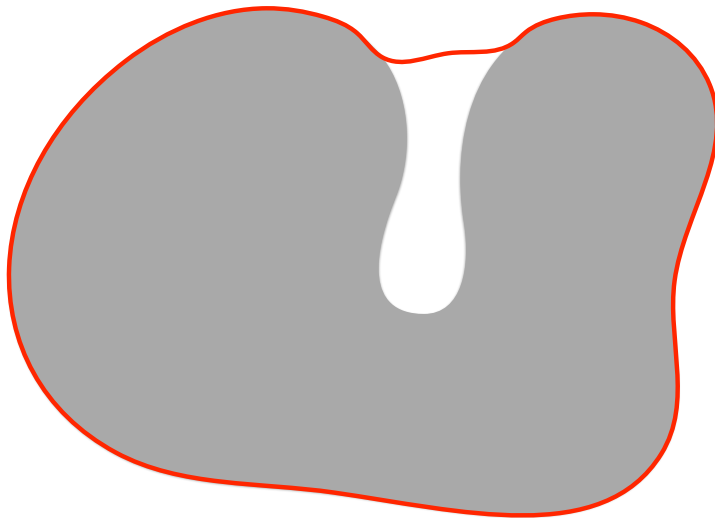


FIGURE 2.4: Geodesic active contours for object segmentation with concave region using a small value of the constant c .

Note that the constant c in the flows (2.26) and (2.30) should be treated carefully. This parameter is used to address the possible shortcuts problem when dealing with the segmentation task for the object with concave region. In this case, when the value of the constant c is very small, the curve evolution might be stopped before it follows the expected boundary. We illustrate this shortcuts problem in Fig. 2.4. However, if the value of c is too large, some parts of the active contours may stop inside the object.

2.2.4 Alignment Active Contours

Kimmel and Bruckstein (2003) and Kimmel (2003) presented a novel active contours model with the energy function consisting of an alignment term:

$$E_{\text{Align}}(\Gamma) = \int_0^1 \langle \nabla I(\Gamma(t)), \mathcal{N} \rangle \|\Gamma'(t)\| dt, \quad (2.33)$$

where ∇I is the gradient vector field of the given image I . This model adds the anisotropy of the path to the energy such that tangents of the obtained optimal curve should be consistent to the image gradient vector field ∇I . The gradient flow of E_{Align} can be expressed as

$$\frac{\partial \Gamma}{\partial \tau} = \Delta I \mathcal{N}, \quad (2.34)$$

where ΔI is defined for each $\mathbf{x} = (x, y) \in \Omega$ as

$$\Delta I(\mathbf{x}) = \frac{\partial^2 I}{\partial x^2}(\mathbf{x}) + \frac{\partial^2 I}{\partial y^2}(\mathbf{x}).$$

A robust version of the energy E_{Align} is proposed by [Kimmel \(2003\)](#); [Kimmel and Bruckstein \(2003\)](#):

$$E_{\text{Ralign}}(\Gamma) = \int_0^1 \left| \langle \nabla I(\Gamma(t)), \mathcal{N} \rangle \right| \|\Gamma'(t)\| dt \quad (2.35)$$

with the gradient flow of

$$\frac{\partial \Gamma}{\partial \tau} = \frac{\langle \nabla I, \mathcal{N} \rangle}{\|\langle \nabla I, \mathcal{N} \rangle\|} \Delta I \mathcal{N}. \quad (2.36)$$

The values of the term $\frac{\langle \nabla I, \mathcal{N} \rangle}{\|\langle \nabla I, \mathcal{N} \rangle\|}$ denote actually the sign map of the align term $\langle \nabla I, \mathcal{N} \rangle$.

2.3 Cohen-Kimmel Minimal Path Model and its Extensions

In this section, we fix the image domain $\Omega \subset \mathbb{R}^d$ where $d = 2$ or $d = 3$. We set the radius-lifted domain as $\hat{\Omega} = \Omega \times [R_{\min}, R_{\max}] \subset \mathbb{R}^{d+1}$ where $[R_{\min}, R_{\max}]$ is the admissible radius space and the orientation-lifted domain $\bar{\Omega} = \Omega \times \mathbb{S}^1 \subset \mathbb{R}^{d+1}$, where $\mathbb{S}^1 = [0, \pi)$ or $[0, 2\pi)$.

2.3.1 From Active Contours to Eikonal PDE-based Minimal Paths

The difficulty of minimizing the non-convex snakes energy (Kass et al., 1988)

$$E_{\text{Snake}}(\Gamma) = \int_0^1 (w_1 \|\Gamma'(t)\|^2 + w_2 \|\Gamma''(t)\|^2 + P(\Gamma(t))) dt, \quad (2.37)$$

leads to important practical problems, since the curve optimization procedure is often stuck at unexpected local minima of the energy functional E_{Snake} (2.37), making the results heavily rely on curve initialization and sensitive to image noise. This is still the case for the level set approach on geometric or geodesic active contours (Caselles et al., 1993, 1997; Malladi et al., 1995). In order to address this local minimum sensitivity issue, Cohen and Kimmel (1997) proposed an Eikonal PDE-based minimal path model, with goal of finding the global minimum of the geodesic energy which is similar to that used in (Caselles et al., 1997), in which the penalty associated to the second-order derivative of the curve was removed from the snakes energy. Thus the reduced energy functional is

$$\int_0^1 (w + P(\Gamma(t))) \|\Gamma'(t)\| dt,$$

the local minimizer of which was proved to be a geodesic in (Caselles et al., 1997). Alternately, Cohen and Kimmel (1997) proposed a non-linear PDE based approach to find the *global* minimizer of this geodesic energy. Thanks to this approach, a fast, reliable and globally optimal numerical method allows to find the energy minimizing curve with prescribed endpoints; namely the fast marching method (Sethian, 1999), based on the formalism of viscosity solutions to Eikonal PDE. These mathematical and algorithmic guarantees of Cohen and Kimmel's minimal path model have important practical consequences, leading to various approaches for image analysis and medical imaging (Benmansour and Cohen, 2011; Cohen, 2001; Deschamps and Cohen, 2001; Li and Yezzi, 2007; Mille et al., 2014; Peyré et al., 2010).

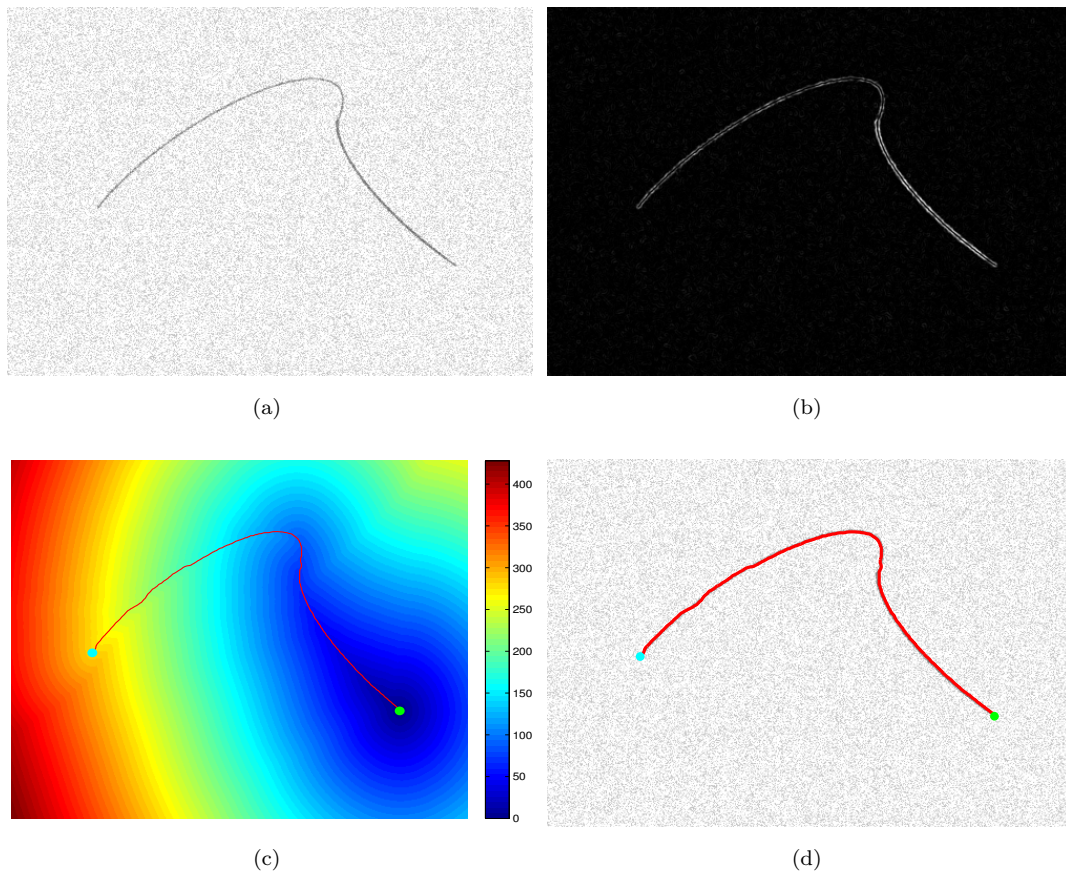


FIGURE 2.5: Minimal path extraction results using Cohen-Kimmel minimal path model on a curve image. **(a)** Original image contains a curve and noise. **(b)** Gradient magnitude map. **(c)** The minimal action map. **(d)** The extracted minimal path indicated by red line. In **(c)** and **(d)** green and cyan dots are the initial source points and end points, respectively.

2.3.2 Cohen-Kimmel Minimal Path Model

The classical Cohen-Kimmel model (Cohen and Kimmel, 1997) was designed to find the global minimum of the following geodesic energy functional as a simplification of the active contour energy (Kass et al., 1988)

$$\mathcal{L}^I(\Gamma) = \int_0^1 \left(w + P(\Gamma(t)) \right) \|\Gamma'(t)\| dt, \quad (2.38)$$

where

$$\Gamma'(t) = \frac{d}{dt}\Gamma(t).$$

$\|\cdot\|$ denotes the canonical Euclidean norm on \mathbb{R}^d and $\Gamma : [0, 1] \rightarrow \Omega$ is a Lipschitz curve. P is the potential function defined over the image domain Ω and w is a positive constant. Potential P usually depends on the image gradient magnitudes or intensities as suggested by Cohen and Kimmel (1997). A minimizer of \mathcal{L}^I is

a single minimal geodesic between two given points in the approach of Eikonal minimal path theorem.

The minimal action map or geodesic distance map \mathcal{U} from a source point \mathbf{s} , is the minimal curve length of \mathcal{L}^1 (2.38) among all regular paths joining the initial source point \mathbf{s} to any point $\mathbf{x} \in \Omega$:

$$\mathcal{U}(\mathbf{x}) := \inf \{ \mathcal{L}^1(\gamma); \gamma \in \mathcal{A}_{\mathbf{s},\mathbf{x}} \}, \quad (2.39)$$

where $\mathcal{A}_{\mathbf{s},\mathbf{x}}$ is the collection of all Lipschitz regular paths:

$$\Gamma : [0, 1] \rightarrow \Omega, \quad s.t. \quad \Gamma(0) = \mathbf{s}, \quad \text{and} \quad \Gamma(1) = \mathbf{x}.$$

The minimal action map \mathcal{U} actually defines a level set function of the arrival time starting from the initial source point s with speed function $1/\tilde{P}$ (Caselles et al., 1997). A level set contour $\Gamma(\tau, \cdot)$ is defined by the time τ :

$$\Gamma := \{ \mathbf{x} \in \Omega; \mathcal{U}(\mathbf{x}) = \tau \}. \quad (2.40)$$

These level set contours follow the level set evolution equation:

$$\frac{\partial \Gamma}{\partial \tau} = \frac{1}{\tilde{P}} \mathcal{N}, \quad (2.41)$$

where \mathcal{N} is the unitary normal vector of Γ . (2.41) is actually a front propagation equation with speed function $1/\tilde{P}$ which can propagate geodesic distance values for each point in the image domain. It acts as the curve evolution driven by a adaptive ballon force $\tilde{P}^{-1}\mathcal{N}$ (Cohen, 1991) with the initial contour as a small circle contour around the initial source point \mathbf{s} .

From (2.40), we can obtain that

$$\mathcal{U}(\Gamma) = \tau,$$

which yields that

$$\frac{\partial \mathcal{U}}{\partial \tau} = \left\langle \nabla \mathcal{U}, \frac{\partial \Gamma}{\partial \tau} \right\rangle = 1.$$

Considering the level set evolution equation (2.41), we obtain that

$$\begin{aligned} \left\langle \nabla \mathcal{U}, \frac{\partial \Gamma}{\partial \tau} \right\rangle &= \frac{1}{\tilde{P}} \left\langle \nabla \mathcal{U}, \frac{\nabla \mathcal{U}}{\|\nabla \mathcal{U}\|} \right\rangle = 1 \\ \Rightarrow \|\nabla \mathcal{U}(\mathbf{x})\| &= \tilde{P}(\mathbf{x}), \quad \mathbf{x} \in \Omega. \end{aligned} \quad (2.42)$$

The nonlinear partial differential equation in (2.42) is the isotropic Eikonal equation:

$$\begin{cases} \|\nabla\mathcal{U}(\mathbf{x})\| = \tilde{P}(\mathbf{x}), & \forall \mathbf{x} \in \Omega \setminus \{\mathbf{s}\}, \\ \mathcal{U}(\mathbf{s}) = 0, \end{cases} \quad (2.43)$$

which is the unique solution of the definition of the minimal action map (2.39). Cohen and Kimmel (1997) provided three methods to solve this Eikonal equation: the front propagation approach, the shape from shading approach and the fast marching method. The authors eventually recommended the fast marching method (Sethian, 1996, 1999) as the numerical Eikonal solver thanks to its efficient geodesic distance computation scheme.

A geodesic $\hat{\mathcal{C}}_{\mathbf{x},\mathbf{s}}$ with $\|\hat{\mathcal{C}}'_{\mathbf{x},\mathbf{s}}(\cdot)\| = 1$ can be obtained through the gradient descent ordinary differential equation (ODE):

$$\begin{cases} \hat{\mathcal{C}}'_{\mathbf{x},\mathbf{s}}(t) \propto -\nabla\mathcal{U}(\hat{\mathcal{C}}_{\mathbf{x},\mathbf{s}}(t)), \\ \hat{\mathcal{C}}_{\mathbf{x},\mathbf{s}}(0) = \mathbf{x}, \end{cases} \quad (2.44)$$

where \propto denotes the positively propositional operator. Then the geodesic $\mathcal{C}_{\mathbf{s},\mathbf{x}}$ is obtained by reversing the path $\hat{\mathcal{C}}_{\mathbf{x},\mathbf{s}}$ with $\mathcal{C}_{\mathbf{s},\mathbf{x}}(0) = \mathbf{s}$ and $\mathcal{C}_{\mathbf{s},\mathbf{x}}(1) = \mathbf{x}$.

Generally, the minimal path extraction can be divided into two steps. The first step is to calculate the minimal action map \mathcal{U} by solving the Eikonal equation (2.43). Next step is to compute the geodesic by solving the ODE (2.44). In Fig. 2.5, we show an example of the Cohen-Kimmel minimal path model. Fig. 2.5a shows the original image contains a curve. Fig. 2.5b shows the gradient magnitude map, Fig. 2.5d shows the minimal action map, and Fig. 2.5c demonstrates the minimal path by red curve. In this figure, green and cyan dots indicate the initial source point and end point respectively.

The Cohen-Kimmel minimal path model is based on the isotropic Riemannian metric \mathcal{R}^I for all $\mathbf{x} \in \Omega$ and any tangent vector $\mathbf{u} \in \mathbb{R}^d$:

$$\mathcal{R}^I(\mathbf{x}, \mathbf{u}) = \sqrt{\langle \mathbf{u}, \mathcal{M}_I(\mathbf{x}) \mathbf{u} \rangle}, \quad (2.45)$$

where $\langle \cdot, \cdot \rangle$ denotes the scalar product over \mathbb{R}^d and \mathcal{M}_I denotes the symmetric positive definite tensor field which is proportional to the identity matrix \mathbf{I}_d with $d = 2$ or 3 denoting the dimension of the image domain Ω :

$$\mathcal{M}_I(\mathbf{x}) = (w + P(\mathbf{x}))^2 \mathbf{I}_d. \quad (2.46)$$

The parameter $w \in \mathbb{R}^+$ in (2.45) controls the bound of the curvature of the minimal geodesic (Cohen and Kimmel, 1997). More precisely, the curvature $|\kappa|$ of

a geodesic \mathcal{C} that is defined by

$$|\kappa| = \left\| \frac{\partial^2 \mathcal{C}}{\partial s^2} \right\|,$$

is bounded by

$$|\kappa| \leq \frac{\|P\|_\infty}{\omega},$$

where s denotes the arclength parameter, i.e., $\|\mathcal{C}'(s)\| = 1$.

For the applications of the image analysis, object boundaries or tubular structures like roads or blood vessels, are extracted under the form of minimal paths with respect to a isotropic Riemannian metric over the image domain (Cohen and Kimmel, 1997).

The extended minimal path models of Cohen-Kimmel model focus on the extensions of the design of metric. The isotropic Riemannian metric \mathcal{R}^I used in (Cohen and Kimmel, 1997) is isotropic since it depends only on the positions of the geodesics. Bougleux et al. (2008), Jbabdi et al. (2008) and Benmansour and Cohen (2011) extended the metric \mathcal{R}^I to anisotropic case in the sense that the geodesic metric depends on both the path orientation and its positions. The isotropic Riemannian metric \mathcal{R}^I can also be defined on the physical space (image domain) Ω , or involve additional abstract variables such as the tubular structure radius (Benmansour and Cohen, 2011; Li and Yezzi, 2007), orientations (Kimmel and Sethian, 2001) or both of the radius and orientations (Péchaud et al., 2009).

2.3.3 Minimal Paths with Isotropic Radius-Lifted Riemannian Metric

The classical minimal path method (Cohen and Kimmel, 1997) models image features as minimal paths. This treatment is suitable for boundary detection but fails in vessel detection. Since in the task of vessel extraction, one would like to obtain both the centrelines and the corresponding radius values.

In order to solve this problem, i.e., to extract the centrelines and boundaries of the tubular structure simultaneously, Li and Yezzi (2007) proposed a novel minimal path model relying on a isotropic radius-lifted Riemannian metric $\mathcal{R}^{IR} : \hat{\Omega} \times \mathbb{R}^{d+1} \rightarrow \mathbb{R}^+$ over the radius-lifted domain $\hat{\Omega} \subset \mathbb{R}^{d+1}$:

$$\mathcal{R}^{IR}(\hat{\mathbf{x}}, \hat{\mathbf{u}}) = P_{IR}(\hat{\mathbf{x}}) \sqrt{\|\mathbf{u}\|^2 + \epsilon |\nu|^2}, \quad (2.47)$$

for all $\hat{\mathbf{x}} \in \hat{\Omega}$ and any vector $\hat{\mathbf{u}} = (\mathbf{u}, \nu) \in \mathbb{R}^d \times \mathbb{R}$. The radius-lifted domain $\hat{\Omega}$ is constructed by adding an additional abstract radius dimension to the image domain. Therefore, a path $\gamma : [0, 1] \rightarrow \hat{\Omega}$ has two components: the physical position



FIGURE 2.6: Single vessel extraction results by the Cohen-Kimmel minimal path model and the Li-Yezzi minimal path model. **Left:** Minimal paths extracted by Cohen-Kimmel model. **Rigth:** Minimal paths extracted by Li-Yezzi model. Red dots are the initial source points and cyan dots are the end points. Red curve is the minimal path and blue contours are the boundaries of vessel tree.

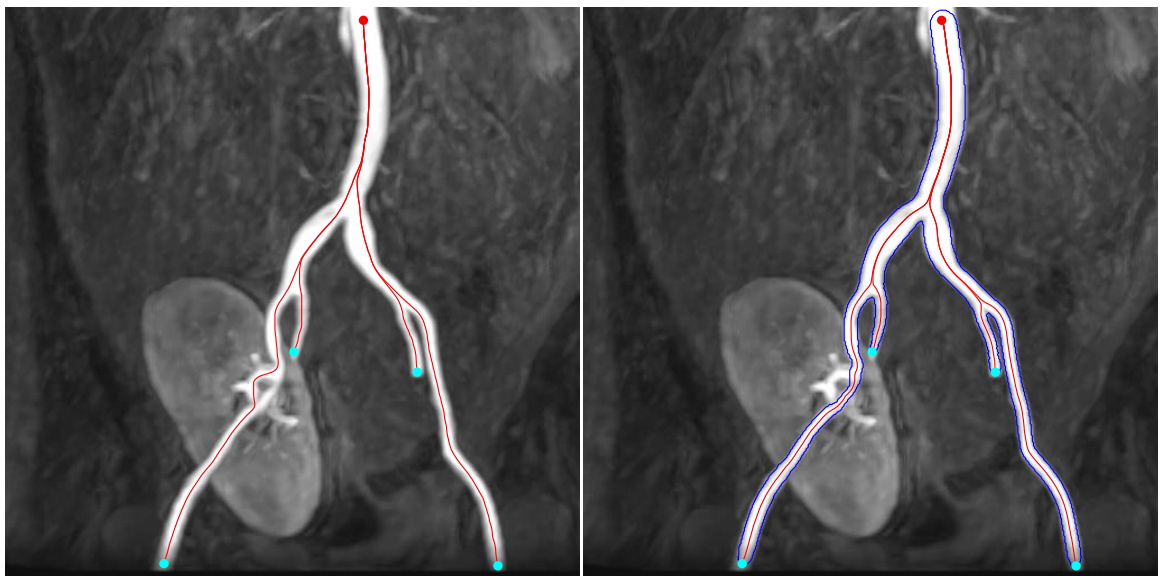


FIGURE 2.7: Comparative vessel tree extraction results by Cohen-Kimmel and Li-Yezzi minimal path models. **Left:** Minimal paths extracted by Cohen-Kimmel model. **Rigth:** Minimal paths extracted by Li-Yezzi model. Red dots are the initial source points and cyan dots are the end points. Red curves are the minimal paths and blue contours are the boundaries of vessel tree.

part and the radius values part. Such a property has important in the clinical applications. In Fig. 2.6, we show the comparison of the Cohen-Kimmel model

(Cohen and Kimmel, 1997) and Li-Yezzi model (Li and Yezzi, 2007) in the vessel extraction experiment. In this figure, the results from the Cohen-Yezzi model are unable to find the centrelines and boundaries simultaneously. In contrast, Li-Yezzi model can obtain the desired results. In Fig. 2.6, we show the vessel tree extraction results from the Cohen-Kimmel model and Li-Yezzi model respectively. It can be seen from Figs. 2.6 and 2.7 that the Li-Yezzi model is able to find the precise centrelines as well as the boundaries of the vessels.

The length of the radius-lifted path $\gamma = (\Gamma, r) : [0, 1] \rightarrow \hat{\Omega}$ can be defined by

$$\mathcal{L}^{\text{IR}}(\gamma) = \int_0^1 \frac{1}{P_{\text{IR}}(\gamma(t))} \sqrt{\|\Gamma'(t)\|^2 + \epsilon |r'(t)|^2} dt, \quad (2.48)$$

where P_{IR} is an image data-driven speed function and ϵ is positive constant. The symmetric positive definite tensor field \mathcal{M}_{IR} for the metric \mathcal{R}^{IR} is expressed by

$$\mathcal{M}_{\text{IR}}(\hat{\mathbf{x}}) = P_{\text{IR}}^2(\hat{\mathbf{x}}) \begin{pmatrix} 1 & 0 & | & 0 \\ 0 & 1 & | & 0 \\ 0 & 0 & | & \epsilon \end{pmatrix}, \quad (2.49)$$

which is proportional to a diagonal matrix. Based on the tensor field \mathcal{M}_{IR} (2.49), the curve length \mathcal{L}^{IR} can be rewritten as

$$\mathcal{L}^{\text{IR}}(\gamma) = \int_0^1 \sqrt{\langle \gamma'(t), \mathcal{M}_{\text{IR}}(\gamma(t)) \gamma'(t) \rangle} dt,$$

where $\gamma'(t) = (\Gamma'(t), r'(t))$, $\forall t \in [0, 1]$.

2.3.4 Minimal Paths with Anisotropic Riemannian Metric

Both the Cohen-Kimmel model (Cohen and Kimmel, 1997) and Li-Yezzi model (Li and Yezzi, 2007) rely only on the position of the geodesics and are unable to take into account of the path orientation, which sometimes leads to the shortcuts problem.

In order to introduce the anisotropy to the minimal path framework, Bougleux et al. (2008) and Jbabdi et al. (2008) extended the isotropic Riemannian metric \mathcal{R}^{I} (2.45) to the anisotropic case, where the symmetric positive definite tensor field \mathcal{M}_{I} in (2.46) can be replaced by \mathcal{M}_{A} defined by:

$$\mathcal{M}_{\text{A}}(\mathbf{x}) = \sum_{i=1}^d P_i^s(\mathbf{x}) \mathbf{v}_i(\mathbf{x}) \mathbf{v}_i^{\text{T}}(\mathbf{x}), \quad (2.50)$$

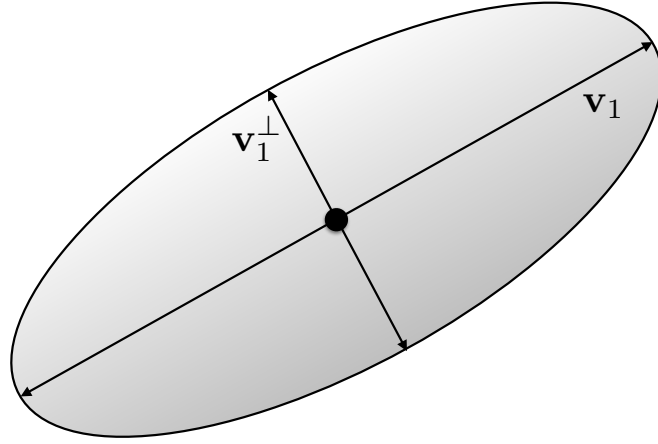


FIGURE 2.8: Visualization for a typical 2D positive definite symmetric tensor by an ellipse.

where d is the dimension of the image domain Ω . P_i^s is image data dependent function associated to the direction $\mathbf{v}_i \in \mathbb{R}^d$. Particularly, when $d = 2$, one has

$$\mathcal{M}_A(\mathbf{x}) = P_1^s(\mathbf{x}) \mathbf{v}_1(\mathbf{x}) \mathbf{v}_1^T(\mathbf{x}) + P_2^s(\mathbf{x}) \mathbf{v}_2(\mathbf{x}) \mathbf{v}_2^T(\mathbf{x}), \quad (2.51)$$

where $\mathbf{v}_2(\mathbf{x})$ is perpendicular to vector $\mathbf{v}_1(\mathbf{x})$ for all $\mathbf{x} \in \Omega$.

Based on the tensor field \mathcal{M}_A , the anisotropic Riemannian metric $\mathcal{R}^A : \Omega \times \mathbb{R}^d \rightarrow \mathbb{R}^+$ can be expressed as:

$$\mathcal{R}^A(\mathbf{x}, \mathbf{u}) = \sqrt{\langle \mathbf{u}, \mathcal{M}_A(\mathbf{x}) \mathbf{u} \rangle}, \quad \forall \mathbf{x} \in \Omega \text{ and } \forall \mathbf{u} \in \mathbb{R}^d. \quad (2.52)$$

In Fig. 2.8, we visualize the 2-D tensor \mathcal{M}_A^{-1} (2.51) by an ellipse. The black dot denotes the centre point \mathbf{x} . In this figure, we suppose that $P_1^s(\mathbf{x}) \leq P_2^s(\mathbf{x}), \forall \mathbf{x} \in \Omega$.

The anisotropy ratio μ of the metric \mathcal{R}^A is defined by

$$\mu(\mathcal{R}^A) := \sup_{\mathbf{x} \in \Omega} \left\{ \max_{\|\mathbf{u}\|=\|\mathbf{v}\|=1} \frac{\mathcal{R}^A(\mathbf{x}, \mathbf{u})}{\mathcal{R}^A(\mathbf{x}, \mathbf{v})} \right\}. \quad (2.53)$$

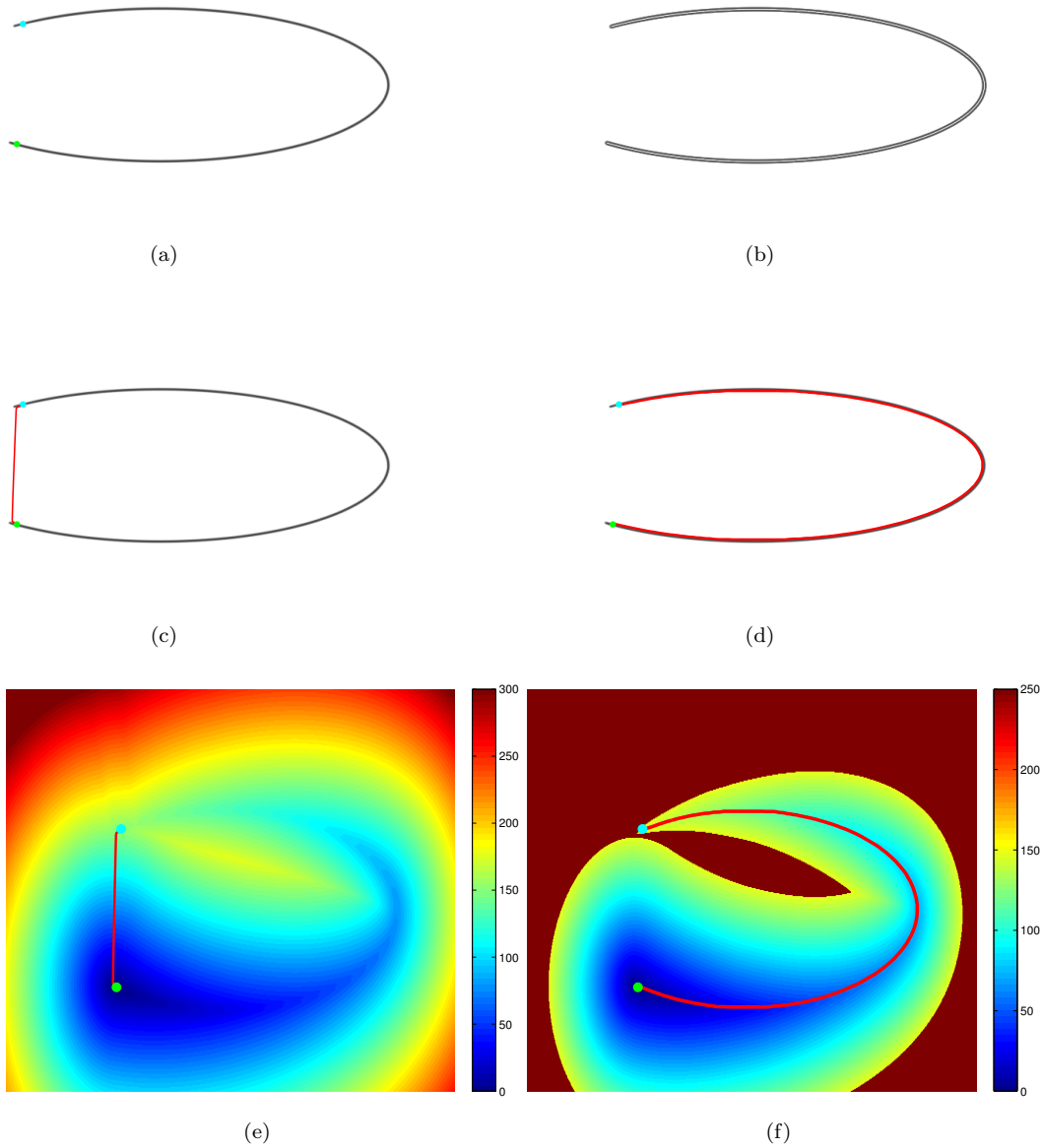


FIGURE 2.9: Comparative minimal paths extraction results by using the isotropic and anisotropic Riemannian metrics, respectively. **(a)** is the original image with initial source point (green dot) and end point (cyan dot). **(b)** Potential function used in the isotropic metric. **(c)** and **(d)** are the minimal paths extracted by using the isotropic metric and anisotropic metric respectively. **(e)** and **(f)** are the corresponding geodesic maps of **(c)** and **(d)**.

The minimal action map or geodesic distance map \mathcal{U} from the initial source point \mathbf{s} with respect to the anisotropic Riemannian metric \mathcal{R}^A can be obtained by solving the following anisotropic Eikonal PDE:

$$\begin{cases} \|\nabla \mathcal{U}(\mathbf{x})\|_{\mathcal{M}_A^{-1}(\mathbf{x})} = 1, & \forall \mathbf{x} \in \Omega \setminus \{\mathbf{s}\}, \\ \mathcal{U}(\mathbf{s}) = 0, \end{cases} \quad (2.54)$$

where the norm $\|\mathbf{u}\|_{\mathcal{M}(\mathbf{x})} = \sqrt{\langle \mathbf{u}, \mathcal{M}(\mathbf{x}) \mathbf{u} \rangle}$.

The minimal path $\mathcal{C}_{\mathbf{s},\mathbf{x}}$ that joins the initial source point \mathbf{s} to point \mathbf{x} can be recovered by reversing the path $\hat{\mathcal{C}}_{\mathbf{x},\mathbf{s}}$ as the solution to the following ODE:

$$\begin{cases} \hat{\mathcal{C}}'_{\mathbf{x},\mathbf{s}}(t) \propto -\mathcal{M}_A^{-1}(\hat{\mathcal{C}}_{\mathbf{x},\mathbf{s}}(t)) \nabla \mathcal{U}(\hat{\mathcal{C}}_{\mathbf{x},\mathbf{s}}(t)), \\ \hat{\mathcal{C}}_{\mathbf{x},\mathbf{s}}(0) = \mathbf{x}. \end{cases} \quad (2.55)$$

For the anisotropic Riemannian metric-based minimal path models (Benmansour and Cohen, 2011; Bougleux et al., 2008; Jbabdi et al., 2008), the geodesic curve length in (2.68) will depend on both the orientations and positions of the path. With the orientation enhancement, the short cuts problem sometimes suffered by the classical Cohen-Kimmel model will be avoided in some image processing applications such as perceptual grouping and tubular structure segmentation. In Fig. 2.9, we show the extracted minimal paths by using the isotropic metric and anisotropic metrics. Fig. 2.9a is the original image with the initial source point and end point, indicated by green dot and cyan dot respectively. Fig. 2.9a is the potential function P used in isotropic metric \mathcal{R}^I (2.38). We define P by the gradient of image I :

$$P(\mathbf{x}) = \exp\left(-\alpha \frac{\|\nabla G_\sigma * I(\mathbf{x})\|}{\|\nabla G_\sigma * I\|_\infty}\right), \quad \forall \mathbf{x} \in \Omega. \quad (2.56)$$

where G_σ is a Gaussian kernel with variance σ . For fair comparison, the anisotropic tensor field \mathcal{M}_A (2.51) is constructed based on the gradient vector field of image I . Letting $\mathbf{x} = (x, y) \in \Omega$, one has

$$\mathbf{v}_1(\mathbf{x}) = \left(G_x * I(\mathbf{x}), G_y * I(\mathbf{x})\right), \quad \forall \mathbf{x} \in \Omega.$$

Thus the tensor field \mathcal{M}_s can be constructed as

$$\mathcal{M}_A(\mathbf{x}) = P(\mathbf{x})\mathbf{v}_1(\mathbf{x})\mathbf{v}_1^T(\mathbf{x}) + \mathbf{v}_1^\perp(\mathbf{x})(\mathbf{v}_1^\perp(\mathbf{x}))^T. \quad (2.57)$$

Fig. 2.9c and Fig. 2.9d are the minimal paths extracted using the isotropic metric with potential P defined in (2.56) and the anisotropic metric defined in (2.57) respectively. It can be seen that the minimal path extracted by the isotropic metric suffers from the shortcut problem while the result by anisotropic metric is the expected one. The corresponding minimal action maps of Fig. 2.9c and Fig. 2.9d are demonstrated in Fig. 2.9e and Fig. 2.9f, respectively. Note that in this experiment the parameter is set as $\alpha = -4.2$.

In Fig. 2.10, the effect of the anisotropy ratio μ (2.53) is studied. In each figures, the red region contains all the grid points, of which the geodesic distance values are larger than that of the end point. We can see that with a larger value of

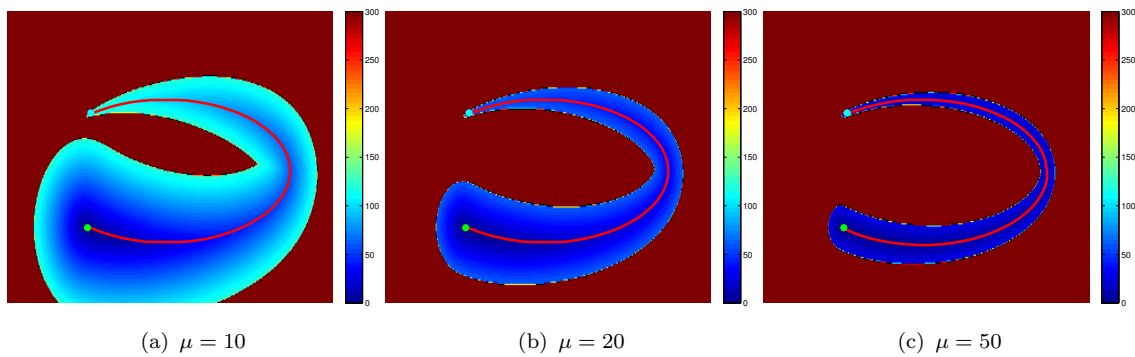


FIGURE 2.10: Geodesic distance maps with different values of anisotropy ratio. The original image is shown in Fig. 2.9(a) with the same initial source point and end point.

anisotropic, less grid points are passed by the fast marching front before the end point is reached. In this figure, the original image is demonstrated in Fig. 2.9a and the anisotropic tensor \mathcal{M}_A is constructed by (2.57).

2.3.5 Minimal Paths with Anisotropic Radius-Lifted Riemannian Metric

Benmansour and Cohen (2011) extended Li-Yezzi minimal path model (Li and Yezzi, 2007) to the anisotropic case by lifting the anisotropic tensor field \mathcal{M}_A (2.50) to radius-lifted tensor field \mathcal{M}_r :

$$\mathcal{M}_r(\mathbf{x}, r) = \begin{pmatrix} \mathcal{M}_s(\mathbf{x}, r) & \mathbf{0} \\ \mathbf{0} & P_r(\mathbf{x}, r) \end{pmatrix}, \quad (2.58)$$

where \mathcal{M}_s is constructed by:

$$\mathcal{M}_s(\mathbf{x}, r) = \sum_{i=1}^d P_i^s(\mathbf{x}, r) \mathbf{v}_i(\mathbf{x}, r) \mathbf{v}_i^T(\mathbf{x}, r), \quad (2.59)$$

where P_i^s are the potential functions along the orientation vector $\mathbf{v}_i \in \mathbb{R}^d$. P_r is a positive scalar function defined over the radius-lifted domain $\hat{\Omega}$. Note that the dimension of the domain $\hat{\Omega}$ is $d + 1$.

\mathcal{M}_r is a positive symmetric definite tensor field which is the special case of the tensor field \mathcal{M}_A defined in (2.50):

$$\mathcal{M}_r(\mathbf{x}, r) = \sum_{i=1}^d P_i^s(\mathbf{x}, r) \hat{\mathbf{v}}_i(\mathbf{x}, r) \hat{\mathbf{v}}_i^T(\mathbf{x}, r) + P_r(\mathbf{x}, r) \hat{\mathbf{v}}_0(\mathbf{x}, r) \hat{\mathbf{v}}_0^T(\mathbf{x}, r), \quad (2.60)$$

where $\hat{\mathbf{v}}_i := (\mathbf{v}_i, 0) \in \mathbb{R}^{d+1}$ and $\hat{\mathbf{v}}_0 = (0, \dots, 0, 1) \in \mathbb{R}^{d+1}$. We use the vector $\hat{\mathbf{v}}_i$ where the last entry is zero, since it makes no sense to add anisotropy in the radius dimension.

In Eqn. (3.10), we give the computation example of \mathcal{M}_s using the optimally oriented flux filter (Law and Chung, 2008). The anisotropic radius-lifted Riemannian metric $\mathcal{R}^{\text{AR}} : \hat{\Omega} \times \mathbb{R}^{d+1} \rightarrow \mathbb{R}^+$ can be defined as

$$\mathcal{R}^{\text{AR}}(\hat{\mathbf{x}}, \hat{\mathbf{u}}) := \sqrt{\langle \hat{\mathbf{u}}, \mathcal{M}_r(\hat{\mathbf{x}}) \hat{\mathbf{u}} \rangle}, \quad (2.61)$$

for all $\hat{\mathbf{x}} \in \hat{\Omega}$ and any vector $\hat{\mathbf{u}} \in \mathbb{R}^d \times \mathbb{R}$.

2.3.6 Minimal Paths with Isotropic Orientation-Lifted Riemannian Metric

In order to take into account the local orientation in the image, it is possible to include orientation information in the energy minimization. For this purpose, the image domain space $\Omega \subset \mathbb{R}^2$ can be extended to the orientation lifted space $\bar{\Omega}$ by product with an abstract orientation space \mathbb{S}^1 (Kimmel and Sethian, 2001), i.e., $\bar{\Omega} = \Omega \times \mathbb{S}^1 \subset \mathbb{R}^3$ and the problem is to find a minimal path in the new lifted space $\bar{\Omega}$. Each point $\bar{\mathbf{x}}$ in the orientation lifted path is thus a pair composed of a point \mathbf{x} in the image domain Ω and an orientation θ , i.e., $\bar{\mathbf{x}} = (\mathbf{x}, \theta)$.

For any orientation-lifted vector $\bar{\mathbf{u}} = (\mathbf{u}, \nu) \in \mathbb{R}^2 \times \mathbb{R}$ and any orientation-lifted point $\bar{\mathbf{x}} = (\mathbf{x}, \theta) \in \bar{\Omega}$, the isotropic orientation-lifted Riemannian metric $\mathcal{R}^{\text{IO}} : \bar{\Omega} \times \mathbb{R}^3 \rightarrow \mathbb{R}^+$ can be defined by:

$$\mathcal{R}^{\text{IO}}(\bar{\mathbf{x}}, \bar{\mathbf{u}}) = \frac{1}{P_{\text{IO}}(\bar{\mathbf{x}})} \sqrt{\|\mathbf{u}\|^2 + \rho|\nu|^2}, \quad (2.62)$$

The curve length of an orientation-lifted path $\gamma := (\Gamma, \theta)$, where $\gamma : [0, 1] \rightarrow \bar{\Omega}$, can be measured with respect to the isotropic orientation-lifted Riemannian metric \mathcal{R}^{IO} :

$$\mathcal{L}^{\text{IO}}(\gamma) = \int_0^1 \frac{1}{P_{\text{IO}}(\gamma(t))} \sqrt{\|\Gamma'(t)\|^2 + \rho|\theta'(t)|^2} dt, \quad (2.63)$$

The symmetric positive definite tensor field \mathcal{M}_{IO} is defined by

$$\mathcal{M}_{\text{IO}}(\bar{\mathbf{x}}) = P_{\text{IO}}^2(\bar{\mathbf{x}}) \begin{pmatrix} 1 & 0 & | & 0 \\ 0 & 1 & | & 0 \\ \hline 0 & 0 & | & \rho \end{pmatrix},$$

where P_{IO} is an image data-driven speed function defined over the orientation-lifted domain $\bar{\Omega}$ and ρ is a positive constant.

The idea of orientation lifting provides an alternate way to make use of the path orientation. Péchaud et al. (2009) combined the ideas of orientation lifting and radius lifting to construct a Riemannian metric over the orientation-radius lifting domain $\Omega \times \mathbb{S}^1 \times [R_{\min}, R_{\max}]$. The corresponding tensor field for the orientation and radius-lifted metric \mathcal{R}^{OR} is defined by

$$\mathcal{M}_{\text{OR}}(\bar{\mathbf{x}}) = P_{\text{OR}}^2(\bar{\mathbf{x}}) \begin{pmatrix} 1 & 0 & | & 0 & 0 \\ 0 & 1 & | & 0 & 0 \\ \hline 0 & 0 & | & \rho & 0 \\ 0 & 0 & | & 0 & \epsilon \end{pmatrix}, \quad (2.64)$$

where P_{OR} is an image data-driven speed function relying on both the orientation and position of the minimal paths. Based on \mathcal{M}_{OR} , the orientation and radius-lifted Riemannian metric is expressed as

$$\mathcal{R}^{\text{OR}}(\bar{\mathbf{x}}, \bar{\mathbf{u}}) = \sqrt{\langle \bar{\mathbf{u}}, \mathcal{M}_{\text{OR}}(\bar{\mathbf{x}}) \bar{\mathbf{u}} \rangle}, \quad \forall \bar{\mathbf{x}} \in \Omega \times \mathbb{S}^1 \times [R_{\min}, R_{\max}], \forall \bar{\mathbf{u}} \in \mathbb{R}^4. \quad (2.65)$$

Since this radius and orientation-lifted minimal path is defined over the 4D domain, the computation complexity is extremely high compared to the anisotropic radius-lifted metric based minimal path model (Benmansour and Cohen, 2011).

2.3.7 General Minimal Path Model and Finsler Metric

The minimal path problem (Peyré et al., 2010) is posed on a bounded domain $\Omega \in \mathbb{R}^d$ equipped with a metric $\mathcal{F}(\mathbf{x}, \mathbf{u})$ depending on location $\mathbf{x} \in \Omega$ and orientation $\mathbf{u} \in \mathbb{R}^d$, where $d = n$ or $d = n + 1$ with n being the dimension of the image domain or physical domain. This metric \mathcal{F} defines at each point $\mathbf{x} \in \Omega$ a norm:

$$\mathcal{F}_{\mathbf{x}}(\mathbf{u}) = \mathcal{F}(\mathbf{x}, \mathbf{u}) \quad (2.66)$$

These norms must be positive $\mathcal{F}_{\mathbf{x}}(\mathbf{u}) > 0$ whenever $\mathbf{u} \neq 0$, 1-homogeneous, and obey the triangular inequality. In general, we allow them to be asymmetric:

$$\mathcal{F}_{\mathbf{x}}(\mathbf{u}) \neq \mathcal{F}_{\mathbf{x}}(-\mathbf{u}). \quad (2.67)$$

Based on the metric \mathcal{F} , one can measure the curve length of any regular curve γ :

$$\mathcal{L}(\gamma) = \int_0^1 \mathcal{F}(\gamma(t), \gamma'(t)) dt. \quad (2.68)$$

The minimal action map $\mathcal{U}(\mathbf{x})$, or geodesic distance from the source point \mathbf{s} , is the minimal length (2.68) among all paths contained in the collection $\mathcal{A}_{\mathbf{s}, \mathbf{x}}$ joining the

initial source point \mathbf{s} to any point $\mathbf{x} \in \Omega$:

$$\mathcal{U}(\mathbf{x}) := \inf\{\mathcal{L}(\gamma); \gamma \in \mathcal{A}_{\mathbf{s},\mathbf{x}}\}. \quad (2.69)$$

The minimal action map \mathcal{U} in (2.69) is the unique viscosity solution to an Eikonal PDE (Lions, 1982; Sethian and Vladimirsky, 2003):

$$\begin{cases} \mathcal{F}_{\mathbf{x}}^*(-\nabla\mathcal{U}(\mathbf{x})) = 1, & \text{for all } \mathbf{x} \in \Omega, \\ \mathcal{U}(\mathbf{s}) = 0, \end{cases} \quad (2.70)$$

where $\nabla\mathcal{U}$ is the gradient of \mathcal{U} with respect to the position in the domain Ω and $\mathcal{F}_{\mathbf{x}}^*$ is the dual norm of $\mathcal{F}_{\mathbf{x}}$ defined for all $\mathbf{u} \in \mathbb{R}^d$ by

$$\mathcal{F}_{\mathbf{x}}^*(\mathbf{u}) = \sup_{\mathbf{v} \neq \mathbf{0}} \frac{\langle \mathbf{u}, \mathbf{v} \rangle}{\mathcal{F}_{\mathbf{x}}(\mathbf{v})}, \quad (2.71)$$

where $\langle \cdot, \cdot \rangle$ denotes the scalar product over \mathbb{R}^d .

Randers Metric

The metrics \mathcal{F} considered in this thesis combine a symmetric part, defined in terms of a positive definite tensor field \mathcal{M} , and an asymmetric part involving a vector field $\omega \in \mathbb{R}^d$:

$$\mathcal{F}(\mathbf{x}, \mathbf{u}) = \sqrt{\langle \mathbf{u}, \mathcal{M}(\mathbf{x}) \mathbf{u} \rangle} + \langle \omega(\mathbf{x}), \mathbf{u} \rangle, \quad \forall \mathbf{x} \in \Omega \text{ and } \forall \mathbf{u} \in \mathbb{R}^m. \quad (2.72)$$

In this case, the Finsler metric \mathcal{F} (2.72) is regarded as the Randers metric (Randers, 1941). *Note that in the following part of this thesis, whenever we mention the Finsler metric, we mean the Randers metric with the form formulated in (2.72).*

The Finsler metric or the Randers metric \mathcal{F} (2.72) should obey the following *smallness* condition (Mirebeau, 2014b) to ensure that the metric \mathcal{F} is positive:

$$\forall \mathbf{x} \in \Omega, \quad \langle \omega(\mathbf{x}), \mathcal{M}^{-1}(\mathbf{x}) \omega(\mathbf{x}) \rangle < 1. \quad (2.73)$$

The anisotropy ratio $\mu(\mathcal{F})$ characterizes the distortion between different orientations induced by a Finsler metric \mathcal{F} on a domain Ω . The anisotropic ratio $\mu(\mathcal{F})$ of the metric \mathcal{F} (2.72) is defined by:

$$\mu(\mathcal{F}) := \sup_{\mathbf{x} \in \Omega} \left\{ \max_{\|\mathbf{u}\|=\|\mathbf{v}\|=1} \left\{ \frac{\mathcal{F}_{\mathbf{x}}(\mathbf{u})}{\mathcal{F}_{\mathbf{x}}(\mathbf{v})} \right\} \right\}. \quad (2.74)$$

Equation (2.72) defines an anisotropic Finsler metric in general. This is an anisotropic Riemannian metric if the vector field ω is identically zero, and an isotropic metric if in addition the tensor field \mathcal{M} is proportional to the identity matrix.

Based on the definition of the dual norm in (2.71), the corresponding optimal direction map Ψ is then obtained by

$$\Psi(\mathbf{x}, \mathbf{u}) := \arg \max_{\mathbf{v} \neq \mathbf{0}} \frac{\langle \mathbf{u}, \mathbf{v} \rangle}{\mathcal{F}_{\mathbf{x}}(\mathbf{v})}, \quad \forall \mathbf{x} \in \Omega, \forall \mathbf{u} \in \mathbb{R}^n. \quad (2.75)$$

Again, the geodesic $\mathcal{C}_{\mathbf{s}, \mathbf{x}}$ is obtained by reversing the path $\hat{\mathcal{C}}_{\mathbf{x}, \mathbf{s}}$ with $\mathcal{C}_{\mathbf{s}, \mathbf{x}}(0) = \mathbf{s}$ and $\mathcal{C}_{\mathbf{s}, \mathbf{x}}(1) = \mathbf{x}$, where $\hat{\mathcal{C}}_{\mathbf{x}, \mathbf{s}}$ is tracked through the following ODE involving the minimal action map \mathcal{U} and the optimal direction map Ψ

$$\begin{cases} \hat{\mathcal{C}}'_{\mathbf{x}, \mathbf{s}}(t) \propto -\Psi\left(\hat{\mathcal{C}}_{\mathbf{x}, \mathbf{s}}(t), \nabla \mathcal{U}(\hat{\mathcal{C}}_{\mathbf{x}, \mathbf{s}}(t))\right), \\ \hat{\mathcal{C}}_{\mathbf{x}, \mathbf{s}}(0) = \mathbf{x}. \end{cases} \quad (2.76)$$

Numerically, the ODE in (2.76) can be solved by using the Runge-Kutta's method, or more robustly using the numerical method proposed by Mirebeau (2014a).

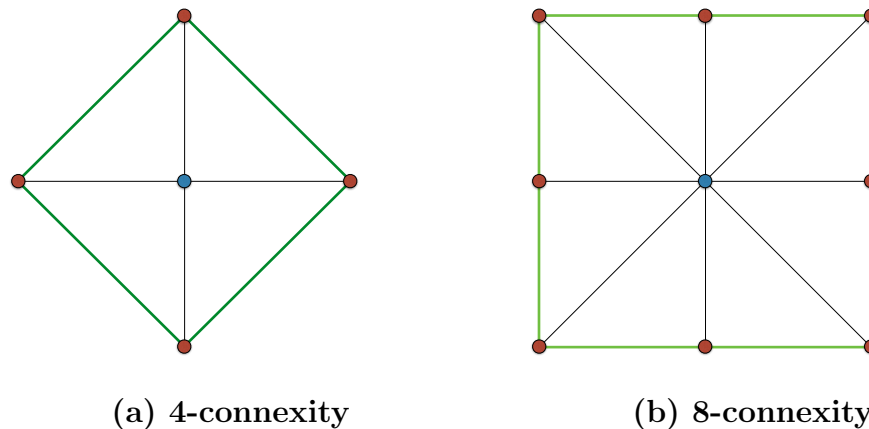


FIGURE 2.11: Stencil examples: 4-connectivity and 8-connectivity stencils on 2D cartesian grid. **(a)** 4-connectivity stencil. **(b)** 8-connectivity stencil. Blue dots are the centre points of the stencils. Red dots are the neighbourhood points. Green lines denote the boundaries of the stencils.

2.4 Fast Marching Method

2.4.1 Overview of the Fast Marching Method

The fast marching method was developed independently by [Sethian \(1996, 1999\)](#) and [Tsitsiklis \(1995\)](#) to address the problem of the computation of the minimal action map or geodesic distance map with respect to isotropic Riemannian metric. The essential difference between the fast marching methods [Sethian \(1996, 1999\)](#) and [Tsitsiklis \(1995\)](#) lies at the discretization scheme for the local geodesic distance update, where Sethian's method made use of the upwind discretization form of the Eikonal equation (2.43) itself, while Tsitsiklis's shortest path method utilized the Hopf-Lax update scheme. Both the fast marching methods mentioned above are similar to Dijkstra's non-iterative algorithm ([Dijkstra, 1959](#)) in a monotonically advancing wave propagation manner. Compared to the fast marching methods, it is known that Dijkstra's shortest path algorithm may suffer from the metrication error problem ([Cohen and Kimmel, 1997](#)).

For the purpose of estimation of the minimal action map \mathcal{U} in (2.69) and (2.70) by the fast marching method, we first introduce some basic notations:

Notation 2.4.1. let Z be a discretization orthogonal grid of the domain Ω with dimension d and let $N = \#Z$ be the total number of grid points of Z .

Notation 2.4.2. For each grid point \mathbf{x}_0 , a stencil $S(\mathbf{x}_0)$ is a neighbourhood of \mathbf{x}_0 with vertices in Z . We introduce a translated stencil \wp defined by offset-based

Algorithm 1 General Fast Marching Method**Input:**

- Metric \mathcal{F} .
- Initial source points collection \mathcal{W} .

Output:

- Minimal action map \mathcal{U} .

Initialization:

- For each point $\mathbf{x} \in Z$, set $\mathcal{U}(\mathbf{x}) \leftarrow +\infty$ and $\mathcal{V}(\mathbf{x}) \leftarrow \textit{Far}$.
- For each point $\mathbf{y} \in \mathcal{W}$, set $\mathcal{U}(\mathbf{y}) \leftarrow 0$ and $\mathcal{V}(\mathbf{y}) \leftarrow \textit{Trial}$.

Main Loop

```

1: while at least one grid point is tagged as Trial do
2:   Find  $\mathbf{x}_{\min}$ , the Trial point which minimizes  $\mathcal{U}$ .
3:    $\mathcal{V}(\mathbf{x}_{\min}) \leftarrow \textit{Accepted}$ .
4:   for all neighbourhood points  $\mathbf{y}$  of  $\mathbf{x}_{\min}$  and  $\mathcal{V}(\mathbf{y}) \neq \textit{Accepted}$  do
5:     Compute  $\mathcal{U}_{\text{new}}(\mathbf{y})$  by local geodesic distance update scheme.
6:     if  $\mathcal{V}(\mathbf{y}) = \textit{Far}$  then
7:       Set  $\mathcal{V}(\mathbf{y}) \leftarrow \textit{Trial}$ .
8:     end if
9:     if  $\mathcal{U}_{\text{new}}(\mathbf{y}) < \mathcal{U}(\mathbf{y})$  then
10:      Set  $\mathcal{U}(\mathbf{y}) \leftarrow \mathcal{U}_{\text{new}}(\mathbf{y})$ ,
11:    end if
12:   end for
13: end while

```

coordinate system:

$$\wp(\mathbf{x}_0) := S(\mathbf{x}_0) - \mathbf{x}_0. \quad (2.77)$$

A common simplex $T \in \wp(\mathbf{x}_0)$ is defined as the convex envelop of vertices in the set $\{\mathbf{0}\} \cup \{\mathbf{x}_1 - \mathbf{x}_0, \dots, \mathbf{x}_d - \mathbf{x}_0\}$ where $\{\mathbf{x}_1, \dots, \mathbf{x}_d\}$ are a subset of the vertices contained by $S(\mathbf{x}_0)$. The translated stencil $\wp(\mathbf{x}_0)$ is the union of non-zero vertices of all the simplices T .

In Figs. 2.11a and 2.11b we show the 4-connectivity and 8-connectivity stencils on 2D cartesian grid respectively. The blue dots indicate the centre points of the stencils. Red dots represent the vertices of the stencils. The green lines denote the boundaries of the stencils. The 4-connectivity stencil shown in Fig. 2.11a was adopted by Sethian (1996, 1999) and Tsitsiklis (1995) for isotropic fast marching algorithm on 2D grid.

The fast marching method is a single-pass algorithm where the cartesian grid points in Z are visited by the front in an ordered way. The behaviour of the fast marching method is like a monotonically advancing wave propagation: starting from the initial source points, the front will propagate outward until filling the whole domain combining with a point labelling procedure. In the course of the

fast marching front propagation, each grid point in Z is tagged as either *Accepted*, *Trial* or *Far* by a labelling function $\mathcal{V} : Z \rightarrow \{\textit{Accepted}, \textit{Trial}, \textit{Far}\}$:

- *Accepted* points are the grid points for which minimal action values of \mathcal{U} have been estimated and been frozen.
- *Trial* points are the grid points for which the minimal action values have been estimated but not frozen.
- *Far* points are the grid points for which the minimal action values have not been estimated.

All the *Trial* points form the fast marching front which is considered as the interface between the points tagged as *Accepted* and the points tagged as *Far*. We illustrate the fast marching front in Fig. 2.12, where the *Accepted*, *Trial* and *Far* points are represented by red, green and black dots respectively. The front consisting of all the *Trial* points are indicated by green region. The values of minimal action map \mathcal{U} for all *Trial* points have been updated at least once. These *Trial* points are stored in a priority queue such that the *Trial* point \mathbf{x}_{\min} with the smallest value of \mathcal{U} can be identified efficiently. By marching the front in an ordered way, the minimal action map \mathcal{U} can be obtained within a finite number of local geodesic distance update steps.

The overview of the fast marching method can be found in Algorithm 1. In each step, the grid point \mathbf{x}_{\min} with the smallest value of \mathcal{U} among all the *Trial* points is selected and tagged as *Accepted* as described in Line 2 of Algorithm 1. The crucial point of the fast marching method is to update all the neighbourhood points \mathbf{y} of \mathbf{x}_{\min} obeying $\mathcal{V}(\mathbf{y}) \neq \textit{Accepted}$ by the local geodesic distance update scheme detailed in Sections 2.4.2, 2.4.3 and 2.4.5. Note that the neighbourhood points \mathbf{y} of \mathbf{x}_{\min} is defined by the local mesh $S(\mathbf{x}_{\min})$.

The general stopping criterion for fast marching algorithm can be formulated as: once all the grid points in Z have been tagged as *Accepted*, the fast marching front propagation can be stopped. In order to reduce the computation time of the minimal action map computation, the early abort scheme can be applied: once all the end points are tagged as *Accepted*, we stop the fast marching completely.

2.4.2 Isotropic Fast Marching Method with Sethian's Update Scheme

In the classical minimal path model, Cohen and Kimmel (1997) recommended Sethian's fast marching method (Sethian, 1999) as their Eikonal PDE solver for

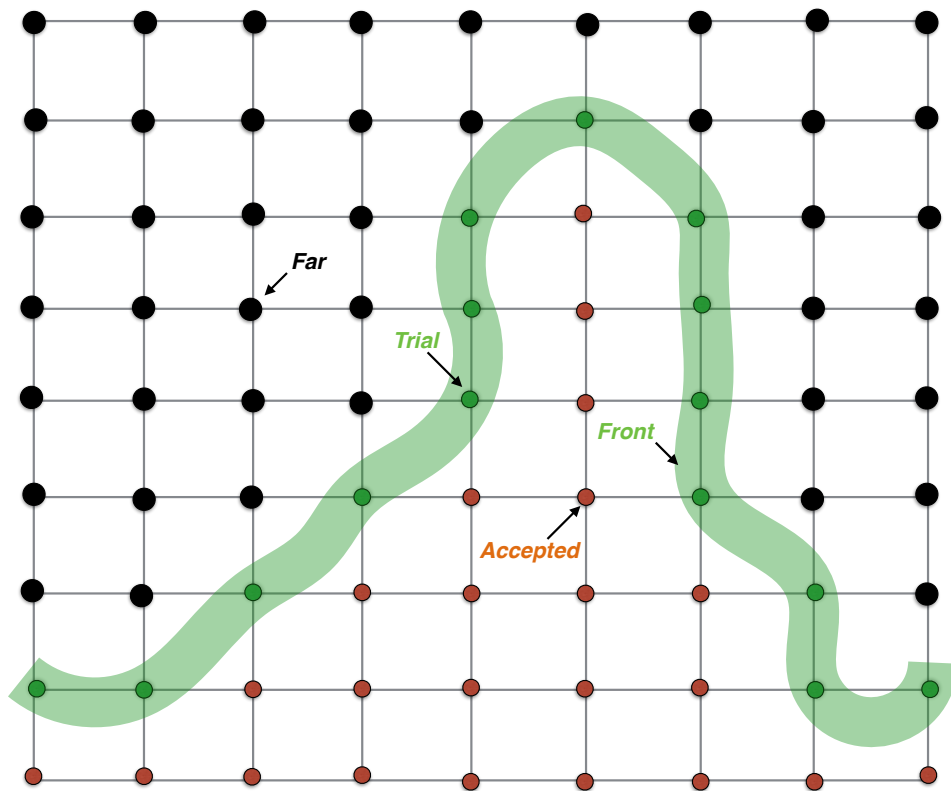


FIGURE 2.12: Example for fast marching front. Red, green and black dots denote the *Accepted*, the *Trial* and the *Far* points respectively. Green shadow region denotes the fast marching front consists of all the *Trial* points.

real time applications. We recall the Eikonal PDE in (2.43) used by Cohen and Kimmel (1997):

$$\begin{cases} \|\nabla \mathcal{U}(\mathbf{x})\| = \tilde{P}(\mathbf{x}), & \forall \mathbf{x} \in \Omega, \\ \mathcal{U}(\mathbf{s}) = 0, \end{cases} \quad (2.78)$$

where $\tilde{P} = w + P$ and w is a positive constant. P is a decreasing function that is usually dependent of the image gradient magnitude or image gray levels.

To solve the Eikonal PDE in a grid Z , we should discrete the minimal action map \mathcal{U} and the potential function \tilde{P} on Z . For the sake of simplicity, we consider the 2D case ($d = 2$) of the Eikonal PDE (2.78). Let Δx and Δy be the grid spacings in the x and y directions respectively. A grid point $(m, n) \in Z$ corresponds to a point $(m\Delta x, n\Delta y) \in \Omega$ such that

$$\tilde{P}_{m,n} = \tilde{P}(m\Delta x, n\Delta y), \quad \mathcal{U}_{m,n} = \mathcal{U}(m\Delta x, n\Delta y). \quad (2.79)$$

It is proved by Rouy and Tourin (1992) that the unique viscosity solution for the minimal action map $\mathcal{U}_{m,n} := \mathcal{U}_{\text{new}}$ (\mathcal{U}_{new} is used in Line 5 of Algorithm 1) can be

obtained by solving the following discretization form of the Eikonal PDE (2.78):

$$\begin{aligned} & \left(\frac{\max\{\mathcal{U}_{\text{new}} - \mathcal{U}_{m-1,n}, \mathcal{U}_{\text{new}} - \mathcal{U}_{m+1,n}, 0\}}{\Delta x} \right)^2 \\ & + \left(\frac{\max\{\mathcal{U}_{\text{new}} - \mathcal{U}_{m,n-1}, \mathcal{U}_{\text{new}} - \mathcal{U}_{m,n+1}, 0\}}{\Delta y} \right)^2 = \tilde{P}_{m,n}^2, \end{aligned} \quad (2.80)$$

for each grid point $(m, n) \in Z$. In the following, we set $\Delta x = \Delta y = 1$ for simplicity.

We denote $(A_1, A_2) = (\mathcal{U}_{m-1,n}, \mathcal{U}_{m+1,n})$ and $(B_1, B_2) = (\mathcal{U}_{m,n-1}, \mathcal{U}_{m,n+1})$. Without loss of generality, we suppose that $A_1 \leq A_2$ and $B_1 \leq B_2$. Cohen (2001) presented a simple way to solve (2.80) based on the fact that only the *Accepted* points in the neighbourhood points $\{(m+1, n), (m-1, n), (m, n+1), (m, n-1)\}$ are considered. Hence the equation (2.80) can be simplified as

$$(\mathcal{U}_{\text{new}} - A_1)^2 + (\mathcal{U}_{\text{new}} - B_1)^2 = \tilde{P}_{m,n}^2. \quad (2.81)$$

The discriminant Δ of the quadratic equation (2.81) is expressed by

$$\Delta_{m,n} = 4(2\tilde{P}_{m,n}^2 - (A_1 - B_1)^2). \quad (2.82)$$

When $\Delta_{m,n} \geq 0$, we obtain the following solution

$$u = \frac{A_1 + B_1 + \sqrt{2\tilde{P}_{m,n}^2 - (A_1 - B_1)^2}}{2}. \quad (2.83)$$

The solution \mathcal{U}_{new} of equation (2.82) can be obtained by the following upwind scheme:

1. If $\Delta_{m,n} \geq 0$ and $u > \max\{A_1, B_1\}$, we have $\mathcal{U}_{\text{new}} := u$.
2. If $\Delta_{m,n} \geq 0$ and $u < \max\{A_1, B_1\}$, we have $\mathcal{U}_{\text{new}} := \min\{A_1, B_1\} + \tilde{P}_{m,n}$.
3. If $\Delta_{m,n} < 0$, we have $\mathcal{U}_{\text{new}} := \min\{A_1, B_1\} + \tilde{P}_{m,n}$.

In each fast marching step, we find a grid point \mathbf{x}_{\min} , a *Trial* point that minimizes the minimal action map \mathcal{U} . For each neighbourhood point $\mathbf{y} = (m, n)$ of \mathbf{x}_{\min} where $\mathcal{V}(\mathbf{y}) \neq \text{Accepted}$, we solve the equation (2.81) by the above upwind scheme to update the value of $\mathcal{U}(\mathbf{y})$. The minimal action map \mathcal{U} can be obtained in a single pass way with computation complexity $\mathcal{O}(N(\log N))$.

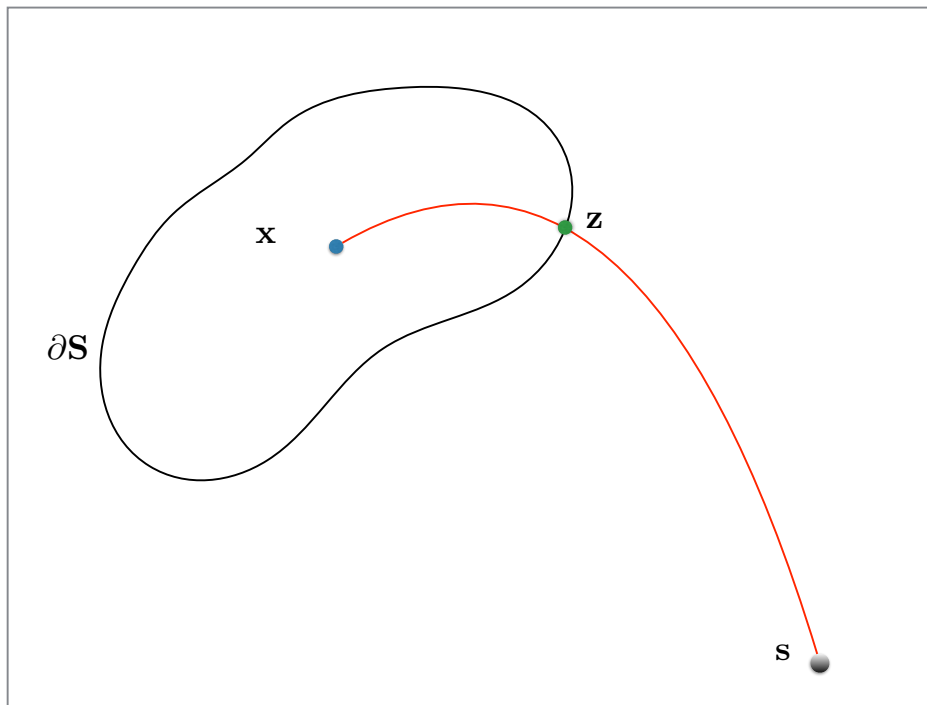


FIGURE 2.13: Illustration for Bellman's optimality principle. \mathbf{s} is the initial source point. ∂S is the boundary of stencil $S(\mathbf{x})$. z is the intersection points of ∂S and geodesic $\mathcal{C}_{\mathbf{s},\mathbf{x}}$.

2.4.3 Hopf-Lax Update Scheme

In contrast with Sethian's fast marching method which solves the Eikonal PDE with an upwind discretization scheme, the basic idea of Tsitsiklis' geodesic distance computation method (Tsitsiklis, 1995) is to approximate the minimal action map \mathcal{U} by the Hopf-Lax update scheme. Note that Tsitsiklis' method is only suitable for the geodesic distance computation with respect to a isotropic Riemannian metric. In this section, a more general metric \mathcal{F} as discussed in Section 2.3.7 is considered.

The minimal action map \mathcal{U} associated to a general metric \mathcal{F} satisfies the anisotropic Eikonal PDE or the static Hamilton-Jacobi PDE

$$\begin{cases} \mathcal{F}_x^*(-\nabla\mathcal{U}(\mathbf{x})) = 1, & \forall \mathbf{x} \in \Omega \setminus \{\mathbf{s}\}, \\ \mathcal{U}(\mathbf{s}) = 0, \end{cases} \quad (2.84)$$

As discussed in (Kushner, 1990; Mirebeau, 2014b; Sethian and Vladimirovsky, 2003), the discretization of the Eikonal PDE can be interpreted as a fixed point problem based on the Hopf-Lax update scheme

$$\begin{cases} \mathcal{U}(\mathbf{x}) = \Lambda\mathcal{U}(\mathbf{x}), & \forall \mathbf{x} \in Z, \\ \mathcal{U}(\mathbf{s}) = 0, \end{cases} \quad (2.85)$$

where Z is the discretization orthogonal grid of the domain Ω . Λ is the Hopf-Lax update operator that is defined by:

$$\Lambda\mathcal{U}(\mathbf{x}) := \min_{\mathbf{z} \in \partial S(\mathbf{x})} \left\{ \mathcal{F}(\mathbf{x}, \mathbf{x} - \mathbf{z}) + I_{S(\mathbf{x})}\mathcal{U}(\mathbf{z}) \right\}, \quad (2.86)$$

where $S(\mathbf{x})$ is the local stencil centred at point $\mathbf{x} \in Z$ and $I_{S(\mathbf{x})}$ denotes the piecewise linear interpolation operator on the mesh $S(\mathbf{x})$. Note that \mathbf{z} lies on the boundary $\partial S(\mathbf{x})$. The value of $I_{S(\mathbf{x})}\mathcal{U}(\mathbf{z})$ can be obtained by linear interpolation on the boundary $\partial S(\mathbf{x})$ of the stencil $S(\mathbf{x})$. The equality $\mathcal{U}(\mathbf{x}) = \Lambda\mathcal{U}(\mathbf{x})$, replacing in (2.85) the Eikonal PDE, is a discretization of Bellman's optimality principle which states that

$$\mathcal{U}(\mathbf{x}) = d_{\mathcal{F}}(\mathbf{x}, \mathbf{z}) + \mathcal{U}(\mathbf{z}), \quad (2.87)$$

where $d_{\mathcal{F}}(\mathbf{x}, \mathbf{z})$ denotes the geodesic distance between points \mathbf{x} and \mathbf{z} .

Bellman's optimality principle (2.87) reflects the fact that the minimal geodesic $\mathcal{C}_{\mathbf{s}, \mathbf{x}}$, from \mathbf{s} to \mathbf{x} , has to cross the mesh boundary $\partial S(\mathbf{x})$ at least once at some point \mathbf{z} ; thus it is the concatenation of a geodesic $\mathcal{C}_{\mathbf{s}, \mathbf{z}}$ from \mathbf{s} to \mathbf{z} , as shown in Fig. 2.13. Using the Hopf-Lax update operator (2.86) to estimate the values of the minimal action map \mathcal{U} in (2.87) which length is approximated by piecewise linear interpolation, and a very short geodesic $\mathcal{C}_{\mathbf{z}, \mathbf{x}}$ from \mathbf{z} to \mathbf{x} , approximated by a segment with geodesic curve length $\mathcal{F}(\mathbf{x}, \mathbf{x} - \mathbf{z})$.

2.4.4 Anisotropic Fast Marching Method

The stencil plays an important role in the computation of the minimal action map \mathcal{U} by the fast marching method (Chopp, 2001; Sethian and Vladimirsky, 2003). The fast marching methods proposed by Sethian (1999) and Tsitsiklis (1995) making use of the square formed stencil (see Fig. 2.11a) have difficulty to deal with the anisotropic metrics-based minimal action maps computation, especially when the anisotropy ratio μ (2.53) or (2.74) gets large, since both methods rely on the assumption that the tangent directions of the geodesics are proportional to the gradient of the minimal action map (Chopp, 2001).

Let us Consider the gradient descent ODE used to recover the geodesic $\mathcal{C}_{\mathbf{x}, \mathbf{s}}$, joining \mathbf{x} to the initial source point \mathbf{s} , with respect to a general metric:

$$\begin{cases} \mathcal{C}'_{\mathbf{x}, \mathbf{s}}(t) \propto -\Psi\left(\mathcal{C}_{\mathbf{x}, \mathbf{s}}(t), \nabla\mathcal{U}(\mathcal{C}_{\mathbf{x}, \mathbf{s}}(t))\right), \\ \mathcal{C}_{\mathbf{x}, \mathbf{s}}(0) = \mathbf{x}. \end{cases} \quad (2.88)$$

where $\mathcal{F}_{\mathbf{x}}^*$ is the dual norm of $\mathcal{F}_{\mathbf{x}}(\cdot) = \mathcal{F}(\mathbf{x}, \cdot)$ and Ψ is the optimal direction map defined in (2.75). It can be seen from (2.88) that the tangents \mathcal{C}' depend on both

the metric \mathcal{F} and the gradient of \mathcal{U} . This means the classical fast marching methods invoking 4-connected neighbourhood stencil will not give accurate minimal action map computation results.

Let us recall the Hopf-Lax update scheme with respect to a Fislner metric \mathcal{F} defined in (2.72):

$$\mathcal{U}(\mathbf{x}) = \min_{\mathbf{z} \in \partial S(\mathbf{x})} \left\{ \mathcal{F}(\mathbf{x}, \mathbf{x} - \mathbf{z}) + \mathbb{I}_{S(\mathbf{x})} \mathcal{U}(\mathbf{z}) \right\}, \quad \forall \mathbf{x} \in Z. \quad (2.89)$$

The minimization problem of (2.86) can be solved using the vertices of the simplex $T \in \wp(\mathbf{x})$ where \wp is the translated stencil defined in (2.77). Let \mathbf{x}_i^T be the vertices of the stencil $S(\mathbf{x})$ where $i \in \{1, 2, \dots, d\}$ and d is the dimension the domain. For each simplex $T \in \wp(\mathbf{x})$, the Hopf-Lax update operator Λ defined in (2.86) can be approximated by

$$u(T) = \min_{\eta \in \Xi} \left\{ \mathcal{F}(\mathbf{x}, \mathbf{v}_\eta^T) + \sum_{i=1}^d \eta_i \mathcal{U}(\mathbf{x}_i^T) \right\}, \quad (2.90)$$

where the convex set

$$\Xi := \left\{ \eta = (\eta_1, \eta_2, \dots, \eta_d); \sum_{i=1}^d \eta_i = 1, \forall \eta_i \geq 0 \right\},$$

and vector

$$\mathbf{v}_\eta^T = \sum_{i=1}^d \eta_i (\mathbf{x}_i^T - \mathbf{x}).$$

The minimal action map value $\mathcal{U}(\mathbf{x}) := \mathcal{U}_{\text{new}}$ at point \mathbf{x} can be obtained by

$$\mathcal{U}_{\text{new}} = \min_{T \in S(\mathbf{x})} u(T),$$

where \mathcal{U}_{new} is used in Line 5 of Algorithm 1.

There are two ways to solve the anisotropic Eikonal PDE, both of which are based on the local Hopf-Lax update scheme (2.89):

- The first method to solve the anisotropic Eikonal PDE is the Bellman-Ford inspired adaptive Gauss-Seidel iteration (AGSI) method that is proposed by Bornemann and Rasch (2006). The AGSI numerical method has the computation complexity of $\mathcal{O}(\mu N^{1+1/d})$, where μ is the anisotropy ratio value defined by (2.74). The AGSI method solves the fixed point problem (2.85) by using the Hopf-Lax update operator (2.89) in an iterative way based on a simple local stencil. However, when the value of anisotropy ratio μ gets very large, the iteration numbers for the Hopf-Lax update operator (2.89) required by the AGSI method will get extremely large. In some real-time

Algorithm 2 Adaptive Stencils Construction (Mirebeau, 2014b)

Input:

- Norm \mathcal{F}_x .

Output:

- Translated stencil $\wp(\mathbf{x})$.

Initialization:

- Initialize two lists: $\mathbb{M}(\mathbf{x}) \leftarrow \{(1, 0)\}$ and $\mathbb{L} \leftarrow \{(1, 0), (0, -1), (-1, 0), (0, 1)\}$.

Marching Loop:

- 1: **while** \mathbb{L} is non-empty **do**
 - 2: Let \mathbf{a} and \mathbf{b} be the last two elements of \mathbb{M} and \mathbb{L} respectively.
 - 3: **if** \mathbf{a} and \mathbf{b} agree with the acuteness condition (2.93) **then**
 - 4: $\mathbb{L} \leftarrow \mathbb{L} \cup \{\mathbf{b}\}$.
 - 5: Remove \mathbf{b} from \mathbb{M} .
 - 6: **else**
 - 7: Append $\mathbf{a} + \mathbf{b}$ to \mathbb{M} .
 - 8: **end if**
 - 9: **end while**
 - 10: Append all the elements of \mathbb{L} to \wp .
-

applications in the fields of computer vision and medical imaging, the AGSI method will be impractical, as pointed out by Mirebeau (2014a,b).

- Alternately, one-pass fast marching method with metric dependent stencils can be applied to solve the anisotropic Eikonal PDE. Sethian and Vladimirsky (2003) proposed an ordered upwind (OU) method where the local stencil are built in the course of the fast marching propagation. The sizes of the stencils used in OU fast marching method rely on the values of anisotropy ratio μ : a large value of μ implies a large size of stencil to cover the regions passed by the local optimal path. Contrary to the dynamic stencil construction based OM fast marching method (Sethian and Vladimirsky, 2003), Alton and Mitchell (2012) proposed a static stencil based method where the stencil will be constructed before the fast marching front propagation is performed. Both the mentioned fast marching methods have computation complexity $\mathcal{O}(\mu^d N \ln N)$ which are unworkable for large values of anisotropy ratio μ .

For the purpose of improving the stability and accuracy of the computation of the minimal action map with respect to a high anisotropic geodesic metric, a novel adaptive stencil construction method was introduced by Mirebeau (2014a) for 3D anisotropic Riemannian metric and by Mirebeau (2014b) for arbitrary 2D Finsler metric with computation complexity $\mathcal{O}(N \ln \mu + N \ln N)$ as described in next section. In this thesis, we make use of these adaptive stencil based fast marching method as our numerical tools for the proposed anisotropic Riemannian metrics by (Mirebeau, 2014a) and for novel anisotropic and asymmetric Finsler metrics.

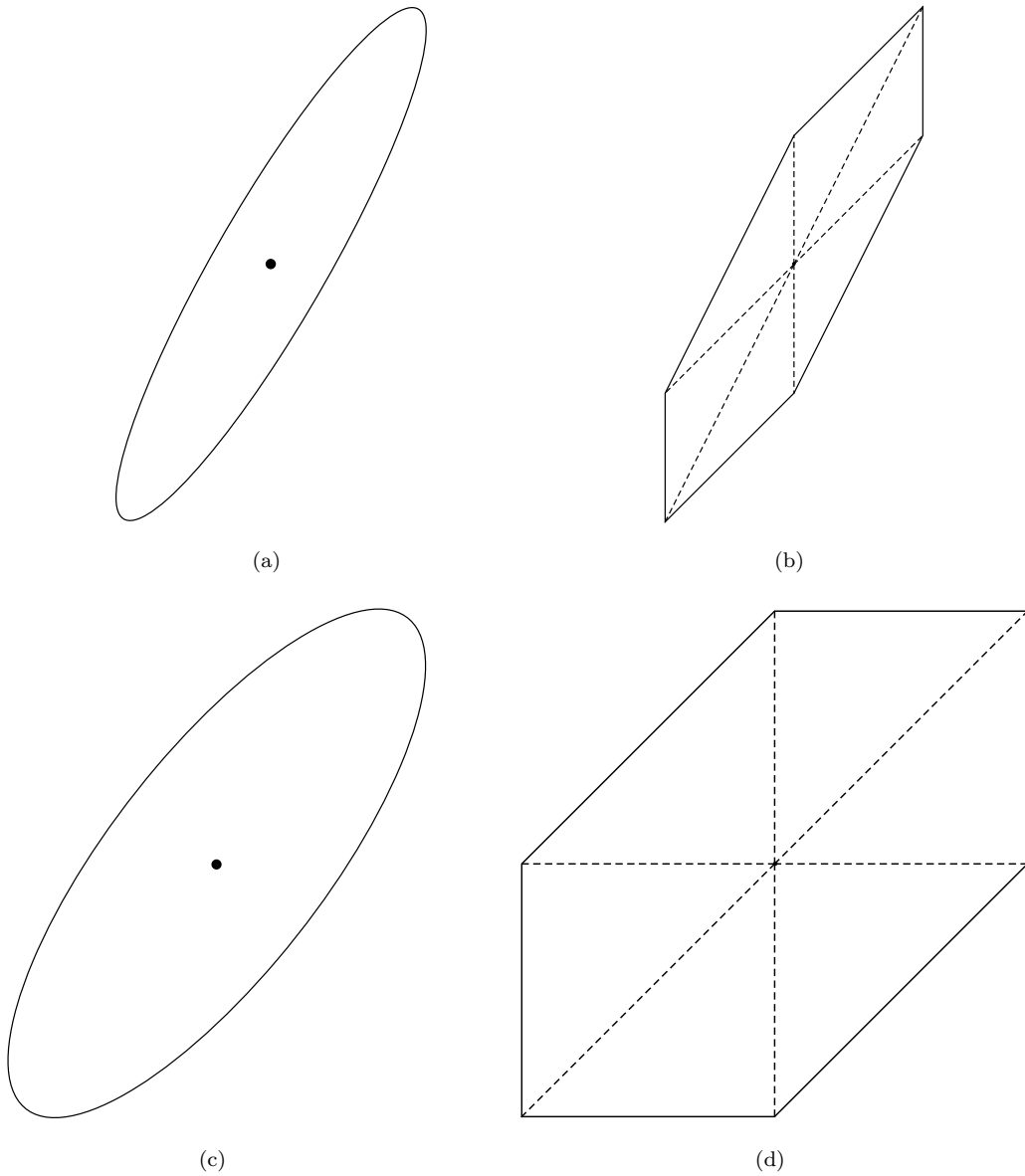


FIGURE 2.14: Demonstrations of the Uint balls for Riemannian Metrics and the respective stencils which are constructed using the method proposed by Mirebeau (2014a). (a) and (c) are the uint balls for different Riemannian metrics. (b) and (d) are the corresponding stencils. Black dots in (a) and (c) denote the origin of the stencils.

2.4.5 Adaptive Stencil-based Anisotropic Fast Marching Method

Mirebeau (2014b) proposed an anisotropic stencil refinement based fast marching method (FM-ASR) for the minimal action map computation with respect to an arbitrary Finsler metric with the form of

$$\mathcal{F}(\mathbf{x}, \mathbf{u}) = \sqrt{\mathbf{u}, \mathcal{M}(\mathbf{x}) \mathbf{u}} - \langle \omega, \mathbf{u} \rangle, \quad \forall \mathbf{x} \in \Omega, \mathbf{u} \in \mathbb{R}^2. \quad (2.91)$$

\mathcal{F} defines a general Finsler metric and will degenerate to a anisotropic Riemannian metric if $\omega = \mathbf{0}$ with respect to a non-diagonal symmetric positive definite tensor field \mathcal{M} . In the following, we introduce the stencil construction for 2D Finsler metric.

The \mathcal{F} dependent stencil construction is based on the geometrical concept of \mathcal{F}_x -acute angle (Mirebeau, 2014b). Two non-zero vectors $\mathbf{u}, \mathbf{v} \in \mathbb{R}^2$ form an \mathcal{F}_x -acute angle if they obey that for all $\delta > 0$

$$\mathcal{F}_x(\mathbf{u} + \delta\mathbf{v}) \geq \mathcal{F}_x(\mathbf{u}) \quad \text{and} \quad \mathcal{F}_x(\mathbf{v} + \delta\mathbf{u}) > \mathcal{F}_x(\mathbf{v}). \quad (2.92)$$

If \mathcal{F}_x is differentiable at \mathbf{u} and \mathbf{v} , the definition of \mathcal{F}_x -acute (2.92) is equivalent to the following condition:

$$\langle \mathbf{u}, \nabla \mathcal{F}_x(\mathbf{v}) \rangle \geq 0 \quad \text{and} \quad \langle \mathbf{v}, \nabla \mathcal{F}_x(\mathbf{u}) \rangle \geq 0, \quad (2.93)$$

where $\mathcal{F}_x(\cdot) = \mathcal{F}(\mathbf{x}, \cdot)$ is a norm on \mathbb{R}^2 .

Note that when \mathcal{F} is a Riemannian metric, i.e, the vector field $\omega = \mathbf{0}$ and

$$\mathcal{F}_x(\mathbf{u}) = \sqrt{\langle \mathbf{u}, \mathcal{M}(\mathbf{x}) \mathbf{u} \rangle},$$

then the condition (2.93) is reduced to

$$\langle \mathbf{u}, \mathcal{M}(\cdot) \mathbf{v} \rangle \geq 0, \quad \text{for } \mathbf{u}, \mathbf{v} \in \mathbb{R}^2 \text{ with } \mathbf{u} \neq \mathbf{0}, \mathbf{v} \neq \mathbf{0}. \quad (2.94)$$

Note that both (2.93) and (2.94) are the sufficient and necessary conditions for the \mathcal{F}_x -acute angle (Mirebeau, 2014b). The proof of the equivalence between (2.92) and (2.93) can be found from (Mirebeau, 2014b).

The translated stencil \wp can be constructed in terms of the concept of acuteness (2.93), as introduced in (Mirebeau, 2014a,b). A translated stencil \wp consists of a collection of non-zero vertices of triangles T (one of the vertices of each T is the origin $\mathbf{0}$) and corresponds to a stencil S (2.77) with vertices lying on the grid Z . \wp is said to be \mathcal{F}_x -acute if each triangle $T \in \wp$ has area 1/2 and obeys that the two non-zero vertices of the triangle T agree with (2.93). The procedure of the translated stencil construction can be found in Algorithm 2. This procedure computes the translated stencils in a recursive refinement manner. We demonstrate the translated stencils for anisotropic Riemannian metrics in Fig. 2.14 and for anisotropic and asymmetric Finsler metrics in Fig. 2.15 and Fig. 2.16.

The stencil S can be recovered by (2.77). A point $\mathbf{y} \in Z$ is a $S(\mathbf{x})$ -dependent

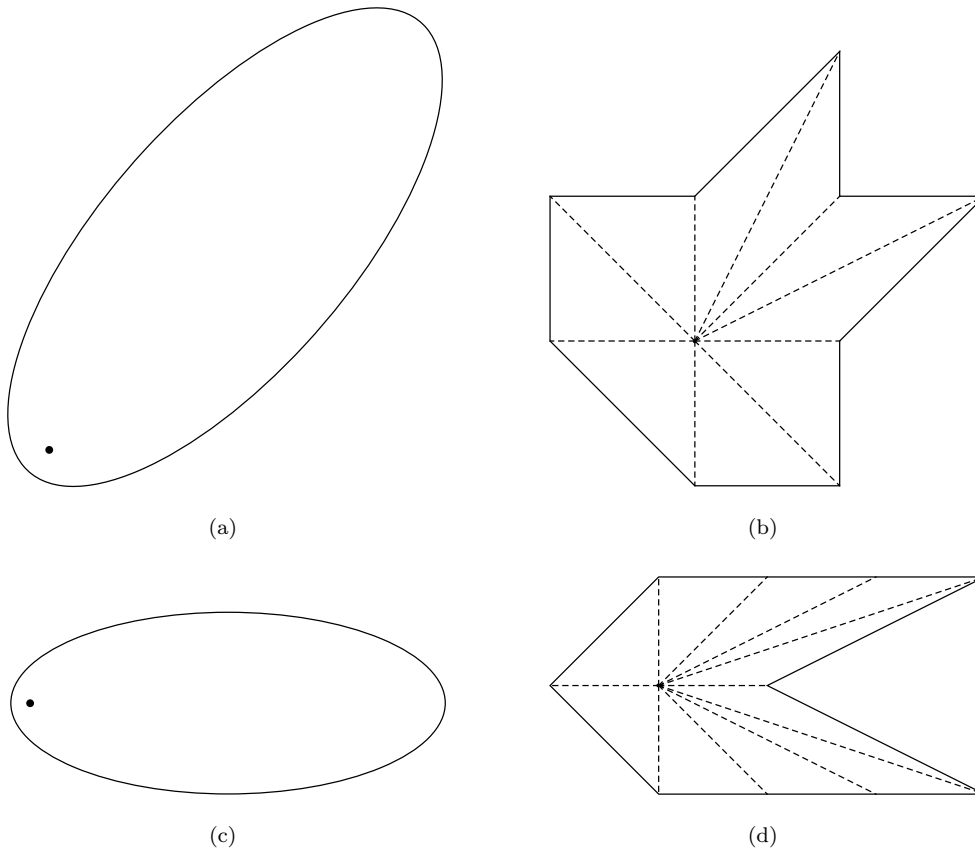


FIGURE 2.15: Demonstrations of the Uint balls for Finsler Metrics and the respective stencils which are constructed using the method proposed by Mirebeau (2014b). (a) and (c) are the uint balls for different Finsler metrics. (b) and (d) are the corresponding stencils. Black dots in (a) and (c) denote the origin of the stencils.

neighbourhood point of $\mathbf{x} \in Z$ if it obeys $\mathbf{x} \in S(\mathbf{y})$. In other words, the neighbourhood point set N_e of \mathbf{x} is defined in terms of $S(\mathbf{x})$ by

$$N_e(\mathbf{x}) := \{\mathbf{y} \in Z; \mathbf{x} \in S(\mathbf{y})\}.$$

Stencils Construction for Lifted Metrics

We take the radius-lifted anisotropic Riemannian metric as an example. The anisotropic Riemannian metric with radius lifting for tubular structure extraction survives over the domain $\hat{\Omega} \subset \mathbb{R}^2 \times \mathbb{R}^1$ with general tensor field form of (2.58) or (2.60). For completeness, we rewrite the radius-lifted tensor field \mathcal{M}_r

$$\mathcal{M}_r(\mathbf{x}, r) = \begin{pmatrix} \mathcal{M}_s(\mathbf{x}, r) & \mathbf{0} \\ \mathbf{0} & P_r(\mathbf{x}, r) \end{pmatrix}, \quad (2.95)$$

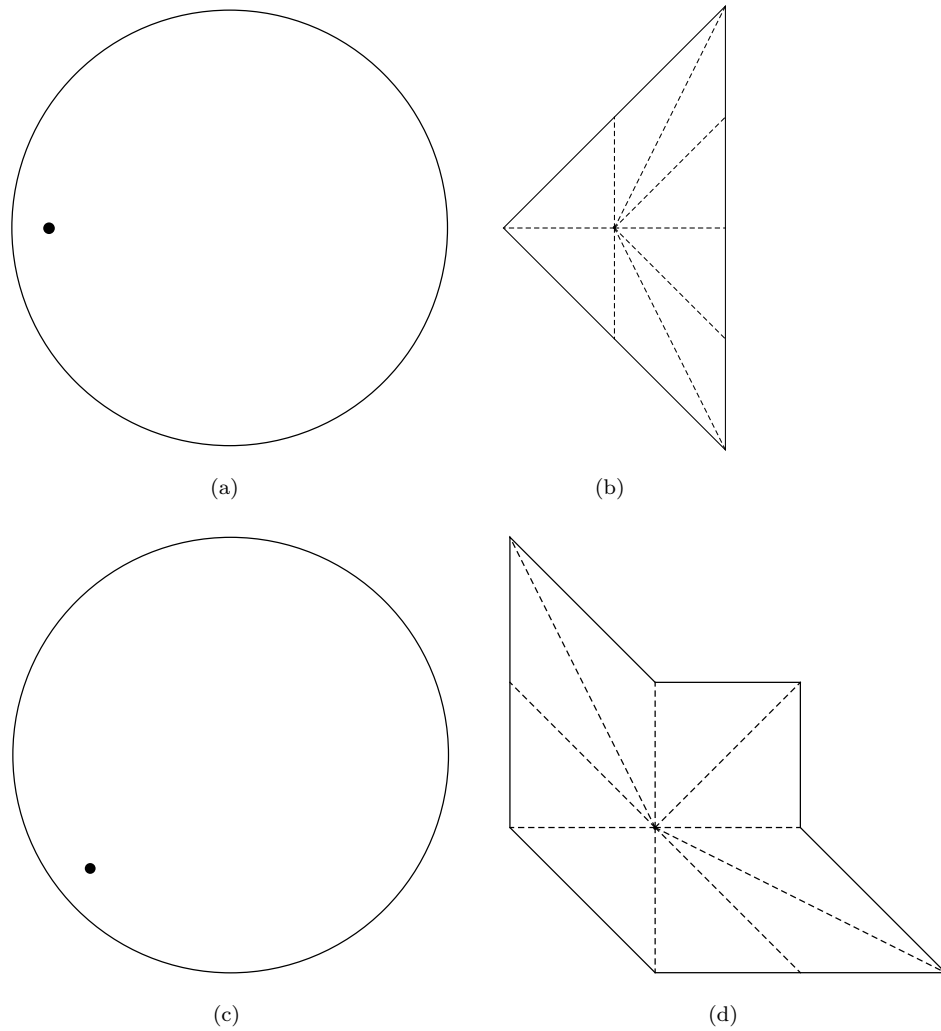


FIGURE 2.16: Demonstrations of the Uint balls for Finsler Metrics and the respective stencils which are constructed using the method proposed by Mirebeau (2014b). (a) and (c) are the uint balls for different Finsler metrics. (b) and (d) are the corresponding stencils. Black dots in (a) and (c) denote the origin of the stencils.

The anisotropy for this metric depends on the tensor \mathcal{M}_s (2.59), where the 2D case is

$$\mathcal{M}_s(\mathbf{x}, r) = P_1^s(\mathbf{x}, r) \mathbf{v}_1(\mathbf{x}, r) \mathbf{v}_1^T(\mathbf{x}, r) + P_2^s(\mathbf{x}, r) \mathbf{v}_2(\mathbf{x}, r) \mathbf{v}_2^T(\mathbf{x}, r). \quad (2.96)$$

Note that the vectors $\mathbf{v}_1(\mathbf{x}), \mathbf{v}_2(\mathbf{x}) \in \mathbb{R}^2$.

The steps for the stencil construction with respect to \mathcal{M}_r are listed as follows:

- We first invoke the method described in Algorithm 2 with respect to tensor field \mathcal{M}_s (2.95) to obtain the local translated stencils $\varphi(\mathbf{x})$, for any $\mathbf{x} \in Z$.
- The \mathcal{M}_r -based translated local stencil $\hat{\varphi}(\hat{\mathbf{x}})$ can be constructed as

- For each vertex $\mathbf{a} \in \wp(\mathbf{x})$, we append $(\mathbf{a}, 0)$ to $\hat{\wp}(\hat{\mathbf{x}})$.
- Append $(0, 0, 1)$ and $(0, 0, -1)$ to $\hat{\wp}(\hat{\mathbf{x}})$.

In this thesis, we make use of the above stencil construction scheme for the geodesic distance map computation with respect to the anisotropic *radius-lifted* Riemannian metric and the anisotropic and asymmetric *orientation-lifted* Finsler elastica metric.

Chapter 3

Retinal Vessel Segmentation via New Minimal Paths Models

Abstract

The retinal vessel extraction, including both the blood vessel centreline positions and their respective thickness values at the corresponding centreline points, has important medical and clinical applications. To satisfy this requirement, a retinal blood vessel can be modelled as a minimal geodesic in the sense that this geodesic involves both the vessel centreline positions and the corresponding vessel radii information. The minimal path models are therefore very suitable and intuitive for the retinal blood vessel extraction task. They are particularly efficient to extract a tubular structure in the way of giving two points at the ends of a retinal vessel ([Benmansour and Cohen, 2011](#); [Li and Yezzi, 2007](#)). However, there exist some difficulties suffered by these classical isotropic or anisotropic minimal path models, like the shortcuts problem and the short branches combination problem, leading to unexpected vessel extraction results.

In this chapter, we propose three novel minimal paths models to solve these existing problems in the task of retinal vessels extraction suffered by the classical minimal path models. These new minimal paths models include the mask-based keypoints detection model, the dynamic anisotropic Riemannian metric-based minimal path model and the region-constrained minimal paths model. All of these three models are devoted to extract both centrelines and the respective width values of vessels, combining with different retinal vessels properties, vessel orientation enhancement, and the prior vessel segmentation results. The vessel orientation is detected in this chapter by the optimally oriented flux filter proposed in ([Law and Chung, 2008](#)).

We perform the numerical experiments involving the comparative results for the proposed new minimal paths models in the retinal images. Actually, these proposed minimal paths models can also be adapted to extract vessels and roads from various types of medical images or aerial images, in either automatic or interactive ways.

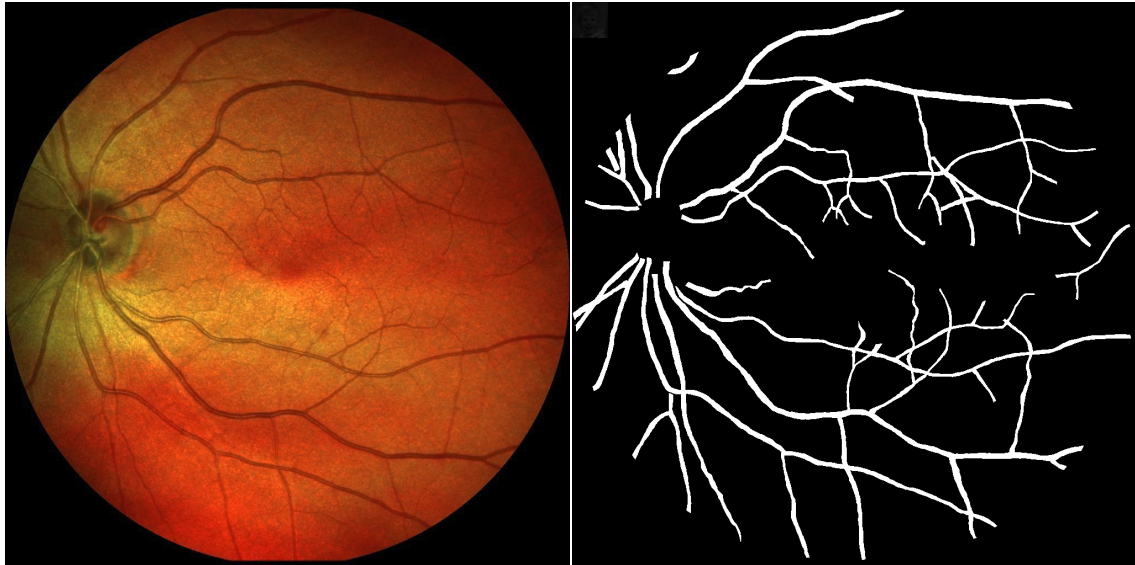


FIGURE 3.1: A Retinal vessel network image (left) and the corresponding vessel ground truth image (right).

3.1 Introduction

Vessel extraction is an essential component of computer-aided diagnosis methods for the diagnosis of disorders and pathologies. Various vasculature structure segmentation methods, such as vessel enhancement methods and deformable models have been studied during the passed three decades (Fraz et al., 2012; Kirbas and Quek, 2004; Lesage et al., 2009). Retinal vessel segmentation and extraction is a difficult task due to the complicated vessel network and inhomogeneous intensities distribution, see Fig. 3.1 for an example of a color retinal vessel image and its groundtruth image. Manually segmenting retinal vessels costs expensive time and requires to train medical experts. Thus accurate and efficient automatic and semi-automatic methods for generation of retinal vessel binary segmented map are extremely helpful to the clinical diagnosis for various related diseases such as diabetes, and biometric identification since the retinal vessel tree is unique individually (Dominguez et al., 2015; Koch et al., 2014; Mariño et al., 2006).

Retinal Vessel Tracking Models

Retinal vessel tracking methods can find both the centrelines and radii values for each individual vessel. Generally, the tracking methods consider to describe a piece of vessel by a collection of ordered vessel profiles, which can be determined either by minimizing the distance between the detected local cross sectional image feature and the prior ideal vessel model, or by optimizing the computed local

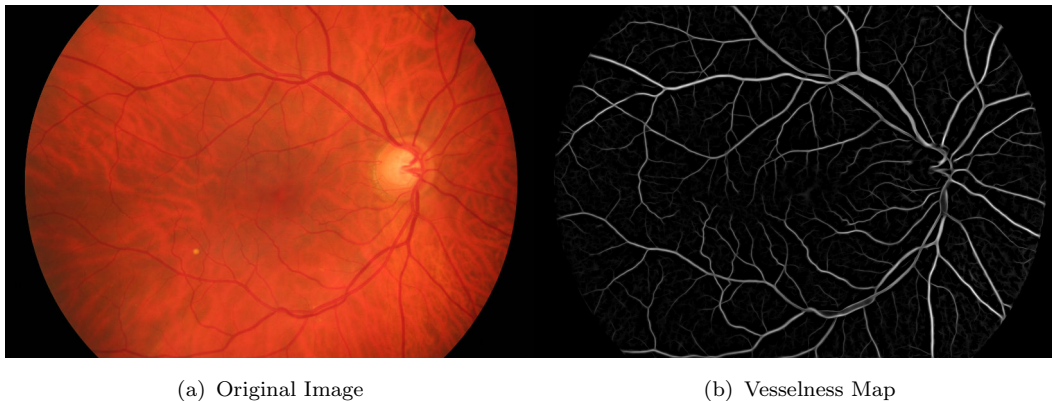


FIGURE 3.2: An example of retinal vessel image and its vesselness map.

image features¹. These tracking methods can start from a initial profile, and then recursively add new vessel profiles until stopping criterion are reached (Bekkers et al., 2014; Chutatape et al., 1998; Lowell et al., 2004; Yin et al., 2012). Each vessel profile consists of one centre point and two edge points². In each iteration, the basic procedure of the class of these vessel tracking models can be roughly divided into two steps:

- Growing stage. The centre point and edge points in the current profile can be used to determine the local orientation of the vessel at the centre point. By going ahead a small distance along this detected orientation, the initial guess of the next centre point can be obtained.
- Configuration stage. The vessel profile associated to the initial centre point from the growing stage can be determined.

The main difference of the vessel tracking methods with growing scheme lies at the configuration stage. Different criterion have been proposed to obtain the optimal vessel profiles. For example, Lowell et al. (2004) used two Gaussian kernels to fit the vessel cross sectional gray level distribution to reduce the influences leading by centre reflection. Bekkers et al. (2014) proposed to use the orientation score computed by wavelet methods (Duits et al., 2007; Jones and Palmer, 1987) to detect the edge points.

Retinal Vessel Segmentation Models

The basic idea of the vessel enhancement methods (Chaudhuri et al., 1989; Frangi et al., 1998; Hannink et al., 2014; Law and Chung, 2008; Xiao et al., 2013) is to

¹Such as the norm of image gradient.

²Note that in (Yin et al., 2012), the authors used four and eight edge points to describe bifurcation and crossing respectively

convert the original vessel image into the vesselness map for which the value of each pixel indicates the probability of this pixel belonging to a vessel, see Fig. 3.2 for an example. Then the binary segmented vessel map can be obtained either by thresholding the vesselness map by a constant value, or by an adaptive thresholding procedure (Hoover et al., 2000; Jiang and Mojon, 2003). The adaptive thresholding methods use a set of threshold values to test each point by taking into account both the position and vesselness value of this point. The crucial point of these methods is the vesselness map, which can be computed by matched filter (Chaudhuri et al., 1989), Hessian matrix (Frangi et al., 1998; Sato et al., 1998), flux (Law and Chung, 2008) or orientation score (Hannink et al., 2014).

The main contents of this chapter were presented at the ICIP 2014 conference (Chen et al., 2014), the EMBC 2015 conference (Chen and Cohen, 2015a) and the SSVM 2015 conference (Chen and Cohen, 2015b).

3.2 Anisotropy Descriptor: Optimally Oriented Flux Filter

Detecting both the orientations and positions of the blood vessels are essential task of tubular structure detection. The enhancement based blood vessel detectors such as the Hessian based filter (Frangi et al., 1998) and the optimally oriented flux filter (Law and Chung, 2008) can achieve this goal by the use of the image gradient field. They can assign each pixel in the image domain a value denoting the probability that this pixel appearing as a vessel point, and a vector indicating the optimal orientation of the possible vessel at this point. It is demonstrated in (Benmansour and Cohen, 2011; Law and Chung, 2008) that the optimally oriented flux filter has better performance than Hessian based filter (Frangi et al., 1998) for the vessel branches detection. In this section, we focus on the 2D optimal oriented flux filter.

Definition

The oriented flux f of an image I , of dimension 2, is defined by the amount of the image gradient projected along the orientation \mathbf{n} flowing out from a 2D circle at point \mathbf{x} with radius r :

$$f(\mathbf{x}; r, \mathbf{p}) := \oint_{\partial S_r} (\nabla(G_\sigma * I)(\mathbf{x} + r\mathbf{n}) \cdot \mathbf{p})(\mathbf{p} \cdot \mathbf{n}) ds, \quad (3.1)$$

where G_σ is a Gaussian function with variance σ and \mathbf{n} is the outward unit normal vector along ∂S_r . ds is the infinitesimal length on ∂S_r . ∇ is the gradient operator and $*$ is the convolution operator.

By the divergence theorem, it is proved that the oriented flux f in (3.1) can be rewritten as a quadratic function by a symmetric matrix \mathcal{Q} . Therefore, one has

$$f(\mathbf{x}; r, \mathbf{p}) = \langle \mathbf{p}, \mathcal{Q}(\mathbf{x}, r) \mathbf{p} \rangle,$$

where the eigenvalues and eigenvectors of the symmetric matrix $\mathcal{Q}(\mathbf{x}, r)$ we denote by $\lambda_i(\mathbf{x}, r)$ and $\mathbf{v}_i(\mathbf{x}, r)$, $i = 1, 2$. One has

$$\mathcal{Q}(\mathbf{x}, r) = \sum_{i=1}^2 \lambda_i(\mathbf{x}, r) \mathbf{v}_i(\mathbf{x}, r) \mathbf{v}_i^T(\mathbf{x}, r). \quad (3.2)$$

We refer to the symmetric matrix \mathcal{Q} as the oriented flux matrix. Law and Chung (2008) used the normalized summation of the non-zero eigenvalues to compute the vesselness map, which takes its largest values for points \mathbf{x} in vessel centrelines. Indeed, the eigenvector of $\mathcal{Q}(\mathbf{x})$ oriented tangentially to the vessel is associated to

an eigenvalue with small or zero magnitude, whereas another eigenvector oriented transversally to the vessel are associated to eigenvalue with large magnitude. We assume that points inside a vessel have higher intensity values than those in the background. Without loss of generality, we assume that $\lambda_1(\cdot) \leq \lambda_2(\cdot) \approx 0$ such that the eigenvalue λ_1 can be used to compute the vesselness map which is defined by $\mathbb{V}_{\text{ness}} : \Omega \rightarrow \mathbb{R}$ as follows:

$$\mathbb{V}_{\text{ness}}(\mathbf{x}) := \max \left\{ \max_r \left\{ -\frac{1}{r} \lambda_1(\mathbf{x}, r) \right\}, 0 \right\}. \quad (3.3)$$

The normalized factor $1/r$ is used to remove the scale bias of the optimal oriented flux filter to ensure that the vesselness map \mathbb{V}_{ness} is scale invariant. The vesselness map $\mathbb{V}_{\text{ness}}(\mathbf{x})$ in (3.3) has a large value if \mathbf{x} is located inside the vessels, which means that we can take into account this vesselness map to indicate the the probability of each pixel appearing as a vessel point.

For each pixel, we can assign an optimal scale value, by using the following optimal scale map \mathcal{S}_{opt} :

$$\mathcal{S}_{\text{opt}}(\mathbf{x}) = \arg \max_r \left\{ -\frac{1}{r} \lambda_1(\mathbf{x}, r) \right\}. \quad (3.4)$$

Based on the map \mathcal{S} , the optimal oriented flux matrix \mathcal{Q}_{opt} can be expressed by:

$$\mathcal{Q}_{\text{opt}}(\mathbf{x}) = \mathcal{Q}(\mathbf{x}, \mathcal{S}_{\text{opt}}(\mathbf{x})). \quad (3.5)$$

By the matrix decomposition method, the optimal oriented flux matrix \mathcal{Q}_{opt} can be expressed as

$$\mathcal{Q}_{\text{opt}}(\mathbf{x}) = \Lambda_1(\mathbf{x}) \mathbf{V}_1(\mathbf{x}) \mathbf{V}_1^T(\mathbf{x}) + \Lambda_2(\mathbf{x}) \mathbf{V}_2(\mathbf{x}) \mathbf{V}_2^T(\mathbf{x}), \quad (3.6)$$

where the vector $\mathbf{V}_1(\mathbf{x})$ can be considered as the tubular structure orientation at point \mathbf{x} if it is located inside a vessel. Thus the vector field \mathbf{V}_2 are the orthogonal vector field of \mathbf{V}_1 . Note that vector fields \mathbf{V}_1 and \mathbf{V}_2 will be used to constructed to the anisotropic Riemannian metric in the following section.

Scalar fields $\Lambda_1, \Lambda_2 : \Omega \rightarrow \mathbb{R}$ are the eigenvalues at the optimal scale for all the points $\mathbf{x} \in \Omega$, which are defined by:

$$\Lambda_1(\mathbf{x}) = \lambda_1(\mathbf{x}, \mathcal{S}_{\text{opt}}(\mathbf{x})), \quad (3.7)$$

$$\Lambda_2(\mathbf{x}) = \lambda_2(\mathbf{x}, \mathcal{S}_{\text{opt}}(\mathbf{x})). \quad (3.8)$$

Note that maps \mathbb{V}_{ness} , \mathcal{S} and \mathcal{Q}_{opt} are all defined over the image domain $\Omega \subset \mathbb{R}^2$ instead of the radius-lifted space $\hat{\Omega}$.

3.3 Optimally Oriented Flux Filter-based Anisotropic radius-lifted Riemannian Metric Construction

Benmansour and Cohen (2011) introduced a way to construct the anisotropic radius-lifted Riemannian metric \mathcal{R}^{AR} (2.61) by using the optimally oriented flux filter (Law and Chung, 2008). Let us recall the radius-lifted tensor field \mathcal{M}_r :

$$\mathcal{M}_r(\hat{\mathbf{x}}) = \begin{pmatrix} \mathcal{M}_s(\hat{\mathbf{x}}) & \mathbf{0} \\ \mathbf{0} & P_r(\hat{\mathbf{x}}) \end{pmatrix}, \quad (3.9)$$

where \mathcal{M}_s is a symmetric tensor with size 2×2 :

$$\mathcal{M}_s(\hat{\mathbf{x}}) = \exp(\alpha \lambda_2(\hat{\mathbf{x}})) \mathbf{v}_1(\hat{\mathbf{x}}) \mathbf{v}_1^{\text{T}}(\hat{\mathbf{x}}) + \exp(\alpha \lambda_1(\hat{\mathbf{x}})) \mathbf{v}_2(\hat{\mathbf{x}}) \mathbf{v}_2^{\text{T}}(\hat{\mathbf{x}}), \quad (3.10)$$

and $P_r : \hat{\Omega} \rightarrow \mathbb{R}^+$ is a scalar potential function penalizing the variations of the tubular structure thickness which can be expressed as:

$$P_r(\mathbf{x}, r) = \beta \exp\left(\alpha \frac{\lambda_1(\mathbf{x}, r) + \lambda_2(\mathbf{x}, r)}{2}\right), \quad (3.11)$$

where λ_1, λ_2 are the eigenvalues of the matrix \mathcal{Q} (3.2) and $\mathbf{v}_1, \mathbf{v}_2$ are the corresponding eigenvectors. The constant $\beta > 0$ controls the speed along the radius direction, and constant α controls the anisotropy ratio $\mu \geq 1$ for the anisotropic Riemannian metric \mathcal{R}^{AR} :

$$\mu(\mathcal{R}^{\text{AR}}) = \max_{(\mathbf{x}, r)} \sqrt{\frac{\exp(\alpha \lambda_2(\mathbf{x}, r))}{\exp(\alpha \lambda_1(\mathbf{x}, r))}} = \sqrt{\exp\left(\alpha \max_{(\mathbf{x}, r)} (\lambda_2(\mathbf{x}, r) - \lambda_1(\mathbf{x}, r))\right)}.$$

In practice, we use the values of the anisotropy ratio μ and the constant β to construct the tensor field \mathcal{M}_r . The local adaptive stencils for the fast marching method (Mirebeau, 2014a) can be computed by the metric \mathcal{R}^{AR} . It is reported by Mirebeau (2014a,b) that the fast marching method can compute the minimal action map precisely and efficiently for any $\mu \in [1, 100]$.

Based on the constructed tensor field \mathcal{M}_r (3.9), one can find a geodesic which can describe both the centreline points and radius values by globally minimizing the the following curve energy

$$\mathcal{L}(\gamma) = \int_0^1 \sqrt{\langle \gamma'(t), \mathcal{M}_r(\gamma(t)) \gamma'(t) \rangle} dt, \quad (3.12)$$

where $\gamma : [0, 1] \rightarrow \hat{\Omega}$ is a regular curve.

3.4 Mask-based Keypoints Detection

We address a more difficult problem in this section, comparing to the classical minimal path models: the extraction of a full vessel tree structure given a single initial root point, by growing a collection of keypoints or new initial source points, connected by minimal geodesic paths. In this section, these keypoints are iteratively added, using a new detection criteria, which utilize the weighted geodesic distances with respect to an anisotropic radius-lifted Riemannian metric, the standard Euclidean curve length and a path score.

3.4.1 Brief Introduction to Existing KeyPoints Models

The basic minimal path models such as (Benmansour and Cohen, 2011; Cohen and Kimmel, 1997; Li and Yezzi, 2007), require user input initial source points and endpoints as the prior knowledge to track the minimal paths. The initial source points, considered as the boundaries of the nonlinear Eikonal equation, are necessary initialize the fast marching algorithm. The end points are used to start the geodesics back-tracking scheme. In some cases, to provide both initial source points and end points are difficult and time-consuming. In another aspect, for vessel tree extraction, the positions of the initial source points can be detected by, for example, finding the points with local minimum of the vesselness map. Therefore, efforts have been devoted to reduce the end points input.

For the purpose mentioned above, Benmansour and Cohen (2009) proposed a new approach: a keypoints searching method to detect recursively new startpoints (or keypoints) along the expected features named. Kaul et al. (2012) improved this idea using a new stopping criterion for both open and closed curve detection and a new method to compute the Euclidean curve length different to (Benmansour and Cohen, 2009; Deschamps and Cohen, 2001). li20093d proposed to detect the tubular structure using the extra radii model with isotropic Riemannian metric Li and Yezzi (2007) and the original keypoints searching criteria proposed by Benmansour and Cohen (2009).

Two main weaknesses of the classical keypoints searching approach proposed by (Benmansour and Cohen, 2009) are that the geodesic distance and the Euclidean path length do not take into account the orientation of the tubular structure or object boundaries, due to the use of an isotropic geodesic Riemannian metric, and suffer from a leakage problem. In contrast, we use an anisotropic geodesic Riemannian metric, and develop new criteria for selecting keypoints based on the path score and automatically stopping the tree growth. Experimental results demonstrate that our method can obtain the expected results which can extract vessel structures at a finer scale, with increased accuracy.

In this section, we proposed a new vessel tree extraction method based on the automatic keypoints detection and state-of-the-art anisotropic fast marching method proposed by Mirebeau (2014a) for an open source library. The pairwise distances between keypoints are fixed by a curve length threshold; classical keypoints searching method (Benmansour and Cohen, 2009) tends to overlook parts of the vessel tree when the curve length threshold is small, and to leak or take shortcuts between distinct branches of the vessel tree for large curve length threshold. We substantially improve the performance for small curve length threshold, by incorporating in the keypoint detection criterion a path score computed from the optimally oriented flux vesselness map for each keypoint candidate detected by the classical definition. Furthermore, The above mentioned keypoints-based minimal path models use the isotropic metric. In contrast, we make use of the anisotropic Riemannian metric, integrating with the path orientation, to enforce the geodesic agree with the vessel orientation. The Euclidean curve length computation method associated to an anisotropic Riemannian metric is also presented, based on the Hopf-Lax formula.

Summarily, our contribution in this section is as follows:

- We redefine the keypoints to make them reasonable even for small curve length threshold.
- We present the extension of the curve length calculation in the anisotropic case, in itself a different contribution.
- We give a stopping criterion to automatically stop the keypoints searching scheme.

3.4.2 Euclidean Curve Length Calculation

One of the critical points of keypoints method is the calculation of the geodesic curve length (geodesic distance) map and the Euclidean curve length map using fast marching method (Mirebeau, 2014a) simultaneously. Letting \mathcal{K} be the collection of keypoints which are taken as new source points, for any geodesic $\mathcal{C}_{\hat{s}, \hat{x}}$ where $\hat{s} \in \mathcal{K}$ is an initial source point, the Euclidean curve length map $L(\hat{x}) = L(\mathcal{C}_{\hat{s}, \hat{x}})$ can be formulated as:

$$L(\hat{x}) := \int_{\mathcal{C}_{\hat{s}, \hat{x}}} \|\mathcal{C}'_{\hat{s}, \hat{x}}(t)\| dt. \quad (3.13)$$

A natural approach of computing the Euclidean curve length map L , is to extract for each $\hat{x} \in \hat{\Omega}$ a minimal geodesic $\mathcal{C}_{\hat{s}, \hat{x}}$ by solving the ODE (2.55), and then calculating its Euclidean curve length. This first method turns out unfortunately to be too expensive in terms of computational cost.

Deschamps and Cohen (2001) and Benmansour and Cohen (2009) proposed a fast method for approximating the Euclidean curve length in the course of the fast marching front propagation. However, their methods depend only on the isotropic Riemannian metrics over the image domain Ω . In this section, we extend this method to the radius-lifted anisotropic Riemannian metric case to blend the benefits of both orientation enhancement and radius lifting.

Based on the tensor field \mathcal{M}_r as shown in (3.9), the geodesic distance map $\mathcal{U}(\hat{\mathbf{x}})$ denoting the geodesic curve length of $\mathcal{C}_{\hat{\mathbf{s}}, \hat{\mathbf{x}}}$ can be obtained by solving the Eikonal PDE

$$\begin{cases} \|\nabla \mathcal{U}(\hat{\mathbf{x}})\|_{\mathcal{M}_r^{-1}(\hat{\mathbf{x}})} = 1, & \forall \hat{\mathbf{x}} \in \hat{\Omega} \setminus \{\hat{\mathbf{s}}\} \\ \mathcal{U}(\hat{\mathbf{s}}) = 0. \end{cases} \quad (3.14)$$

The Eikonal PDE (3.14) can be approximated by the fixed point system (2.85) with a Hopf-Lax update operator Λ :

$$\begin{aligned} \Lambda \mathcal{U}(\hat{\mathbf{x}}) &= \min_{\hat{\mathbf{y}} \in \partial S(\hat{\mathbf{x}})} \left\{ \mathcal{R}_{\text{AR}}(\hat{\mathbf{x}}, \hat{\mathbf{y}} - \hat{\mathbf{x}}) + I_{S(\hat{\mathbf{x}})} \mathcal{U}(\hat{\mathbf{y}}) \right\}, \\ &= \min_{\hat{\mathbf{y}} \in \partial S(\hat{\mathbf{x}})} \left\{ \|\hat{\mathbf{y}} - \hat{\mathbf{x}}\|_{\mathcal{M}_r(\hat{\mathbf{x}})} + I_{S(\hat{\mathbf{x}})} \mathcal{U}(\hat{\mathbf{y}}) \right\}, \end{aligned} \quad (3.15)$$

where $I_{S(\hat{\mathbf{x}})}$ denotes the piecewise linear interpolation operator on the mesh $S(\hat{\mathbf{x}})$, and $\hat{\mathbf{y}}$ lies on the boundary of $S(\hat{\mathbf{x}})$ (Mirebeau, 2014a). $\mathcal{R}_{\text{AR}}(\hat{\mathbf{x}}, \hat{\mathbf{y}} - \hat{\mathbf{x}})$ is the anisotropic radius-lifted Riemannian metric as described in (2.61).

An approximation of L is given by the solution of the following fixed point problem: find $L : \hat{\Omega} \rightarrow \mathbb{R}$ such that (i) for all $\hat{\mathbf{x}} = (\mathbf{x}, r) \in \mathcal{K}$, $\ell(\hat{\mathbf{x}}) = 0$, and (ii) for all $\hat{\mathbf{x}} \in \hat{\Omega} / \mathcal{K}$, denoting by $\hat{\mathbf{y}}^*$ the point at which the minimum of the Hopf-Lax update operator (3.15) is attained. One can compute L as

$$L(\hat{\mathbf{x}}) = \|\hat{\mathbf{y}}^* - \hat{\mathbf{x}}\|_{M_2} + L(\hat{\mathbf{y}}^*), \quad (3.16)$$

where $L(\hat{\mathbf{y}}^*)$ can be obtained by interpolation. $\|\mathbf{u}\|_{M_2} = \sqrt{\langle \mathbf{u}, M_2 \mathbf{u} \rangle}$ and M_2 with size 3×3 is defined as

$$M_2 = \begin{pmatrix} 1 & 0 & 0 \\ 0 & 1 & 0 \\ 0 & 0 & 0 \end{pmatrix}. \quad (3.17)$$

Equation (3.16) means that we only compute the approximated curve length of the projected path from the radius-lifted domain $\hat{\Omega}$ to the image domain Ω .

Let \hat{Z} be a discretization grid of the radius-lifted domain $\hat{\Omega}$. For concreteness, we give a second description of (3.16), closer to implementation and specialized to 3-dimensional domains as in the 2D with radius lifting case. Opting for offset based notations, we introduce the translated stencil

$$\wp(\hat{\mathbf{x}}) := S(\hat{\mathbf{x}}) - \hat{\mathbf{x}}, \quad \hat{\mathbf{x}} \in \hat{Z} \cap \hat{\Omega}, \quad (3.18)$$

which is a collection of tetrahedra which union is a neighborhood of the origin. A generic boundary stencil point $\hat{\mathbf{y}} \in \partial S(\hat{\mathbf{x}})$ as in optimization (3.16) can then be expressed as:

$$\hat{\mathbf{y}} = \hat{\mathbf{x}} + \sum_{i=1}^3 \psi_i \hat{\mathbf{u}}_i, \quad (3.19)$$

$$s.t. \quad \psi_i > 0, \text{ and } \sum_{i=1}^3 \psi_i = 1, \quad (3.20)$$

where $\hat{\mathbf{u}}_1$, $\hat{\mathbf{u}}_2$ and $\hat{\mathbf{u}}_3$ are non-zero vertices of a common tetrahedron $T \in \wp(\hat{\mathbf{x}})$. Consider the compact and convex set:

$$\Psi := \{\psi = (\psi_1, \psi_2, \psi_3); \psi_i > 0, \sum_{i=1}^3 \psi_i = 1, i = 1, 2, 3\}. \quad (3.21)$$

For each point $\hat{\mathbf{x}} \in \hat{Z} \cap \hat{\Omega}$ and simplex $T \in \wp(\hat{\mathbf{x}})$ we consider the function:

$$\mathcal{J}_{\hat{\mathbf{x}},T}(\psi) = \left\| \sum_{i=1}^3 \psi_i \hat{\mathbf{u}}_i \right\|_{\mathcal{M}_r(\hat{\mathbf{x}})} + \sum_{i=1}^3 \psi_i \mathcal{U}(\hat{\mathbf{x}} + \hat{\mathbf{u}}_i). \quad (3.22)$$

One can see that $\mathcal{J}_{\hat{\mathbf{x}},T}$ is a convex function on the set of Ψ (3.21). Minimizing $\mathcal{J}_{\hat{\mathbf{x}},T}$ can be found in (Mirebeau, 2014a; Sethian and Vladimirsky, 2003). Then equation (3.16) is equivalent to

$$\mathcal{U}(\hat{\mathbf{x}}) = \min_{T \in \wp} \left\{ \min_{\psi \in \Psi} \left\{ \mathcal{J}_{\hat{\mathbf{x}},T}(\psi) \right\} \right\}. \quad (3.23)$$

In offset based coordinates, the minimizer of the fixed point problem formulated in (3.15) is denoted by $\psi^* = (\psi_1^*, \psi_2^*, \psi_3^*)$. Then equation (3.16) can be expressed with respect to ψ^* :

$$L(\hat{\mathbf{x}}) = \left\| \sum_{i=1}^3 \eta_i^* \hat{\mathbf{u}}_i \right\|_{M_2} + \sum_{i=1}^3 \eta_i^* \mathcal{L}(\hat{\mathbf{x}} + \hat{\mathbf{u}}_i). \quad (3.24)$$

Therefore, the minimizer $\hat{\mathbf{y}}^* = \hat{\mathbf{x}} + \sum_{i=1}^3 \psi_i^* \hat{\mathbf{u}}_i$. A single pass solve is again possible: whenever the Fast Marching algorithm updates $\mathcal{U}(\hat{\mathbf{x}})$, simultaneously update $L(\hat{\mathbf{x}})$, using the (just computed) minimizer $\hat{\mathbf{y}}^*$ from (3.15).

3.4.3 Keypoints Definition with a Path Score

The score \mathcal{PS} of a path $\gamma = (\Gamma, r)$ is obtained by averaging the vesselness map \mathbb{V}_{ness} computed from the optimally oriented flux filter proposed by Law and Chung

(2008), see (3.3) for details. One has

$$\mathcal{PS}(\Gamma, \text{Th}) = \frac{\int_{\Gamma} \mathbb{V}_{\text{ness}}(\Gamma(s)) \delta(\text{Th}, \mathbb{V}_{\text{ness}}(\Gamma(s))) ds}{\int_{\Gamma} \delta(\text{Th}, \mathbb{V}_{\text{ness}}(\Gamma(s))) ds}. \quad (3.25)$$

The threshold parameter $\text{Th} > 0$ and selector $\delta(\cdot, \cdot)$ are used to eliminate irrelevant parts of the path

$$\delta(\text{Th}, d) = \begin{cases} 1, & \text{if } d < \text{Th}; \\ 0, & \text{otherwise.} \end{cases} \quad (3.26)$$

For each $\mathbf{x} \in \Omega$, we denote by $\mathcal{PS}(\mathbf{x}, \text{Th}) = \mathcal{PS}(\Gamma_{\mathbf{x}}, \text{Th})$ the path score associated to the geodesic $\mathcal{C}_{s,\mathbf{x}} = (\Gamma_{\mathbf{x}}, r)$ joining $\hat{\mathbf{x}} = (\mathbf{x}, r)$ to the source point \hat{s} .

Our algorithm combines three main ingredients:

- The classical keypoint searching scheme (Benmansour and Cohen, 2009);
- State-of-the-art anisotropic Fast Marching method (Mirebeau, 2014a) with integrated geodesic curve length computation;
- Vessel tree extraction based on original and new keypoints selection criteria as well as the stopping criteria.

In practice, our keypoints detection method is embedded within the inner loop of the fast marching method, which it augments with several robust criteria for keypoints detection, adaptation of a set of path score thresholds, and termination.

Keypoints Selection Method

The approximated geodesic distance \mathcal{U} to the currently extracted tree structure is estimated using the fast marching algorithm update scheme: initialization and steps 2-12 of the loop in Algorithm 3.

Following the dynamic programming principle, image pixels are tagged as either *Trial* or *Accepted*. The *Trial* point $\hat{\mathbf{x}}_{\min}$ currently minimizing \mathcal{U} is tagged as *Accepted* (i.e. frozen), and the value $\mathcal{U}(\hat{\mathbf{y}})$ at neighbouring points $\hat{\mathbf{y}}$ is suitably updated. In addition, line 10, we estimate the geodesic curve length $\mathcal{U}(\hat{\mathbf{y}})$ and Euclidean curve length $L(\hat{\mathbf{y}})$, and potentially tag $\hat{\mathbf{y}}$ as *Trial*. The original keypoints selection method (KPSM) (Benmansour and Cohen, 2009) adds the currently active point (the latest *Accepted* point) $\hat{\mathbf{x}}_{\min}$ to the set \mathcal{K} of keypoints as soon as $L(\hat{\mathbf{x}}_{\min}) \geq \lambda$, where λ is the user chosen Euclidean curve length threshold. The reason of choosing such a point as keypoint is that among all the points with the

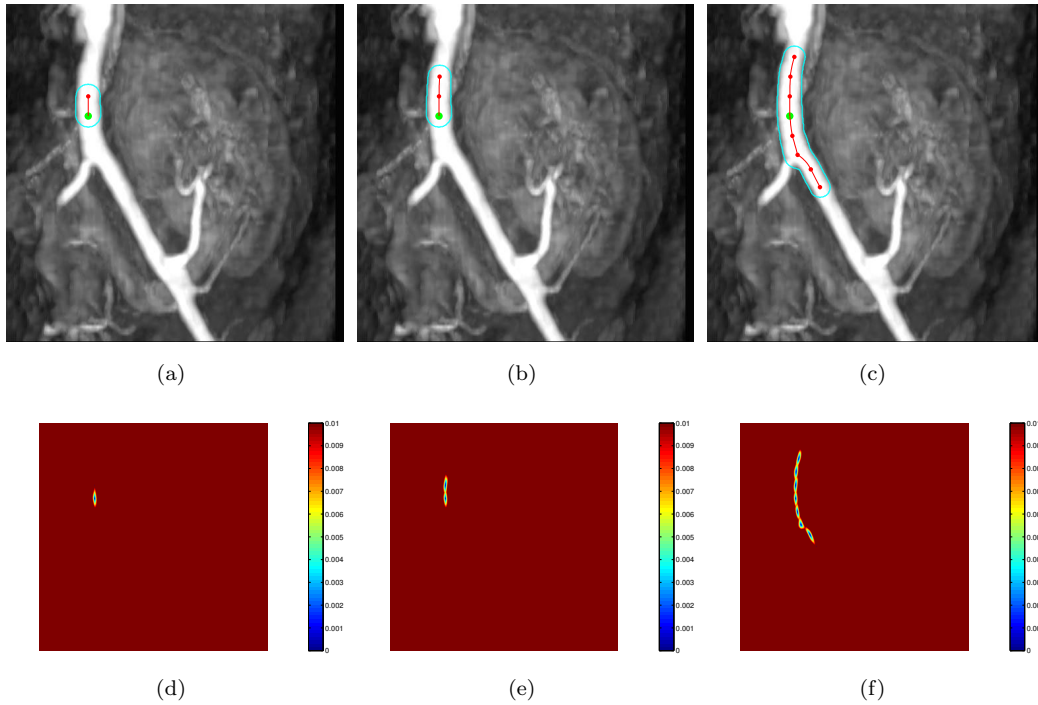


FIGURE 3.3: Steps of keypoints searching scheme. (a) The first keypoint is found. (b) Two keypoints are found. (c) Seven keypoints are found. Cyan contours are the boundaries of the tubular structure and red lines are the centrelines. (d)-(f) are the optimal distance maps \mathcal{U}_{opt} for corresponding to the images of (a)-(c).

same minimal action map value, a point $\hat{\mathbf{q}}$ *globally* maximizing the Euclidean curve length map L will be located in the centreline of the tubular structure (Benmansour and Cohen, 2009; Chen et al., 2014; Kaul et al., 2012; Li et al., 2009).

Keypoints Searching Scheme Based on A Path Score

A point $\hat{\mathbf{x}} = (\mathbf{x}, r)$ is marked as a new keypoint if its Euclidean curve length satisfies $L(\hat{\mathbf{x}}) \in [\lambda, 3\lambda)$, and if additionally it obeys

$$\min \left\{ \mathcal{PS}(\mathbf{x}, \text{Th}_{i-1}), \mathbb{V}_{\text{ness}}(\mathbf{x}) \right\} > \text{Th}_i, \quad (3.27)$$

where \mathbb{V}_{ness} is the vesselness map. The key idea behind this selection criterion is that, among all points for which the action map \mathcal{U} is within a given bound, the point which maximizes the Euclidean curve length map L should be inside the tubular structure. Indeed the large ratio $L(\hat{\mathbf{x}})/\mathcal{U}(\hat{\mathbf{x}})$ reflects the fact that the geodesic $\mathcal{C}_{\hat{\mathbf{x}}}$, joining $\hat{\mathbf{x}}$ to a previous keypoint, has a small action $\mathcal{R}_{\text{AR}}(\mathcal{C}(\cdot), \mathcal{C}'(\cdot))$ in average. Thus, by construction of the metric, this geodesic must lie on the vessel centrelines and be aligned with the vessel orientations.

Here we consider the minimal action map \mathcal{U} for a tubular structure tree with the initial point at the root of this tree. For all the points $\hat{\mathbf{y}}$ in the level set $C = \{\hat{\mathbf{y}} \mid \mathcal{U}(\hat{\mathbf{y}}) = c\}$ where $c > 0$ is a constant, there may be many local maximums of L , some of which are the intersections of the level set C and the tubular structure branch centrelines. Thus we select the maximal local maximum which is inside a tubular structure judging by the equation (3.27). In our keypoints searching method, one or several path score thresholds $Th_1 \geq Th_2 \geq \dots \geq Th_k$ are given as input; generally $k \in \{1, 2\}$, and by convention $Th_0 = +\infty$. If the currently active point $\hat{\mathbf{x}}_{\min}$ has an excessive estimated curve length $L(\hat{\mathbf{x}}_{\min}) \geq 3\lambda$, see line 13, then the next threshold Th_{i+1} is activated in order to discover finer, less visible vessel structures; unless $i = k$ in which case the method ends. If the currently active point $\hat{\mathbf{x}}_{\min}$ has an appropriate estimated curve length $\lambda \leq L(\hat{\mathbf{x}}_{\min}) < 3\lambda$, then it is considered as a candidate new keypoint (i.e. a potential node of the vessel tree structure), see line 23. We extract the geodesic $\mathcal{C}_{\hat{\mathbf{x}}}$ linking $\hat{\mathbf{x}}$ to the already extracted tree structure, and evaluate its relevance using a path score. The selection test line 25 requires the path score to exceed the current selection threshold Th_i . The selector $\delta(T, \cdot)$ appearing in (3.25) is applied with $T := Th_{i-1}$ so as to push the keypoint selection towards finer and less visible structures, when $i > 1$, and leave the vicinity of the tree extracted with the previous threshold Th_{i-1} . Using a hierarchy of successive thresholds, an anisotropic metric, allows in the end to reliably handle a much smaller curve length threshold λ than the inspirational KPSM (Benmansour and Cohen, 2009), without leaking outside of the vessel or tubular structure, but staying right in its centreline. In Fig. 3.3, we show the keypoint searching results using the proposed method. In this figure, the green dot is the user-input initial source point, red dots indicate the searched keypoints with two path score thresholds. Cyan contours are the boundaries of the tubular structures. In Figs. 3.3a to 3.3c, we show one, two and seven keypoints with the corresponding centrelines and contours. In Fig. 3.3d to 3.3f, we show the optimal minimal action map \mathcal{U}_{opt} of \mathcal{U} with respect to Figs. 3.3a to 3.3c, where \mathcal{U}_{opt} is defined as

$$\mathcal{U}_{\text{opt}}(\mathbf{x}) = \min_{r \in [R_{\min}, R_{\max}]} \left\{ \mathcal{U}(\mathbf{x}, r) \right\}. \quad (3.28)$$

Stopping Criterion

The keypoint selection process has to be stopped after all vessel branches have been explored, but before spurious artifacts appear in the reconstructed vessel tree, which requires an adequate stopping criterion. The proposed algorithm terminates when all provided path score thresholds $(Th_i)_{i=1}^k$ have been used, and the value of Euclidean curve length is $L(\hat{\mathbf{x}}_{\min}) > 3\lambda$, where $\hat{\mathbf{x}}_{\min}$ is the latest accepted point in the Fast Marching propagation. In Fig. 3.4, we show the complete keypoints searching result. Green point is the initial source point. Red points

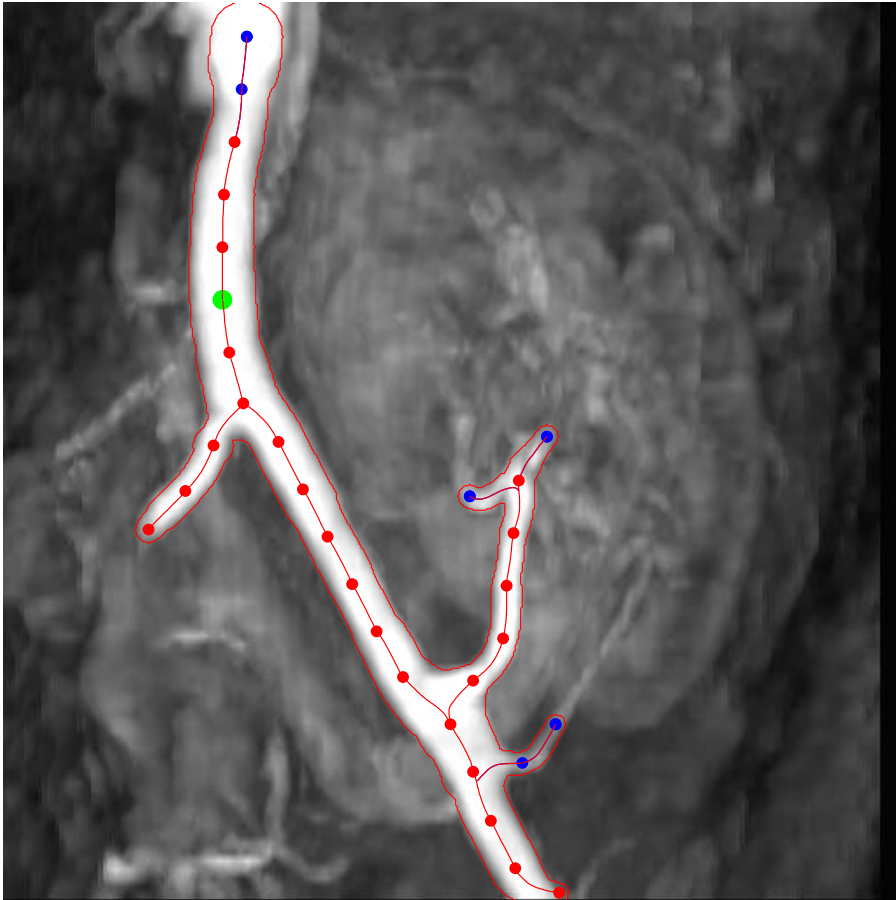


FIGURE 3.4: Keypoints searching result with two path score thresholds. Green dot indicates the initial source point, red dots are the keypoints searched using large path score threshold and blue dots are the keypoints obtained using small path score threshold.

are the keypoints with respect to path score threshold Th_1 . Blue points are the keypoints associated to the path score threshold Th_2 . From Fig. 3.4, we can see that no leakage occurs, even on weak branches which are reliably extracted by our algorithm.

Semi-Automatic Parameter Setting

The proposed algorithm requires a few parameters: a curve length threshold λ , and a collection of thresholds $(Th_i)_{i=1}^k$, one initial source point. The curve length threshold λ should be slightly more than twice the largest radius of the vessels to be detected. We use one or two path score thresholds, depending on the test case, which are automatically selected as quantiles of the vesselness map V_{ness} distribution on image pixels. Finally, the initial source point used in the Fast Marching algorithm can be user provided or automatically selected as the point which maximizes the value of the vesselness map V_{ness} (3.3).

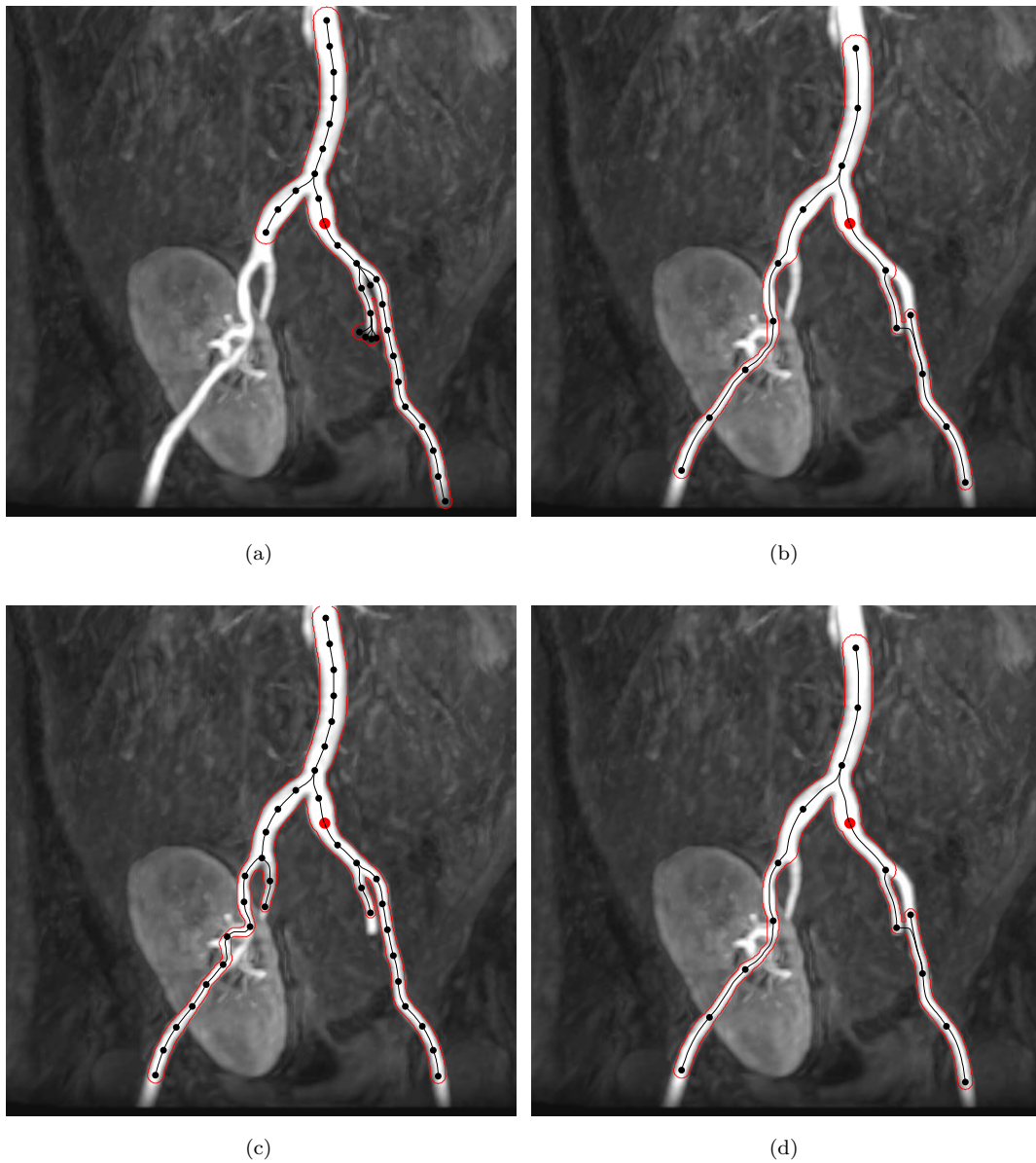


FIGURE 3.5: Comparison between our algorithm and the classical KPSM. (a) and (b) are the results of KPSM with curve length threshold 26 and 60, respectively. (c) and (d) are the results of our algorithm with 26 and 60, respectively.

3.4.4 Numerical Experiments

Small curve length thresholds are a-priori desirable when extracting vessel trees, since they favour the discovery of small structures and avoid the extraction of inadequate shortcuts linking different tree branches. Unfortunately, the classical KPSM (Benmansour and Cohen, 2009) suffers from a leaking problem with small curve length threshold: before the main vessel branches are extracted, multiple irrelevant keypoints are detected outside the vessel structure of interest. This problem, which is mainly caused by noise and intensity inhomogeneities, is avoided

with our new keypoint selection criterion involving a path score, as illustrated on Fig. 3.5. In Fig. 3.5, with a large curve length threshold $\lambda = 60$, the two methods produce similarly inaccurate results: some small branches are missed, and some undesirable shortcuts between different branches are extracted. In Fig. 3.5(a), with a small curve length threshold $\lambda = 26$, the keypoints from the KPSM (Benmansour and Cohen, 2009) leak and begin to accumulate outside the structure; in contrast our method accurately detects the vessel tree and then automatically stops as shown in Fig. 3.5, which can illustrate the advantages of using path score constraint and small curve length threshold. Note that in this experiment, we only use one path score threshold for the keypoints searching scheme.

We illustrate on Fig. 3.6 the results of classical KPSM and our method, with curve the length threshold $\lambda = 12$ which empirically is the best for these two methods on this image. For the classical KPSM, we specify a certain number of keypoints to stop the keypoints searching scheme and for our method, it is stopped automatically. For the proposed method as shown in Fig. 3.6b, we compute the path score threshold Th_1 as the 10% quantile of the vesselness map, in other words $\{\mathbf{x} \in \Omega; \mathbb{V}_{\text{ness}}(\mathbf{x}) \geq T_1\}$ collects 10% of the image pixels. For Th_2 , we use the 12% quantile. On this retinal image, one can see that the classical KPSM suffers from the leakage problem in at least three places due to the gray level inhomogeneities. However, for our method, no leakage happens. Note that in the following experiments with retinal image, we only show the centrelines and keypoints for better visualization. In fact our algorithm also extracts the vessel radii, hence the vessel walls, as illustrated on Fig. 3.4.

Many vessels are missed with a large curve length threshold λ , resulting in the extraction of numerous irrelevant shortcuts, as shown in Fig. 3.7. In this experiment, we use the same retinal image and path score thresholds as which are used in Fig. 3.6b, except that in Fig. 3.7, we use a large curve length threshold $\lambda = 40$. One can see that many finer vessels are missed and some short cuts occurs when compared to Fig. 3.6b.

Again, we have shown the impact of the path score threshold to our algorithm in the same retinal image as Fig. 3.6b. Here we utilize only one large path score threshold Th_1 by specifying the 6% highest vesselness map value among all the pixels. Less keypoints are found due to the larger path score threshold comparing to Fig. 3.6b.

The main drawback of the proposed path score based keypoints searching method is that when handling the tubular structure tree with loops, as shown in Fig. 3.6b, some small tubular segments will be missed due to the existence of the loops and the fast marching scheme.

3.4.5 Conclusion

We propose a new keypoint based tubular structure tree extraction method using anisotropic fast marching, and introducing of a path score selection procedure in the keypoint selection criterion. We also show the possibility that the keypoints searching scheme can be automatically stopped by only providing a set of path score thresholds and the curve length threshold. These ingredients allow our method to search keypoints separated by small curve lengths, leading to better extraction results compared to the classical keypoints searching method ([Benmansour and Cohen, 2009](#)). Numerical experiments illustrate these improvements on two MRA images and one retinal image. The next step is to extend our approach to 3D and to validate it on a large data set.

Algorithm 3 *Vessel Tree Extraction using Path Score based Keypoints Method***Input:**

- Metric \mathcal{M}_r , stencil S and initial source point \hat{s} .
- Curve length threshold λ and path score thresholds $(Th_i)_{1 \leq i \leq k}$.
- Vesselness map \mathbb{V}_{ness} .

Output:

- Minimal path \mathcal{C} , keypoint set \mathcal{K} .

Initialization:

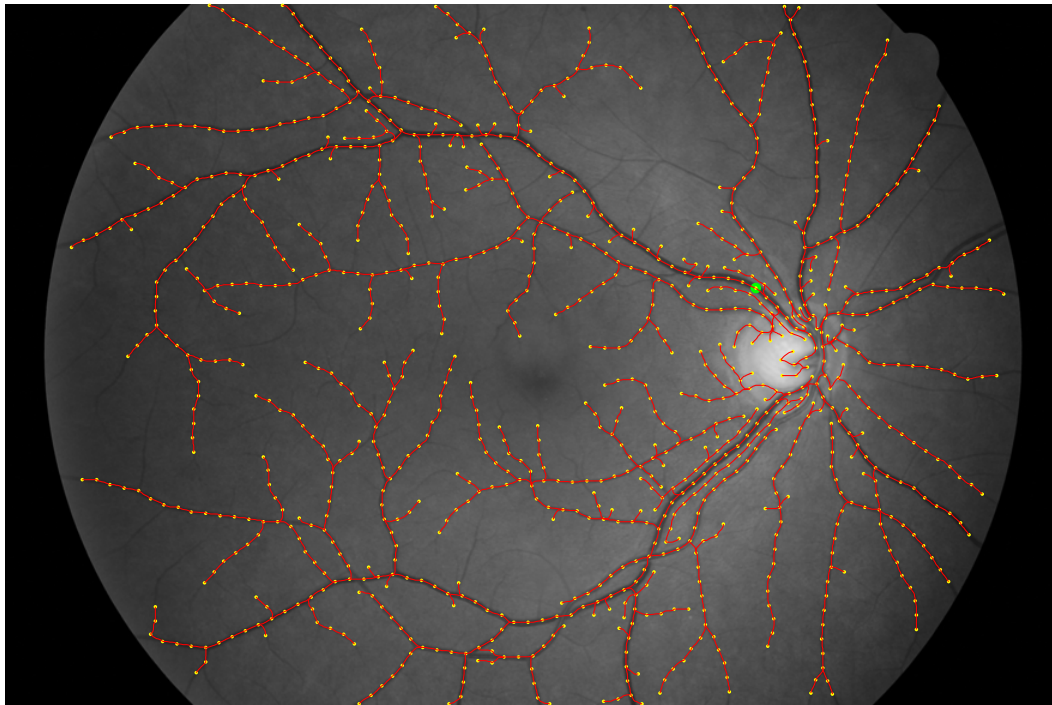
- For each point $\hat{x} \in \hat{Z}$, $\mathcal{U}(\hat{x}) \leftarrow +\infty$, $L(\hat{x}) \leftarrow +\infty$ and $\mathcal{V}(\hat{x}) \leftarrow \text{Far}$.
- $\mathcal{U}(\hat{s}) = \ell(\hat{s}) = 0$, $\mathcal{K} \leftarrow \{\hat{s}\}$, $i \leftarrow 1$ and $\text{IfStop} \leftarrow \text{False}$.

Main Loop

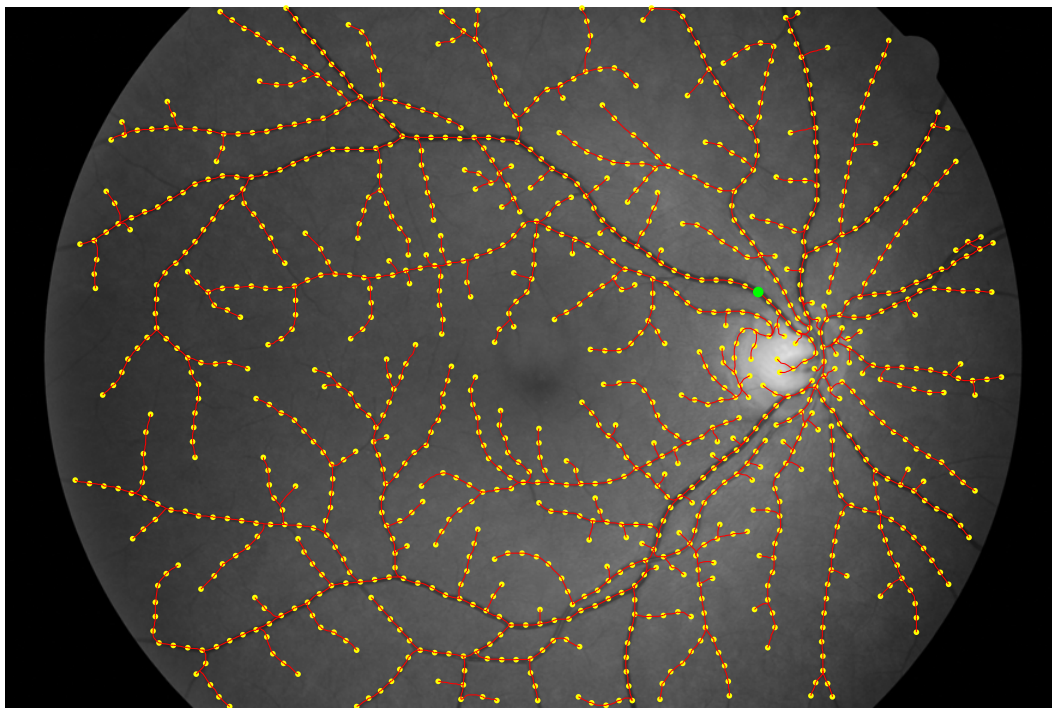
```

1: while  $\text{IfStop} = \text{False}$  do
2:   Find  $\hat{x}_{\min} = (\mathbf{x}_{\min}, r_{\min})$ , the Trial point which minimizes  $\mathcal{U}$ .
3:    $\mathcal{V}(\hat{x}_{\min}) \leftarrow \text{Accepted}$ .
4:   for All  $\hat{y}$  such that  $\hat{x}_{\min} \in S(\hat{y})$  and  $\mathcal{U}(\hat{y}) > \mathcal{U}(\hat{x}_{\min})$  do
5:     Compute  $\mathcal{U}_{\text{new}}(\hat{y})$  using (3.15).
6:     Compute  $L_{\text{new}}(\hat{y})$  using (3.16).
7:      $\mathcal{V}(\hat{y}) \leftarrow \text{Trial}$ .
8:     if  $\mathcal{U}_{\text{new}}(\hat{y}) < \mathcal{U}(\hat{y})$  then
9:        $\mathcal{U}(\hat{y}) \leftarrow \mathcal{U}_{\text{new}}(\hat{y})$ .
10:       $L(\hat{y}) \leftarrow L_{\text{new}}(\hat{y})$ .
11:     end if
12:   end for
13:   if  $L(\hat{x}_{\min}) \geq 3\lambda$  then ▷ Path score threshold reduction.
14:     if  $i = k$  then
15:        $\text{IfStop} \leftarrow \text{True}$ . ▷ Stopping criterion.
16:     else
17:        $i \leftarrow i + 1$ 
18:     end if
19:     for all points  $\hat{z} \in \hat{Z}$  passed by the minimal paths  $\mathcal{C}$  do
20:       Set  $\mathcal{U}(\hat{z}) = \ell(\hat{z}) = 0$ .
21:        $\mathcal{V}(\hat{z}) \leftarrow \text{Trial}$ .
22:     end for
23:     else if  $\ell(\hat{x}_{\min}) \geq \lambda$  then ▷ Keypoint selection.
24:       Track the minimal path  $\mathcal{C}_x$  from  $\hat{x}_{\min}$ .
25:       if  $\min\{\mathcal{PS}(\mathbf{x}_{\min}, Th_{i-1}), \mathbb{V}_{\text{ness}}(\mathbf{x}_{\min})\} \geq Th_i$  then
26:          $\mathcal{K} = \mathcal{K} \cup \{\hat{x}_{\min}\}$ .
27:          $\mathcal{C} = \mathcal{C} \cup \{\mathcal{C}_x\}$ .
28:         Set  $\mathcal{U}(\hat{x}_{\min}) = L(\hat{x}_{\min}) = 0$ .
29:          $\mathcal{V}(\hat{x}_{\min}) \leftarrow \text{Trial}$ .
30:       end if
31:     end if
32: end while

```



(a)



(b)

FIGURE 3.6: Comparison of the classical KPSM and the proposed algorithm in real retinal image. **(a)** Result from the KPSM. **(b)** Result of our algorithm.

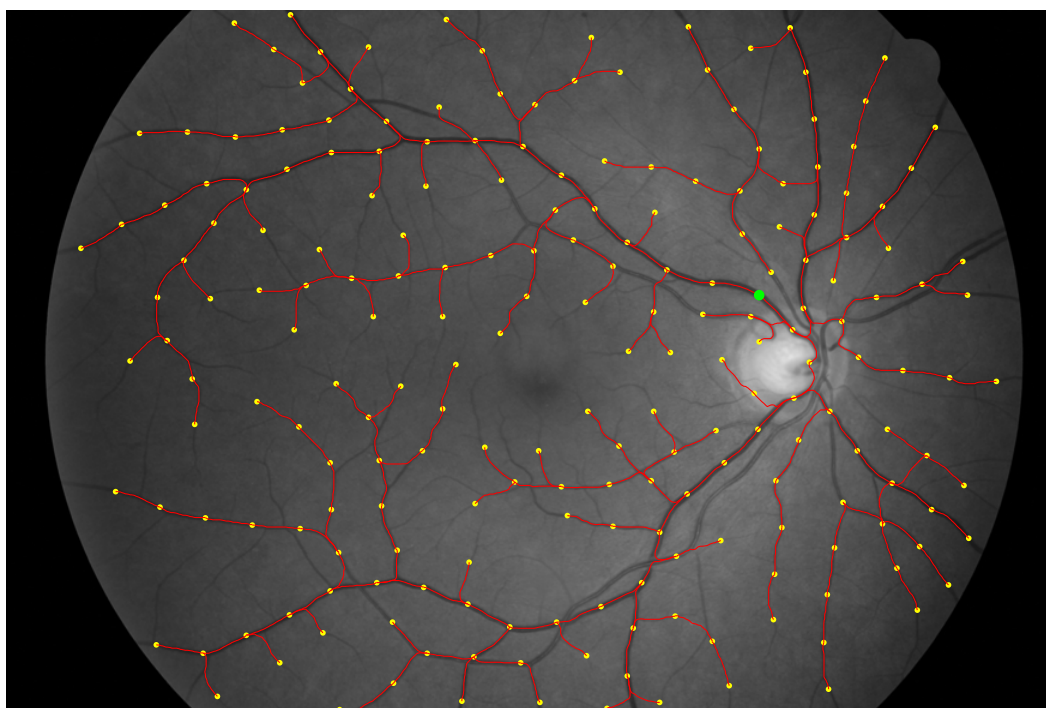


FIGURE 3.7: Keypoints searching result from our algorithm with curve length threshold 40.

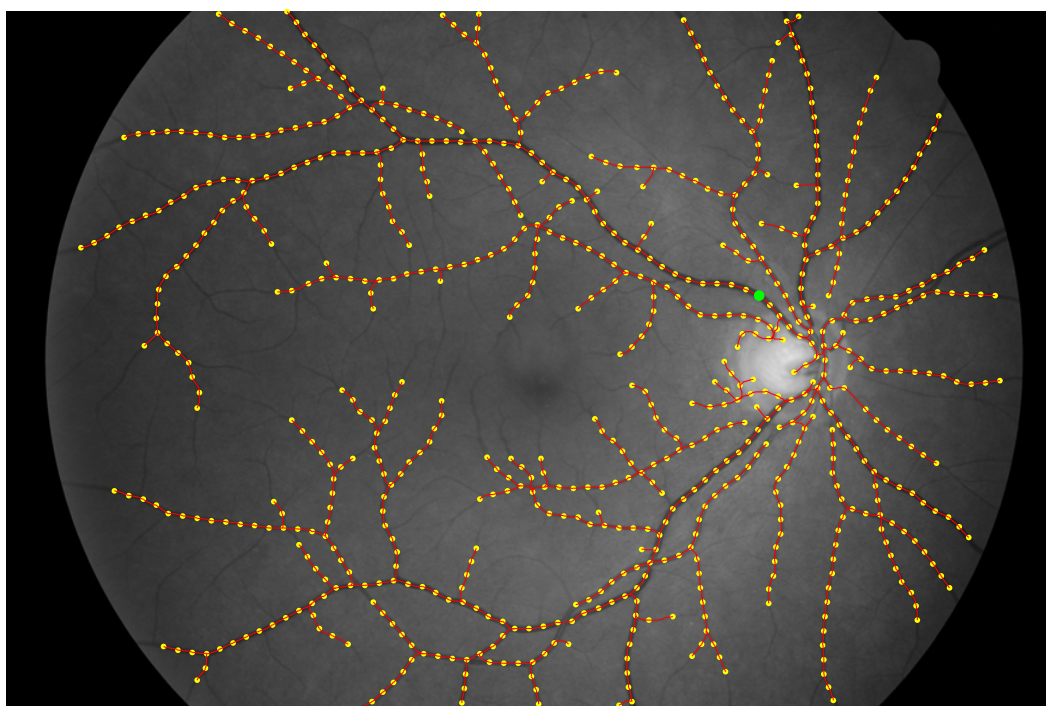


FIGURE 3.8: Keypoints searching result from our algorithm with a large path score threshold.

3.5 Vessel Extraction using Dynamic Riemannian Metric and Region-Constrained Minimal Path Refinement Method

3.5.1 Introduction

The classical Benmansour-Cohen model (Benmansour and Cohen, 2011) can be applied to efficiently extract the vessel boundaries and centrelines by given two endpoints as shown in Fig. 3.9a. However, for the task of extracting a vessel from the complicated network such as the retinal vessel network, global minimizer of the geodesic energy (3.12) with a static metric \mathcal{R}^{AR} cannot obtain the expected results in some cases. In Fig. 3.9b we show the vessel extraction result by using the Benmansour-Cohen model (Benmansour and Cohen, 2011), where cyan line denotes the vessel centerline and red contour is the vessel boundary. The dash yellow curve indicates the expected tubular structure centreline. This means if one would like to extract the vessels crossing one another, some parts of the weaker one will sometimes be missed. One of the possible reasons is that the static metric \mathcal{R}^{AR} depends only on the local pixel-based image features of the vessel detected by the optimally oriented flux filter (Law and Chung, 2008) thus the extracted minimal paths will always favour to pass through the vessels with strong local tubular features. These radius-lifted Riemannian metrics are fixed in the course of the computation of the geodesic distance by fast marching method. Using such kind of metrics for geodesics computation, the non-local image features are missed. Once the geodesic metrics are given, the geodesics can be immediately determined by the computed geodesic distance map.

Let us consider the course of the fast marching method. In each iteration, one *Trial* point with the smallest geodesic distance value will be frozen and a geodesic between this latest *Accepted* point and the initial source point can be obtained at once. This just computed geodesic contains some useful information. In this section, we propose a way to use this geodesic-based information.

In this section, we propose a new class of minimal path model with dynamic anisotropic Riemannian metric and image feature coherence penalty. The proposed dynamic Riemannian metric can penalize the variation of the geodesic-based tubularity features like the gray levels or vesselness values, and meanwhile preserve the anisotropy of the tubular structure. In contrast with the traditional anisotropic Riemannian metrics which depend only on the geodesic positions and orientations, the proposed dynamic Riemannian metric invokes a non-local geodesic-based tubularity features, calculated in the course of the fast marching front propagation.

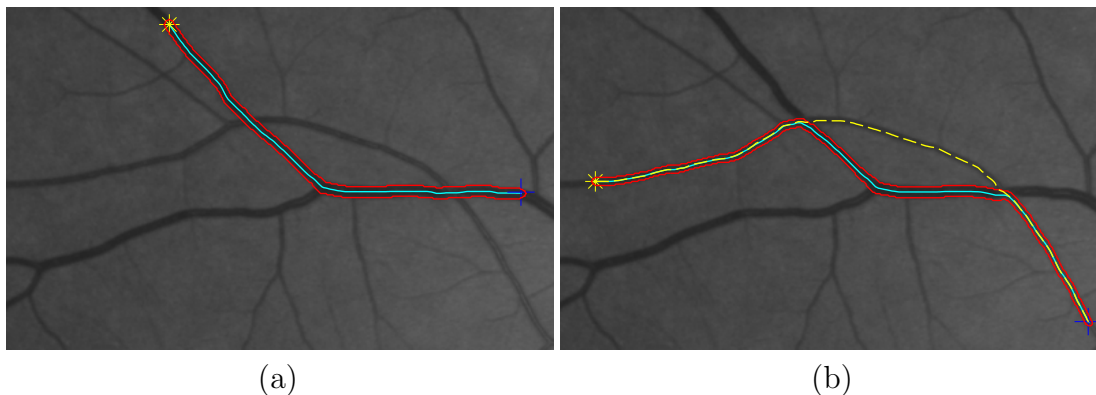


FIGURE 3.9: Vessel extraction results by the Benmansour-Cohen model. Blue cross and yellow star indicate the initial source points and end points respectively. Cyan curves are the centerlines and red contours are the vessel boundaries. Yellow dash curve in (b) indicates the expected centerline.

As the second contribution of this section, we present a region-constrained minimal path model, as the refined processing of the minimal paths obtained by the dynamic Riemannian metric. By this region-constrained minimal path model, we can obtain the expected centerlines and boundaries of the expected vessels. Numerical experiments on the retinal image dataset have demonstrated the advantages of the proposed minimal path models comparing to the classical minimal path models.

3.5.2 Dynamic Riemannian Metric with Feature Consistency Penalty

In this section, we introduce a novel dynamic Riemannian metric by penalizing the feature coherence. This metric is built upon the image domain $\Omega \subset \mathbb{R}^2$ instead of lifting domain.

Dynamic Riemannian Metric Construction

We firstly introduce the definition of the back-tracked point (Chen et al., 2016c; Liao et al., 2012, 2013). In (Liao et al., 2012, 2013), which is used to compute the feature consistency penalization.

A back-tracked point $\mathbf{z} \in \Omega$ located at a geodesic $\mathcal{C}_{\mathbf{s},\mathbf{x}} : [0, 1] \rightarrow \Omega$ joining the initial source point $\mathbf{s} = \mathcal{C}_{\mathbf{s},\mathbf{x}}(0)$ to any domain point $\mathbf{x} = \mathcal{C}_{\mathbf{s},\mathbf{x}}(1)$, which can be defined as a point $\mathbf{z} = \mathcal{C}_{\mathbf{s},\mathbf{x}}(z)$, where $z \in (0, 1)$, being such that:

$$\mathbf{z} = \mathcal{C}_{\mathbf{s},\mathbf{x}}(z), \quad s.t. \quad \int_{1-z}^1 \|\mathcal{C}'_{\mathbf{s},\mathbf{x}}(t)\| dt = \ell. \quad (3.29)$$

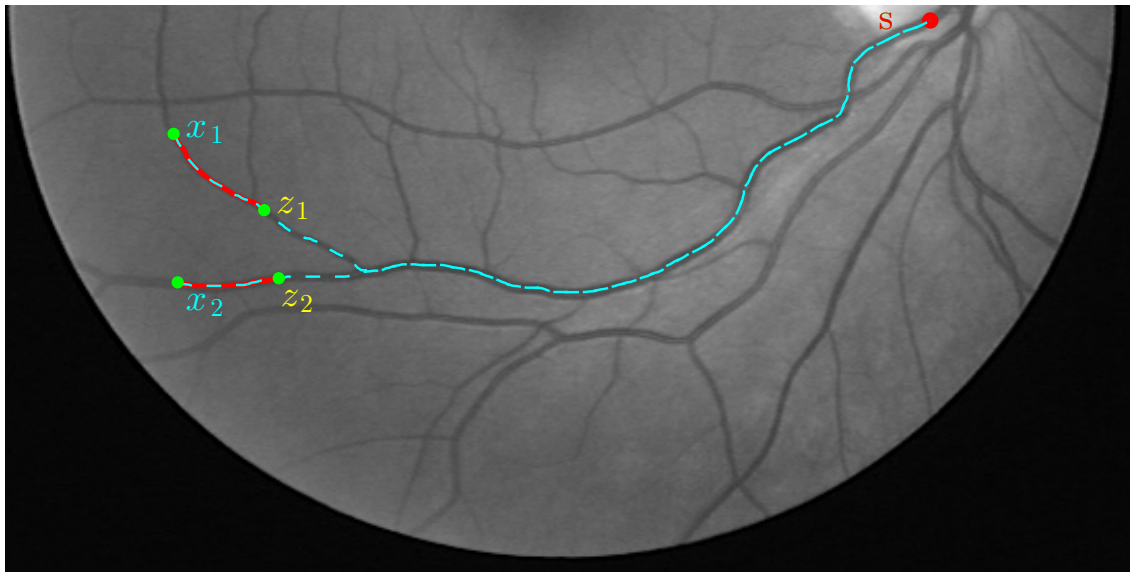


FIGURE 3.10: An example for back-tracked points and the corresponding local geodesics in a patch of a retinal image.

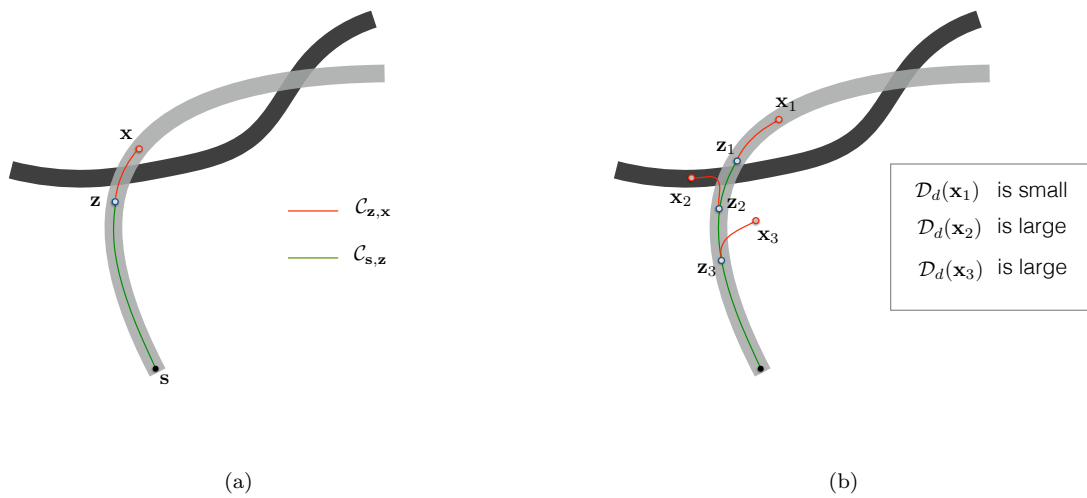


FIGURE 3.11: An example for back-tracked points and the corresponding local geodesics in a synthetic image.

Positive constant ℓ is a given curve length threshold value. Note that when the value of the Euclidean curve length threshold λ is larger than the Euclidean curve length of $C_{s,x}$, we simply set $\mathbf{z} = \mathbf{s}$.

We illustrate the back-tracked points and the corresponding short back-tracked geodesics in a patch of retinal image as shown in Fig. 3.10 and in a synthetic image as shown in Fig. 3.11a.

Denote the tubular feature map by $F : \Omega \rightarrow \mathbb{R}$. $\forall \mathbf{x} \in \Omega$ and its back-tracked point \mathbf{z} defined by (3.29), we introduce two feature coherence functions \mathcal{D}_c and \mathcal{D}_d :

$$\mathcal{D}_c(\mathbf{x}) = \exp(\tau_1 |F(\mathbf{x}) - F(\mathbf{s})|^p), \quad \mathbf{s} \text{ is the initial source point,} \quad (3.30)$$

$$\mathcal{D}_d(\mathbf{x}) = \exp(\tau_2 |F(\mathbf{x}) - F(\mathbf{z})|^p), \quad \mathbf{z} \text{ is the back-tracked point of } \mathbf{x}, \quad (3.31)$$

where τ_1 and τ_2 are two positive constant parameters. p is a positive constant, where we set $p = 1$ in this section. \mathcal{D}_c measures the difference in terms of tubular feature F between each point and the initial source point. \mathcal{D}_d measures the local coherence of the tubular feature F since it computes the difference of F between current point and its back-tracked point. In Fig. 3.11b, we illustrate the values of function \mathcal{D}_d in different positions.

Based on the feature coherence functions \mathcal{D}_c and \mathcal{D}_d , we can define the proposed dynamic Riemannian tensor field \mathcal{M}_d over the image domain Ω :

$$\mathcal{M}_d(\mathbf{x}) = (\mathcal{D}_c(\mathbf{x}) + \mathcal{D}_d(\mathbf{x}))\mathcal{M}_s(\mathbf{x}), \quad \forall \mathbf{x} \in \Omega, \quad (3.32)$$

where \mathcal{M}_s is a tensor field constructed for all the points $\mathbf{x} \in \Omega$ by

$$\mathcal{M}_s(\mathbf{x}) = \exp(\alpha\Lambda_2(\mathbf{x})) \mathbf{V}_1(\mathbf{x})\mathbf{V}_1^T(\mathbf{x}) + \exp(\alpha\Lambda_1(\mathbf{x})) \mathbf{V}_2(\mathbf{x})\mathbf{V}_2^T(\mathbf{x}), \quad (3.33)$$

where Λ_1, Λ_2 are eigenvalues of \mathcal{Q}_{opt} (3.5) and $\mathbf{V}_1, \mathbf{V}_2$ are the corresponding eigenvectors:

$$\mathcal{Q}_{\text{opt}}(\mathbf{x}) = \Lambda_1(\mathbf{x})\mathbf{V}_1(\mathbf{x})\mathbf{V}_1^T(\mathbf{x}) + \Lambda_2(\mathbf{x})\mathbf{V}_2(\mathbf{x})\mathbf{V}_2^T(\mathbf{x}), \quad \forall \mathbf{x} \in \Omega. \quad (3.34)$$

The dynamic tensor field \mathcal{M}_d (3.32) can preserve the anisotropic property of the static tensor field \mathcal{M}_s (3.33). Based on \mathcal{M}_d , the proposed dynamic Riemannian metric can be formulated as:

$$\mathcal{R}^{\text{dyn}}(\mathbf{x}, \mathbf{u}) = \sqrt{\langle \mathbf{u}, \mathcal{M}_d(\mathbf{x}) \mathbf{u} \rangle}. \quad (3.35)$$

For any $\mathbf{x} \in \Omega$ and any vector $\mathbf{u} \in \mathbb{R}^2$.

The minimal action map \mathcal{U}_d associated to the initial source point \mathbf{s} and the dynamic Riemannian metric \mathcal{R}^{dyn} is defined as

$$\mathcal{U}_d(\mathbf{x}) = \min_{\gamma \in \mathcal{A}_{\mathbf{s}, \mathbf{x}}} \left\{ \int_0^1 \mathcal{R}^{\text{dyn}}(\gamma(t), \gamma'(t)) dt \right\}. \quad (3.36)$$

Belleman's optimality principle states that the minimal action map \mathcal{U} defined in (3.36) can be expressed as:

$$\mathcal{U}_d(\mathbf{x}) = \min_{\mathbf{y} \in \mathcal{S}(\mathbf{x})} \{d(\mathbf{x}, \mathbf{y}) + \mathcal{U}_d(\mathbf{y})\}, \quad (3.37)$$

Belleman's optimality principle can be approximated by the Hopf-Lax update operator as shown in Section 2.4.3.

Numerical Implementation based on the Anisotropic Fast Marching Method

The goal is to compute the geodesic distance map associated to the dynamic anisotropic Riemannian metric (3.35) by state-of-the-art anisotropic fast marching method proposed by Mirebeau (2014a). As discussed in Section 2.4, the fast marching method introduces a regular grid Z of the image domain Ω and labels each grid point either *Accepted*, *Trial* or *Far*. Among all the *Trial* points, the point \mathbf{x}_{\min} which minimizes the minimal action map \mathcal{U}_d will be tagged as *Accepted*. Once the latest *Accepted* point $\mathbf{x}_{\min} \in Z$ is found, one can track a minimal geodesic $\mathcal{C}_{\mathbf{z}, \mathbf{x}_{\min}}$. This means that updating the proposed dynamic anisotropic Riemannian metric \mathcal{R}^{dyn} (3.35) is possible during the fast marching propagation by using the approximation of that for all \mathbf{y} such that $\mathbf{x}_{\min} \in S(\mathbf{y})$ one has

$$\mathcal{D}_c(\mathbf{y}) \approx \mathcal{D}_c(\mathbf{x}_{\min}), \quad (3.38)$$

$$\mathcal{D}_d(\mathbf{y}) \approx \mathcal{D}_d(\mathbf{x}_{\min}), \quad (3.39)$$

where \mathbf{x}_{\min} is the latest *Accepted* point and \mathbf{y} denotes any neighbourhood point of \mathbf{x}_{\min} in terms of the local stencil S . Such approximation is reasonable due to the small size of stencil S . For N grid points where $N = \#Z$, it only requires to compute the local geodesic N times.

3.5.3 Region-Constrained Minimal Path Model

The goal in this section is to find a minimal cost path inside a given prior region instead of the whole image domain Ω . For this purpose, we introduce some notations. Given an open subset $U \subseteq \Omega \subset \mathbb{R}^2$, bounded and connected, one has a new radius-lifted domain $\hat{U} = U \times [R_{\min}, R_{\max}]$ ($[R_{\min}, R_{\max}]$ is the admissible radius space). Let $\mathcal{A}_{\hat{U}}$ be the collection of all the regular radius-lifted paths $\gamma_c : [0, 1] \rightarrow \hat{U}$:

$$\mathcal{A}_{\hat{U}} := \{\gamma_c; \gamma_c : [0, 1] \rightarrow \hat{U}, \gamma_c(0) = \hat{\mathbf{s}}, \gamma_c(1) = \hat{\mathbf{x}}\}.$$

Algorithm 4 *Fast Marching Method with Dynamic Riemannian Metric***Input:**

- Tubular feature map F .
- radius-lifted tensor field \mathcal{M}_s (3.33).
- Initial source point \mathbf{s} and end point \mathbf{p} .
- Local stencil S .

Output:

- Minimal action map \mathcal{U}_d and geodesic $\mathcal{C}_{\mathbf{s},\mathbf{p}}$.

Initialization:

- For each point $\mathbf{x} \in Z$, set $\mathcal{U}_d(\mathbf{x}) \leftarrow +\infty$.
- For each point $\mathbf{x} \in Z$, set $\mathcal{V}(\mathbf{x}) \leftarrow \text{Far}$.
- Set $\mathcal{U}_d(\mathbf{s}) \leftarrow 0$ and $\mathcal{V}(\mathbf{x}) \leftarrow \text{Trial}$.
- Set $\text{IfStop} \leftarrow \text{False}$.

Main Loop

```

1: while  $\text{IfStop} = \text{False}$  do
2:   Find  $\mathbf{x}_{\min}$ , the Trial point which minimizes  $\mathcal{U}_d$ .
3:    $\mathcal{V}(\mathbf{x}_{\min}) \leftarrow \text{Accepted}$ .
4:   if  $\mathbf{x}_{\min} = \mathbf{p}$  then
5:     Recover the minimal path  $\mathcal{C}_{\mathbf{s},\mathbf{p}}$ .
6:     Set  $\text{IfStop} \leftarrow \text{True}$ .
7:   end if
8:   Find the back-tracked point  $\mathbf{z}$  of  $\mathbf{x}_{\min}$  by (3.29).
9:   Compute  $\mathcal{D}_c(\mathbf{x}_{\min})$  and  $\mathcal{D}_d(\mathbf{x}_{\min})$  by (3.30) and (3.31) respectively.
10:  for all  $\mathbf{y}$  such that  $\mathbf{x}_{\min} \in S(\mathbf{y})$  and  $\mathcal{V}(\mathbf{y}) \neq \text{Accepted}$  do
11:    if  $\mathcal{V}(\mathbf{y}) = \text{Far}$  then
12:      Set  $\mathcal{V}(\mathbf{y}) \leftarrow \text{Trial}$ .
13:    end if
14:    Compute  $\mathcal{D}_c(\mathbf{y})$  and  $\mathcal{D}_d(\mathbf{y})$  by (3.38) and (3.39) respectively.
15:    Calculate the dynamic tensor  $\mathcal{M}_d(\mathbf{y})$  by (3.32).
16:    Compute  $\mathcal{U}_{\text{new}}(\mathbf{y})$  by solving the Hopf-Lax operator (2.86).
17:    if  $\mathcal{U}_{\text{new}}(\mathbf{y}) < \mathcal{U}(\mathbf{y})$  then
18:       $\mathcal{U}(\mathbf{y}) \leftarrow \mathcal{U}_{\text{new}}(\mathbf{y})$ .
19:    end if
20:  end for
21: end while

```

The geodesic energy \mathcal{L}_c with respect to the radius-lifted metric \mathcal{R}^{AR} (2.61) and the constrained domain \hat{U} can be defined as

$$\mathcal{L}_c(\gamma) := \begin{cases} \int_0^1 \mathcal{R}^{\text{AR}}(\gamma(t), \gamma'(t)) dt, & \text{if } \gamma \in \mathcal{A}_{\hat{U}}, \\ \infty, & \text{otherwise.} \end{cases} \quad (3.40)$$

Algorithm 5 Anisotropic Fast Marching method with Constrained Region**Input:**

- Radius-lifted tensor field \mathcal{M}_r .
- Constrained domain \hat{U} .
- Initial source point $\hat{\mathbf{s}}$.
- Local stencil S .

Output:

- Minimal action map \mathcal{U}_c .

Initialization:

- $\forall \hat{\mathbf{x}} \in \hat{U}, \mathcal{U}_c(\hat{\mathbf{x}}) \leftarrow +\infty$ and $\mathcal{V}(\hat{\mathbf{x}}) \leftarrow \textit{Far}$.
- Set $\mathcal{U}_c(\hat{\mathbf{s}}) \leftarrow 0$ and $\mathcal{V}(\hat{\mathbf{s}}) \leftarrow \textit{Trial}$.

Main Loop

```

1: while at least one grid point is tagged as Trial do
2:   Find  $\hat{\mathbf{x}}_{\min}$ , the Trial point which minimizes  $\mathcal{U}_c$ .
3:   Set  $\mathcal{V}(\hat{\mathbf{x}}_{\min}) \leftarrow \textit{Accepted}$ .
4:   if  $\hat{\mathbf{x}}_{\min} \in \hat{U}$  then
5:     for All  $\hat{\mathbf{y}}$  such that  $\hat{\mathbf{x}}_{\min} \in S(\hat{\mathbf{y}})$  and  $\mathcal{V}(\hat{\mathbf{y}}) \neq \textit{Accepted}$  do
6:       Compute  $\mathcal{U}_{\text{new}}(\hat{\mathbf{y}})$  using Hopf-Lax update in (2.86).
7:       if  $\mathcal{V}(\hat{\mathbf{y}}) \neq \textit{Trial}$  then
8:          $\mathcal{V}(\hat{\mathbf{y}}) \leftarrow \textit{Trial}$ .
9:       end if
10:      if  $\mathcal{U}_{\text{new}}(\hat{\mathbf{y}}) < \mathcal{U}_c(\hat{\mathbf{y}})$  then
11:         $\mathcal{U}_c(\hat{\mathbf{y}}) \leftarrow \mathcal{U}_{\text{new}}(\hat{\mathbf{y}})$ .
12:      end if
13:    end for
14:  else
15:    Set  $\mathcal{U}_c(\hat{\mathbf{x}}_{\min}) = +\infty$ .
16:  end if
17: end while

```

Therefore, the minimal action map \mathcal{U}_c with respect to the initial source point $\hat{\mathbf{s}} \in \hat{U}$, defined over the whole radius-lifted domain $\hat{\Omega}$ can be expressed as:

$$\mathcal{U}_c(\hat{\mathbf{x}}) := \begin{cases} \min \{ \mathcal{L}_c(\gamma); \gamma(1) = \hat{\mathbf{x}}, \gamma(0) = \hat{\mathbf{s}} \}, & \text{if } \hat{\mathbf{x}} \in \hat{U}, \\ \infty, & \text{otherwise.} \end{cases} \quad (3.41)$$

If $\hat{\mathbf{x}} \in \hat{U}$, one can search the optimal path minimizing \mathcal{L}_c inside \hat{U} . Otherwise, for any curve γ such that $\gamma(1) = \hat{\mathbf{x}} \notin \hat{U}$, $\mathcal{L}_c(\gamma) = \infty$.

Numerically, the minimal action map \mathcal{U}_c can be naturally computed by the fast marching method with a freezing scheme as described in Algorithm 5. Comparing against the regular fast marching method, the freezing scheme-based method set the value of the latest *Accepted* point as ∞ if this point is outside the radius-lifted constrained region \hat{U} .

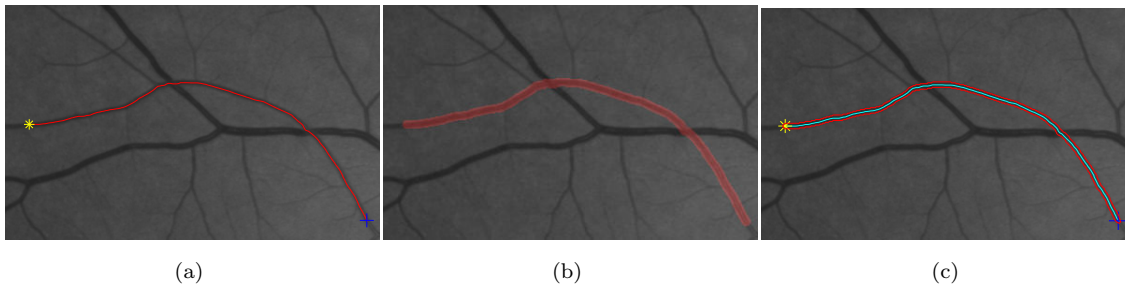


FIGURE 3.12: Steps for the proposed Retinal vessel extraction method. **(a)** Minimal path (red curve) by using the dynamic Riemannian metric. **(b)** Tubular neighbourhood region of the minimal path shown in (a). **(c)** Minimal path extraction result obtained using the region-constrained minimal path model, where the cyan curve denotes the centreline and red curve denotes the vessel boundary.

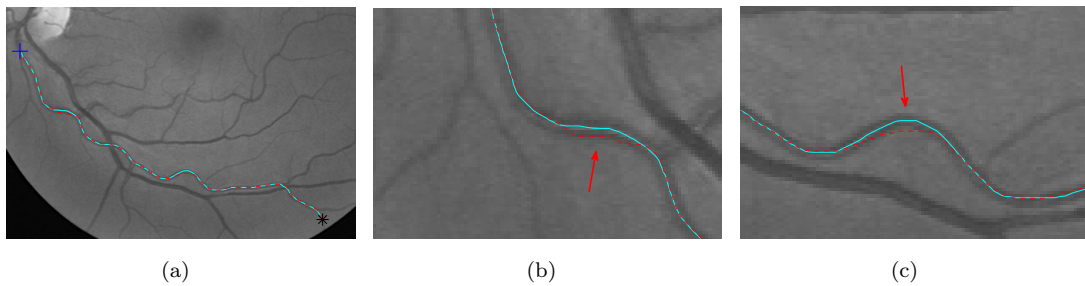


FIGURE 3.13: Centreline bias correction. **(a)** Minimal paths extracted by the proposed region-constrained minimal path model and the dynamic metric model, where the results are indicated by cyan solid line and red dash line respectively. In this figure, we only demonstrate the physical path of the obtain radius-lifted minimal path. **(b)** and **(c)** Details for both the minimal paths in (a).

Summarily, the proposed interactive vessel extraction method can be decomposed to two steps. The first step is to get the rough minimal path \mathcal{C} which pass the vicinity of the true centreline of the expected vessel as demonstrated in Fig. 3.12a. Next step is to build the tubular neighbourhood U of the just computed minimal path \mathcal{C} by dilation operator and perform the region-constrained minimal path model to obtain both the centreline and boundaries of the expected vessel. The neighbourhood U is shown in Fig. 3.12b and the final vessel extraction result is demonstrated in Fig. 3.12c.

Note that the region-constrained minimal path model can be considered as the refined procedure of the minimal path obtained by using the dynamic Riemannian metric. Since the inhomogeneous vesselness distribution along the desired vessel, the extracted minimal path using the feature consistency penalized dynamic Riemannian metric may result in centreline bias as shown in Fig. 3.13. In this figure, a shows two minimal paths: one is the path extracted using the dynamic metric

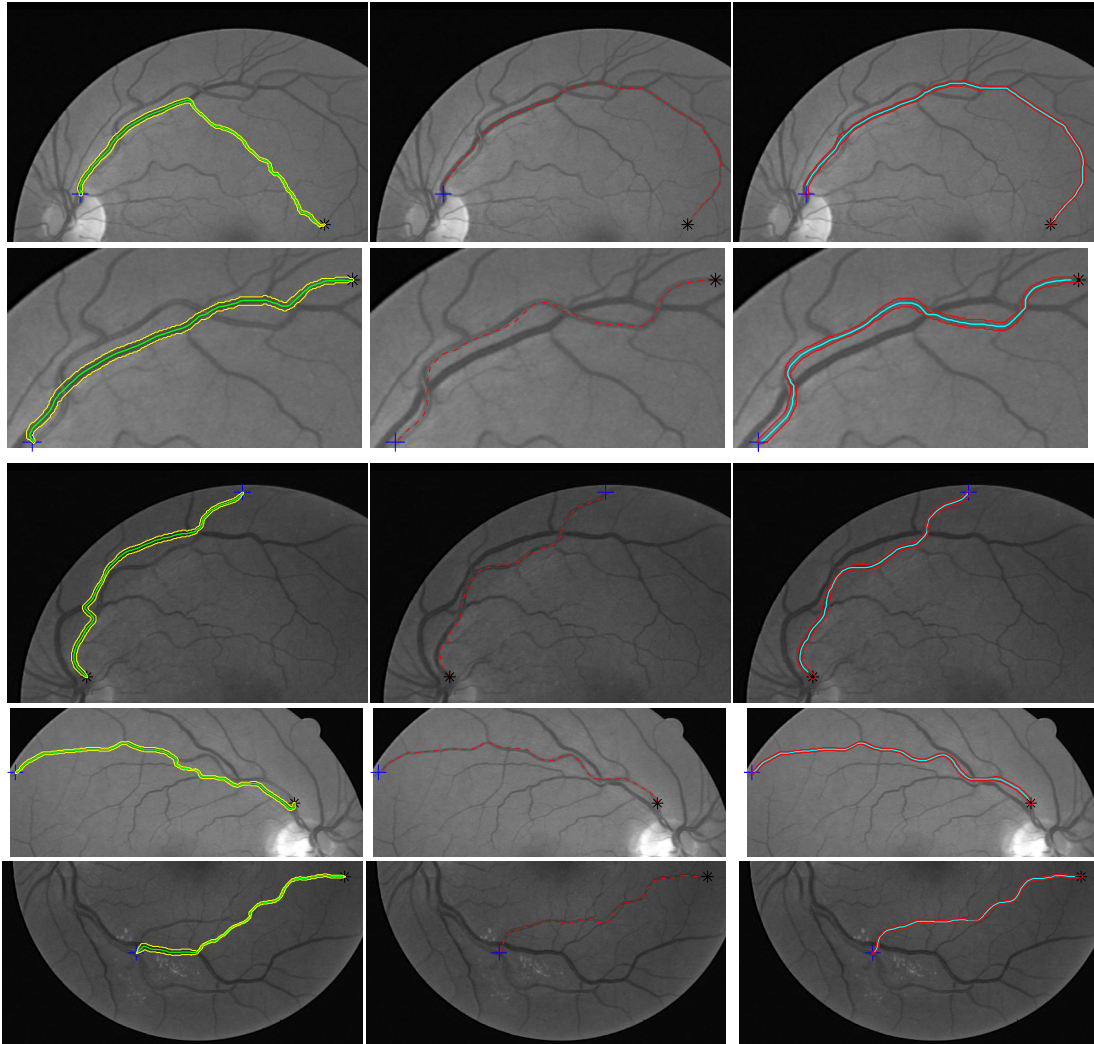


FIGURE 3.14: Comparative Retinal vessel extraction results by the Benmansour-Cohen model and the proposed model. Blue crosses and black stars indicate the initial source points and the end points, respectively. **Column 1** show the vessel extraction results by the Benmansour-Cohen model. **Column 2** show the vessel extraction results by the proposed dynamic anisotropic Riemannian metric. **Column 3** show the refined results by the proposed region-constrained minimal path model.

indicated by red dash line and another is the path obtained using the region-constrained minimal path mode (cyan solid line). In Figs. 3.13b and 3.13c we give the details of the centreline bias.

In Fig. 3.14, more comparative retinal vessel extraction results for the classical Benmansour-Cohen model (Benmansour and Cohen, 2011) and the proposed two-step method is given. The left column of Fig. 3.14 shows the vessel extraction results from the Benmansour-Cohen model where the green curves denote the centerlines and yellow contours denote the boundaries of the retinal vessels. In the middle column, we show the minimal paths extracted by the dynamic Riemannian metric where the paths are indicated by red dash lines. The right column present

TABLE 3.1: Comparison of the vessel extraction results for the Benmansour-Cohen model and the proposed minimal path model.

Measure	N_T^F	N_F^T	N_T^T	N_F^F
	47	2	55	6

the final results from the region-constrained minimal path model where the cyan lines indicate the retinal vessel centrelines and red contours denotes the boundaries of the vessels. From this figure, we can see that the proposed two-step method can obtain the desired results which completely avoid the short branches combination problem.

The proposed minimal path model is evaluated on the Test set of the DRIVE dataset (Staal et al., 2004), which includes 20 retinal images. We choose total 110 vessels which start from the optic disk of the retinal images or those cross another vessel. If the extracted minimal path exactly follows the desire vessel, we consider this is a positive extraction (PE), otherwise a negative extraction (NE). For the proposed two-step vessel extraction method, the number of PE = 102 out of total 110 vessels. For Benmansour-Cohen model, this number is 57. Additionally, we compute the following measures:

- N_F^T : the number of vessels that the proposed method positively extracts and the B-C model fails.
- N_T^F : the number of vessels that the Benmansour-Cohen model positively extracts and the proposed fails.
- N_F^F : the number of vessels that both models fail to extract.
- N_T^T : the number of vessels that both models positively extract.

In Table 3.1, we show these four measures mentioned above. It can be seen that the proposed two-step model obtains better results than the Benmansour-Cohen model (102 against 57).

3.5.4 Conclusion

We present a two-step method for interactive retinal vessel extraction including both the centreline and boundary. In the first step, we invoke a feature consistency penalized dynamic metric to find the rough centreline of the targeted vessel. Then a region-constrained minimal path model is applied to get the extraction results including both accurate centreline and boundary of the vessel.

3.6 Centerlines Extraction and Boundaries Delineation for Retinal Vessels via a Region-Constrained Minimal Path Model

3.6.1 Introduction

Models of tracking vessels constrained by prior centreline points aim to finding the edge points based on various criteria. These models heavily rely on the binary pre-segmented vessel map, since the prior centreline points are obtained by thinning the binary vessel map using morphological filters. [Al-Diri et al. \(2009\)](#) proposed an active contours method to measure the width of the retinal vessels. In their formulation, the centreline points are obtained by a tramline filter and the edge points are computed from the ribbon of twins model. The ribbon of twins model uses two contours to identify one vessel boundary. [Xu et al. \(2011\)](#) proposed a graph search model to delineate vessel boundary by modelling the boundary detection problem as a 3D surface segmentation problem.

In this section, we deal with the same problem in a different way. We model the vessel segments by piecewise geodesics consisting of centreline positions and the corresponding radius values. The main purpose of this work is to introduce an automatic method to extract a tubular tree structure, such as the retinal vessel tree, relying on the region-constrained minimal path model as introduced in Section 3.5.3. The constrained regions are built through the skeletons of the pre-segmented vessels. This method is related to the geodesic or minimal path technique which is particularly efficient to extract a tubular shape, such as a blood vessel. The proposed method utilizes a collection of pairs of points, where each pair of points provides the initial source point and target point for one minimal geodesic. For each pair of initial point and target point, we calculate the region-constrained Riemannian metric with an additional radius dimension to constrain the fast marching propagation so that our method can get a nice path without any shortcut or overlapping to other minimal paths. The given pairs of points can be easily obtained from a pre-segmented skeletonized image by any vessel detection filter like Hessian based filter or optimally oriented flux filter. Experimental results demonstrate that our method can extract vessel segments at a finer scale, with increased accuracy.

3.6.2 PreProcessing

In this step, we use the optimally oriented flux filter ([Law and Chung, 2008](#)) or Hessian Filter ([Frangi et al., 1998](#)) as our vessel detector to filter the image and

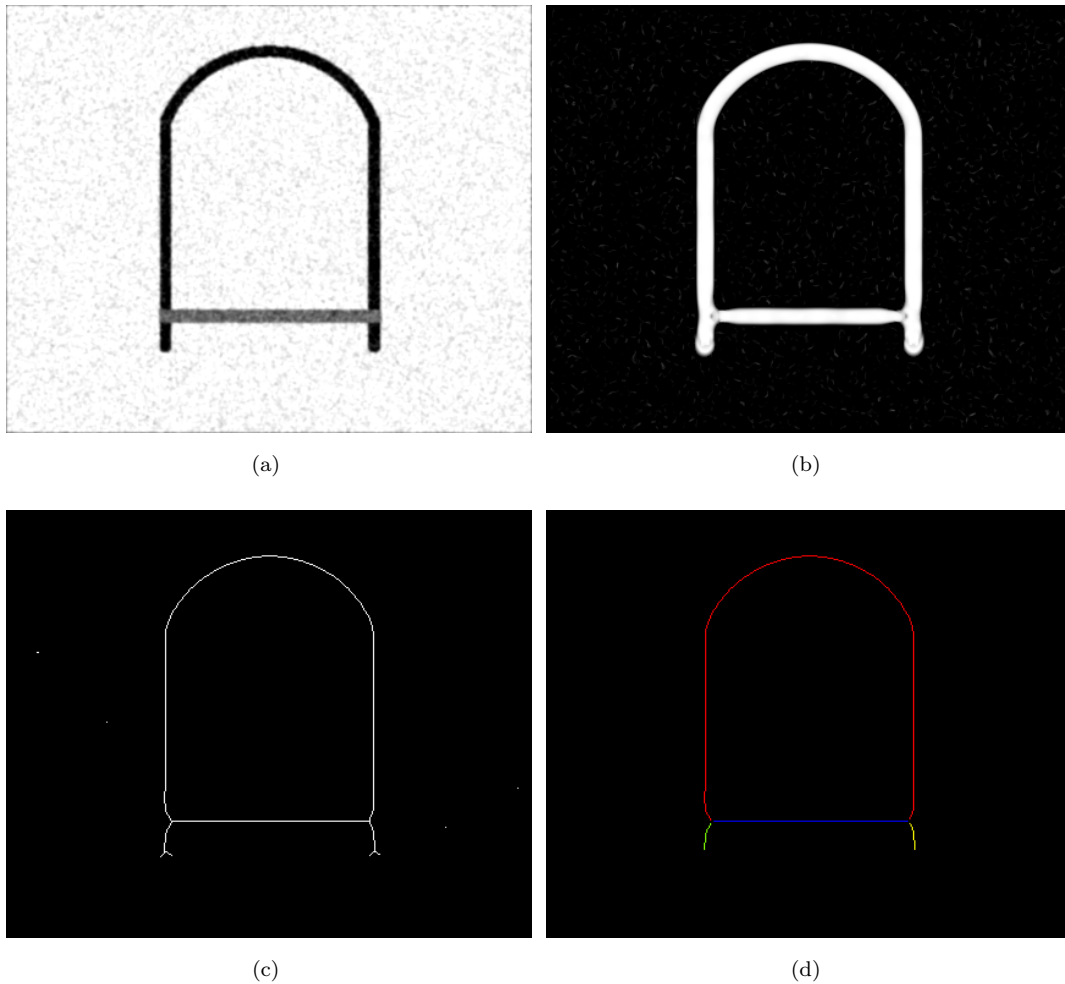


FIGURE 3.15: Tubular structure preprocessing step. **(a)** Original synthetic image. **(b)** Vesselness map computed by Hessian-based Filter (Frangi et al., 1998). **(c)** the Skeleton map of vesselness map in **(b)**. **(d)** Tag different segments with different colours after removing branch and crossover points.

obtain a vesselness map. Once the vesselness map is obtained, a constant threshold is applied to this vesselness map to get the binary vessel map. In order to find the endpoints for each vessel segment, we thin the binary image by a sequential morphological filters (Lam et al., 1992) and remove all the branch points and crossover points. The entire skeleton is broken up into a set of segments, in which each segment consists of two endpoints. The branch or crossover points are defined as any skeleton point having at least three neighbour points in 8-neighbourhood system. Any endpoint is discovered if it has only one neighbour point and segment point has two neighbour points. In Fig. 3.15c, we show the skeletons after applying thinning filter and the labeled segments in different colours in Fig. 3.15(d). The original synthetic image and the corresponding vesselness map are shown in Figs. 3.15a and 3.15b.

In this work, we firstly scan the entire skeleton map to find all the vessel segments

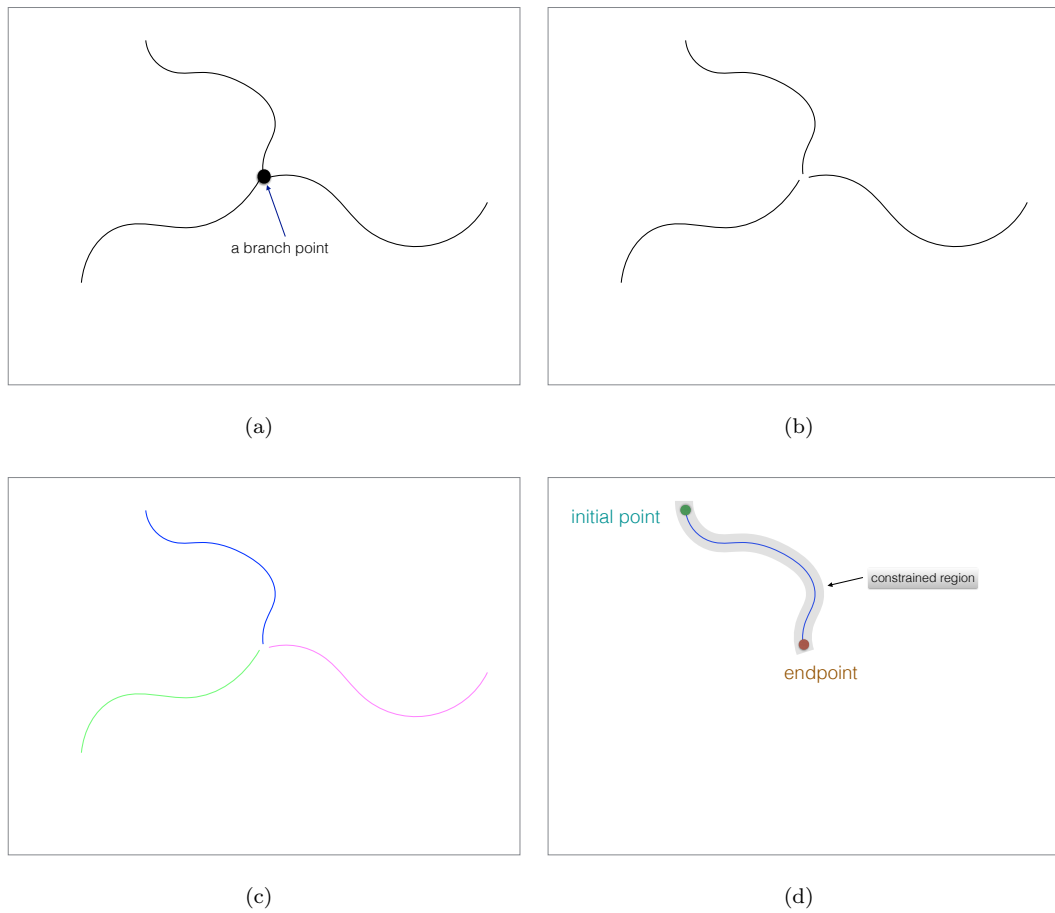


FIGURE 3.16: Identifying the segments by removing the branch points and construct the constrained tubular neighbourhood region. **(a)** Original segments image. **(b)** Separated segments by removing the branch point. **(c)** labeled segments by different colors. **(d)** The constructed tubular neighbourhood region and the identified initial and end points.

with two endpoints and then tag them with different labels. Next, we delete the segments whose length in pixels are smaller than a given threshold T_{len} , but retain the segments who connect two branch or crossover points. Those segments will be stored in the set \mathcal{T} . Note that similar preprocessing operation can be found in (Al-Diri et al., 2009; Xu et al., 2011). In Figs. 3.16a to 3.16c, we show another example of identifying each segment by removing a branch point that connects three segments.

3.6.3 Endpoints Correction

For each segment $h \in \mathcal{T}$, we can obtain a constrained region $U_h \in \Omega$ by dilation operation. In Fig. 3.16d, we demonstrate the constructed tubular neighbourhood region of an identified segment. By adding the radius space $[R_{\min}, R_{\max}]$ to U_h , we get the radius-lifted tubular neighbourhood region $\hat{U}_h = U_h \times [R_{\min}, R_{\max}]$.

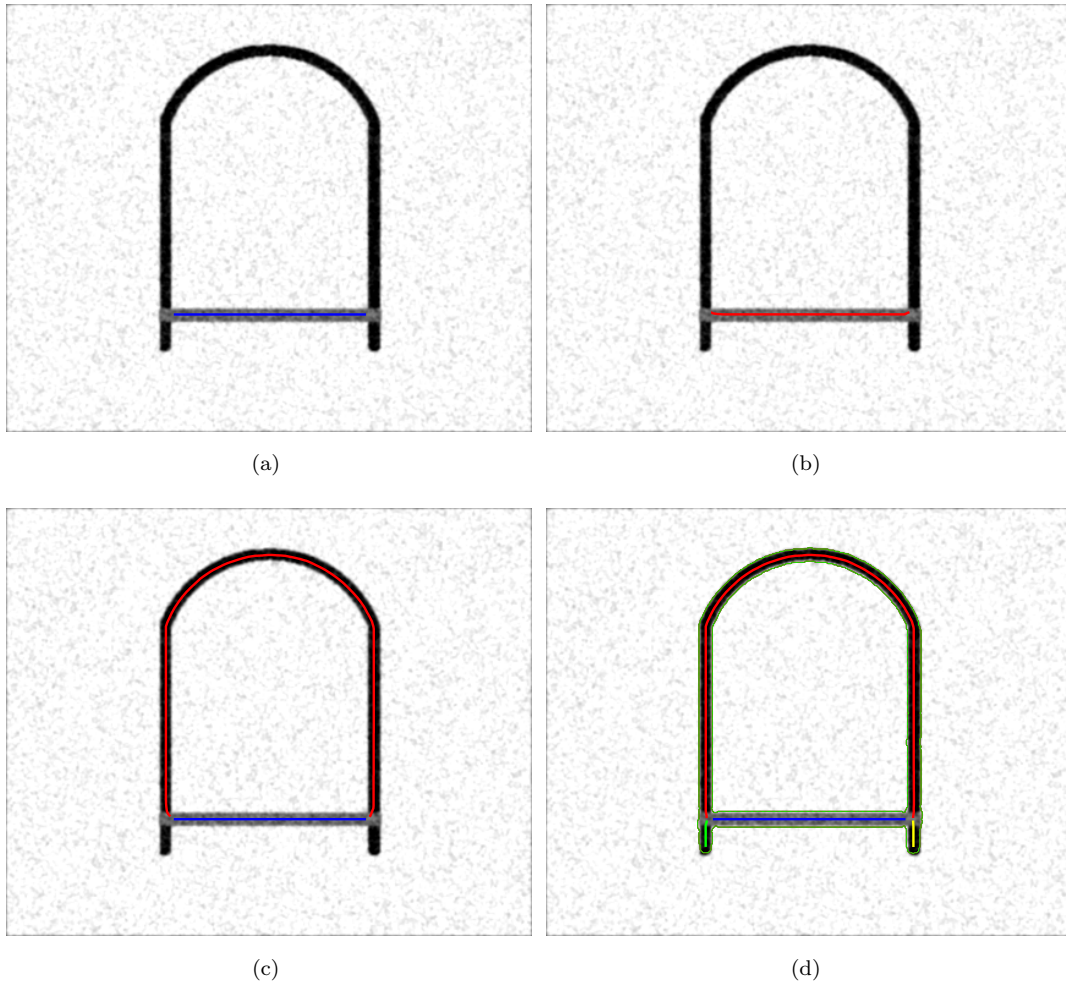


FIGURE 3.17: Comparative extraction results. (a) and (b) are centerlines from Benmansour-Cohen model which correspond to the vessel segments tagged by blue and red colours in Fig. 3.15(d) respectively. (c) shows the results from our region-constrained minimal path model. (d) shows the results from region-constrained minimal path model with endpoints correction.

Therefore, the radius-lifted minimal path corresponding to h can be extracted by applying the region-constrained fast marching algorithm as described in Algorithm 5. The radius-lifted initial source point for Algorithm 5 can be identified by assigning radius 1 to either endpoint of h . The radius-lifted tensor field \mathcal{M}_r (3.9) of the anisotropic Riemannian metric \mathcal{R}^{AR} can be constructed using the optimally oriented flux filter (Law and Chung, 2008) as introduced in Section 3.3. The tubular neighbourhood region \hat{U}_h for segment h is necessary to avoid overlapping extraction as demonstrated in Fig. 3.17a and 3.17b, which show the overlapped minimal paths. In Fig. 3.17a, the minimal path (blue) is extracted based on the two endpoints of segment tagged as blue in Fig. 3.15d. In Fig. 3.17b, the minimal path (red) is extracted based on the information from the red segment Fig. 3.15d. One can see that the red minimal path passes almost the same pixels with the

blue shown in Fig. 3.17a.

However, sometimes the endpoints of the segment h are not located at the exact centre of the tubular structure. As an example, see the two endpoints of the red segment in Fig. 3.15d. This endpoint-bias problem will introduce inaccuracy to the final minimal path extraction results around the initial source points and endpoints (see the red path in Fig. 3.17c). To solve this problem, we propose an endpoint correction method before we apply the minimal paths extraction step. The proposed EC method relies on the Euclidean curve length map L of the minimal path, where L can be computed in the course of the fast marching front propagation as introduced in Section 3.4.

Recall that the Euclidean curve length map $L(\hat{\mathbf{x}}) = L(\mathcal{C}_{\hat{\mathbf{s}}, \hat{\mathbf{x}}})$ can be formulated as:

$$L(\hat{\mathbf{x}}) := \int_{\mathcal{C}_{\hat{\mathbf{s}}, \hat{\mathbf{x}}}} \|\mathcal{C}'_{\hat{\mathbf{s}}, \hat{\mathbf{x}}}(t)\| dt, \quad (3.42)$$

where $\hat{\mathbf{s}} \in \hat{Z}$ is the initial source point and \hat{Z} is the discretization grid of $\hat{\Omega}$.

The EC method is described in Algorithm 6: for a given segment $h \in \mathcal{T}$ with two endpoints $\mathbf{p}_1, \mathbf{p}_2$, we identify its middle point $\mathbf{m} \in h$ and the dilated tubular neighbourhood region U_h with width ℓ . By performing the fast marching algorithm from the radius-lifted point $\hat{\mathbf{m}} = (\mathbf{m}, 1)$, one can compute the geodesic distance \mathcal{U}_h and Euclidean curve length L inside the tubular neighbourhood region U_h simultaneously. Once any radius-lifted endpoint $\hat{\mathbf{p}}_i^* = (\mathbf{p}_i, r) \in \hat{Z}$ is reached, we can search the desired radius-lifted point $\hat{\mathbf{q}}_i$ inside a set \mathcal{B}_i :

$$\mathcal{B}_i := \{\hat{\mathbf{x}} \in \hat{Z}; \|\hat{\mathbf{x}} - \hat{\mathbf{p}}_i^*\|_2 \leq r_{\mathcal{B}}\}, \quad i = 1, 2, \quad (3.43)$$

where $r_{\mathcal{B}} > 0$ is a given constant. As described in Algorithm 6: we find a collection of radius-lifted points

$$A_i := \{\hat{\mathbf{x}} \in \hat{Z}; L(\hat{\mathbf{x}}) \geq [L(\hat{\mathbf{p}}_i)] + 1, \hat{\mathbf{x}} \in \mathcal{B}_i\}, \quad i = 1, 2, \quad (3.44)$$

where $[n]$ means the largest integer which is smaller than $n \in \mathbb{R}$. The collection A_1 (resp. A_2) includes all the radius-lifted points for which the Euclidean curve length values are larger than $L(\hat{\mathbf{p}}_1)$ (resp. $\hat{\mathbf{p}}_2$). Then the desired endpoint can be selected as:

$$\hat{\mathbf{q}}_i = \arg \min_{\hat{\mathbf{x}} \in A_i} \mathcal{U}(\hat{\mathbf{x}}), \quad i = 1, 2. \quad (3.45)$$

Once both endpoints are corrected, i.e., $\hat{\mathbf{q}}_1$ and $\hat{\mathbf{q}}_2$ are found by (3.45), stop the algorithm completely. The criteria are based on the fact that among all the points with the same curve length, any point which is located at the centreline of the tubular structure has a local minimum geodesic distance value. In Fig. 3.17d, we show the results with the boundaries delineation. We can see the endpoints

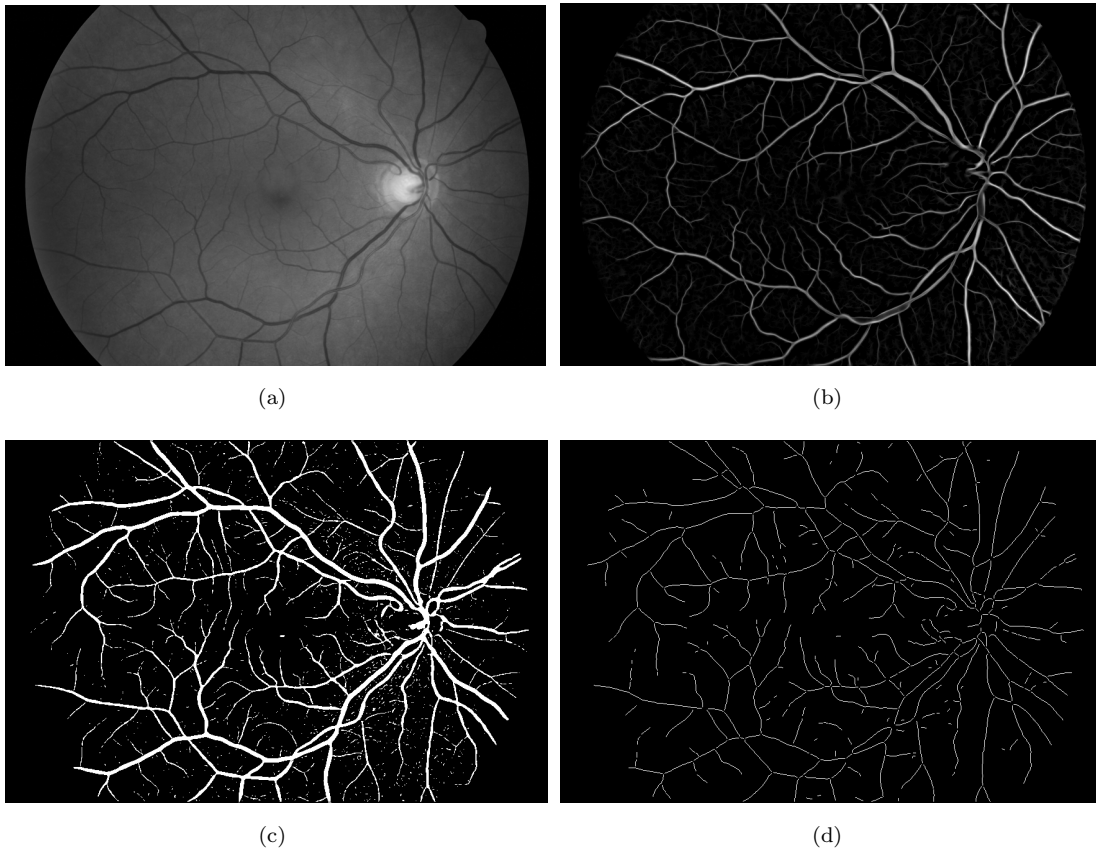


FIGURE 3.18: Illustration for the proposed algorithm step by step. **(a)** The green channel of the original retinal image. **(b)** Vesselness map obtained by using the method presented in (Zhang et al., 2016). **(c)** Binary segmented vessel map after thresholding the vesselness map. **(d)** Skeleton map after removing all the branch points and small segments.

of red, green and yellow lines have been placed at the better positions compared with Fig. 3.17c and Fig. 3.15d.

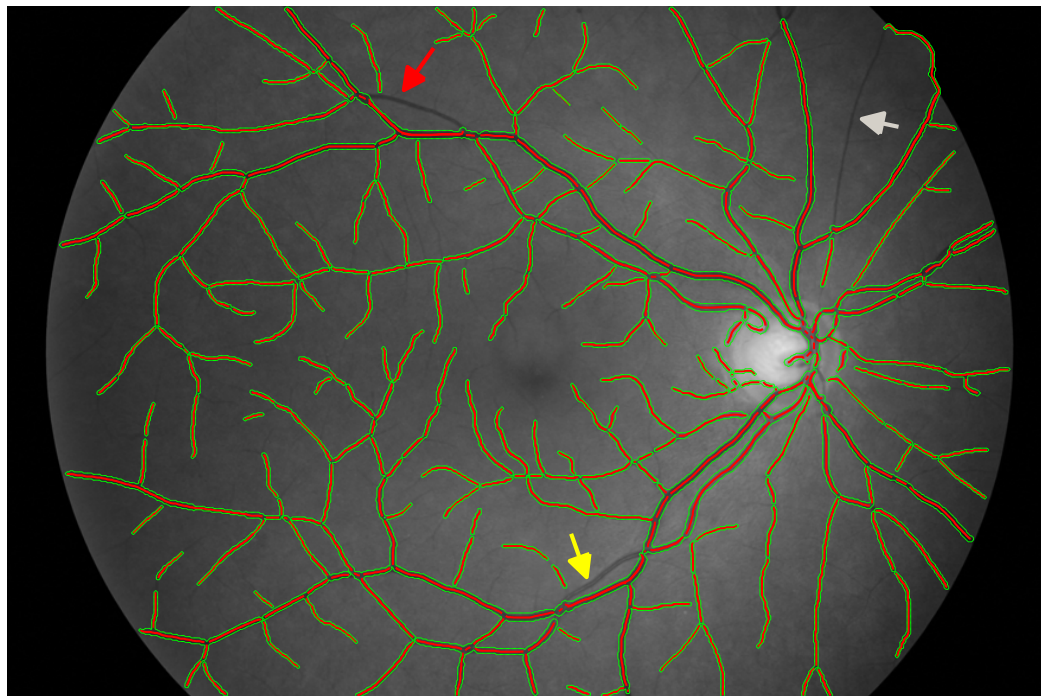
In Algorithm 6, for each segment h , we could get the minimal path \mathcal{C}_h , joining each corrected endpoints $\hat{\mathbf{q}}_i$ and the initial source point $\hat{\mathbf{m}}$:

$$\mathcal{C}_h = \mathcal{C}_{\hat{\mathbf{m}}, \hat{\mathbf{q}}_1} \cup \mathcal{C}_{\hat{\mathbf{m}}, \hat{\mathbf{q}}_2}. \quad (3.46)$$

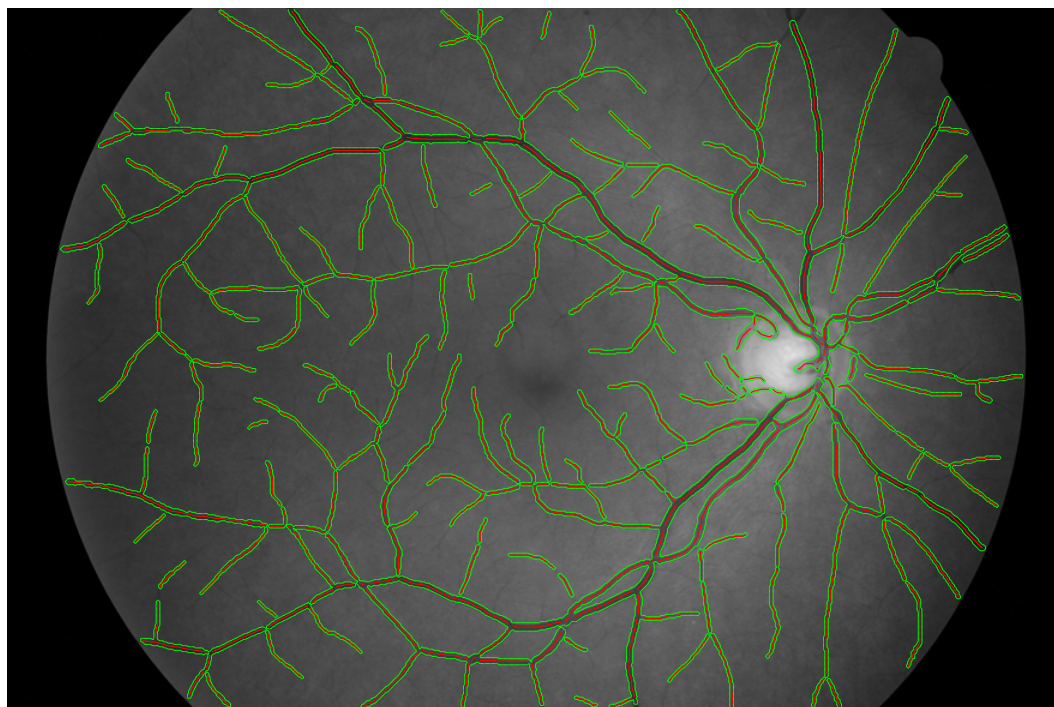
Then we replace the segments collection \mathcal{T} by \mathcal{T}_{new} involving all the minimal paths \mathcal{C}_h .

3.6.4 Experimental Results on Retinal Images

we summary our method as follows:



(a)



(b)

FIGURE 3.19: Segmentation of a retinal image by the proposed method. (a) The result by Benmansour-Cohen model. (b) The result of our method (Green lines are the boundaries and red lines are the centrelines).

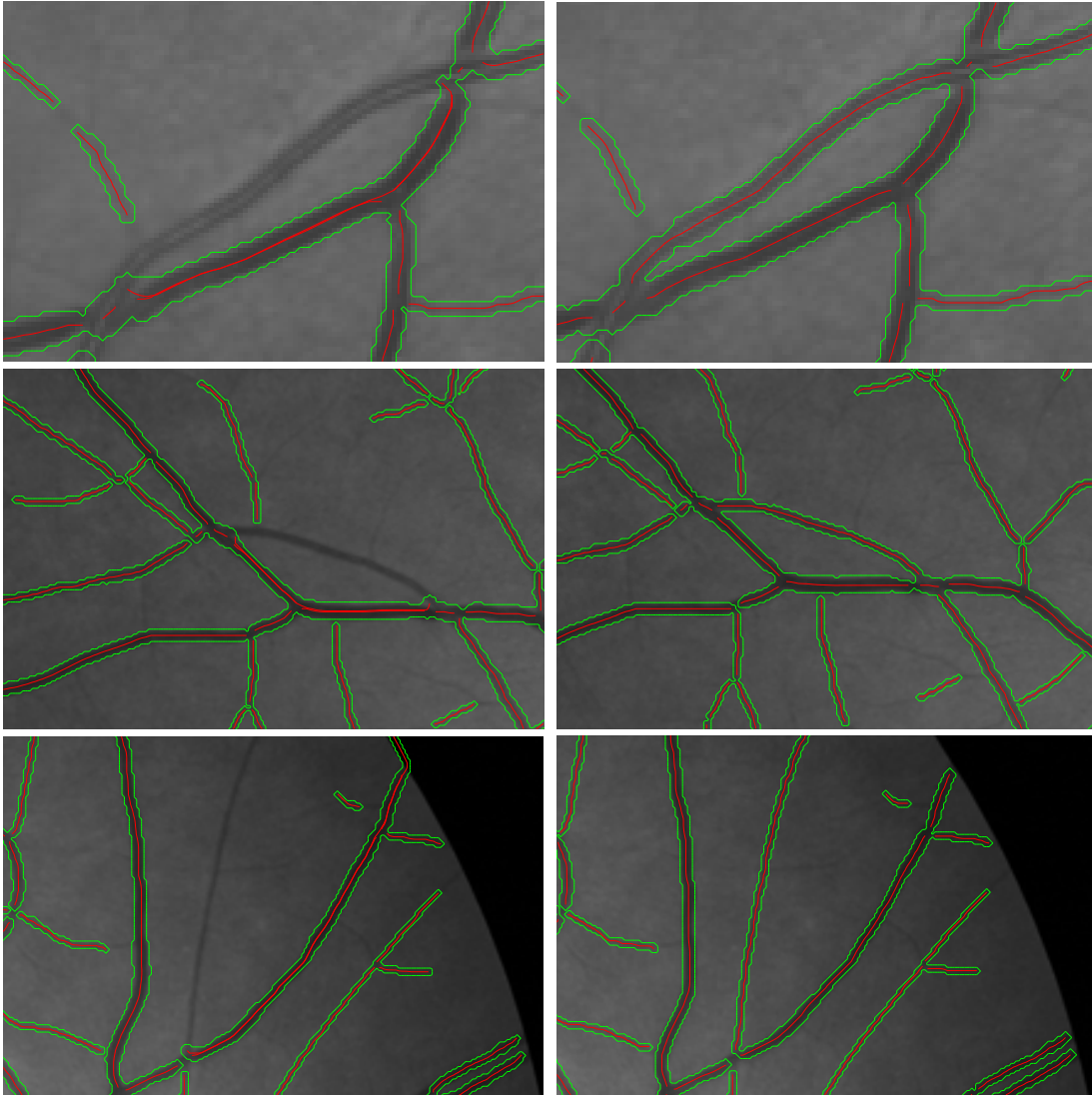


FIGURE 3.20: Details of the segmentation results shown in Fig. 3.19. **Column 1:** details of Fig. 3.19(a) indicated by arrows. **Column 2:** corresponding details of Fig. 3.19(b) .

1. For a given image I , obtain its vessel skeleton map by removing all the branch and crossover points. Tag each segment of the skeleton map and store them in \mathcal{T} .
2. For each segment $h \in \mathcal{T}$, do Endpoints Correction as described in Algorithm 6 to get a new set of segments \mathcal{T}_{new} .
3. For each segment $h_{\text{new}} \in \mathcal{T}_{\text{new}}$, construct the tubular neighbourhood region \hat{U}_h and do region-constrained fast marching algorithm described in Algorithm 5 to obtain a set of minimal paths, in which each minimal path consists of the centrelines and the radius value representing the vessel width.

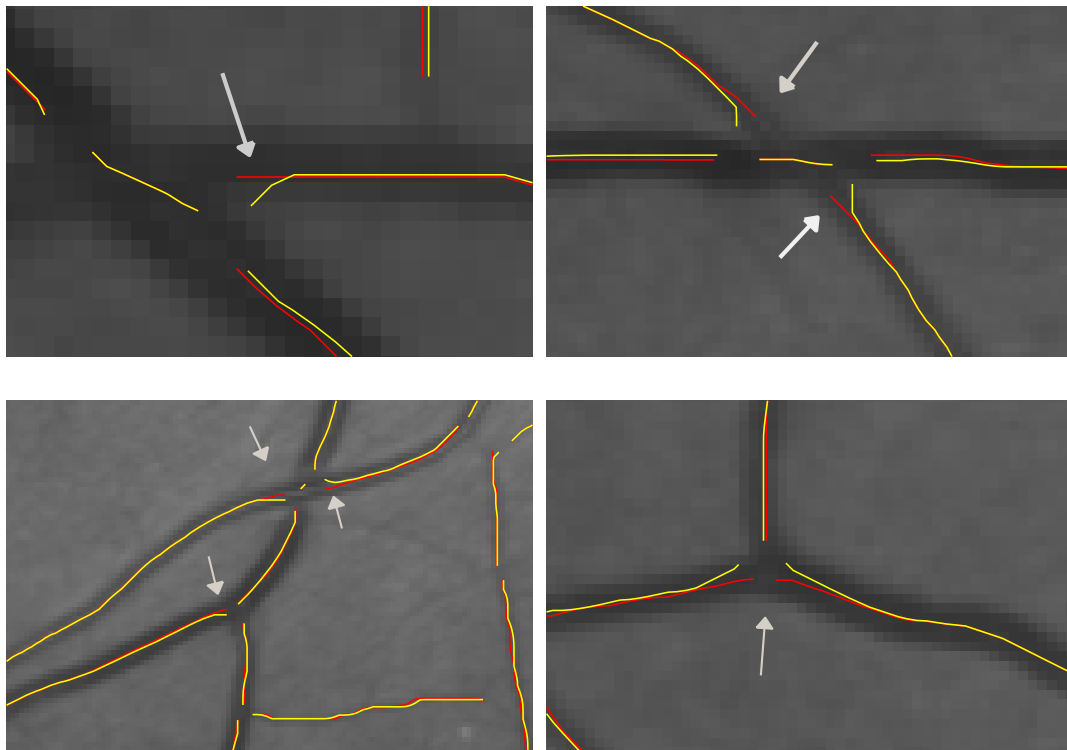


FIGURE 3.21: Improved results by Endpoints Correction. Yellow lines are the paths without Endpoints Correction while red lines are the paths after Endpoints Correction.

We illustrate the first step of the proposed algorithm in Fig. 3.18. Note that in Fig. 3.18a, we only demonstrate the green channel of the colored retinal image.

In Fig. 3.19a we show a complete result obtained by using by Benmansour-Cohen model (Benmansour and Cohen, 2011) for each vessel segment. We can see that there are three vessel segments are missed due to the overlapping extraction problem. The green lines represent the boundaries while the red lines are the centrelines of the vessel segments. In Fig. 3.19b we show the vessel tree extraction results by the proposed model. It can be seen that our method can capture the vessel segments missed in Fig. 3.19a. The pre-segmented vessel map is obtained by applying a constant threshold value to the vesselness map \mathbb{V}_{ness} (3.3) computed using optimally oriented flux filter.

In Column 1 of Fig. 3.20, we illustrate the vessel segments extraction details of In Fig. 3.19a indicated by arrows. For the purpose of comparison, we show the result details of our method in column 2 of Fig. 3.20.

In Fig. 3.21, we show the improved results after endpoints correction. Yellow lines are the paths without endpoints correction. Compared to the red lines which are produced after endpoints correction, we can see the endpoints are located at more precise positions.

TABLE 3.2: Comparison of our segmentation results with the second manual segmentation on the test set of DRIVE dataset.

Methods	Maximum	Minimum	Mean	Standard deviation
Benmansour and Cohen (2011)	0.947	0.9271	0.9372	0.0054
Proposed Method	0.949	0.9305	0.9397	0.0052

TABLE 3.3: Comparison of our segmentations Computation time (in Seconds) with [Benmansour and Cohen \(2011\)](#) model on retinal images from the test set of DRIVE dataset.

	Maximum	Minimum	Mean	Standard deviation
Benmansour and Cohen (2011)	22.6s	9.16s	13.17s	3.2s
Endpoints Correction	5.1s	4.0s	4.39s	0.27s
Constrained Fast Marching	5.6s	4.4s	5.06s	0.353s

For evaluation we apply our method on 20 retinal images got from the test set of the DRIVE dataset ([Staal et al., 2004](#)), acquired through a Canon CR5 non-mydratic 3CCD camera with a 45 degree field of view (FOV). We show the comparison between Benmansour-Cohen model ([Benmansour and Cohen, 2011](#)) and our method in Table 3.2 with evaluation measure Accuracy, which can be computed by the ratio of the summation of the statistical components: the true positive and the true negative to the total number of pixels in the FOV ([Fraz et al., 2012](#)). We erode the FOV region by 11 pixels to remove the effect of the boundaries of the FOV to the vessel pre-segmentation. We evaluate our results only inside this eroded FOV region. In Table 3.3 we show the computation time of our algorithm in endpoints correction and constrained Fast Marching respectively. We also compare the computation time with classical anisotropic Benmansour-Cohen model with the same given segment set. Our method can achieve almost 2 times faster than the Benmansour-Cohen model.

3.6.5 Conclusion

We propose a new tubular structure extraction method based on the region-constrained anisotropic fast marching algorithm, and introduce an endpoints correction method using Euclidean curve length map. These ingredients allow our method to extract piecewise minimal paths from complex tubular network, leading to better extraction results compared to the classic Benmansour-Cohen model.

Algorithm 6 *Endpoints Correction***Input:**

- Metric \mathcal{M} , stencil S , and Dilated tubular neighbourhood region \hat{U}_h
- Endpoints \mathbf{p}_1 and \mathbf{p}_2 , initial source point \mathbf{m} .

Output:

- Path \mathcal{C} and corrected radius-lifted endpoints $\hat{\mathbf{q}}_1, \hat{\mathbf{q}}_2$.

Initialization:

- For each point $\hat{\mathbf{x}} \in \hat{Z}$, set $\mathcal{U}(\hat{\mathbf{x}}) \leftarrow +\infty$, $L(\hat{\mathbf{x}}) \leftarrow +\infty$ and $\mathcal{V}(\hat{\mathbf{x}}) \leftarrow \text{Far}$.
- $\mathcal{U}(\hat{\mathbf{m}}) \leftarrow 0$, $L(\hat{\mathbf{m}}) \leftarrow 0$, $\mathcal{V}(\hat{\mathbf{m}}) \leftarrow \text{Trial}$, and $A_0 \leftarrow \emptyset$.
- Set radius-lifted point collection $A = \emptyset$ and *RemainedEndpoints* = 2
- *IfStop* \leftarrow **False**.

Main Loop

```

1: while IfStop = False do
2:   Find  $\hat{\mathbf{x}}_{\min} = (\mathbf{x}_{\min}, r)$ , the Trial point which minimizes  $\mathcal{U}$ .
3:    $\mathcal{V}(\hat{\mathbf{x}}_{\min}) \leftarrow \text{Accepted}$ .
4:   if RemainedEndpoints = 0 then
5:     Track geodesics  $\mathcal{C}_{\hat{\mathbf{m}}, \hat{\mathbf{q}}_1}$  and  $\mathcal{C}_{\hat{\mathbf{m}}, \hat{\mathbf{q}}_2}$  from both corrected endpoints contained in  $A_0$ .
6:      $\mathcal{C} \leftarrow \mathcal{C}_{\hat{\mathbf{m}}, \hat{\mathbf{q}}_1} \cup \mathcal{C}_{\hat{\mathbf{m}}, \hat{\mathbf{q}}_2}$ .
7:     IfStop  $\leftarrow$  True.
8:   end if
9:   if  $\hat{\mathbf{x}}_{\min} \in \hat{U}_h$  then
10:    Update  $L(\hat{\mathbf{x}}_{\min})$  using (3.16).
11:    if  $\mathbf{x}_{\min} = \mathbf{p}_1$  or  $\mathbf{x}_{\min} = \mathbf{p}_2$  then
12:      RemainedEndpoints  $\leftarrow$  RemainedEndpoints - 1.
13:       $A \leftarrow \emptyset$  and construct the collection  $\mathcal{B}$  using (3.43).
14:      for All  $\hat{\mathbf{x}} \in \mathcal{B}$  centred at  $\hat{\mathbf{x}}_{\min}$  do
15:        if  $L(\hat{\mathbf{x}}) \geq [L(\hat{\mathbf{x}}_{\min})] + 1$  and  $\mathcal{V}(\hat{\mathbf{x}}) = \text{Accepted}$  then
16:           $A \leftarrow A \cup \{\hat{\mathbf{x}}\}$ .
17:        end if
18:      end for
19:      if  $A \neq \emptyset$  then
20:         $A_0 \leftarrow A_0 \cup \left\{ \arg \min_{\hat{\mathbf{x}} \in A} \mathcal{U}(\hat{\mathbf{x}}) \right\}$ .
21:      else
22:         $A_0 \leftarrow A_0 \cup \{\hat{\mathbf{x}}_{\min}\}$ .
23:      end if
24:    end if
25:    for All  $\hat{\mathbf{y}}$  such that  $\hat{\mathbf{x}}_{\min} \in S(\hat{\mathbf{y}})$  and  $\mathcal{V}(\hat{\mathbf{y}}) \neq \text{Accepted}$  do
26:      Compute  $\mathcal{U}_{\text{new}}(\hat{\mathbf{y}})$  using Hopf-Lax update in (2.86).
27:      if  $\mathcal{V}(\hat{\mathbf{y}}) \neq \text{Trial}$  then
28:         $\mathcal{V}(\hat{\mathbf{y}}) \leftarrow \text{Trial}$ .
29:      end if
30:       $\mathcal{U}(\hat{\mathbf{y}}) \leftarrow \min\{\mathcal{U}_{\text{new}}(\hat{\mathbf{y}}), \mathcal{U}(\hat{\mathbf{y}})\}$ .
31:    end for
32:  else
33:     $\mathcal{U}(\hat{\mathbf{x}}_{\min}) \leftarrow +\infty$  and  $L(\hat{\mathbf{x}}_{\min}) \leftarrow +\infty$ .
34:  end if
35: end while

```


Chapter 4

Anisotropic Front Propagation for Tubular Structure Segmentation

Abstract

We present in this chapter a blood vessel segmentation model by anisotropic fast marching front propagation method with respect to an anisotropic dynamic Riemannian metric. The fast marching front is defined as the level set of the geodesic distance map to a set of given initial source points with respect to a dynamic anisotropic Riemannian metric. The boundaries of the vessels are supported to be represented by the level set at the given distance value. The dynamic anisotropic Riemannian metric can be defined using a prior estimate of the vessel orientations and the local intensity difference values, where the vessel orientations are detected by the oriented flux filter.

4.1 Introduction

Flux-based active contours models have been widely applied to tubular structure segmentation since the pioneer work presented in (Vasilevskiy and Siddiqi, 2002), in which the flux magnitude field of the image gradient vector is taken as the dominating external force to drive the active contours (2D) or active surfaces (3D) to sketch the tubular structure boundaries. To solve the expensive computation cost of the local flux for each pixel in the image domain, Law and Chung (2009) proposed a fast flux computation method and its improved version: the optimally oriented flux filter (Law and Chung, 2008) which can be adapted to active contours models (Law and Chung, 2010). However, those deformable models are based on the level set evolution scheme, where the curve or surface is defined as a zero level set with high computation complexity.

Fast marching-based front propagation based segmentation method was developed to overcome the computational complexity of the classical level set numerical scheme by Malladi and Sethian (1998). This method is extremely fast with restriction that the speed has to be positive everywhere. This restriction sometimes will lead to a leakage problem: the front will propagate outside the tubular structure before all the points inside the expected tubularity have been covered. In other words, some parts of the fast marching front need more time to reach the boundaries, and by that time, other parts of the front leak across the boundaries of the vessel. Cohen and Deschamps (2007); Deschamps and Cohen (2002) proposed a front propagation method combining the Euclidean curve length, which can be applied to tag the fast marching front points as either *head* or *tail*. Then the leakages problem can be avoided by freezing all the *tail* points.

In this section, we proposed an alternate way to solve the leakages problem for fast marching front propagation based segmentation method. We take into account the path anisotropy to penalize the front propagation along the directions which do not coincide the vessel orientations. This is done by applying an anisotropic Riemannian metric instead of the isotropic case (Malladi and Sethian, 1998). The proposed anisotropic front propagation method can guarantee a connected segmented vessel tree structure and is easy to combine with manual interventions, compared to the vesselness based segmentation methods like (Law and Chung, 2008). Furthermore, the optimally oriented flux filter may fail to identify a vessel with large scale since the scale normalization. In contrast, we explore a local intensity consistency based metric construction method, which can be integrated with the vessel orientation to achieve better vessel segmentation results than classical methods (Cohen and Deschamps, 2007; Deschamps and Cohen, 2002; Malladi and Sethian, 1998).

The main contents of this chapter were presented at the ISBI 2016 conference (Chen and Cohen, 2016).

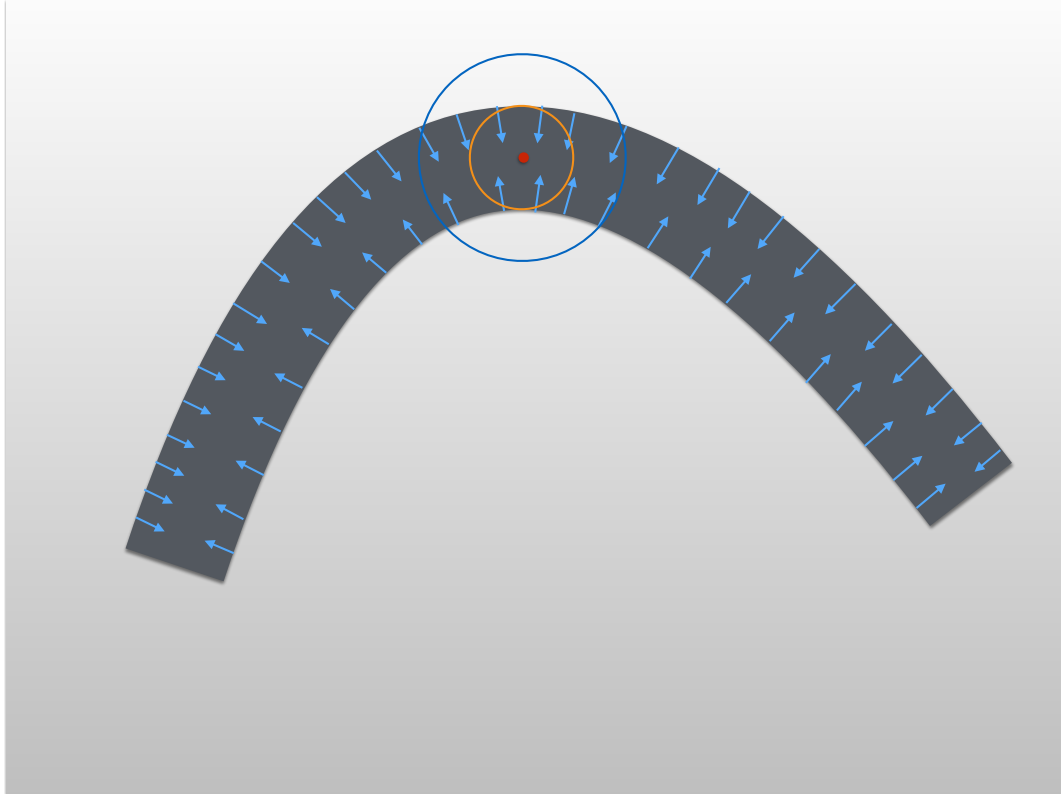


FIGURE 4.1: Illustration of the approximation of the flux computation.

4.2 Front Propagation for Image Segmentation

4.2.1 Flux-based Active Contours Model

Vasilevskiy and Siddiqi (2002) proposed a front propagation method for tubular structure segmentation by maximizing the flux based energy:

$$E_{\text{Flux}}(\Gamma) := \int_0^1 \langle \mathcal{V}, \mathcal{N} \rangle \|\Gamma'(t)\| dt, \quad (4.1)$$

where $\mathcal{V} : \Omega \rightarrow \mathbb{R}^2$ is a vector field and \mathcal{N} is the normal of curve Γ . By the divergence theorem, the curve evolution equation derived from (4.1) with respect to time τ can be expressed as:

$$\frac{\partial \Gamma}{\partial \tau} = (\nabla \cdot \mathcal{V}) \mathcal{N}. \quad (4.2)$$

$\nabla \cdot \mathcal{V}$ is the divergence of vector field \mathcal{V} . This divergence operator is defined by the divergence theorem as

$$\nabla \cdot \mathcal{V}(\mathbf{x}) = \lim_{\text{area}(\mathbf{R}(\mathbf{x})) \rightarrow 0} \frac{\oint_{\partial \mathbf{R}} \langle \mathcal{V}, \mathcal{N}_{\mathbf{R}} \rangle ds}{\text{area}(\mathbf{R}(\mathbf{x}))}, \quad \mathbf{x} \in \Omega. \quad (4.3)$$

where $R(\mathbf{x})$ denotes a round region centred at point \mathbf{x} and $\text{area}(R(\mathbf{x}))$ is its area. ∂R is the boundary with outward normal \mathcal{N}_R . Vasilevskiy and Siddiqi (2002) used an approximation of the flux definition which can be described as: at each point \mathbf{x} , one can compute its flux values using a collection of discs centred at \mathbf{x} with increasing radii. Then the maximum value of these radius dependent flux values can be chosen as the expected flux value of \mathbf{x} to drive the active contours. In Fig. 4.1, we illustrate this approximation of flux computation. Arrows indicate the vector field \mathcal{V} . Red dot denotes the centred point \mathbf{x} and the circles with different colours are the boundaries of discs with different radii. Law and Chung (2009) proposed an fast flux computation method to make the flux based active contours model (Vasilevskiy and Siddiqi, 2002) be practical.

4.2.2 Fast Marching Front Propagation Model

We consider the isotropic Eikonal equation:

$$\|\nabla\mathcal{U}(\mathbf{x})\| = \frac{1}{P(\mathbf{x})}, \quad (4.4)$$

where \mathcal{U} is the minimal action map or minimal arrival time with speed function $P : \Omega \rightarrow \mathbb{R}^+$ with $\Omega \subset \mathbb{R}^2$ being the image domain. This Eikonal equation was first adopted by Malladi and Sethian (1998) for surface segmentation and shape recover. This front propagation scheme assume that $P(\mathbf{x}) > 0$ everywhere. Thanks to this restriction, the front could propagate towards to the object boundaries or surfaces with cheap computation time.

Given a set of initial source points, the behaviour of the front propagation is like the curve evolution driven by a ballon force (Cohen, 1991). Generally, the speed function P should be large inside the flat region in order for the front to propagate very fast. In contrast, at the vicinity of object boundaries or surfaces, P should become small and the front propagation is slow within this region, thus stopping the front to leak out the objects like tubular structures. P might depend on the image gradient magnitudes, intensity values or vesseness values.

Numerically, the Eikonal equation (4.4) can be solved by the isotropic fast marching algorithm (Sethian, 1999). The gradient $\nabla\mathcal{U}$ is approximated by a first-order upwind scheme, satisfied for the isotropic metric. In this section, we focus on the anisotropic Riemannian metric which cannot be solved by such fast marching method. Instead, we utilize the anisotropic fast marching algorithm proposed by Mirebeau (2014a) which is very stable even for large anisotropy ratio.

4.3 Front Propagation with Anisotropic Riemannian Metric and Fast Marching Method

We consider the anisotropic Eikonal equation with anisotropic Riemannian metric. For a symmetric positive definite tensor field \mathcal{M} , the anisotropic Eikonal equation is

$$\|\nabla\mathcal{U}(\mathbf{x})\|_{\mathcal{M}^{-1}(\mathbf{x})} = 1. \quad (4.5)$$

The anisotropic Fast Marching algorithm [Mirebeau \(2014a\)](#) can be used as the numerical solver of distance map \mathcal{U} , by finding the solution, at each update step, of the fixed point problem with respect to the anisotropic metric \mathcal{R}_A (2.52):

$$\mathcal{U}(\mathbf{x}) = \min_{\mathbf{y} \in \partial S(\mathbf{x})} \left\{ \mathcal{R}_A(\mathbf{x}, \mathbf{y} - \mathbf{x}) + I_{S(\mathbf{x})} \mathcal{U}(\mathbf{y}) \right\}, \quad (4.6)$$

$$\mathcal{R}^A(\mathbf{x}, \mathbf{y} - \mathbf{x}) = \sqrt{\langle \mathbf{y} - \mathbf{x}, \mathcal{M}(\mathbf{x}) (\mathbf{y} - \mathbf{x}) \rangle}, \quad (4.7)$$

where $I_{S(\mathbf{x})}$ is a piecewise linear interpolation operator on a mesh $S(\mathbf{x})$. The local mesh or stencil S can be adaptively constructed according to the given Riemannian metric \mathcal{M} by the tool of Lattice Basis Reduction, as introduced in [Mirebeau \(2014a\)](#), leading to breakthrough improvements in terms of computational time and accuracy when dealing with metrics having strong anisotropy ratio.

As initialization, the fast marching algorithm tags all the points of discretization grid Z of Ω to either *Accepted* (points have been computed and frozen), *Trial* (points have been updated at least once but not frozen) or *Far* (points have not been estimated yet). The fast marching *front* consists of all the *Trial* points. The *Trial* point \mathbf{x}_{\min} minimizing \mathcal{U} will be tagged as *Accepted* and all its neighbourhood points $\{\mathbf{y} \in \Omega; \mathbf{x} \in S(\mathbf{y})\}$ will be updated by solving (4.6). More details about the fast marching method can be seen in Section 2.4.

For convenience, we say that point \mathbf{x} is **base-point** of all its neighbour points \mathbf{y} .

4.4 Dynamic Riemannian Metric Construction

Traditional anisotropic Eikonal equation uses static metric field independent of the fast marching front and relies only on the positions and orientations of the path. For blood vessels segmentation application, one has to deal with the problem of intensities inhomogeneities which is not suitable for the static metric, thus we propose to take into account the front location to calculate the *dynamic* Riemannian metric.

Let $A \subseteq \Omega$ be a collection of all points tagged as *Accepted*. In Fig. 4.2, we denote A by the red region. Assuming that vessels are brighter than background, we define

Algorithm 7 *Front Propagation with Dynamic Metric***Input:**

- Tensor field \mathcal{M}_c .
- Initial point set \mathcal{W} and stencil S .

Output:

- Minimal action map \mathcal{U} .

Initialization:

- For each point $\mathbf{x} \in \Omega$, set $\mathcal{U}(\mathbf{x}) \leftarrow +\infty$ and $\mathcal{V}(\mathbf{x}) \leftarrow \textit{Far}$.
- For each point $\mathbf{x} \in \mathcal{W}$, set $\mathcal{U}(\mathbf{x}) \leftarrow 0$ and $\mathcal{V}(\mathbf{x}) \leftarrow \textit{Trial}$.

Main Loop

```

1: while at least one grid point is tagged as Trial do
2:   Find  $\mathbf{x}_{\min}$ , the Trial point which minimizes  $\mathcal{U}$ .
3:    $A \leftarrow \{A \cup \mathbf{x}_{\min}\}$ 
4:    $\mathcal{V}(\mathbf{x}_{\min}) \leftarrow \textit{Accepted}$ .
5:   Compute  $K(\mathbf{x}_{\min})$  using (4.8).
6:   for All  $\mathbf{y}$  such that  $\mathbf{x}_{\min} \in S(\mathbf{y})$  and  $\mathcal{V}(\mathbf{y}) \neq \textit{Accepted}$  do
7:     if  $\mathcal{V}(\mathbf{y}) \neq \textit{Trial}$  then
8:        $\mathcal{V}(\mathbf{y}) \leftarrow \textit{Trial}$ .
9:     end if
10:    Update  $\mathcal{J}(\mathbf{y})$  using (4.12).
11:    Construct the tensor field  $\mathcal{M}_d$  using (4.13).
12:    Compute  $\mathcal{U}_{\text{new}}(\mathbf{y})$  using (4.6).
13:    if  $\mathcal{U}_{\text{new}}(\mathbf{y}) < \mathcal{U}(\mathbf{y})$  then
14:       $\mathcal{U}(\mathbf{y}) \leftarrow \mathcal{U}_{\text{new}}(\mathbf{y})$ .
15:    end if
16:  end for
17: end while

```

a local mean intensity function $K : \Omega \rightarrow \mathbb{R}^+$ and a local intensity dissimilarity function $\mathcal{J} : \Omega \rightarrow \mathbb{R}^+$:

$$K(\mathbf{x}) := \frac{\sum_{\mathbf{y} \in A \cap \mathcal{B}_r(\mathbf{x})} I(\mathbf{y})}{\#\{A \cap \mathcal{B}_r(\mathbf{x})\}}, \quad (4.8)$$

$$\mathcal{J}(\mathbf{x}) := \exp(\alpha |\min\{I(\mathbf{x}) - K(\mathbf{x}), 0\}|), \quad \mathbf{x} \in \Omega, \quad (4.9)$$

where α is a positive constant. $\mathcal{B}_r(\mathbf{x})$ is collection defined as

$$\mathcal{B}_r(\mathbf{x}) := \{\mathbf{y}; \|\mathbf{x} - \mathbf{y}\| \leq r\}. \quad (4.10)$$

$\#\{A \cap \mathcal{B}_r(\mathbf{x})\}$ is the number of points contained in the set $A \cap \mathcal{B}_r(\mathbf{x})$ which is indicated by the cyan region in Fig. 4.2. K is computed only inside a local region such that the proposed front propagation method is robust when dealing with intensity inhomogeneities and noise. By assuming that vessels have higher gray levels, we consider that if a pixel \mathbf{x} has higher intensity than the average intensity value of its vicinity points defined by $\mathcal{B}_r(\mathbf{x}) \cap A$, \mathbf{x} is likely to be located inside a vessel. Therefore we use $|\min\{I(\mathbf{x}) - K(\mathbf{x}), 0\}|$ to calculate $\mathcal{J}(\mathbf{x})$ in (4.9) instead



FIGURE 4.2: Illustration for the various regions used in the proposed model in the course of the fast marching front propagation. Black dot is the initial source point and blue contour denotes the fast marching front. Red region indicates the collection A including all the *Accepted* points. Cyan circle indicates the boundary of the ball $\mathcal{B}_r(\mathbf{x})$ where the centre point \mathbf{x} is denoted by blue dot. The cyan region denotes $A \cap \mathcal{B}_r(\mathbf{x})$.

of using $|I(\mathbf{x}) - K(\mathbf{x})|$.

Numerically, local intensity dissimilarity function \mathcal{J} can be updated in each update iteration of the fast marching algorithm. To reduce the computational complexity, we use the following approximation:

$$K(\mathbf{x}) \approx K(\mathbf{z}), \quad (4.11)$$

where \mathbf{z} is a *base-point* of \mathbf{x} . Then \mathcal{J} can be approximated by

$$\mathcal{J}(\mathbf{x}) \approx \exp(\alpha |\min\{I(\mathbf{x}) - K(\mathbf{z}), 0\}|). \quad (4.12)$$

With this approximation, the function K only requires to be updated N times where N is the total number of grid points in I .

The dynamic tensor field (anisotropic Riemannian metric) \mathcal{M}_d can be constructed by combination of \mathcal{J} as:

$$\mathcal{M}_d(\mathbf{x}) = \mathcal{J}(\mathbf{x}) \mathcal{M}_c(\mathbf{x}), \quad (4.13)$$

where the tensor field \mathcal{M}_c is constructed by

$$\mathcal{M}_c(\mathbf{x}) = \mathbf{V}_1(\mathbf{x})\mathbf{V}_1^T(\mathbf{x}) + \mu \mathbf{V}_2(\mathbf{x}) \mathbf{V}_2^T(\mathbf{x}), \quad (4.14)$$

where \mathbf{V}_1 is the detected tubular structure orientation defined in (3.6) and \mathbf{V}_2 is the vector field orthogonal to \mathbf{V}_1 . Parameter μ is the anisotropy ratio. One can see that \mathcal{M}_c is a non-changed tensor field during the fast marching front propagation. In contrast, \mathcal{M}_d will be dynamically updated due to the computation of \mathcal{J} . In Algorithm 7, we present the details of our algorithm. A , K , and \mathcal{J} are updated in lines 4, 5 and 10 respectively. The stopping criterion is a threshold computed by making sure that $T\%$ of pixels having the lowest minimal action map \mathcal{U} , among all pixels, have been chosen. For the proposed fast marching front propagation-based segmentation, this stopping criterion is equivalent to find $N * T\%$ points tagged as *Accepted*, where N is the total number of image pixels.

4.5 Experimental Results

We first show the advantage of using anisotropic Riemannian metric comparing to the results using isotropic Riemannian metric. Fig. 4.3 shows four front propagation results with the same number of points tagged as *Accepted*. The anisotropy ratio values for Figs. 4.3a to 4.3d are 1, 10, 30, and 50 respectively. It can be seen that a large anisotropy ratio could make the front propagate along the vessel structure as far as possible before the front leaks out of the vessels. In the following experiments, we set the anisotropy ratio value to be 30 for the proposed method.

In Fig. 4.4, we show the segmentation results using $1/\mathcal{J}$ as the speed for the front propagation with isotropic Riemannian metric. At the beginning of the front propagation in Figs. 4.4a and 4.4b, no leakage happens. However, as the front goes further along interior region of the vessel tree, it leaks from some weak vessels. This is why we utilize the anisotropic front propagation method.

In Fig. 4.5, we show the segmentation results from three segmentation methods: the second column shows the results by thresholding the vesselness map \mathbb{V}_{ness} in (3.3); the third column is obtained from a front propagation based method, in which we set the metric as

$$\mathcal{M}(\mathbf{x}) = \exp(\beta \mathbb{V}_{\text{ness}}(\mathbf{x}))(\mathbf{V}_1 \mathbf{V}_1^T(\mathbf{x}) + \mu \mathbf{V}_2 \mathbf{V}_2^T(\mathbf{x})), \quad (4.15)$$

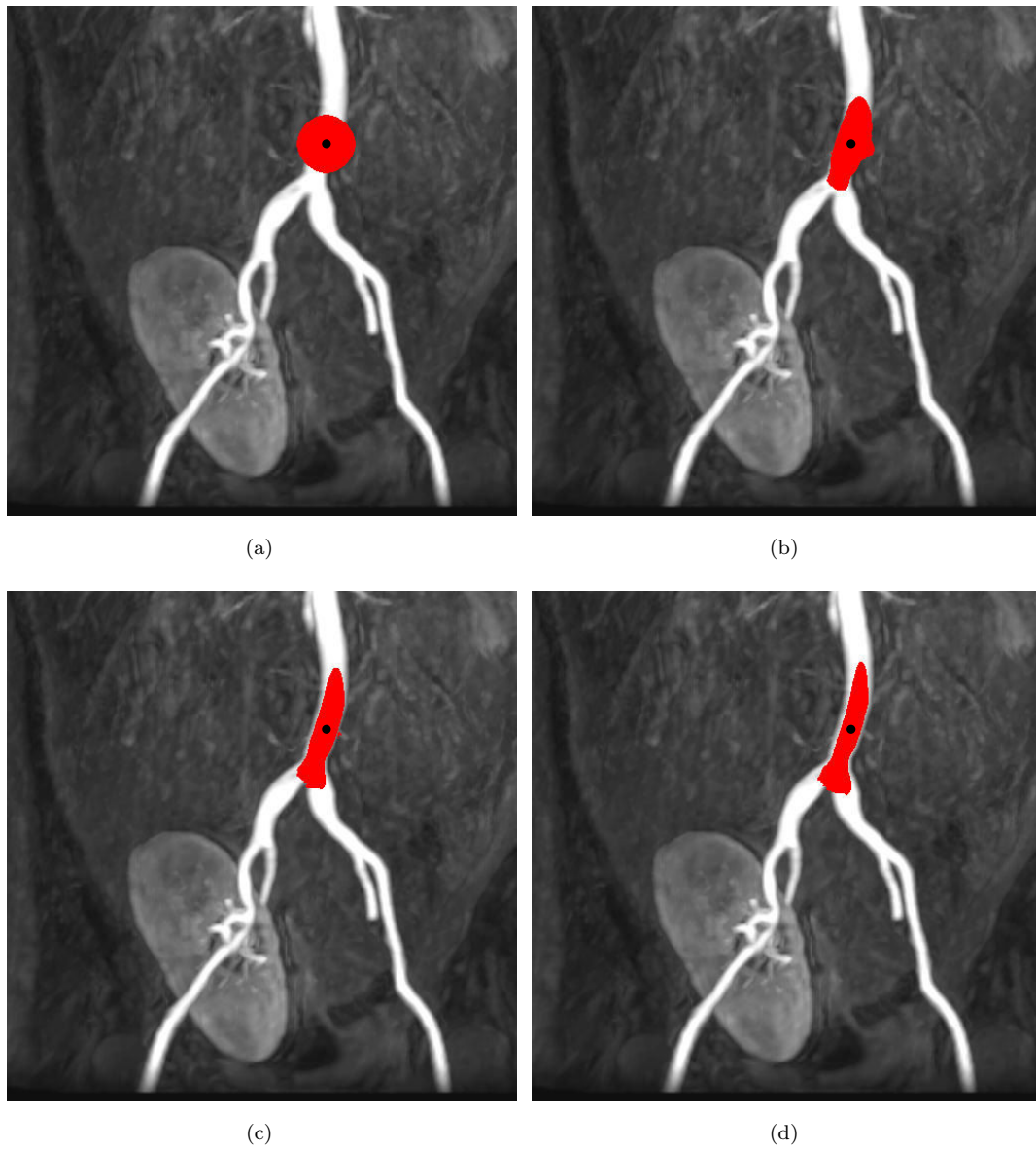


FIGURE 4.3: Front propagation based on the tensor field \mathcal{M}_c in (4.14) for different values of anisotropy ratio. (a) to (d): the values of the anisotropy ratio are 1, 10, 30 and 50 respectively. Black dots indicate the initial source points and red regions include all the *Accepted* points.

with $\beta < 0$. For fair comparison, we use the same fast marching algorithm proposed by Mirebeau (2014a) with the proposed method to compute the minimal action map. Black points in the third and last columns are the initial source points. The last column gives the results by the proposed method. All the three methods require thresholding to get the final segmentation results. One can see that the vesselness based results have many holes and scale overfitting. The vesselness-based front propagation method also suffers from the similar problems since the distance maps are heavily affected by the vesselness. In contrast, the proposed method can avoid the mentioned problems. In this experiment, we choose the

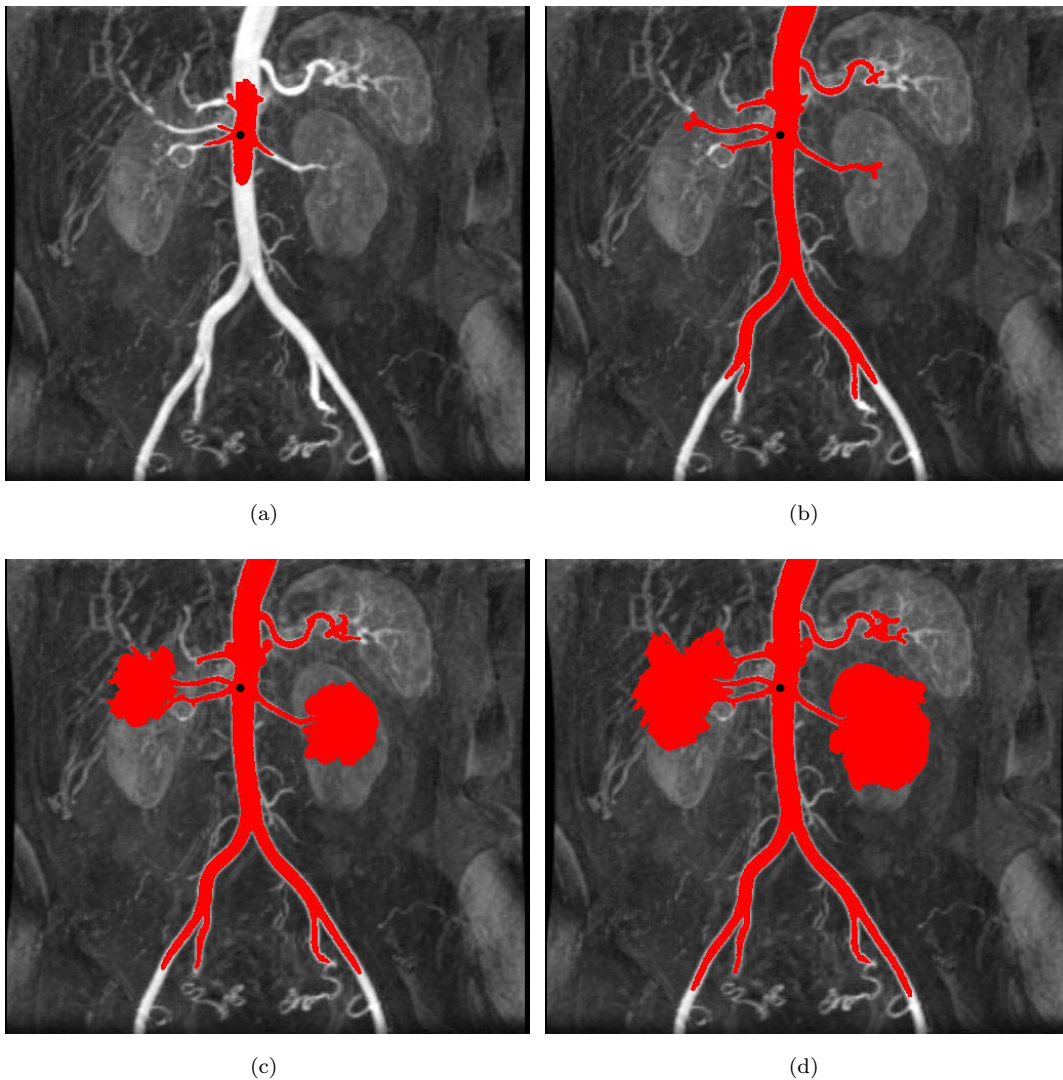


FIGURE 4.4: The course of the fast marching front propagation using isotropic fast marching front propagation method. Black dots indicate the initial source points and red regions include all the *Accepted* points. (a) to (d) demonstrate the front propagation results. In (c) and (d), the fast marching fronts propagate outside the vessel trees.

same T for the front propagation methods (third and last columns) but a little bigger T_1 to threshold the \mathbb{V}_{ness} in the second column.

4.6 Conclusion

In this chapter, we propose a new front propagation method for vessel segmentation with the dynamic anisotropic Riemannian metric and anisotropic fast marching method. The main contribution of this section lie at the use of the anisotropy enhancement for the front propagation-based segmentation and local region information-based Riemannian construction. We make use of the local intensity coherence to

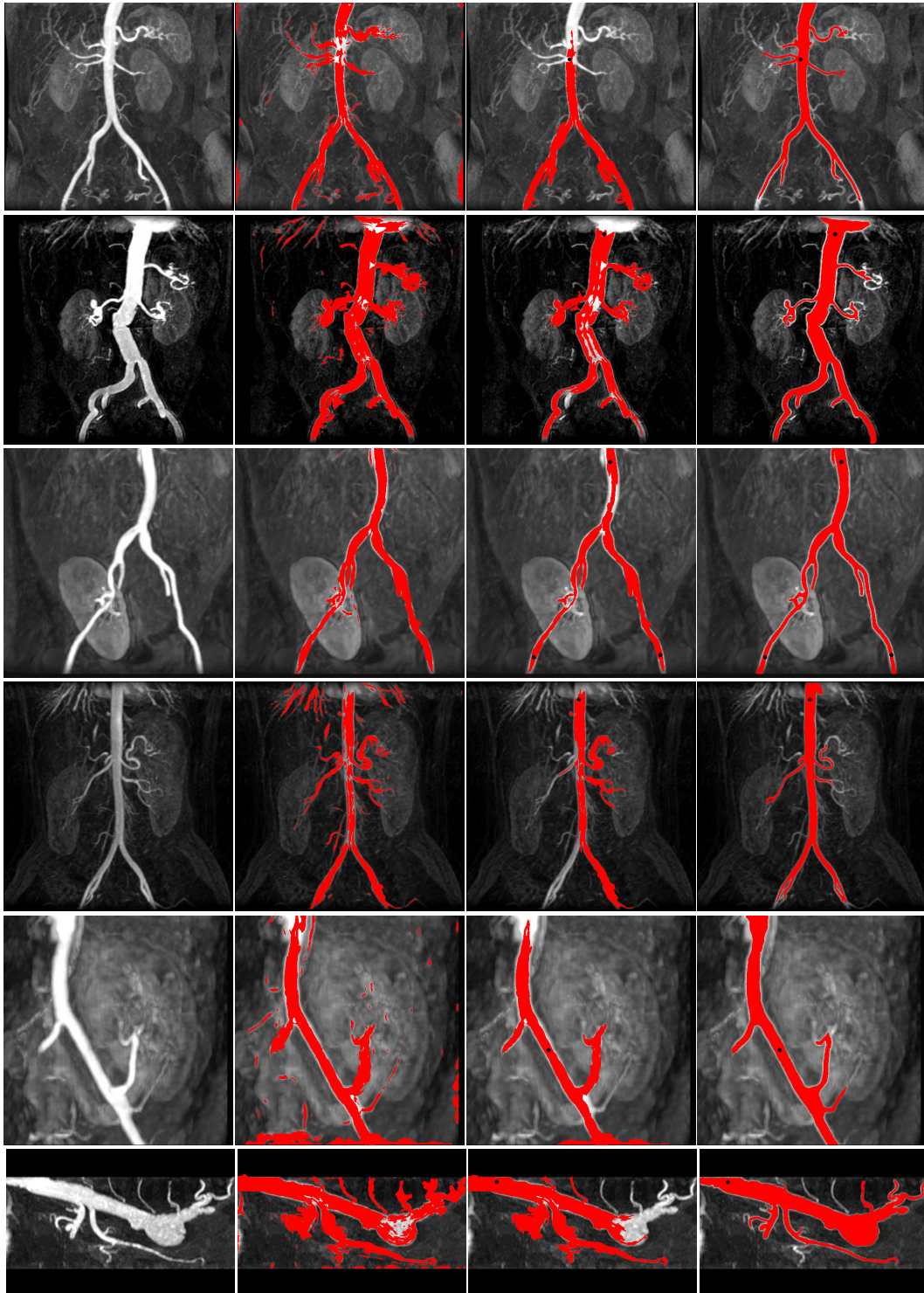


FIGURE 4.5: Comparative vessel tree segmentation results from different methods. **Column 1** Original images. **Column 2** Results from optimally oriented flux filter. **Column 3** Results from fast marching front propagation using eigenvalues of optimally oriented flux filter. **Column 4** Results from the proposed model.

penalize the tensor field constructed by the vessel anisotropy to make the fast marching front propagation robust to vessel intensity inhomogeneities and noise.

Numerical Experimental results show that our model indeed obtains expected results on vessel tree images. Compared against the isotropic front propagation-based image segmentation method, the proposed model can overcome the front leaking problem.

Chapter 5

Global Minimum for a Finsler Elastica Minimal Path Approach

Abstract

In this chapter, we present a novel curvature-penalized minimal path model via an orientation-lifted Finsler metric and the Euler elastica curve. Original minimal path model computes the globally minimal geodesic by solving an Eikonal partial differential equation (PDE). Essentially, this first-order model is unable to penalize curvature that is related to the path rigidity property in the classical active contour models. To solve this problem, we present an Eikonal PDE-based Finsler elastica minimal path approach to deal with the curvature-penalized geodesic energy minimization problem. We are able to add the curvature penalization to the classical geodesic energy (Caselles et al., 1997; Cohen and Kimmel, 1997). The basic idea of this work is to interpret the Euler elastica bending energy via a novel Finsler elastica metric embedding curvature penalty. This metric is non-Riemannian, anisotropic and asymmetric, defined over an orientation-lifted space by adding to the image domain the orientation as an extra space dimension. Based on this orientation lifting, the proposed minimal path model can benefit from both the curvature and orientation of paths. Thanks to the fast marching method with stencils refinement scheme, the global minimum of the curvature-penalized geodesic energy can be computed efficiently and precisely.

For the goal of applying the proposed Finsler elastica metric to image analysis, we introduce two image data-driven speed functions which are derived by steerable filters dependent on orientations. These orientation dependent speed functions are anisotropic, based on which we apply the Finsler elastica minimal path model to the applications of interactive image segmentation, perceptual grouping and tubular structure extraction. We design different algorithms for each applications

mentioned above, in terms of the smoothness and asymmetry properties. Numerical experiments on both synthetic and real images show that these applications of the proposed model indeed obtain promising results.

5.1 Introduction

Snakes or Active contour models have been considerably studied and used for object segmentation and feature extraction during almost three decades, since the pioneering work of the snakes model proposed by [Kass et al. \(1988\)](#). A snake is a parametrized curve Γ (locally) minimizing the energy:

$$E(\Gamma) = \int_0^1 (w_1 \|\Gamma'(t)\|^2 + w_2 \|\Gamma''(t)\|^2 + P(\Gamma(t))) dt$$

with appropriate boundary conditions at the endpoints $t = 0$ and $t = 1$. Γ' and Γ'' are the first and second order derivatives of curve Γ respectively. Positive constants w_1 and w_2 relate to the elasticity and rigidity of the curve Γ , hence weight its internal forces. This approach models contours as curves Γ locally minimizing an objective energy functional E consisting of an internal and an external force. The internal force terms depend on the first and second order derivatives of the curves (snakes), and respectively account for a prior of small length and of low curvature of the contours. The external force is derived from a potential function P , depending on image features like gradient magnitude, and designed to attracting the active contours or snakes to the image features of interest such as object boundaries.

The drawbacks of the classical active contours model proposed by [Kass et al. \(1988\)](#) are its sensitivity to initialization, the difficulty of handling topological changes, and of minimizing the strongly non-convex path energy as discussed in ([Cohen and Kimmel, 1997](#)). Regarding initialization, the snakes model requires an initial guess close to the desired image features, and preferably enclosing them because energy minimization tends to shorten the snakes. The introduction of an expanding balloon force allows to be less demanding on the initial curve given inside the objective region ([Cohen, 1991](#)). The issue of topology changes led, on the other hand, to the development of active contour methods, which represent object boundaries as the zero level set of the solution to a PDE ([Caselles et al., 1993, 1997](#); [Malladi et al., 1994](#); [Osher and Sethian, 1988](#); [Yezzi et al.](#)).

The difficulty of minimizing the non-convex snakes energy ([Kass et al., 1988](#)) leads to important practical problems, since the curve optimization procedure is often stuck at local minima of the energy functional, making the results sensitive to curve initialization and image noise. This is still the case for the level set approach on geodesic active contours ([Caselles et al., 1997](#); [Malladi et al., 1995](#)). To address this local minimum sensitivity issue, [Cohen and Kimmel \(1997\)](#) proposed an Eikonal PDE based minimal path model to find the global minimum of the geodesic active contours energy ([Caselles et al., 1997](#)), in which the penalty associated to the second order derivative of the curve was removed from the snakes energy. Thanks to this simplification, a fast, reliable and globally optimal numerical method allows to find the energy minimizing curve with prescribed endpoints; namely the

fast marching method (Sethian, 1999), based on the formalism of viscosity solutions to Eikonal PDE. These mathematical and algorithmic guarantees of Cohen and Kimmel's minimal path model have important practical consequences, leading to various approaches for image analysis and medical imaging (Cohen, 2001; Deschamps and Cohen, 2001; Peyré et al., 2010).

In the basic formulations of the minimal paths based interactive image segmentation models (Appia and Yezzi, 2011; Appleton and Talbot, 2005; Mille and Cohen, 2009; Mille et al., 2014), the common proposal is that the object boundaries were delineated by a set of minimal paths constrained by user-specified points. In general, these points serve as constraints for minimal paths. In (Benmansour and Cohen, 2011; Li and Yezzi, 2007), tubular structures were extracted under the form of minimal paths over the radius-lifted domain. Therefore, each extracted minimal path consists of both the centreline positions and the corresponding thickness values of a vessel.

In order to reduce the user intervention, Benmansour and Cohen (2009) proposed a growing minimal path model for object segmentation with unknown endpoints. This model can recursively detect keypoints, each of which can be taken as new initial source point for the fast marching front propagation. Thus this model requires only one user-provided point to start the keypoints detection procedure. Kaul et al. (2012) applied the growing minimal path model for extraction of complicated curves with arbitrary topologies and developed criteria to stop the growth of the minimal paths. Rouchdy and Cohen (2013) proposed a minimal path voting model for vessel tree extraction by a voting score map constructed from a set of geodesics with a common initial source point.

Recently, improvements of the minimal path model are devoted to extend the isotropic Riemannian metrics to the more general anisotropic Riemannian metrics by taking into account the orientation of the curves (Benmansour and Cohen, 2011; Bougleux et al., 2008; Jbabdi et al., 2008). Such orientation enhancement can solve, for example some shortcuts problems suffered by the isotropic metrics based minimal path models (Cohen and Kimmel, 1997; Li and Yezzi, 2007). Kimmel and Sethian (2001) designed an orientation-lifted Riemannian metric for the application of path planning, providing an alternative way to take advantages of the path orientation. This isotropic orientation-lifted Riemannian metric (Kimmel and Sethian, 2001) was built over the higher dimensional domain by adding an extra orientation space to the image domain.

Schoenemann et al. (2009, 2012) proposed a model to deal with the problems of using curvature regularization for region-based image segmentation by a graph-based combinational optimization method. This curvature regularization model can find a solution that corresponds to the globally optimal segmentation in the sense that it does not rely on initialization, and has proven to obtain promising segmentation

and inpainting results especially for objects with long and thin structures. [Ulen et al. \(2015\)](#) proposed a curvature and torsion regularized shortest path model for extracting thin and long structures such as coronary artery segmentation, where the curvature and torsion properties are approximately computed by B-Splines. Their energy functional including curvature and torsion penalization terms can be efficiently optimized by line graphs and Dijkstra's algorithm ([Dijkstra, 1959](#)).

([Tai et al., 2011](#)) presented an efficient method to solve the minimization problem of the Euler elastica energy, and demonstrated that this fast method can be applied to image denoising, image inpainting, and image zooming. Other curvature-penalized approaches of interest include the curvature regularization based image segmentation models such as ([El-Zehiry and Grady, 2010](#); [Schoenemann et al., 2011](#); [Zhu et al., 2013](#)), curvature-regularized inpainting model ([Shen et al., 2003](#))

Sub-Riemannian Geodesic Models

[Bekkers et al. \(2015a,b\)](#) considered a data-driven extension of the sub-Riemannian metric on $SE(2)$, which shows that the sub-Riemannian structure outperforms the isotropic Riemannian structures on $SE(2)$ in the application of retinal vessel tracking. The cusp surface is also analysed in this paper. However, the numerical solver used by [Bekkers et al. \(2015a,b\)](#) is based on a PDE approach with an upwind discretization and iterative evolution scheme thus requiring expensive computation time. To solve this problem, [Sanguinetti et al. \(2015\)](#) proposed to use the state of art anisotropic fast marching method ([Mirebeau, 2014a](#)) as the numerical solver of the Eikonal equation that is associated to the data-driven sub-Riemannian metrics. They also showed that an anisotropic Riemannian metric with a very high anisotropy ratio can approximate well the sub-Riemannian metric. Later on, this sub-Riemannian fast marching-based numerical tool is employed to compute the geodesic distance associated to the sub-Riemannian metrics in $SO(3)$ ([Mashtakov et al., 2016](#)). The sub-Riemannian geodesic model ([Citti and Sarti, 2006](#); [Petitot, 2003](#)) reintroduced curvature penalization to the geodesic energy, similarly to the Euler elastica bending energy ([Nitzberg and Mumford, 1990](#)) considered in this chapter, yet it differs in two ways: firstly, Euler elastica bending energy involves the squared curvature, a stronger penalization than the sub-Riemannian geodesic energy which is roughly linear in the curvature. Secondly, minimal geodesics for sub-Riemannian geodesic model occasionally feature *cusps*¹, which sometimes may not be desirable for the applications of interest. In contrast, Euler elastica curves can avoid such cusps.

¹The cusps of the sub-Riemannian geodesic have been deeply studied in ([Bekkers et al., 2015b](#); [Boscain et al., 2010](#); [Duits et al., 2013, 2014](#)). They can be used for the geometric keypoints detection.

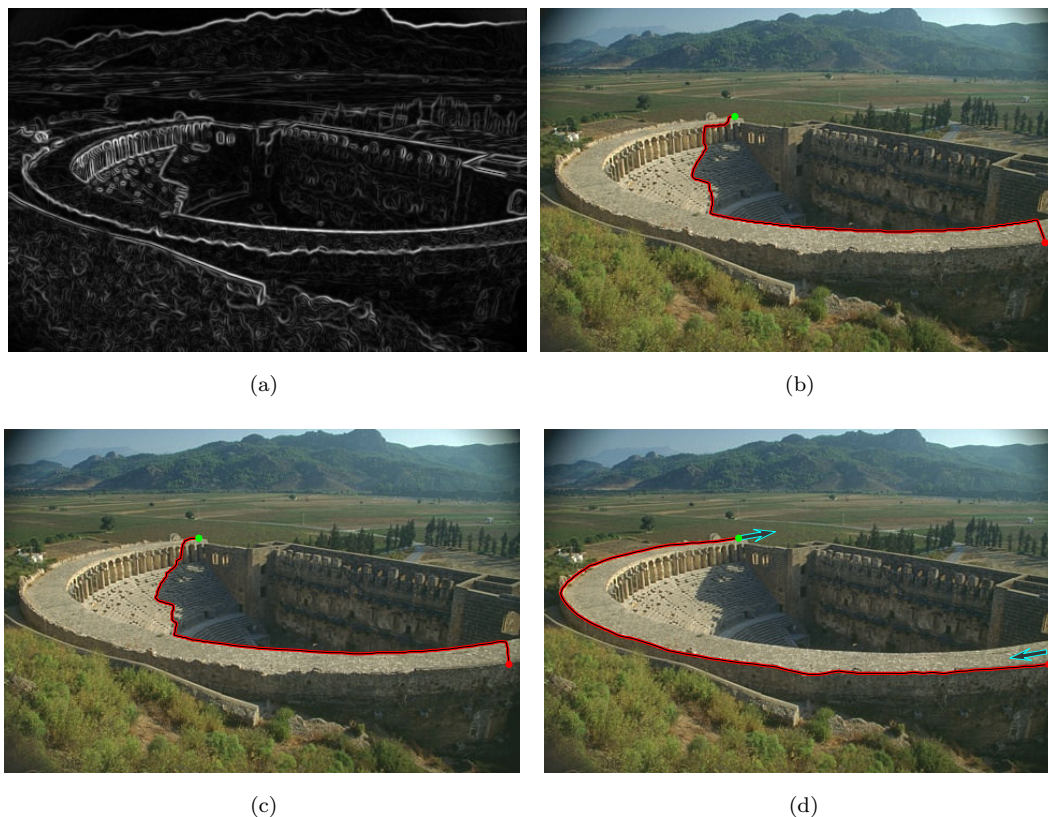


FIGURE 5.1: Minimal path extraction results using different metrics. (a) edge saliency map, (b): minimal path with isotropic Riemannian metric, (c) minimal path with anisotropic Riemannian metric, (d) minimal path with the proposed Finsler elastica metric. Red curves are the extracted minimal paths with initial source positions and end positions indicated by red and green dots respectively. Arrows in (d) indicate the tangents.

5.1.1 Motivation

In contrast with the classical snakes energy (Kass et al., 1988), Eikonal PDE-based minimal path methods are first-order models, which do not penalize the second-order derivative of the curves, i.e. the curvature, and therefore do not enforce the smoothness of the extracted geodesics, leading sometimes to undesired results as shown in Fig. 5.1, in which we would like to extract a boundary as smooth as possible between two given points indicated by red and green dots. In Fig. 5.1a we show the edge saliency map. Figs. 5.1b and 5.1c are the extracted minimal paths using the isotropic Riemannian metric (Cohen and Kimmel, 1997) and the anisotropic Riemannian metric (Bougleux et al., 2008) respectively, both of which are unable to find expected smooth boundaries and suffer from shortcuts problem due to the lack of curvature penalization in these metrics. In contrast, the minimal path model presented in this section reintroduces curvature, in the form of weighted Euler elastica curves as studied in (Mumford, 1994; Nitzberg and Mumford, 1990). Therefore the geodesics extracted by the proposed model

can sketch the smooth object boundary, as demonstrated in Fig. 5.1d, with arrows indicating the corresponding tangents at the given positions.

The main contents of this chapter were presented at the BMVC 2015 conference (Chen et al., 2015) and the CVPR 2016 conference (Chen et al., 2016b).

5.1.2 Contributions

The contribution of this chapter is three fold:

1. Firstly, we propose a novel globally minimized minimal path model, namely the Finsler elastica minimal path model, with curvature penalty and Finsler metric. We establish the connection between the Euler elastica and minimal path with respect to an orientation-lifted Finsler elastica metric. With an adequate numerical implementation, leveraging orientation lifting, asymmetric Finsler metrics and anisotropic fast marching method, the proposed model still allows to find the globally minimizing curves with prescribed points and tangents.
2. As a second contribution, we present the mathematical convergence analysis of the Finsler elastica metrics, and of their corresponding Finsler elastica minimal paths. Furthermore, we discuss numerical options for geodesic distance and minimal paths computation, and settle for an adaptation of the fast marching method proposed by Mirebeau (2014b).
3. Finally, we provide two types of image data-driven speed functions computed by steerable filters. These data-driven speed functions are therefore orientation dependent, by which we apply the proposed Finsler elastica minimal path model to the applications of closed contour detection, perceptual grouping and tubular structure extraction. Closed contour detection is performed in an interactive manner, where the contour is concatenated by a set of piecewise smooth geodesics. It connects a set of user-provided orientation-lifted points. With a procedure similar to the closed contour detection method, we apply our model to perceptual grouping based on the criteria of connectivity and smoothness. Moreover, we also provide a method to simplify the tubular structure extraction.

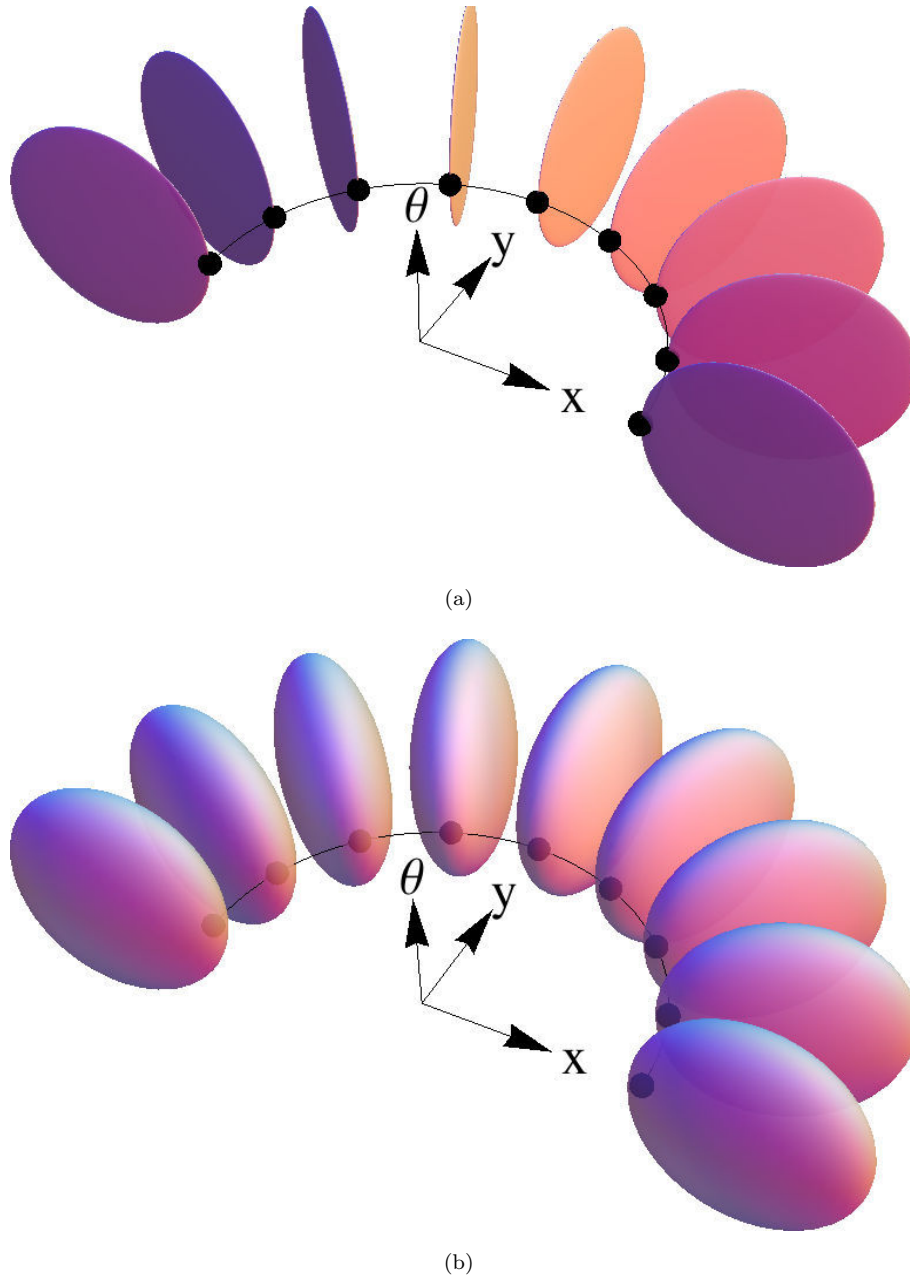


FIGURE 5.2: Visualization for the metrics \mathcal{F}^∞ and \mathcal{F}^λ with $\alpha = 1$ by Tissot's indicatrix. (a): Tissot's indicatrix for the metric \mathcal{F}^∞ (5.12) with $\alpha = 1$ are flat 2D disks embedded in 3D space, aligned with the direction \mathbf{v}_θ (several directions θ are shown). (b): Tissot's indicatrix for the Finsler elastica metrics \mathcal{F}^λ are ellipsoids, which flatten and approximate a limit disk as $\lambda \rightarrow \infty$.

5.2 Finsler Elastica Minimal Path Model

In this section, we present the core contribution of this paper: the orientation-lifted Finsler metric embedding curvature penalty term, defined over the orientation-lifted domain $\bar{\Omega} = \Omega \times \mathbb{S}^1 \subset \mathbb{R}^3$, where $\mathbb{S}^1 = [0, 2\pi)$ denotes the angle space with periodic boundary conditions and $\Omega \subset \mathbb{R}^2$ denotes the image domain.

5.2.1 Geodesic Energy Interpretation of the Euler Elastica Bending Energy via a Finsler Metric

The Euler elastica curves were introduced to the field of computer vision by [Nitzberg and Mumford \(1990\)](#) and [Mumford \(1994\)](#). They minimized the following elastica bending energy:

$$\mathcal{L}(\hat{\Gamma}) := \int_0^L \frac{1}{\Phi_0(\hat{\Gamma}(s))} (1 + \alpha \kappa^2(s)) ds, \quad (5.1)$$

where $\hat{\Gamma} : [0, L] \rightarrow \Omega$ is a regular curve with non-vanishing velocity, κ is the curvature of curve $\hat{\Gamma}$, L is the classical Euclidean curve length and s is the arc-length. Parameter $\alpha > 0$ is a constant. Φ_0 is an image data-driven speed function, which takes large values around the interesting image features and low values otherwise.

For the sake of simplicity in the coming calculus, we set $\Phi_0 \equiv 1$, yielding the simplified Euler elastica bending energy:

$$\ell(\hat{\Gamma}) = \int_0^L (1 + \alpha \kappa^2(s)) ds, \quad (5.2)$$

where the general case will be studied in Section [5.2.4](#).

The goal of this section is to cast the Euler elastica bending energy ℓ ([5.2](#)) in the form of curve length with respect to a relevant asymmetric Finsler metric. We firstly transform the elastica problem into finding a geodesic in an orientation-lifted space. For this purpose, we denote by

$$\mathbf{v}_\theta = (\cos \theta, \sin \theta) \quad (5.3)$$

the unit vector corresponding to $\theta \in \mathbb{S}^1$.

Let $\Gamma : [0, 1] \rightarrow \Omega$ be a regular curve with non-vanishing velocity and $\gamma = (\Gamma, \theta) : [0, 1] \rightarrow \bar{\Omega}$ be its canonical orientation lifting. For any $t \in [0, 1]$, $\theta(t)$ is defined as being such that:

$$\mathbf{v}_{\theta(t)} := \frac{\Gamma'(t)}{\|\Gamma'(t)\|}. \quad (5.4)$$

According to the definition of \mathbf{v}_θ in ([5.3](#)), one has

$$\begin{aligned} \left(\frac{\Gamma'(t)}{\|\Gamma'(t)\|} \right)^\perp &= (\mathbf{v}_{\theta(t)})^\perp \\ &= (-\sin \theta(t), \cos \theta(t)), \end{aligned} \quad (5.5)$$

where \mathbf{u}^\perp denotes the the vector that is perpendicular to a vector \mathbf{u} .

It is known that

$$\frac{d}{dt} \left(\frac{\Gamma'(t)}{\|\Gamma'(t)\|} \right) = \kappa(t) \|\Gamma'(t)\| \left(\frac{\Gamma'(t)}{\|\Gamma'(t)\|} \right)^\perp, \quad (5.6)$$

where κ is the curvature of path Γ . Then we have the following equations:

$$\begin{aligned} \frac{d}{dt} \mathbf{v}_{\theta(t)} &= \frac{d}{dt} (\cos \theta(t), \sin \theta(t)) \\ &= \theta'(t) (-\sin \theta(t), \cos \theta(t)) \\ &= \theta'(t) \left(\frac{\Gamma'(t)}{\|\Gamma'(t)\|} \right)^\perp. \end{aligned}$$

Thus, using (5.4) and (5.6), we have

$$\theta'(t) \left(\frac{\Gamma'(t)}{\|\Gamma'(t)\|} \right)^\perp = \kappa(t) \|\Gamma'(t)\| \left(\frac{\Gamma'(t)}{\|\Gamma'(t)\|} \right)^\perp, \quad (5.7)$$

which yields to

$$\theta'(t) = \kappa(t) \|\Gamma'(t)\|, \quad \forall t \in [0, 1]. \quad (5.8)$$

Using (5.4) and (5.8), one has

$$\begin{aligned} \ell(\Gamma) &= \int_0^L (1 + \alpha \kappa^2(s)) ds \\ &= \int_0^1 \left(1 + \alpha \frac{|\theta'(t)|^2}{\|\Gamma'(t)\|^2} \right) \|\Gamma'(t)\| dt \\ &= \int_0^1 \left(\|\Gamma'(t)\| + \alpha \frac{|\theta'(t)|^2}{\|\Gamma'(t)\|} \right) dt, \end{aligned} \quad (5.9)$$

where the Euclidean arc-length is defined as

$$ds = \|\Gamma'(t)\| dt.$$

By the definition of γ , for any $t \in [0, 1]$ we have $\gamma'(t) = (\Gamma'(t), \theta'(t))$ and

$$\ell(\Gamma) = \int_0^1 \mathcal{F}^\infty(\gamma(t), \gamma'(t)) dt, \quad (5.10)$$

where we define the Finsler metric \mathcal{F}^∞ on the orientation-lifted domain $\bar{\Omega}$ by

$$\mathcal{F}^\infty(\bar{\mathbf{x}}, \bar{\mathbf{u}}) := \begin{cases} \|\mathbf{u}\| + \alpha \frac{|\nu|^2}{\|\mathbf{u}\|}, & \text{if } \mathbf{u} \propto \mathbf{v}_\theta, \\ +\infty, & \text{otherwise.} \end{cases} \quad (5.11)$$

for any orientation-lifted point $\bar{\mathbf{x}} = (\mathbf{x}, \theta) \in \bar{\Omega}$, any vector $\bar{\mathbf{u}} = (\mathbf{u}, \nu) \in \mathbb{R}^2 \times \mathbb{R}$ in the tangent space, and where α denotes positive collinearity. Note that any other lifting $\tilde{\gamma}(t) = (\Gamma(t), \tilde{\theta}(t))$ of $\Gamma(t)$ would by construction of (5.11) have infinite energy, i.e., $\ell(\Gamma) = \infty$.

5.2.2 λ Penalized Asymmetric Finsler Elastica Metric \mathcal{F}^λ

The Finsler metric \mathcal{F}^∞ (5.11) is too singular to compute the global minimum of ℓ (5.2) by directly applying the numerical algorithm such as the fast marching method (Mirebeau, 2014b). Hence we introduce a family of orientation-lifted Finsler metrics over the orientation-lifted domain $\bar{\Omega}$, depending on a penalization parameter $\lambda \gg 1$ as follows:

$$\mathcal{F}^\lambda(\bar{\mathbf{x}}, \bar{\mathbf{u}}) := \sqrt{\lambda^2 \|\mathbf{u}\|^2 + 2\alpha\lambda|\nu|^2} - (\lambda - 1)\langle \mathbf{v}_\theta, \mathbf{u} \rangle, \quad (5.12)$$

for any orientation-lifted point $\bar{\mathbf{x}} = (\mathbf{x}, \theta) \in \bar{\Omega}$ and any vector $\bar{\mathbf{u}} = (\mathbf{u}, \nu) \in \mathbb{R}^2 \times \mathbb{R}$, and where $\mathbf{v}_\theta = (\cos \theta, \sin \theta)$ is the unit vector associated to θ which denotes the position of $\bar{\mathbf{x}}$ in the orientation space \mathbb{S}^1 .

As $\lambda \rightarrow \infty$, the λ penalized Finsler elastica metric \mathcal{F}^λ can be expressed as:

$$\begin{aligned} \mathcal{F}^\lambda(\bar{\mathbf{x}}, \bar{\mathbf{u}}) &= \sqrt{\lambda^2 \|\mathbf{u}\|^2 + 2\alpha\lambda|\nu|^2} - (\lambda - 1)\langle \mathbf{v}_\theta, \mathbf{u} \rangle \\ &= \lambda \|\mathbf{u}\| \sqrt{1 + \alpha \frac{2|\nu|^2}{\lambda \|\mathbf{u}\|^2}} - (\lambda - 1)\langle \mathbf{v}_\theta, \mathbf{u} \rangle \\ &= \lambda \|\mathbf{u}\| \left(1 + \frac{\alpha|\nu|^2}{\lambda \|\mathbf{u}\|^2} + \mathcal{O}\left(\frac{1}{\lambda^2}\right)\right) - (\lambda - 1)\langle \mathbf{v}_\theta, \mathbf{u} \rangle \\ &= \|\mathbf{u}\| + \frac{\alpha|\nu|^2}{\|\mathbf{u}\|} + (\lambda - 1)(\|\mathbf{u}\| - \langle \mathbf{v}_\theta, \mathbf{u} \rangle) + \mathcal{O}(\lambda^{-1}) \end{aligned} \quad (5.13)$$

The term $\|\mathbf{u}\| - \langle \mathbf{v}_\theta, \mathbf{u} \rangle$ will vanish if vector \mathbf{u} is positively proportional to \mathbf{v}_θ . Therefore, one has for any $\bar{\mathbf{x}}$ and any $\bar{\mathbf{u}}$

$$\mathcal{F}^\lambda(\bar{\mathbf{x}}, \bar{\mathbf{u}}) \rightarrow \mathcal{F}^\infty(\bar{\mathbf{x}}, \bar{\mathbf{u}}), \quad \text{as } \lambda \rightarrow \infty.$$

The Finsler elastica metric \mathcal{F}^λ (5.12) has precisely the required form formulated in (2.72), with tensor field $\mathcal{M} := \mathcal{M}_F$ as:

$$\mathcal{M}_F(\bar{\mathbf{x}}) = \begin{pmatrix} \lambda^2 & 0 & 0 \\ 0 & \lambda^2 & 0 \\ 0 & 0 & 2\alpha\lambda \end{pmatrix} \quad (5.14)$$

and vector field $\vec{\omega} := \vec{\omega}_F$

$$\vec{\omega}_F(\bar{\mathbf{x}}) = (\lambda - 1)(\mathbf{v}_\theta, 0), \quad (5.15)$$

for any $\bar{\mathbf{x}} = (\mathbf{x}, \theta) \in \bar{\Omega}$. Note that the definiteness constraint (2.73) is satisfied:

$$\langle \vec{\omega}_F(\bar{\mathbf{x}}), \mathcal{M}_F^{-1}(\bar{\mathbf{x}}) \vec{\omega}_F(\bar{\mathbf{x}}) \rangle = (1 - \lambda^{-1})^2 < 1, \quad \forall \bar{\mathbf{x}} \in \bar{\Omega} \text{ and } \lambda > 1.$$

The anisotropy ratio $\mu(\mathcal{F})$ characterizes the distortion between different orientations induced by a metric \mathcal{F} on a domain $\bar{\Omega}$. Letting $\bar{\mathbf{x}} = (\mathbf{x}, \theta) \in \bar{\Omega}$, the anisotropy ratio $\mu(\mathcal{F}^\lambda)$ of the Finsler elastica metric \mathcal{F}^λ (5.12) is defined by:

$$\mu(\mathcal{F}^\lambda) := \sup_{\bar{\mathbf{x}} \in \bar{\Omega}} \left\{ \max_{\|\bar{\mathbf{w}}\|=\|\bar{\mathbf{v}}\|=1} \left\{ \frac{\mathcal{F}_{\bar{\mathbf{x}}}^\lambda(\bar{\mathbf{w}})}{\mathcal{F}_{\bar{\mathbf{x}}}^\lambda(\bar{\mathbf{v}})} \right\} \right\}, \quad (5.16)$$

where the norm $\mathcal{F}_{\bar{\mathbf{x}}}^\lambda(\cdot) := \mathcal{F}^\lambda(\bar{\mathbf{x}}, \cdot)$. As an example, for the Finsler elastica metric \mathcal{F}^λ defined in (5.12) with $\lambda \geq 2$ and $\alpha = 1$, we can show that $\mu(\mathcal{F}^\lambda)$ in (5.16) can be obtained by choosing $\bar{\mathbf{w}} = (-\mathbf{v}_\theta, 0)$ and $\bar{\mathbf{v}} = (\mathbf{v}_\theta, 0)$, so that

$$\mu(\mathcal{F}^\lambda) = 2\lambda - 1.$$

Moreover, one can define the *physical* anisotropy ratio of the Finsler elastica metric \mathcal{F}^λ defined in (5.12) by replacing by $\bar{\mathbf{w}}_s = (\mathbf{w}, 0)$ and $\bar{\mathbf{v}}_s = (\mathbf{v}, 0)$ the variables $\bar{\mathbf{w}}$ and $\bar{\mathbf{v}}$. In this case, for any α , the physical anisotropy ratio is equal to $2\lambda - 1$ and only depends on λ .

A crucial object for studying and visualizing the geometry distortion induced by a metric is Tissot's indicatrix defined as the collection of unit balls in the tangent space. For point $\bar{\mathbf{x}} = (\mathbf{x}, \theta) \in \bar{\Omega}$ and $\lambda \in [1, \infty)$, we define the unit balls for metrics \mathcal{F}^∞ and \mathcal{F}^λ respectively by

$$B_{\bar{\mathbf{x}}}^\infty := \{\bar{\mathbf{u}} = (\mathbf{u}, \nu) \in \mathbb{R}^2 \times \mathbb{R}; \mathcal{F}^\infty(\bar{\mathbf{x}}, \bar{\mathbf{u}}) \leq 1\}. \quad (5.17)$$

and

$$B_{\bar{\mathbf{x}}}^\lambda := \{\bar{\mathbf{u}} = (\mathbf{u}, \nu) \in \mathbb{R}^2 \times \mathbb{R}; \mathcal{F}^\lambda(\bar{\mathbf{x}}, \bar{\mathbf{u}}) \leq 1\}. \quad (5.18)$$

Then any tangent $\bar{\mathbf{u}} = (\mathbf{u}, \nu) \in B_{\bar{\mathbf{x}}}^\infty$ is characterized by:

$$u_\perp = 0, \quad u_\parallel > 0, \quad \text{and} \quad u_\parallel + \alpha \frac{|\nu|^2}{u_\parallel} \leq 1, \quad (5.19)$$

where we introduce u_\parallel and u_\perp as follows:

$$u_\parallel := \langle \mathbf{u}, \mathbf{v}_\theta \rangle, \quad u_\perp := \langle \mathbf{u}, \mathbf{v}_\theta^\perp \rangle.$$

Using (5.19), one has

$$\left(u_\parallel - \frac{1}{2} \right)^2 + \alpha |\nu|^2 \leq \frac{1}{4}. \quad (5.20)$$

Thus $B_{\bar{\mathbf{x}}}^\infty$ is a flat 2D ellipse embedded in the 3D tangent space, and containing the origin on its boundary. Particularly, when $\alpha = 1$, $B_{\bar{\mathbf{x}}}^\infty$ turns to a flat 2D disk of radius $1/2$ as shown in Fig. 5.2(a).

On the other hand, when $\lambda < \infty$, a short computation shows that vector $\bar{\mathbf{u}} = (\mathbf{u}, \nu) \in B_{\bar{\mathbf{x}}}^\lambda$ is characterized by a quadratic equation

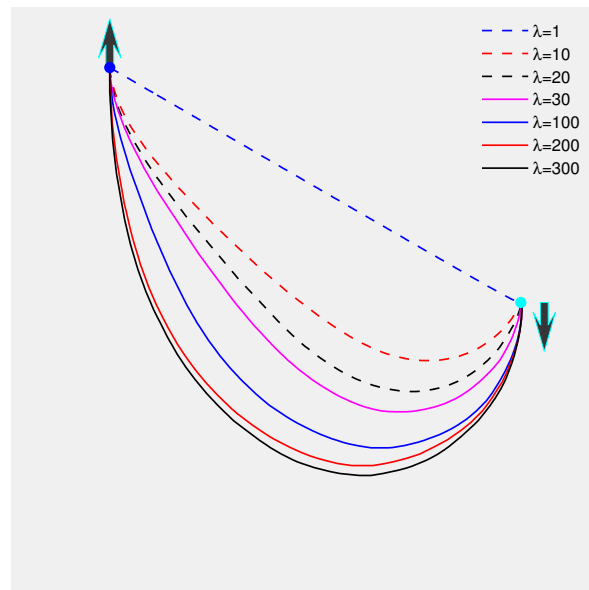
$$\frac{\lambda}{2} u_\perp^2 + a_\lambda \left(u_\parallel - \frac{b_\lambda}{2} \right)^2 + \alpha |\nu|^2 \leq \frac{c_\lambda}{4}, \quad (5.21)$$

where $a_\lambda, b_\lambda, c_\lambda$ are all $1 + \mathcal{O}(1/\lambda)$. Hence $B_{\bar{\mathbf{x}}}^\lambda$ is an ellipsoid, for instance see Fig. 5.2b with $\alpha = 1$, almost flat in the direction of \mathbf{v}_θ^\perp due to the large factor $\lambda/2$, which converges to the flat disk $B_{\bar{\mathbf{x}}}^\infty$ in the Hausdorff distance as $\lambda \rightarrow \infty$.

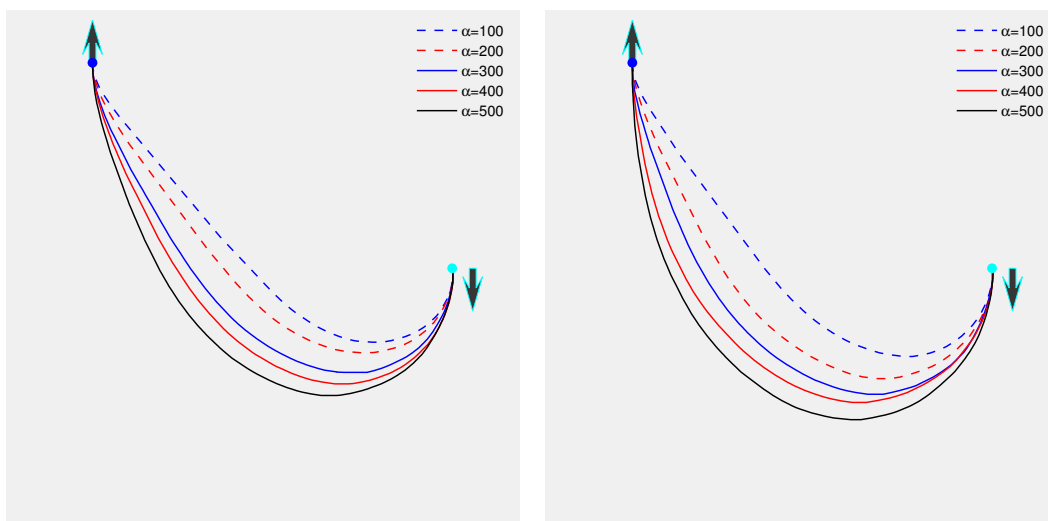
Tissot's indicatrix is also the control set in the optimal control interpretation of the Eikonal PDE (2.70). The Hausdorff convergence of the control sets guarantees that the minimal action map and minimal paths for the metric \mathcal{F}^λ converge towards those of \mathcal{F}^∞ as $\lambda \rightarrow \infty$. Elements of proof of convergence can be found in Appendix B.

5.2.3 Numerical Implementations

Numerically, anisotropy is related to the problem stiffness, hence to its difficulty. The classical fast marching methods (Sethian, 1999; Tsitsiklis, 1995) using the square formed neighbourhood S have difficulty to deal with the computation of geodesic distance maps with respect to anisotropic metrics, especially when the anisotropy gets large. An adaptive construction method of such stencils S was introduced in (Mirebeau, 2014a) for anisotropic 3D Riemannian metric, and in (Mirebeau, 2014b) for arbitrary anisotropic 2D Finsler metric, providing that the stencils or mesh $S(\mathbf{x})$ at each point $\mathbf{x} \in \Omega$ or $\bar{\Omega}$ satisfies some geometric acuteness property depending on the local metric $\mathcal{F}(\mathbf{x}, \cdot)$. Such adaptive stencils-based fast marching methods lead to breakthrough improvements in terms of computation time and accuracy for strongly anisotropic geodesic metrics. When the above mentioned geometric properties do not hold, the fast marching method is in principle not applicable, and slower multiple pass methods must be used instead such as the Adaptive Gauss Siedel Iteration (AGSI) of Bornemann and Rasch (2006). The present paper involves the 3D Finsler metric \mathcal{F}^λ (5.12), for which we constructed stencils by adapting the 2D construction of Mirebeau (2014b). Although these stencils lack the geometric acuteness condition, we found that the fast marching method still provided good approximations of the paths, while vastly improving computation performance.



(a)



(b)

(c)

FIGURE 5.3: Approximating Euler elastica curves by Finsler elastica minimal paths with uniform speed. **(a)** Finsler elastica minimal paths with $\alpha = 500$ and different values of λ . **(b)** and **(c)** Finsler elastica minimal paths with $\lambda = 100$ and $\lambda = 300$ respectively, and different values of α .

Note that whenever we mention fast marching method in the remaining part of this chapter, we mean the fast marching method with adaptive stencils proposed by Mirebeau (2014b).

In Table 5.1, we show the computation time and the average number of Hopf-Lax updates required for each grid point by the adaptive stencils based fast marching method (Mirebeau, 2014b) for $\alpha = 500$ and different values of λ on a $300^2 \times 108$

TABLE 5.1: Computation time (in seconds) and average number of Hopf-Lax updates required for each grid point by fast marching method with $\alpha = 500$ and different values of λ on a $300^2 \times 108$ grid.

λ	1	10	20	30	100	200	300	500	1000
time	13.9s	25.3s	27.3s	27.7s	31.7s	33.9s	34.7s	35.0s	36.8s
number	3	5.49	6.06	6.49	7.27	7.82	7.83	7.92	8.12

grid. This experiment was performed with a C++ implementation running on a standard 2.7 GHz Intel I7 laptop with 16 Gb RAM.

We observe on Table 5.1 a logarithmic dependence of computation time and average number of the Hopf-Lax updates per grid point with respect to anisotropy. These observations agree with the complexity analysis of the fast marching method presented in (Mirebeau, 2014b), yielding the upper bound $\mathcal{O}(N \ln^3 \mu + N \ln N)$, depending poly-logarithmically on the anisotropy ratio μ (5.16), and quasi-linearly on the number N of discretization points in the orientation-lifted domain $\bar{\Omega}$. In contrast, numerical methods such as (Sethian and Vladimirsky, 2001) displaying a polynomial complexity $\mathcal{O}(\mu^2 N \ln N)$ in the anisotropy ratio would be unworkable. The iterative AGSI method (Bornemann and Rasch, 2006), on the other hand, requires hundreds of evaluations of the Hopf-Lax operator (2.86) per grid point to converge for large anisotropies, which also leads to prohibitive computation time, thus impractical. For $\lambda = 30$ or 100 , the average numbers of the Hopf-Lax updates per grid required by the AGSI method are approximately 86 and 182 respectively, while the numbers of Hopf-Lax from the fast marching method are only 6.49 and 7.27 respectively (see Table 5.1).

In Fig. 5.3(a), we show different Finsler elastica minimal paths, computed by the fast marching method (Mirebeau, 2014b), with $\alpha = 500$ (see (5.12)) and different values of λ . The arrows indicate the initial and end points tangents. Cyan point is initial position and blue point is end position. In Figs. 5.3b and 5.3c, we show the Finsler elastica minimal paths for different values of α , with $\lambda = 100$ and $\lambda = 300$ respectively. In this experiment, we set the angle resolution to be $\theta_s = 2\pi/108$ and the image size is 300×300 . When $\lambda = 1$, the metric \mathcal{F}^λ is constant over the domain $\bar{\Omega}$ and degenerates to the isotropic orientation-lifted metric \mathcal{R}^I in (2.62), since the coefficient in front of the term $\langle \mathbf{v}_\theta, \cdot \rangle$ in (5.12) vanishes. Hence the minimal geodesics are straight lines, see Fig. 5.3a, that do not align with the prescribed endpoints tangents. From Fig. 5.3, one can point out that as λ and α increasing, curvature penalization forces the extracted paths to gradually align with the prescribed endpoints tangents and take the elastica shape.

5.2.4 Image Data-Driven Finsler Elastica Metric \mathcal{P}

We set the data-driven speed function $\Phi_0 \equiv 1$ in Section 5.2.1 for the sake of simplicity. In the general case, in order to apply the proposed Finsler elastica minimal path model to image analysis applications, the metric \mathcal{F}^∞ (5.11) and its approximation \mathcal{F}^λ (5.12) should be respectively replaced by $\Phi_0^{-1}\mathcal{F}^\infty$ and $\Phi_0^{-1}\mathcal{F}^\lambda$. Furthermore, in order to take into account the orientation information, we use an orientation dependent speed function $\Phi : \bar{\Omega} \rightarrow \mathbb{R}^+$ to replace Φ_0 . In this case, the data-driven Finsler elastica metric can be defined by

$$\mathcal{P}(\bar{\mathbf{x}}, \bar{\mathbf{u}}) = \frac{1}{\Phi(\bar{\mathbf{x}})} \mathcal{F}^\lambda(\bar{\mathbf{x}}, \bar{\mathbf{u}}), \quad \forall \bar{\mathbf{x}} \in \bar{\Omega}, \forall \bar{\mathbf{u}} \in \mathbb{R}^3, \quad (5.22)$$

and minimizing the general Euler elastica bending energy \mathcal{L} in (5.1) is approximated for large values of λ by minimizing

$$\begin{aligned} \mathcal{L}(\Gamma) &= \int_0^1 \frac{1}{\Phi(\gamma(t))} \mathcal{F}^\lambda(\gamma(t), \gamma'(t)) dt \\ &= \int_0^1 \mathcal{P}(\gamma(t), \gamma'(t)) dt, \end{aligned}$$

where γ is the orientation lifted curve of Γ .

Based on the data-driven function Φ , the metric \mathcal{P} is asymmetric in the sense that for any vector $\bar{\mathbf{u}} \neq \mathbf{0}$, one has

$$\mathcal{P}(\bar{\mathbf{x}}, \bar{\mathbf{u}}) \neq \mathcal{P}(\bar{\mathbf{x}}, -\bar{\mathbf{u}}), \quad \forall \bar{\mathbf{x}} \in \bar{\Omega}. \quad (5.23)$$

This asymmetric property can help to build a closed contour passing a collection of orientation-lifted points as discussed in Section 5.4.1.

The minimal action map associated to data-driven Finsler elastica metric \mathcal{P} and initial source point $\bar{\mathbf{s}}$, denoted by $\mathcal{W}_{\bar{\mathbf{s}}}$, is the unique viscosity solution to the corresponding Eikonal PDE (2.70) (Lions, 1982). Specifically, we have

$$\begin{cases} \mathcal{P}_{\bar{\mathbf{x}}}^*(-\nabla \mathcal{W}_{\bar{\mathbf{s}}}(\bar{\mathbf{x}})) = 1, & \forall \bar{\mathbf{x}} \in \bar{\Omega} \setminus \{\bar{\mathbf{s}}\}, \\ \mathcal{W}_{\bar{\mathbf{s}}}(\bar{\mathbf{s}}) = 0, \end{cases} \quad (5.24)$$

where $\mathcal{P}_{\bar{\mathbf{x}}}^*$ is the dual norm of $\mathcal{P}_{\bar{\mathbf{x}}} := \mathcal{P}(\bar{\mathbf{x}}, \cdot)$ defined by (2.71). We take the fast marching method (Mirebeau, 2014b) as the Eikonal solver. When λ is sufficiently large, the spatial and angular resolutions are sufficiently small, the fixed point system (2.85) is properly solved, and the minimal paths are properly extracted by (2.76).

5.3 Computation of Data-Driven Speed Functions by Steerable Filters

In this section, we introduce two types of orientation dependent speed functions Φ for the applications of image segmentation and tubular structure extraction respectively, both of which are based on the steerable filters.

5.3.1 Steerable Edge Detector

Jacob and Unser (2004) proposed a new class of edge detection filters combining the computational framework and the steerable property. Letting G_σ be a 2D isotropic Gaussian kernel with variance σ and $\mathbf{x} = (x, y)$, the computational steerable filter F_θ^M with order M (Jacob and Unser, 2004) can be expressed as:

$$F_\theta^M(\mathbf{x}) = \sum_{\tau=1}^M \sum_{\xi=0}^{\tau} \mathcal{K}_{\tau,\xi}(\theta) \frac{\partial^{(\tau-\xi)}}{\partial x^{(\tau-\xi)}} \frac{\partial^\xi}{\partial y^\xi} G_\sigma(\mathbf{x}), \quad (5.25)$$

where $\theta \in [0, 2\pi)$ and $\mathcal{K}_{\tau,\xi}$ are orientation-dependent coefficients which can be computed in terms of some optimality criteria. Particularly when $M = 1$, the steerable filter F_θ^1 becomes the classical Canny detector (Canny, 1986). For higher order steerable filters, for example, $M = 3$ or $M = 5$, the orientation dependent responses of the filters will be more robust to noise. Therefore, we choose the steerable filter order $M = 5$ for the relevant numerical experiments. Regarding the details of the computation of $\mathcal{K}_{\tau,\xi}$, we refer to (Jacob and Unser, 2004).

A color image is regarded as a vector-valued map $\mathbf{I} : \Omega \rightarrow \mathbb{R}^3$. For each $\mathbf{x} \in \Omega$, we denote that $\mathbf{I}(\mathbf{x}) = [I_1(\mathbf{x}), I_2(\mathbf{x}), I_3(\mathbf{x})]$. In this section, we consider a multi-orientation response of color image \mathbf{I} , where the response $h : \bar{\Omega} \rightarrow \mathbb{R}^+$ can be computed by the steerable filter F_θ^M (5.25) as follows:

$$h(\mathbf{x}, \theta) = \frac{1}{3} \sum_{i=1}^3 |I_i(\mathbf{x}) * F_\theta^M(\mathbf{x})|. \quad (5.26)$$

For a gray level image $I : \Omega \rightarrow \mathbb{R}$, we have the simple computation of h :

$$h(\mathbf{x}, \theta) = |I(\mathbf{x}) * F_\theta^M(\mathbf{x})|. \quad (5.27)$$

When M is an odd number, the response $I_i * F_\theta^M$ is asymmetric with respect to $\theta \in [0, 2\pi)$, which may lead to difficult initializations for the proposed Finsler elastica minimal paths-based image analysis applications, such as boundary detection and image segmentation. Thus we remove the asymmetry of the response by using $|I_i * F_\theta^M|$ instead of $I_i * F_\theta^M$ in (5.26).

5.3.2 Multi-Orientation Optimally Oriented Flux Filter

Optimally oriented flux filter is used to extract the local geometry of the image. The oriented flux (Law and Chung, 2008) of an image $I : \Omega \rightarrow \mathbb{R}^+$, of dimension 2, is defined by the amount of the image gradient projected along the orientation \mathbf{v} flowing out from a 2D circle at point $\mathbf{x} = (x, y) \in \Omega$ with radius r :

$$f(\mathbf{x}; r, \mathbf{v}) = \int_{\partial\mathcal{C}_r} (\nabla(G_\sigma * I)(\mathbf{x} + r\mathbf{n}) \cdot \mathbf{v})(\mathbf{v} \cdot \mathbf{n}) ds, \quad (5.28)$$

where G_σ is a Gaussian with variance σ , \mathbf{n} is the outward unit normal vector along $\partial\mathcal{C}_r$, and ds is the infinitesimal length on the boundary of \mathcal{C}_r . According to the divergence theorem, one has

$$f(\mathbf{x}; r, \mathbf{v}) = \mathbf{v}^T \mathbf{Q}(\mathbf{x}, r) \mathbf{v},$$

for some symmetric matrix $\mathbf{Q}(\mathbf{x}, r)$:

$$\mathbf{Q}(\mathbf{x}, r) = \begin{pmatrix} \partial_{xx}G_\sigma & \partial_{xy}G_\sigma \\ \partial_{yx}G_\sigma & \partial_{yy}G_\sigma \end{pmatrix} * \mathbb{1}_r * I(\mathbf{x}), \quad (5.29)$$

where $\mathbb{1}_r$ is an indicator function of the circle \mathcal{C}_r .

Let $\lambda_1(\mathbf{x}, r)$ and $\lambda_2(\mathbf{x}, r)$ be the eigenvalues of symmetric matrix $\mathbf{Q}(\mathbf{x}, r)$ (5.29) and assume that $\lambda_1(\mathbf{x}, r) \geq \lambda_2(\mathbf{x}, r)$. Supposing that the intensities inside the tubular structures are darker than the background so that inside the tubular structure, one has $\lambda_1(\mathbf{x}, r^*) \gg 0$ and $\lambda_2(\mathbf{x}, r^*) \approx 0$, where r^* is the optimal scale map defined by

$$r^*(\mathbf{x}) = \arg \max_r \left\{ \frac{1}{r} \lambda_1(\mathbf{x}, r) \right\}, \quad \forall \mathbf{x} \in \Omega, \quad (5.30)$$

where $1/r$ is the scale normalized factor (Law and Chung, 2008). As shown in (Benmansour and Cohen, 2011), the optimally oriented flux filter is a steerable filter which means that we can construct the multi-orientation response function $\hat{g} : \bar{\Omega} \rightarrow \mathbb{R}$ for any $\theta \in [0, 2\pi)$ by:

$$\hat{g}(\mathbf{x}, \theta) = \mathbf{u}_\theta^T \mathbf{Q}(\mathbf{x}, r^*(\mathbf{x})) \mathbf{u}_\theta, \quad \forall \mathbf{x} \in \Omega, \quad (5.31)$$

where $\mathbf{u}_\theta = (\cos \theta, \sin \theta)^T$ is a unit vector associated to θ and r^* is the optimal scale map defined in (5.30).

Based on the multi-orientation response \hat{g} , we can obtain the desired orientation dependent function

$$g(\bar{\mathbf{x}}) = \max\{\hat{g}(\bar{\mathbf{x}}), 0\}, \quad (5.32)$$

In addition, the vesselness map $V_n : \Omega \rightarrow \mathbb{R}$, which indicates the probability of a pixel \mathbf{x} belonging to a vessel, can be calculated by:

$$V_n(\mathbf{x}) = \max \left\{ \max_r \left\{ \frac{1}{r} \lambda_1(\mathbf{x}, r) \right\}, 0 \right\}. \quad (5.33)$$

The vesselness map will be used to compute the isotropic Riemannian metric in the experiments.

Note that an alternate approach for orientation-dependent image data-driven function computation method can be found in (Bekkers et al., 2015a). In that paper, the authors make use of the multi-orientation wavelet to calculate the data-driven function.

5.3.3 Computation of the Data-Driven Speed Function Φ

Based on the orientation-dependent response functions of the steerable filters discussed in Sections 5.3.1 and 5.3.2, the speed function Φ used by Finsler elastica metric \mathcal{P} (5.2) can be computed by the response h (5.26):

$$\Phi(\mathbf{x}, \theta) = 1 + \eta \left(\frac{h(\mathbf{x}, \theta)}{\|h\|_\infty} \right)^p. \quad (5.34)$$

Similarly, based on the orientation dependent response g (5.32), one can define the speed function for tubular structure extraction by:

$$\Phi(\mathbf{x}, \theta) = 1 + \eta \left(\frac{g(\mathbf{x}, \theta)}{\|g\|_\infty} \right)^p, \quad (5.35)$$

where η, p are positive constants and $\theta \in [0, 2\pi)$. In this chapter, we use $p = 2$ for all the relevant experiments.

Since it relies on the multi-orientation response functions h (5.26) and g (5.32), the speed function Φ is symmetric in the sense that for any orientation $\theta_\pi \in [0, \pi)$, one has

$$\Phi(\mathbf{x}, \theta_\pi) = \Phi(\mathbf{x}, \theta_\pi + \pi), \quad \mathbf{x} \in \Omega.$$

5.4 Closed Contour Detection and Tubular Structure Extraction

We use the following convention in the remaining part of this paper: if $\bar{\mathbf{p}} = (\mathbf{p}, \theta)$ is a point in the orientation-lifted domain $\bar{\Omega}$, then we use $\bar{\mathbf{p}}^\dagger = (\mathbf{p}, \text{mod}((\theta + \pi), 2\pi))$



FIGURE 5.4: Steps for the closed contour detection procedure. (a) original image and all vertices in \mathcal{D} denoted by dots and arrows. (b) The first pairs of successive vertices (\bar{q}_1, \bar{q}_2) is detected. (c) The third vertex \bar{q}_3 is detected. (d) The final vertex \bar{q}_4 is detected and the closed contour detection procedure is stopped. (e) Geodesic joining \bar{q}_4 and \bar{q}_1 is tracked. (f) The final closed contour is obtained.

to denote the orientation-lifted point which has the same physical position \mathbf{p} with $\bar{\mathbf{p}}$ but opposite direction, where $\theta \in [0, 2\pi)$.

5.4.1 Closed Contour Detection as a Set of Piecewise Smooth Finsler Elastica Minimal Paths

In this section, we present an interactive image segmentation model via a closed contour detection procedure based on the Finsler elastica metric \mathcal{P} in (5.34).

Consider a collection of user-specified physical positions

$$\mathcal{H} := \{\mathbf{x}_i \in \Omega, i = 1, 2, \dots, m; m \geq 2\},$$

all of which are on the boundary of the object. The goal is to automatically find a closed contour, linking those physical points in \mathcal{H} by Finsler elastica minimal paths to form a complete boundary of the object. For this purpose, we denote the orientation-lifted collection \mathcal{D} of \mathcal{H} by

$$\mathcal{D} := \left\{ \bar{\mathbf{x}}_i = (\mathbf{x}_i, \theta_i), \bar{\mathbf{x}}_i^\dagger = (\mathbf{x}_i, \text{mod}(\theta_i + \pi, 2\pi)); \right. \\ \left. i = 1, 2, \dots, m, \text{ and } \theta_i \in [0, 2\pi) \right\}, \quad (5.36)$$

where the directions θ_i are manually specified in this section. Corresponding to each physical point $\mathbf{x}_i \in \mathcal{H}$, there exist two orientation-lifted vertices: $\bar{\mathbf{x}}_i$ and $\bar{\mathbf{x}}_i^\dagger$ in \mathcal{D} with opposite tangents. We show these vertices in Fig. 5.4(a) by blue and red dots denoting physical positions and by green arrows indicating the corresponding tangents.

We start the proposed closed contour detection method by selecting the first physical position, say \mathbf{x}_1 . The corresponding orientation-lifted vertices of \mathbf{x}_1 are denoted by $\bar{\mathbf{x}}_1, \bar{\mathbf{x}}_1^\dagger \in \mathcal{D}$. Once \mathbf{x}_1 is specified, we remove both vertices $\bar{\mathbf{x}}_1$ and $\bar{\mathbf{x}}_1^\dagger$ from \mathcal{D} . As shown in Fig. 5.4(a), $\bar{\mathbf{x}}_1$ and $\bar{\mathbf{x}}_1^\dagger$ are denoted by a red dot and two arrows with opposite directions.

Let $\bar{\mathbf{a}}^* \in \mathcal{D}$ be the closest vertex to $\bar{\mathbf{x}}_1$ in terms of curvatur penalized geodesic distance $\mathcal{W}_{\bar{\mathbf{x}}_1}$ (5.24) with respect to the Finsler elastica metric \mathcal{P} (5.22), i.e.,

$$\bar{\mathbf{a}}^* := \arg \min_{\bar{\mathbf{z}} \in \mathcal{D}} \mathcal{W}_{\bar{\mathbf{x}}_1}(\bar{\mathbf{z}}). \quad (5.37)$$

Similarly to $\bar{\mathbf{a}}^*$, the closest vertex $\bar{\mathbf{c}}^* \in \mathcal{D}$ of $\bar{\mathbf{x}}_1^\dagger$ can be detected. By these definitions, the first pair of successive vertices $(\bar{\mathbf{q}}_1, \bar{\mathbf{q}}_2)$ are determined simultaneously using the following criterion:

$$(\bar{\mathbf{q}}_1, \bar{\mathbf{q}}_2) := \begin{cases} (\bar{\mathbf{x}}_1, \bar{\mathbf{a}}^*), & \text{if } \mathcal{W}_{\bar{\mathbf{x}}_1}(\bar{\mathbf{a}}^*) < \mathcal{W}_{\bar{\mathbf{x}}_1^\dagger}(\bar{\mathbf{c}}^*), \\ (\bar{\mathbf{x}}_1^\dagger, \bar{\mathbf{c}}^*), & \text{otherwise.} \end{cases} \quad (5.38)$$

In Fig. 5.4(b), we show $\bar{\mathbf{q}}_1$ and $\bar{\mathbf{q}}_2$ by red and green dots with arrows respectively. If the minimal action map $\mathcal{W}_{\bar{\mathbf{x}}_1}$ (resp. $\mathcal{W}_{\bar{\mathbf{x}}_1^\dagger}$) is computed via the fast marching

method (Mirebeau, 2014b), vertex $\bar{\mathbf{a}}^*$ (resp. $\bar{\mathbf{c}}^*$) is the first vertex reached by the fast marching front, which is monotonically advancing. Once the first pair of successive vertices $(\bar{\mathbf{q}}_1, \bar{\mathbf{q}}_2)$ are found, the geodesic $\mathcal{C}_{\bar{\mathbf{q}}_1, \bar{\mathbf{q}}_2}$ (red curve in Fig. 5.4(b)) can be recovered using (2.76) and both $\bar{\mathbf{q}}_2, \bar{\mathbf{q}}_2^\dagger$ will be removed from \mathcal{D} .

If the number of physical points $m = 2$, the closed contour detection procedure can be stopped. The geodesic $\mathcal{C}_{\bar{\mathbf{q}}_2, \bar{\mathbf{q}}_1}$, joining $\bar{\mathbf{q}}_2$ to $\bar{\mathbf{q}}_1$, can be tracked by reversing the geodesic which is the solution to the gradient descent ODE (2.76).

If $m > 2$, we take $\bar{\mathbf{q}}_2$ as the initial source point for minimal action map $\mathcal{W}_{\bar{\mathbf{q}}_2}$. Next vertex $\bar{\mathbf{q}}_3$ can be found by

$$\bar{\mathbf{q}}_3 := \arg \min_{\bar{\mathbf{z}} \in \mathcal{D}} \mathcal{W}_{\bar{\mathbf{q}}_2}(\bar{\mathbf{z}}), \quad (5.39)$$

and remove both $\bar{\mathbf{q}}_3, \bar{\mathbf{q}}_3^\dagger$ from \mathcal{D} . Again the geodesic $\mathcal{C}_{\bar{\mathbf{q}}_2, \bar{\mathbf{q}}_3}$, linking $\bar{\mathbf{q}}_2$ to $\bar{\mathbf{q}}_3$ can be recovered, as denoted by green curve in Fig. 5.4c.

This closed contour detection procedure will stop when the final orientation-lifted point $\bar{\mathbf{q}}_m$ is found, as an example see $\bar{\mathbf{q}}_3$ in Fig. 5.4c. Then the geodesic $\mathcal{C}_{\bar{\mathbf{q}}_m, \bar{\mathbf{q}}_1}$, as the cyan curve in Fig. 5.4d, can be recovered by using the minimal action map where the initial source and end points are $\bar{\mathbf{q}}_m$ and $\bar{\mathbf{q}}_1$, respectively. The final closed contour, denoted \mathcal{C} , is defined as the concatenation of all the detected minimal paths.

This method simply matches orientation-lifted points by pairs, joining a vertex to the remaining nearest neighbour with respect to the curvature-penalized geodesic distance, so as to form a closed contour located at the expected object boundaries. Note importantly, that the obtained piecewise geodesic contour is *smooth* (C^1 differentiable) since the initial source and end orientation-lifted points of consecutive geodesics have both matching positions \mathbf{q}_i and orientations θ_i . In fact, we find a closed contour passing all the orientation-lifted points in a greedy manner. Instead of trying all possible combinations of Finsler elastica minimal paths, we use a greedy searching strategy done in a low complexity. The problem we solve here is similar to the NP-hard traveling salesman problem, where the cities are represented by the orientation-lifted points $\bar{\mathbf{q}}_i \in \mathcal{D}$.

In summary, the proposed closed contour detection procedure aims to seeking a set χ of pairs of successive orientation-lifted points:

$$\chi = \bigcup_{i=1}^{m-1} \{(\bar{\mathbf{q}}_i, \bar{\mathbf{q}}_{i+1})\} \cup \{(\bar{\mathbf{q}}_m, \bar{\mathbf{q}}_1)\}, \quad (5.40)$$

and a closed contour \mathcal{C} contains a set of Finsler elastica minimal paths, joining all the pairs of vertices in χ .

5.4.2 Perceptual Grouping

Perceptual grouping is relevant to the task of curve reconstruction and completion (Cohen, 2001). Geodesic distance based perceptual grouping model was firstly introduced by Cohen (2001) using the concept of saddle point. The basic idea of this model is to identify each pair of points which has to be linked by minimal path from a set of key points. Later on, Bougleux et al. (2008) improved this grouping model by using path orientation and structure tensors. However, neither of the mentioned grouping methods considered curvature regularization.

In this section, we focus on the perceptual grouping problem of finding n closed curves, each of which formed by a set of piecewise Finsler elastica minimal paths with initial source points and endpoints in $\mathcal{D}_i \subseteq \mathcal{D}$, where \mathcal{D} is defined in (5.36) and $i = 1, 2, 3, \dots, n$.

We initialize the perceptual grouping method by selecting a physical position \mathbf{x}_1 . The corresponding orientation-lifted points of \mathbf{x}_1 , denoted by $\bar{\mathbf{x}}_1, \bar{\mathbf{x}}_1^\dagger$, can be automatically chosen from \mathcal{D} and will be removed from \mathcal{D} . Then the closest vertices corresponding to $\bar{\mathbf{x}}_1$ and $\bar{\mathbf{x}}_1^\dagger$ can be detected by (5.37) respectively. As a consequence, the first pair of vertices $(\bar{\mathbf{q}}_1, \bar{\mathbf{q}}_2)$ is computed using (5.38) and the geodesic $\mathcal{C}_{\bar{\mathbf{q}}_1, \bar{\mathbf{q}}_2}$ is recovered. Once the first pair of vertices $(\bar{\mathbf{q}}_1, \bar{\mathbf{q}}_2)$ is found, we add $\bar{\mathbf{q}}_1, \bar{\mathbf{q}}_2$ to \mathcal{D}_1 , remove $\bar{\mathbf{q}}_2, \bar{\mathbf{q}}_2^\dagger$ from \mathcal{D} and compensate $\bar{\mathbf{q}}_1$ to \mathcal{D} .

Similar to the closed contour detection procedure, the next vertex $\bar{\mathbf{q}}_k$ with $k \geq 3$ is found based on the criterion of (5.39) and the detected vertex $\bar{\mathbf{q}}_{k-1}$. Following the detection of vertex $\bar{\mathbf{q}}_k$, we add $\bar{\mathbf{q}}_k$ to \mathcal{D}_1 , remove $\bar{\mathbf{q}}_k, \bar{\mathbf{q}}_k^\dagger$ from \mathcal{D} , and track the geodesic $\mathcal{C}_{\bar{\mathbf{q}}_{k-1}, \bar{\mathbf{q}}_k}$ that joins $\bar{\mathbf{q}}_{k-1}$ to $\bar{\mathbf{q}}_k$. This perceptual grouping procedure is carried out by recursively searching for new vertices. Once the vertex $\bar{\mathbf{q}}_1$ is detected again according to the criterion (5.39), we stop the construction of \mathcal{D}_1 after removing $\bar{\mathbf{q}}_1$ from \mathcal{D} , and recover the geodesic ending at vertex $\bar{\mathbf{q}}_1$. The desired closed contour \mathcal{C}_1 can be obtained by concatenating all the detected Finsler elastica minimal paths with source and end points in \mathcal{D}_1 .

We start to build the collection \mathcal{D}_2 by choosing a new physical point as initialization. This initial physical point is obtained from the remaining orientation lifted points of \mathcal{D} . Similar to the procedure of constructing \mathcal{D}_1 , we build the collection \mathcal{D}_2 from the remaining orientation lifted points of \mathcal{D} . The procedure of building the collections \mathcal{D}_i can be terminated when n such collections have been identified or when the collection \mathcal{D} is empty. One can note that the constructed collections \mathcal{D}_i follow

$$\mathcal{D}_i \cap \mathcal{D}_j = \emptyset, \quad \forall i \neq j.$$

In contrast to the closed contour detection method described in Section 5.4.1, we do not enforce all of the orientation lifted points in \mathcal{D} to be used in the perceptual grouping procedure.

5.4.3 Tubular Structure Extraction

In this section, we apply the proposed Finsler elastica minimal path model to the tubular structure extraction combining with the optimally oriented flux filter (Law and Chung, 2008), where the centrelines of tubular structures are represented by the Finsler elastica minimal paths.

The minimal paths with the proposed Finsler elastica metric depend on the tangents of both the initial source point and end point. In order to simplify the initialization procedure, we firstly compute the optimal orientation map, denoted by $\Theta : \Omega \rightarrow [0, \pi)$, which minimizes the multi-orientation response function g in (5.32):

$$\Theta(\mathbf{x}) = \arg \min_{\theta \in [0, \pi)} \{g(\mathbf{x}, \theta)\}, \quad \forall \mathbf{x} \in \Omega. \quad (5.41)$$

Once the optimal orientation map Θ is defined, for one initial position $\mathbf{p}_s \in \Omega$, one can obtain two orientation-lifted points $\bar{\mathbf{p}}_s = (\mathbf{p}_s, \Theta(\mathbf{p}_s))$ and $\bar{\mathbf{p}}_s^\dagger$. Also, for n end positions $\mathbf{p}_i \in \Omega$ ($i = 1, 2, \dots, n$), the corresponding orientation-lifted points are defined by $\bar{\mathbf{p}}_i = (\mathbf{p}_i, \Theta(\mathbf{p}_i))$ and $\bar{\mathbf{p}}_i^\dagger$ respectively.

For each set of orientation lifted end points $\{\bar{\mathbf{p}}_i, \bar{\mathbf{p}}_i^\dagger\}$, we can extract four possible *geodesics*, each of which joins an initial source point in $\{\bar{\mathbf{s}}, \bar{\mathbf{s}}^\dagger\}$ to an end point in $\{\bar{\mathbf{p}}_i, \bar{\mathbf{p}}_i^\dagger\}$. The goal in this section is to search for a geodesic \mathcal{C}_i^* with *minimal* geodesic curve length associated to the metric \mathcal{P} , among all the four possible geodesics.

Let us denote the initial source point and the end point of the geodesic \mathcal{C}_i^* by $\bar{\mathbf{a}}^*$ and $\bar{\mathbf{c}}_i^*$, respectively. If the geodesic curve length is estimated by the fast marching method (Mirebeau, 2014b), this procedure can be simplified as follows: starting the fast marching front propagation from both of the initial source points $\bar{\mathbf{s}}$ and $\bar{\mathbf{s}}^\dagger$, the orientation lifted point $\bar{\mathbf{c}}_i^* \in \{\bar{\mathbf{p}}_i, \bar{\mathbf{p}}_i^\dagger\}$ is the first point that is reached by the front. The desired geodesic \mathcal{C}_i^* can be determined by reversing the geodesic that is the solution to the ODE (2.76). As a result, a set $\{\mathcal{C}_i^*; 1 \leq i \leq n\}$ of all the desired geodesics can be extracted from the same minimal action map generated by a single fast marching propagation.

In these applications, the geodesic distance maps with respect to the Finsler elastica metric are computed in a manner of early abort, i.e., once the geodesic distance values of all the orientation-lifted endpoints have been reached by the fast marching front, we stop the geodesic distance computation. The early abort trick can greatly reduce the computation time. This is similar to the partial front propagation described in (Deschamps and Cohen, 2001) with a simple extension to multiple points.

5.5 Experimental Results

We show the advantages of using curvature penalization for minimal paths extraction in the following experiments involving a study of the proposed metric itself, and comparative results against the isotropic Riemannian (IR) metric, the anisotropic Riemannian (AR) metric and the isotropic orientation lifted Riemannian (IOLR) metric in the applications of closed contour detection and tubular structure extraction.

5.5.1 Riemannian Metrics Construction

We construct the 2D anisotropic and isotropic Riemannian metrics for color image segmentation using the color gradient proposed by [Di Zenzo \(1986\)](#).

Considering a color image $\mathbf{I} = (I_1, I_2, I_3) : \Omega \rightarrow \mathbb{R}^3$ and a Gaussian kernel G_σ with fixed variance σ , the gradient $\nabla(G_\sigma * \mathbf{I})$ can be expressed as a Jacobian matrix:

$$\nabla(G_\sigma * \mathbf{I}) = \begin{pmatrix} \mathbf{I}_x^\sigma \\ \mathbf{I}_y^\sigma \end{pmatrix} = \begin{pmatrix} \partial_x G_\sigma * \mathbf{I} \\ \partial_y G_\sigma * \mathbf{I} \end{pmatrix}, \quad (5.42)$$

where $\mathbf{I}_x^\sigma(\cdot)$ and $\mathbf{I}_y^\sigma(\cdot)$ should be understood as 1×3 vectors, i.e.,

$$\begin{aligned} \mathbf{I}_x^\sigma(\cdot) &= \left(\partial_x G_\sigma * I_1(\cdot), \partial_x G_\sigma * I_2(\cdot), \partial_x G_\sigma * I_3(\cdot) \right), \\ \mathbf{I}_y^\sigma(\cdot) &= \left(\partial_y G_\sigma * I_1(\cdot), \partial_y G_\sigma * I_2(\cdot), \partial_y G_\sigma * I_3(\cdot) \right). \end{aligned}$$

Based on the above matrix $\nabla(G_\sigma * \mathbf{I})$ defined in (5.42), a tensor \mathcal{E} of size 2×2 can be constructed for all $\mathbf{x} \in \Omega$:

$$\mathcal{E}(\mathbf{x}) = \begin{pmatrix} \|\mathbf{I}_x^\sigma(\mathbf{x})\|^2 & \langle \mathbf{I}_x^\sigma(\mathbf{x}), \mathbf{I}_y^\sigma(\mathbf{x}) \rangle \\ \langle \mathbf{I}_x^\sigma(\mathbf{x}), \mathbf{I}_y^\sigma(\mathbf{x}) \rangle & \|\mathbf{I}_y^\sigma(\mathbf{x})\|^2 \end{pmatrix}.$$

We decompose the tensor $\mathcal{E}(\mathbf{x})$ in terms of its eigenvalues and eigenvectors as

$$\mathcal{E}(\mathbf{x}) = \varphi_1(\mathbf{x}) \mathbf{g}_1(\mathbf{x}) \mathbf{g}_1^T(\mathbf{x}) + \varphi_2(\mathbf{x}) \mathbf{g}_2(\mathbf{x}) \mathbf{g}_2^T(\mathbf{x}),$$

where $\varphi_1(\mathbf{x})$ and $\varphi_2(\mathbf{x})$ are the eigenvalues of tensor $\mathcal{E}(\mathbf{x})$. Vectors $\mathbf{g}_1(\mathbf{x})$ and $\mathbf{g}_2(\mathbf{x})$ are the eigenvectors corresponding to $\varphi_1(\mathbf{x})$ and $\varphi_2(\mathbf{x})$, respectively. Without loss of generality, we assume that $\varphi_1 \leq \varphi_2$ such that \mathbf{g}_2 denotes the unit color gradient vector field. Further details for color image gradient computation can be found in ([Di Zenzo, 1986](#)).

For a gray level image $I : \Omega \rightarrow \mathbb{R}^2$, one has $\varphi_1 = 0$ and φ_2 is defined by

$$\varphi_2(\mathbf{x}) = \|\nabla(G_\sigma * I)(\mathbf{x})\|.$$

\mathbf{g}_2 is defined as the normalized gradient vector field of the blurred image $G_\sigma * I$ and $\mathbf{g}_1(\mathbf{x}) = \mathbf{g}_2^\perp(\mathbf{x})$, $\forall \mathbf{x} \in \Omega$.

Therefore, the tensor field \mathcal{M}_A for the anisotropic Riemannian metric \mathcal{R}^A , the general form of which is defined in (2.52), can be computed by

$$\begin{aligned} \mathcal{M}_A(\mathbf{x}) &= \exp(-\tau \varphi_2(\mathbf{x})) \mathbf{g}_1(\mathbf{x}) \mathbf{g}_1^T(\mathbf{x}) \\ &\quad + \exp(-\tau \varphi_1(\mathbf{x})) \mathbf{g}_2(\mathbf{x}) \mathbf{g}_2^T(\mathbf{x}), \end{aligned} \quad (5.43)$$

where the positive constant τ controls the anisotropy ratio of \mathcal{R}^A .

Moreover, based on the scalar field φ_2 , the isotropic Riemannian metric \mathcal{R}^I (2.45) can be constructed by

$$\mathcal{R}^I(\mathbf{x}, \mathbf{u}) = \left(\beta_1 + \beta_2 \varphi_2^p(\mathbf{x}) \right)^{-1} \|\mathbf{u}\|, \quad (5.44)$$

where β_1 and β_2 are positive constants. In the following relevant experiments, we set $p = 2$ and $\beta_1 = 1$.

In the tubular structure extraction experiments, regarding the construction of the AR metric, we make use of the radius-lifted tensor field introduced by [Benmansour and Cohen \(2011\)](#), instead of using the tensor field \mathcal{M}_A defined in (5.43). For the construction of the IR metric, we simply replace the eigenvalue φ_2 in (5.44) by the vesselness map V_n described in (5.33). It is known that the vesselness map indicates the probability of each pixel to belong to the tubular structure. Hence the vesselness values inside the tubular structure are higher than those on the background, leading to that the fast marching front propagate fast inside the tubular structure.

The speed function P_{IL} for the IOLR metric \mathcal{R}^{IL} (2.62) should be dependent of the orientations. Simply, one can compute the speed function Φ^{IL} using the following equation:

$$P_{\text{IL}}(\mathbf{x}, \theta) = \Phi(\mathbf{x}, \theta), \quad \forall \theta \in [0, \pi), \forall \mathbf{x} \in \Omega, \quad (5.45)$$

where Φ is the orientation dependent speed function defined in (5.34) and (5.35). The parameter ρ of the IOLR metric \mathcal{F}^{IL} penalizing the variations of the orientation θ , is set as $\rho = \alpha$, where α is the parameter for the curvature term in the bending energy \mathcal{L} (5.1) or the data-driven Finsler elastica metric \mathcal{P} (5.22).

5.5.2 Parameters Setting

Curvature penalization in the proposed Finsler elastica metric relies on two parameters, α and λ (5.12). The choice of λ is dictated by algorithmic compromises. Indeed, minimal paths with respect to Finsler elastica metric \mathcal{P} converge to the elastica curves in the limit $\lambda \rightarrow \infty$, hence a large value of λ is desirable. However, large values of λ yield metrics with strong anisotropy ratio $\mu(\mathcal{P})$ (5.16). As a result, the numerical algorithm used, adapted from Mirebeau (2014b), uses larger discretization stencils, which increases its numerical cost and reduces its locality. For instance, $\lambda = 30$ (resp. 100 or 300) leads to stencils with a radius of 4 pixels (resp. 8 or 13). We typically use $\lambda = 100$.

On the other hand, the parameter α is used to weight the curvature penalty in the Finsler elastica metric \mathcal{P} . In the course of fast marching method, a large value of α makes the front to propagate slowly along the orientation dimension, implying that the obtained geodesics tend to be smooth, i.e., with low curvature. When α is very small, the extracted geodesics mainly depend on the image data-driven speed function Φ defined in Section 5.3.3. Therefore, the choice of α should depend on the desired image features. Basically, we make use of the following heuristics. There is a natural candidate α_* for the parameter α , dictated by the physical units of the parameters, namely

$$\alpha_* = (R_*/\Phi_*)^2,$$

where R_* is the smallest radius of curvature of the image features to be extracted, measured in pixels, and Φ_* is the typical value of the speed function Φ around these features.

The parameter η for image data-driven speed function Φ is set for each tested image individually. The parameter β_2 in the IR metric \mathcal{R}^I (5.44) is set as $\beta_2 = 2\eta$ for all the comparative experiments. We set τ in the AR metric \mathcal{R}^{AR} or its radius-lifted version such that the anisotropy ratio equals 20 in all the experiments except for Fig 5.6.

The angular resolution is set as $\theta_s = 2\pi/72$ for both the IOLR metric and the proposed Finsler elastica metric.

5.5.3 Smoothness and Asymmetry of the Finsler Elastic Minimal Paths

The proposed Finsler elastica metric invoking orientation lifting and curvature penalty benefits from the smooth and asymmetric properties of the minimal paths. We demonstrate the smooth and asymmetric properties in a synthetic image as shown in Fig. 5.5, where two ellipses-like shapes cross each other. Red dots and

green dots are initial source and end positions respectively. Arrows indicate the tangents at the corresponding positions. One can see that for the fixed initial source and end positions, changing the corresponding tangents will give different minimal geodesics. As shown in the first two columns of Fig. 5.5, the two geodesics with the same initial source and end positions could form a complete ellipse shape.

In Fig. 5.6, we design a spiral with high anisotropy. The initial source position and the end position are placed at the ends of the spiral. In the top row we add high noise to the spiral while in the bottom row we blur the spiral. In columns 1-4, we show the minimal paths extracted by using the IR metric, the AR metric, the IOLR metric and the Finsler elastica metric respectively. One can see that by using the IR and AR metrics, where the shortcuts occur near the initial source position (red dot) as shown in columns 1 and 2. In the top row of the column 3, the minimal path extracted by the IOLR metric is improved compared to the results from the IR and AR metrics. However, a segment of the spiral, near the initial source position, is missed again due to the shortcut problem. In contrast, the minimal paths shown in column 4 which are extracted by the Finsler elastica metric exactly follow the spiral shape thanks to the curvature penalty embedded in the metric. In this experiment, we make use of a anisotropy ratio value of 100 for the AR metric. For the Finsler elastica metric, we set $\alpha = 500$ to ensure the Finsler elastica minimal paths to be smooth enough.

In Fig. 5.7a, we illustrate six orientation-lifted candidates $\bar{\mathbf{q}}_i, i = 1, 2, \dots, 6$, denoted by green dots with arrows, and an orientation-lifted initial source point $\bar{\mathbf{s}}$ (red dot with arrow). Among all the candidates, we would like to find the closest orientation-lifted point to the initial source point $\bar{\mathbf{s}}$, in terms of geodesic distance with respect to the data-driven Finsler elastica metric \mathcal{P} (5.22). In Fig. 5.7b, it is shown that the closest orientation lifted point to $\bar{\mathbf{s}}$ is the candidate $\bar{\mathbf{q}}_6$, even though the geodesic (red curve), joining the orientation lifted points $\bar{\mathbf{s}}$ and $\bar{\mathbf{q}}_6$, passes through the vicinity of the physical position of $\bar{\mathbf{q}}_1$. Moreover, one can claim that the Euclidean distance value between the physical positions of $\bar{\mathbf{s}}$ and $\bar{\mathbf{q}}_6$ is the largest one among all of the Euclidean distance values between the physical positions of $\bar{\mathbf{s}}$ and any remaining orientation lifted candidate $\bar{\mathbf{q}}_i$. This experiment demonstrates the asymmetric and smooth properties of the proposed Finsler elastica minimal path model.

In Fig. 5.8, we show the minimal path extraction results on three natural images, where each pair of the prescribed initial source positions and end positions is very close to each other in terms of the Euclidean distance. For each image, we expect to detect a long boundary between the two given orientation lifted points. It can be observed that the extracted geodesics associated to the Finsler elastica metric are able to catch the desired boundaries. In Fig. 5.8, the images shown in columns 1 and 2 are from the Berkeley Segmentation Dataset (Arbelaez et al., 2011) and the image in column 3 is from the Weizmann dataset (Alpert et al., 2012).

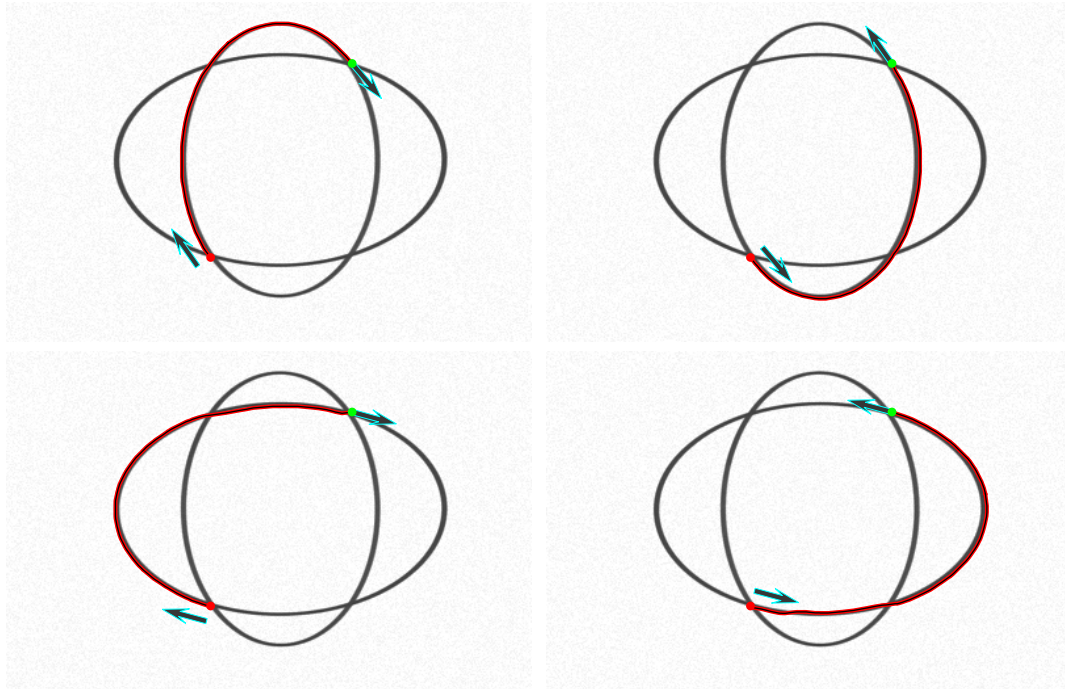


FIGURE 5.5: Flexible Finsler minimal paths extraction on ellipse-like curves. Red dots and green dots denote the initial and end positions respectively. Arrows indicate the tangents.

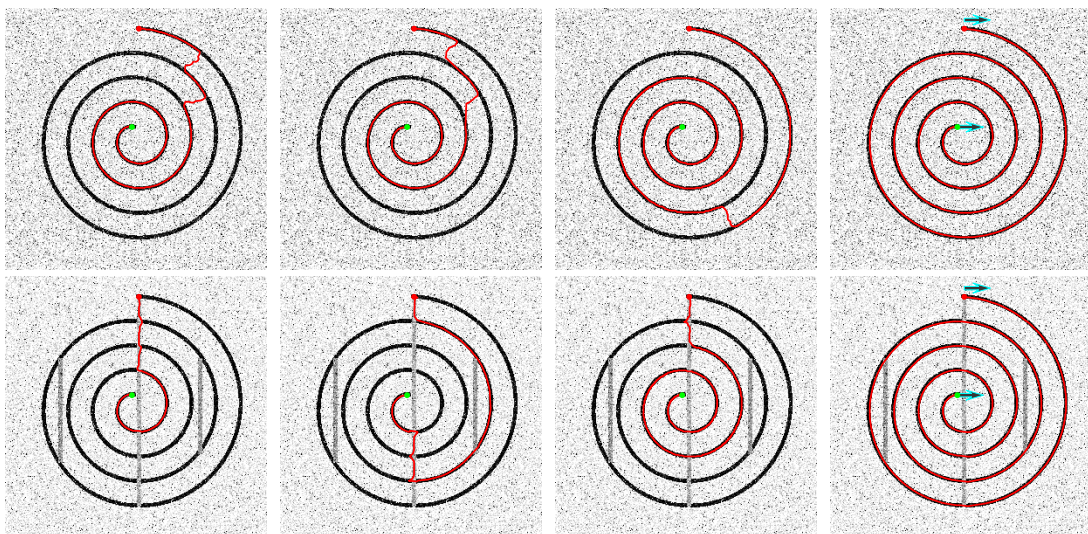


FIGURE 5.6: Comparative minimal paths extraction results on Spirals. **Columns 1-4** Minimal paths extracted by using the IR metric, the AR metric, the IOLR metric and the proposed Finsler elastica metric, respectively. Red dots are initial source positions and green dots are end positions. Arrows indicate the tangents.

5.5.4 Closed Contour Detection and Image Segmentation

Fig. 5.9 shows the closed contour detection results with three prescribed physical positions using different metrics, where each position are assigned two opposite

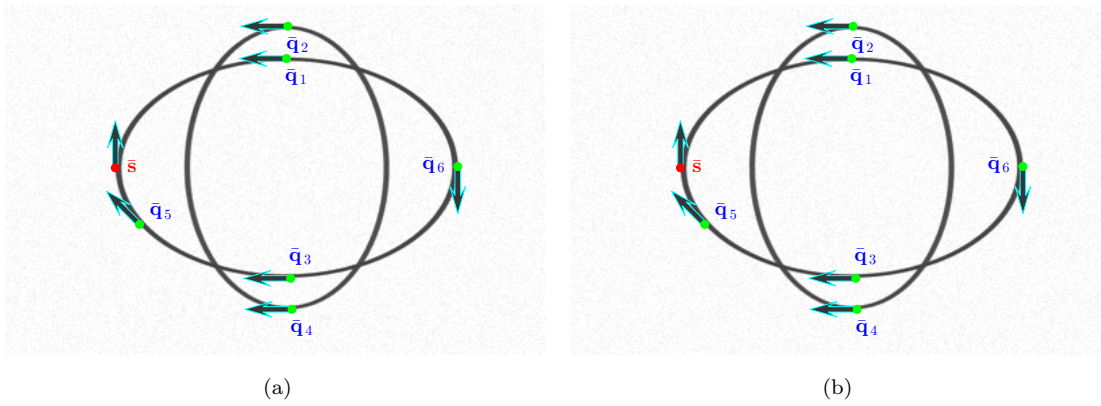


FIGURE 5.7: Finding the nearest orientation-lifted candidate to the orientation-lifted initial source point in terms of geodesic distance associated to data-driven Finsler elastica metric. (a) Red dot denotes the initial source position and green dots are the end positions. Arrows indicate the tangents for each position. (b) \bar{q}_6 denoted by green dot with the arrow is the closest orientation-lifted point to \bar{s} .



FIGURE 5.8: Finsler elastica minimal paths extraction results. Red and green dots are the initial source and end positions respectively. Arrows indicate the corresponding tangents.

orientations². In this experiment, we firstly build the collection χ (5.40) by the proposed contour detection procedure using the Finsler elastica metric as described in Section 5.4.1, where the detection results are shown in column 5. Columns 2-4 show the closed contour detection results using the IR metric, the AR metric, and the IOLR metric, respectively. The minimal paths shown in columns 2 to 4 are obtained by simply linking each pair of vertices by the respective metrics involved in χ . The red, yellow, and green dots are the physical positions of the vertices \bar{q}_1 , \bar{q}_2 , \bar{q}_3 , respectively. The arrows shown in column 5 indicate the tangents of

²For the IR metric and the AR metric, only the physical positions of these orientation lifted vertices are used.

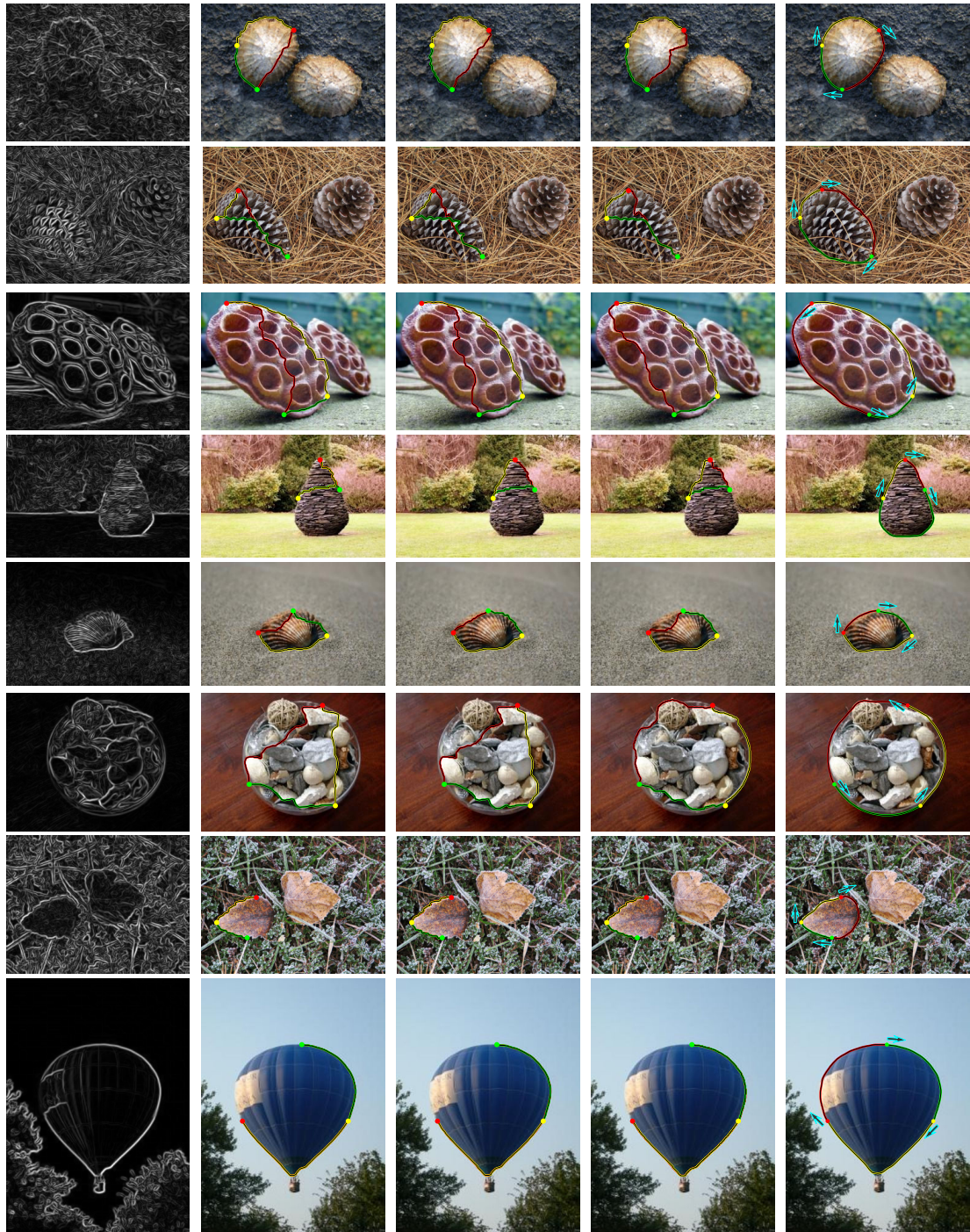


FIGURE 5.9: Comparative closed contour detection results obtained by using different metrics. **Column 1** Edge saliency map. **Columns 2-5** Contour detection results from the IR metric, the AR metric, the IOLR metric and the proposed data-driven Finsler elastica metric, respectively.

the geodesics at the corresponding positions. We assign each geodesic the same color as its initial source position. In these images, most parts of the desired boundaries appear to be weak edges which can be observed from the edge saliency map in column 1. The detected contours associated to the Finsler elastica metric

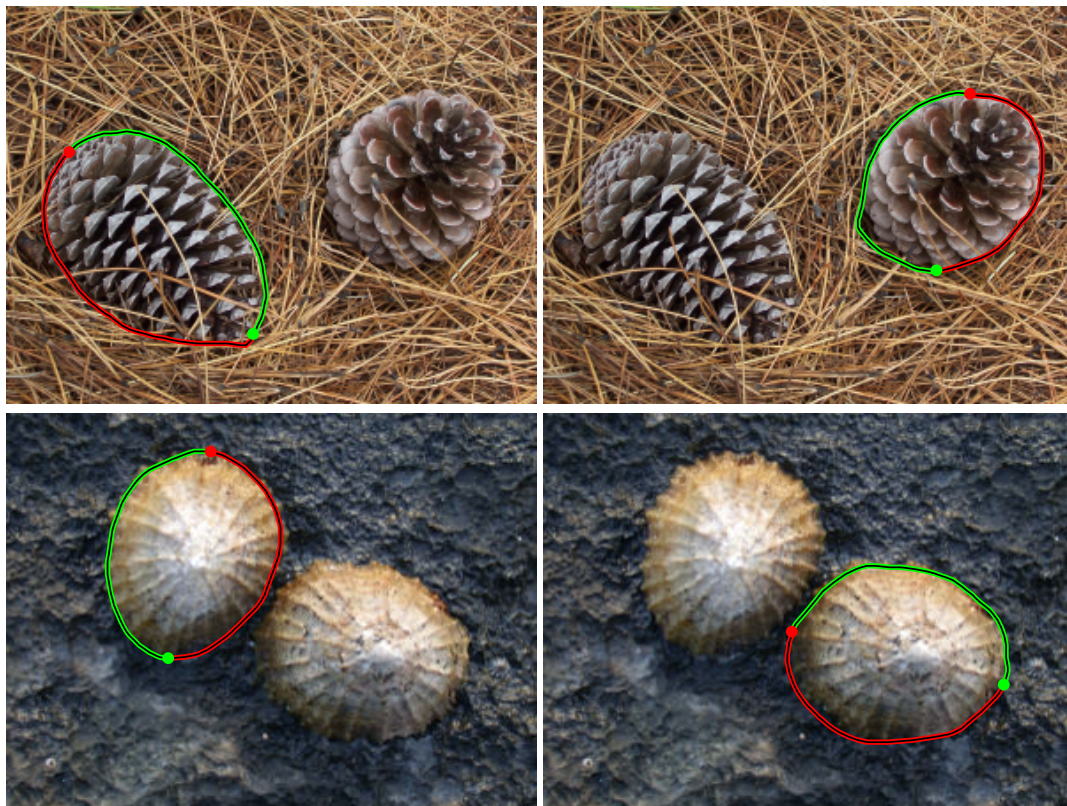


FIGURE 5.10: Closed contour detection results by using only two given physical positions and the corresponding orientations.

succeed at catching the desired boundaries due to the curvature penalization and asymmetric property. In contrast, the three Riemannian metrics without curvature penalization fail to extract the expected boundaries. The images used in this experiment are from the Weizmann dataset.

In Fig. 5.10, we show the closed contour detection results obtained by the proposed method with only two given physical positions and the corresponding orientations. One can see that the proposed method can indeed reduce user intervention at least for objects with smooth boundaries.

For the proposed data-driven Finsler elastica metric \mathcal{P} defined in (5.22), the curvature penalization relies on the parameter α (λ is fixed to 100). In Fig. 5.11, we show the closed contour detection results by varying α to demonstrate the influence of the curvature term in our approach. In column 1, we show the closed contour detection results with suitable values of α , say α_0 . In columns 2 and 3, the closed contour detection results using $\alpha_0/10$ and $5\alpha_0$ are demonstrated. One can see that it could lead to shortcuts by using small values of α in rows 1-3 of column 2. In contrast, with a larger α , the detected closed contour can catch the optimal boundaries of the objects, which supports the effect of using curvature penalization. The edge saliency maps for each image in this experiments can be found from the first column of Fig. 5.9.



FIGURE 5.11: Contour detection results with different values of curvature penalization parameter α . **Column 1** Results by suitable parameters of α and λ . **Columns 2** Results by small values of α . **Column 3** Results by large values of α .

5.5.5 Perceptual Grouping

The perceptual grouping result on a synthetic noisy image is shown in Fig. 5.12. In Fig. 5.12a, we demonstrate the original image consisting of a set of edges. Red and blue dots with arrows are the orientation-lifted points provided by user as initializations, where the red dot is the selected initial physical position. 5.12b shows the perceptual grouping results by the proposed method. The identified orientation-lifted points in the set \mathcal{D}_1 are denoted by red dots with arrows. Red curves linking the points in \mathcal{D}_1 indicate the expected closed curves.

Fig. 5.13 illustrates the capacity of the proposed method to deal with the perceptual grouping problem with spurious points. Different initializations are shown in Figs. 5.13a and 5.13c, where the red dots are the selected initial physical positions.

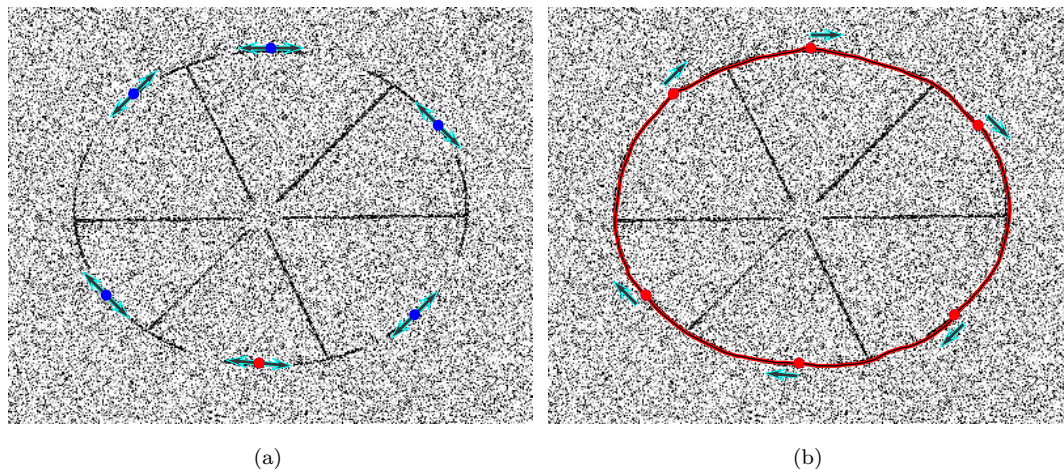


FIGURE 5.12: Perceptual grouping results by the proposed method and Finsler elastica metric. (a) Initialization: red and blue dots are physical positions, in which the red dot is the selected initial position. (b) The corresponding perceptual grouping results. Arrows indicate the tangents for each physical position.

Figs. 5.13b and 5.13d are the grouping results. Red curves indicate the detected closed curves.

The proposed perceptual grouping method has the ability to detect multiple closed curves by only specifying the number of expected closed curves. In Fig. 5.14, three closed curves are detected. Row 1 shows different initializations where red dots denote the selected initial physical positions. Row 2 illustrates the first detected closed curve indicated by red curves. Red dots with arrows denote the selected orientation-lifted points in the set \mathcal{D}_1 . Row 3 illustrates the second detected closed curve indicated by orange curves. Orange dots with arrows indicate the orientation-lifted points in the set \mathcal{D}_2 . The initial physical positions are selected randomly after \mathcal{D}_1 is detected. Column 3 demonstrates the third closed curve using the similar procedure to the detection of \mathcal{D}_2 . We show the final closed curve detection results in row 4. One can claim that our algorithm indeed has the ability to deal with curves intersecting each others.

5.5.6 Tubular Structure Extraction

In this section, we show the tubular structure extraction results, where the initial source and end positions are indicated by red and green dots, respectively. In Figs. 5.15 to 5.19, only the physical positions are provided manually. The corresponding orientations of these physical positions are computed automatically by (5.41). In Fig. 5.20, the corresponding tangents for the physical positions are provided manually because high noise could lead to failure of the optimal orientation

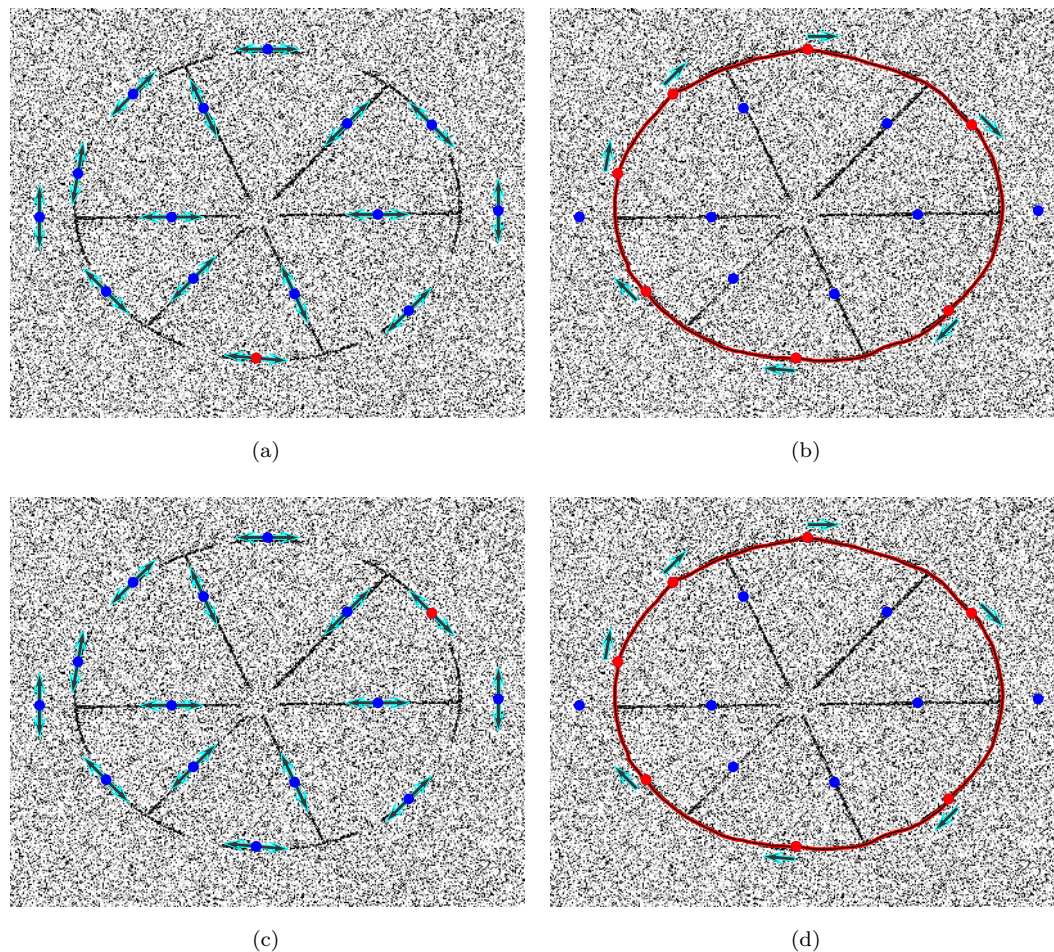


FIGURE 5.13: Perceptual grouping results by the proposed method and Finsler elastica metric. (a) Initialization 1. Red dot is the selected initial position. (b) Perceptual grouping result for initialization 1. Red dots with the corresponding arrows are the orientation points chosen to form a closed curve. (c) Initialization 2. Red dot is the selected initial position. (d) Perceptual grouping result for initialization 2.

detection using (5.41). We use the extraction strategy described in Section 5.4.3 for the Finsler elastica metric.

In Fig. 5.15, the retinal vessels are extracted by the IR metric, the AR metric, the IOLR metric and the proposed data-driven Finsler elastica metric as shown in columns 1 to 4, respectively. One can see that in columns 1 to 3, the minimal paths suffer from the short branches combination problem, i.e., those minimal paths prefer to choose a shortest way depending only on the image data-driven speed functions. In contrast, the minimal paths obtained by the proposed data-driven Finsler elastica metric can obtain the correct combination of vessel branches, leading to smooth segmentation results between the initial source and end orientation-lifted points.

Similar vessel extraction results are observed in Fig. 5.16. Again, the short

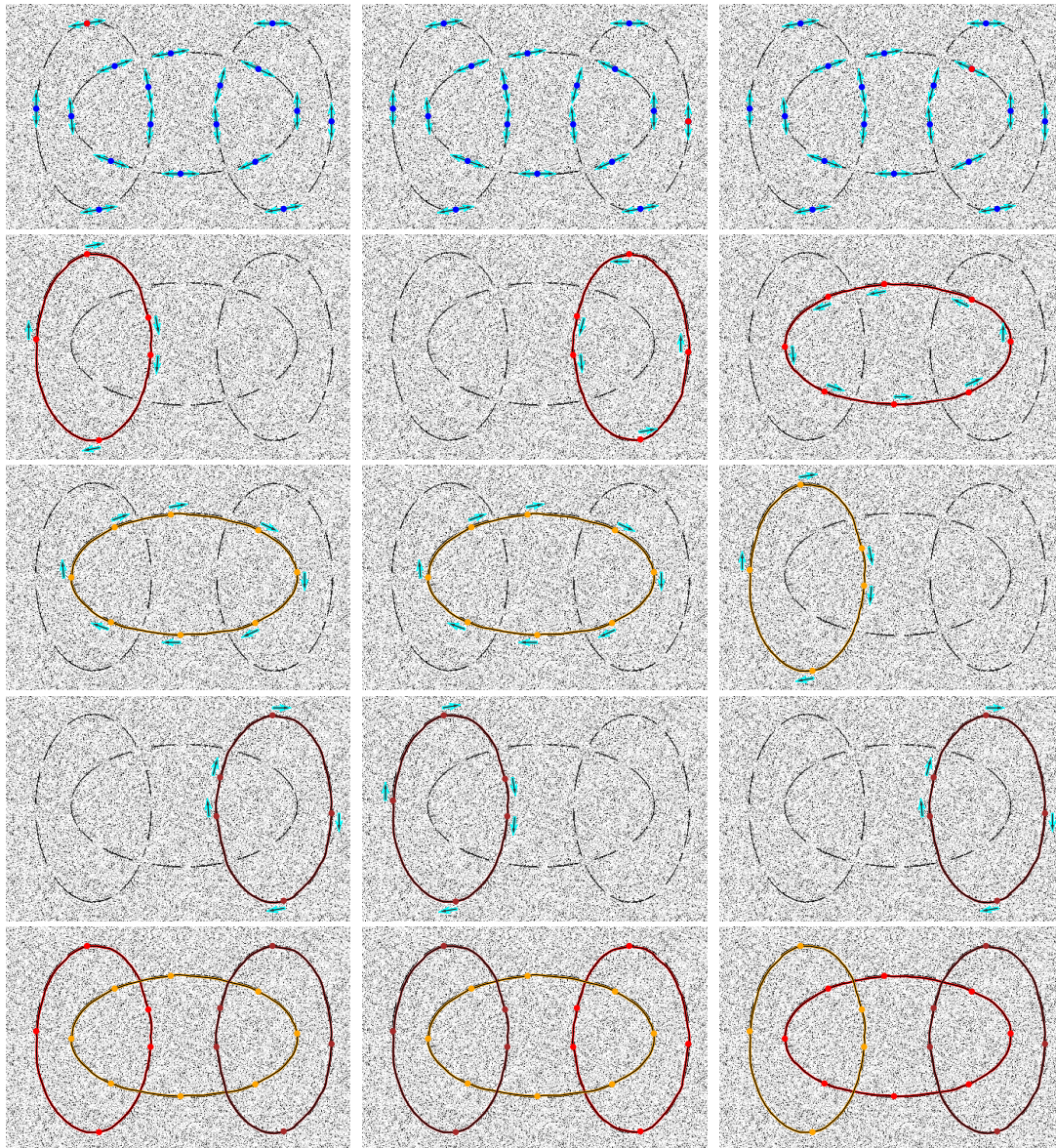


FIGURE 5.14: Perceptual grouping results by the proposed method where three groups are identified. **Row 1** Initializations. Red dots are the selected initial positions. **Rows 2-4** Intermediate grouping results for the corresponding initializations. **Row 5** Final grouping results.

branches combination problem occurs in columns 1 to 3 which are obtained by the IR metric, the AR metric and the IOLR metric, respectively. Instead, the proposed Finsler elastica metric can obtain the correct vessels extraction thanks to the curvature penalty.

In Fig. 5.17, we present the extraction results of the retinal artery centerlines in three patches of retinal images³. The centerline of a retinal artery usually appears as a smooth curve. In column 1, we show the retinal artery-vein ground

³Many thanks to Dr. Jiong Zhang to provide us these images.

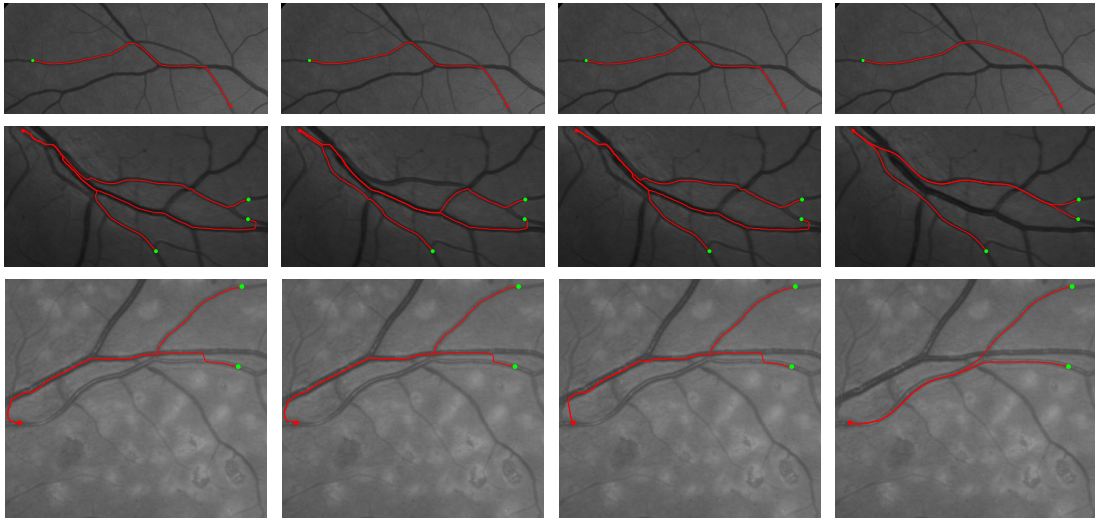


FIGURE 5.15: Comparative blood vessel extraction results on retinal images. **Columns 1-4** The extracted minimal paths using the IR metric, the AR metric, the IOLR metric, and the proposed Finsler elastica metric respectively.

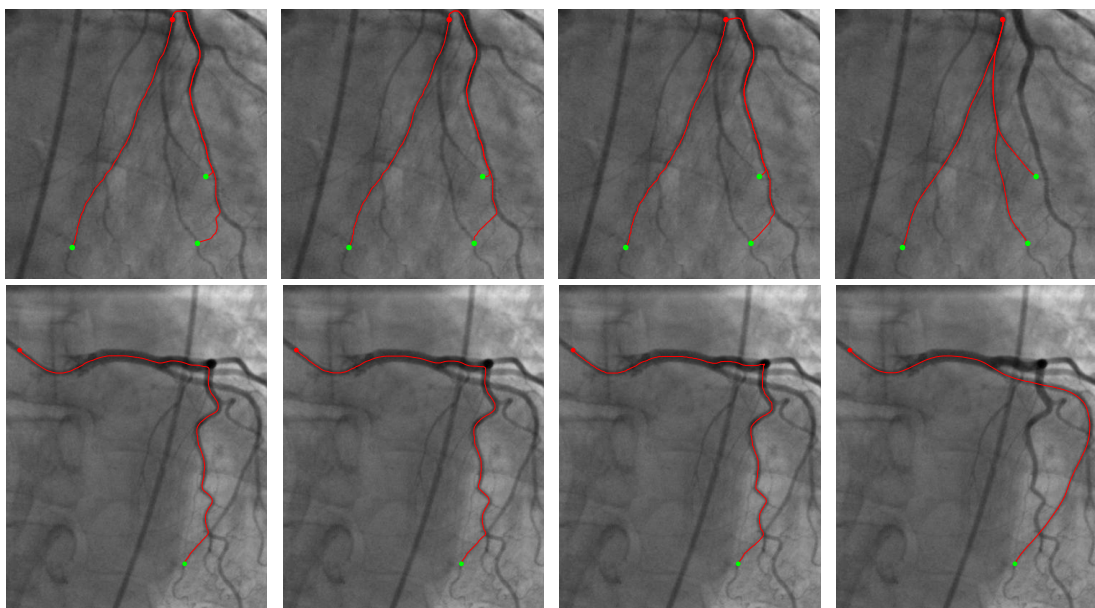


FIGURE 5.16: Comparative blood vessel extraction results on fluoroscopy images. **Columns 1-4** The extracted minimal paths using the IR metric, the ARLR metric, the IOLR metric, and the proposed Finsler elastica metric respectively.

truth maps, where the red and blue regions indicate the arteries and veins, respectively. Note that the small vessels have been removed from the ground truth maps. Columns 2 to 5 show the centerlines extraction results by using the IR metric, the ARLR metric, the IOLR metric and the Finsler elastica metric, respectively. One can see that the minimal paths demonstrated in columns 2 to 4 pass through the wrong vessels due to the low gray-level contrast of the retinal arteries. The proposed model can obtain the correct artery centerlines as shown in column 5, thanks to the curvature penalization.

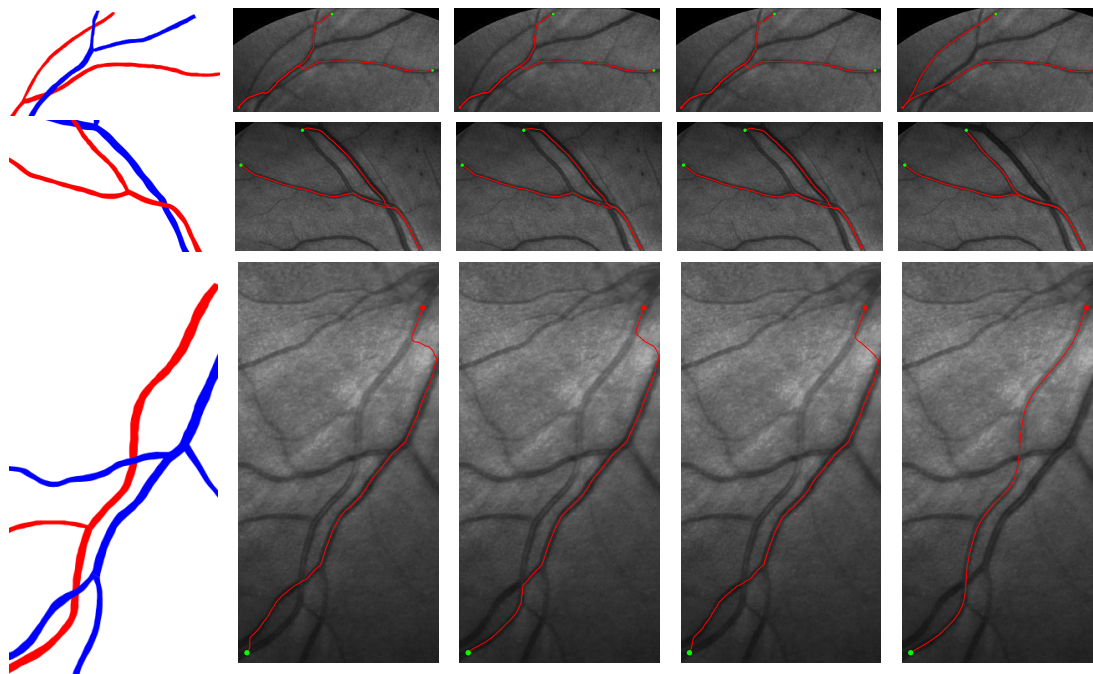


FIGURE 5.17: Comparative arteries vessels extraction results on retinal images. **Column 1** The retinal artery-vein vessels ground truth maps. **Columns 2-5** The extracted minimal paths by the IR metric, the AR metric, the IOLR metric, and the Finsler elastica metric respectively.

In Fig. 5.18, we demonstrate the retinal veins extraction results (blue curves) in the same patches which are used in rows 1-2 of Fig. 5.17. The extracted paths (blue curves) are shown in columns 2-5 by using the IR metric, the AR metric, the IOLR metric and the proposed Finsler elastica metric respectively. In this experiment, we can see that all the extracted minimal paths can successfully follow the retinal veins indicated by red regions in the artery-vein ground truth maps shown in column 1.

In Fig. 5.19, vessel extraction results on a patch of retinal image are demonstrated, where the vessels are blurred by other tissues. The vessel extraction results from the three Riemannian metrics fail to follow the desired vessel due to the weak contrast as shown in Figs. 5.19a to 5.19c. In 5.19d, the extracted minimal path by the proposed Finsler elastica metric can successfully delineate the centreline of the desired vessel thanks to the curvature penalization.

In Fig. 5.20, we show the road segmentation results on an aerial image by the proposed Finsler elastica metric. The road images are blurred by Gaussian noise with different variances. One can claim that our method can obtain smooth and accurate minimal paths on noisy images.

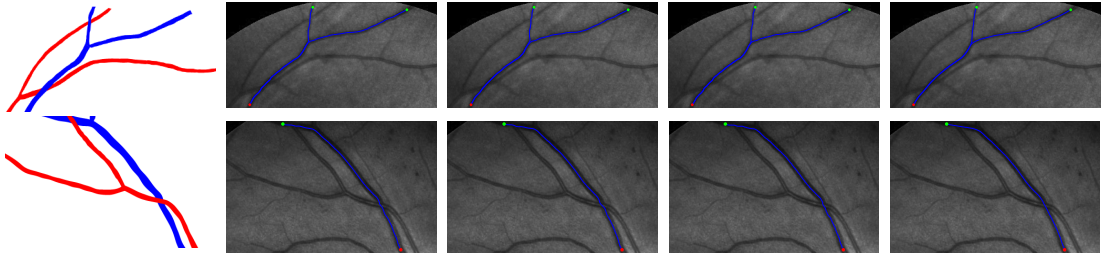


FIGURE 5.18: Retinal veins extraction results from different metrics. **Column 1** The retinal artery-vein vessels ground truth maps. **Columns 2-5** The extracted minimal paths by the IR metric, the AR metric, the IOLR metric, and the Finsler elastica metric respectively. Blue curves denote the extracted minimal paths.

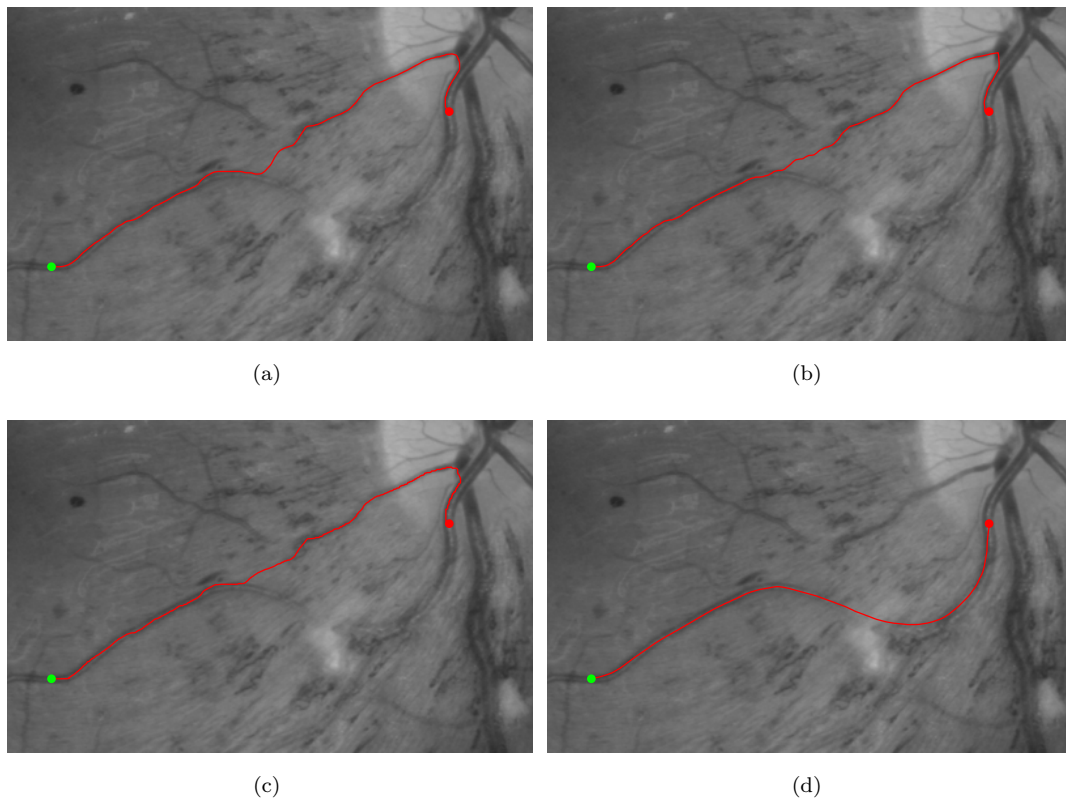


FIGURE 5.19: Comparative blood vessel extraction results on blurred retinal image. (a)-(d) The extracted minimal paths by the IR metric, the AR metric, the IOLR metric, and the proposed data-driven Finsler metric, respectively.

5.6 Conclusion

The core contributions of this paper lie at the introduction of curvature penalty to the Eikonal PDE based minimal path model. This is done by establishing the connection between the Euler elastica bending energy and the geodesic energy via a family of orientation-lifted Finsler elastica metrics. Solving the Eikonal PDE with respect to the proposed Finsler elastica metric, our model thus can determine globally minimizing curves with curvature penalty between two orientation-lifteds-

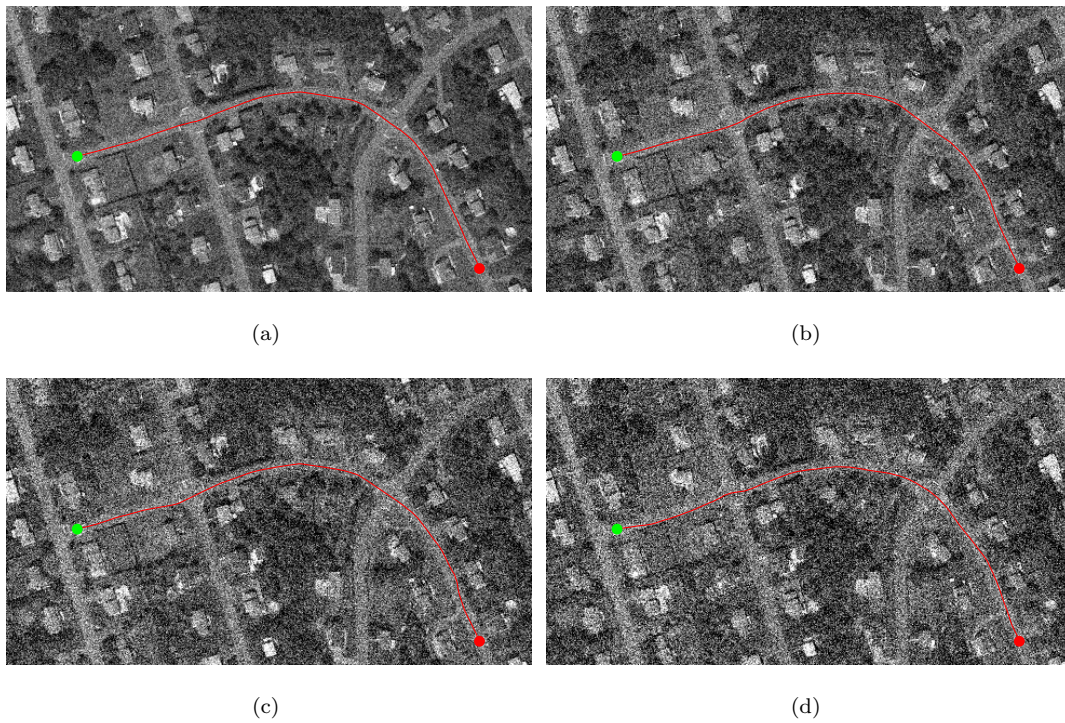


FIGURE 5.20: Roads extraction results by the proposed Finsler elastica metric in aerial image blurred by Gaussian noise.

points. These minimal curves are asymmetric and smooth, benefiting from the orientation lifting and curvature penalty. Combining with orientation dependent data-driven speed function, we apply the proposed Finsler elastica minimal path model to the applications of interactive image segmentation, perceptual grouping and tubular structure extraction. Experimental results on both synthetic and real images demonstrate the advantages of the Finsler elastica metric approach.

Chapter 6

Finsler Geodesics Evolution Model for Region-based Active Contours

Abstract

In this chapter, a new geodesics extraction framework is proposed for region-based active contours and image segmentation. The basic idea is to reformulate a region-based active contours energy into a geodesic contour energy involving a Finsler metric. As a consequence, the region-based active contours energy minimization problem is solved without resorting to level set functions, but using a robust non-linear Eikonal partial differential equation framework. By sampling a set of control points from the closed active contour in a clockwise order, the active contours evolution problem is turned into finding a collection of minimal geodesics joining all the successive control points. Globally optimal minimal curves are obtained by solving an Eikonal partial differential equation, involving a Finsler metric, which is achieved at a modest numerical cost using a variant of the fast marching algorithm.

6.1 Introduction

The image segmentation problem plays an essential role in the field of computer vision and medical imaging. Various partial differential equation (PDE) inspired image segmentation models, such as the deformable models, have been extensively studied during the last three decades. The Active contour models or snakes, firstly introduced to the applications of image analysis by [Kass et al. \(1988\)](#), are designed for image feature extraction by minimizing the associated energy functional in the form of edge integration with initial conditions.

One of the main drawbacks suffered by the classical edge-based snakes model ([Kass et al., 1988](#)) is that it requires fastidious initialization. In some cases, for example, it requires the initial curves to be very close to the targeted boundaries. Various approaches such as the balloon active contour model ([Cohen, 1991](#); [Cohen and Cohen, 1993](#)), gradient vector flow based models ([Paragios et al., 2001](#); [Xu and Prince, 1998](#)) and physical laws based model ([Jalba et al., 2004](#); [Xie and Mirmehdi, 2008](#)), were devoted to solve this initialization sensitivity problem, allowing initial curves to be far from the desired boundaries or even cross them. With the level set numerical tool ([Osher and Sethian, 1988](#)), the evolution of the edge-based active contours with balloon force can be efficiently implemented as the geometric active contour models ([Caselles et al., 1993, 1997](#); [Malladi et al., 1994](#)).

Region-based active contour models aim at partitioning the image into regions with homogeneous features like gray levels, colors or texture [Cohen \(1997\)](#); [Mumford and Shah \(1989\)](#). Comparing to edge-based active contour models, using global region information can sometimes avoid trapping the active contours at spurious edges, since most of the edge detectors are based on the local image gradients. In [Chan and Vese \(2001\)](#); [Tsai et al. \(2001\)](#); [Vese and Chan \(2002\)](#), the curve evolution strategy and level set method ([Osher and Sethian, 1988](#)) were adapted to efficiently minimize the various forms of the Mumford-Shah functional ([Mumford and Shah, 1989](#)), known as the piecewise constant case ([Chan and Vese, 2001](#)) and piecewise smooth case ([Tsai et al., 2001](#); [Vese and Chan, 2002](#)). The pairwise-based active contour models were proposed in ([Bertelli et al., 2008](#); [Dubrovina-Karni et al., 2015](#); [Jung et al., 2012](#); [Sumengen and Manjunath, 2006](#)), where the basic idea is to measure the similarity distance between each pair of pixels within the same region or dissimilarity distance for a pair of pixels in different regions ([Bertelli et al., 2008](#)). Local region-based active contour models are based on the homogeneous intensities ([Lankton and Tannenbaum, 2008](#); [Li et al., 2008](#)) or texture features ([Brox and Cremers, 2009](#)) within a local region. Hybrid active contour models ([Kimmel, 2003](#); [Paragios and Deriche, 2002](#); [Sagiv et al., 2006](#); [Zhu and Yuille, 1996](#)) consider the image edge information and region homogeneous properties simultaneously. Hence the hybrid models can share the advantages from both the edge-based and region-based active contour models.

Cohen and Kimmel (1997) proposed a minimal path model to find the global minimum of the geodesic energy based on the formalism of viscosity solutions to the Eikonal PDE, which can be solved by a fast and reliable Fast Marching method (Sethian, 1999). The mathematical and algorithmic properties of the classic minimal path model (Cohen and Kimmel, 1997) have important practical consequences, allowing deep applications of the minimal path model and its extensions to image segmentation (Appia and Yezzi, 2011; Mille et al., 2014; Peyré et al., 2010) and medical imaging (Chen and Cohen, 2015b). Benmansour and Cohen (2009) proposed a growing minimal path model to obtain a closed contour by detecting a set of keypoints. Mille et al. (2014) proposed a combinational minimal path model for interactive image segmentation by finding the optimal combination of geodesics between each pair of given points. A curvature-penalized minimal path model with a Finsler elastic metric was recently proposed by Chen et al. (2015) to build the connection between the geodesic energy and the Euler elastic bending energy.

In this chapter, we propose a Finsler metric based minimal path model for region-based active contours and image segmentation. The Finsler metric is induced from the region-based active contour energy functionals by an application of the divergence theorem to a well chosen vector field. The Eikonal PDE associated to the Finsler metric is efficiently solved via an adaptive variant of the fast marching method (Mirebeau, 2014b).

6.2 Region-based Active Contours Models

6.2.1 Mumford-Shah Functional Inspired Active Contours Models

The classical Mumford-Shah (MS) functional (Mumford and Shah, 1989) consisting of a region based image data term and a curve length regularization term

$$E^{\text{MS}}(g, \gamma) = \alpha \int_{\Omega} (I(\mathbf{x}) - g(\mathbf{x}))^2 d\mathbf{x} + \beta \int_{\Omega \setminus \gamma} \|\nabla g(\mathbf{x})\|^2 d\mathbf{x} + \lambda \int_0^1 \|\dot{\gamma}(t)\| dt, \quad (6.1)$$

where $\Omega \subset \mathbb{R}^2$ is the image domain and $I : \Omega \rightarrow \mathbb{R}$ is an observed gray level image. g is a piecewise smooth image data function used to approximate I inside each region component and $\gamma : [0, 1] \rightarrow \Omega$ is a smooth curve. α , β and λ are positive constants. It is known that minimizing the original MS functional E^{MS} is a difficult task. Vese and Chan (2002) and Tsai et al. (2001) independently proposed numerical approaches to the original MS problem based on active contours evolution. Along the same research line, Brox and Cremers (2009) statistically interpreted the piecewise smooth MS functional by a local region based model.

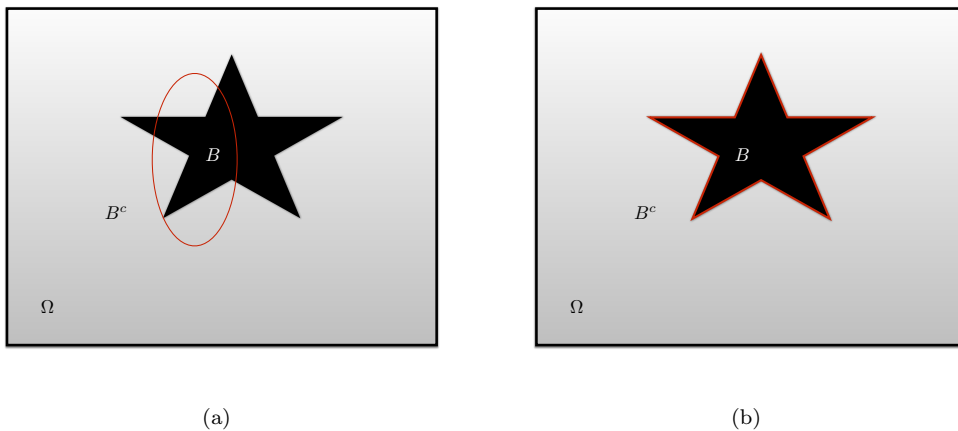


FIGURE 6.1: Illustration of the Chan-Vese active contours model. (a) original image and initial contour (red curve). (b) Final segmentation result.

6.2.2 Piecewise Constant Chan-Vese Active Contours Model

Chan and Vese (2001) presented a region based active contours model where the energy functional is obtained from the reduced form of the original MS functional by setting the piecewise smooth function g to be a constant c_1 inside γ and to be a constant c_2 outside γ . Letting B denote the regions inside and outside B^c outside the contour γ respectively, one has $\Omega = B \cup B^c$. In Fig. 6.1, we demonstrate how this model works. It assumes that the image can be approximated by the constant c_1 inside B and by c_2 inside B^c . The Chan-Vese energy functional can be expressed as

$$E^{\text{CV}}(\gamma, c_1, c_2) = \alpha_1 \int_B (I(\mathbf{x}) - c_1)^2 d\mathbf{x} + \alpha_2 \int_{B^c} (I(\mathbf{x}) - c_2)^2 d\mathbf{x} + \lambda \int_0^1 \|\gamma'(t)\| dt + \nu \int_B d\mathbf{x}, \quad (6.2)$$

where the last term of above energy functional is an optional balloon force firstly introduced by Cohen (1991). Parameters α_1 , α_2 , λ and ν are constants, where we set $\alpha_1 = \alpha_2$ and $\nu = 0$.

In its basic formulation (Osher and Sethian, 1988), the contour γ was represented by the zero-value of the level set function $\Phi : \Omega \rightarrow \mathbb{R}$, i.e.,

$$\gamma =: \{\mathbf{x} \in \Omega; \Phi(\mathbf{x}) = 0\}.$$

By a variational level set approach proposed by Zhao et al. (1996) invoking a Heaviside function $H : \Omega \rightarrow \{0, 1\}$, the variational level set based Chan-Vese

energy functional (Chan and Vese, 2001) can be expressed as

$$\begin{aligned}
 E^{\text{CV}}(\Phi, c_1, c_2) &= \alpha_1 \int_{\Omega} (I(\mathbf{x}) - c_1)^2 H(\Phi(\mathbf{x})) d\mathbf{x} + \alpha_2 \int_{\Omega} (I(\mathbf{x}) - c_2)^2 H(-\Phi(\mathbf{x})) d\mathbf{x} \\
 &\quad + \lambda \int_{\Omega} \|\nabla H(\Phi(\mathbf{x}))\| d\mathbf{x} + \nu \int_{\Omega} H(\Phi(\mathbf{x})) d\mathbf{x}.
 \end{aligned} \tag{6.3}$$

The Heaviside function obeys $H(-\Phi(\mathbf{x})) = 1 - H(\Phi(\mathbf{x}))$.

The CV model made use of a two-step minimization scheme to get the final optimal contour \mathcal{C}^* . The first step is to fix c_1 and c_2 to update the level set function Φ with respect to time τ in a gradient descent manner by

$$\begin{aligned}
 \frac{\partial \Phi}{\partial \tau} &= - \frac{\partial E^{\text{CV}}}{\partial \Phi} \\
 &= \delta(\Phi) \left(\alpha_2 (I - c_2)^2 - \alpha_1 (I - c_1)^2 + \lambda \operatorname{div} \left(\frac{\nabla \Phi}{\|\nabla \Phi\|} \right) - \nu \right),
 \end{aligned} \tag{6.4}$$

with suitable boundary condition. Function δ is the Dirac measure that is defined as

$$\delta(z) = \frac{d}{dz} H(z).$$

The second step is to fix Φ to update c_1 and c_2 by

$$c_1 = \frac{\int_{\Omega} I(\mathbf{x}) H(\Phi(\mathbf{x})) d\mathbf{x}}{\int_{\Omega} H(\Phi(\mathbf{x})) d\mathbf{x}}, \tag{6.5}$$

$$c_2 = \frac{\int_{\Omega} I(\mathbf{x}) H(-\Phi(\mathbf{x})) d\mathbf{x}}{\int_{\Omega} H(-\Phi(\mathbf{x})) d\mathbf{x}}. \tag{6.6}$$

to minimize the energy E^{CV} (6.3). Hence as $\tau \rightarrow \infty$, the final optimal contour is expected to converge to the boundaries of the object. As discussed in (Chan and Vese, 2001), numerically, the Heaviside function H and Dirac measure function δ are approximated respectively by their regularized functions H_{ϵ} and δ_{ϵ} :

$$\begin{aligned}
 H_{\epsilon}(z) &= \frac{1}{2} \left(1 + \frac{2}{\pi} \arctan\left(\frac{z}{\epsilon}\right) \right), \\
 \delta_{\epsilon}(z) &= \frac{1}{\pi} \frac{\epsilon}{\epsilon^2 + z^2}.
 \end{aligned}$$

6.2.3 Locally Binary Fitting Model

The locally binary fitting active contours model was introduced by Li et al. (2008) to deal with inhomogeneous intensities problem. In this case, the Chan-Vese active contours model (Chan and Vese, 2001) cannot obtain good segmentation results

since the image intensity values are unable to be approximated well by two constants c_1 and c_2 .

The locally binary fitting model (Li et al., 2008) introduced a local gaussian kernel G_σ with variance σ to the active contour energy:

$$\begin{aligned}
 E^{\text{LBF}}(\gamma, u_1, u_2) &= \alpha_1 \int_{\Omega} \int_B G_\sigma(\mathbf{x}, \mathbf{y})(I(\mathbf{x}) - u_1(\mathbf{y}))^2 d\mathbf{x}d\mathbf{y} \\
 &\quad + \alpha_2 \int_{\Omega} \int_{B^c} G_\sigma(\mathbf{x}, \mathbf{y})(I(\mathbf{x}) - u_2(\mathbf{y}))^2 d\mathbf{x}d\mathbf{y} + \lambda \int_0^1 \|\gamma'(t)\| dt \\
 &= \alpha_1 \int_B \int_{\Omega} G_\sigma(\mathbf{x}, \mathbf{y})(I(\mathbf{y}) - u_1(\mathbf{x}))^2 d\mathbf{y}d\mathbf{x} \\
 &\quad + \alpha_2 \int_{B^c} \int_{\Omega} G_\sigma(\mathbf{x}, \mathbf{y})(I(\mathbf{y}) - u_2(\mathbf{x}))^2 d\mathbf{y}d\mathbf{x} + \lambda \int_0^1 \|\gamma'(t)\| dt
 \end{aligned} \tag{6.7}$$

$$= \alpha_1 \int_B \mathcal{J}_1(\mathbf{x})d\mathbf{x} + \alpha_2 \int_B \mathcal{J}_2(\mathbf{x})d\mathbf{x} + \lambda \int_0^1 \|\gamma'(t)\| dt, \tag{6.8}$$

where the functions \mathcal{J}_1 and \mathcal{J}_2 are defined as

$$\mathcal{J}_1(\mathbf{x}) = \int_{\Omega} G_\sigma(\mathbf{x}, \mathbf{y})(I(\mathbf{y}) - u_1(\mathbf{x}))^2 d\mathbf{y}, \tag{6.9}$$

$$\mathcal{J}_2(\mathbf{x}) = \int_{\Omega} G_\sigma(\mathbf{x}, \mathbf{y})(I(\mathbf{y}) - u_2(\mathbf{x}))^2 d\mathbf{y}. \tag{6.10}$$

The Gaussian kernel G_σ obeys

$$\int_{\mathbb{R}^2} G_\sigma(\mathbf{x}, \mathbf{y})d\mathbf{y} = 1,$$

for any point $\mathbf{x} \in \Omega$. Based on the variation level set framework (Zhao et al., 1996), the locally binary fitting model energy E^{LBF} can be expressed as

$$\begin{aligned}
 E^{\text{LBF}}(\Phi, u_1, u_2) &= \alpha_1 \int_{\Omega} \mathcal{J}_1(\mathbf{x})H(\Phi(\mathbf{x}))d\mathbf{x} + \alpha_2 \int_{\Omega} \mathcal{J}_2(\mathbf{x})H(-\Phi(\mathbf{x}))d\mathbf{x} \\
 &\quad + \lambda \int_{\Omega} \|\nabla H(\Phi(\mathbf{x}))\|d\mathbf{x}.
 \end{aligned} \tag{6.11}$$

Keeping u_1 and u_2 fixed, the corresponding level set evolution equation is

$$\begin{aligned}
 \frac{\partial \Phi}{\partial \tau} &= -\frac{\partial E^{\text{LBF}}}{\partial \Phi} \\
 &= \delta(\Phi) \left(\lambda \operatorname{div} \left(\frac{\nabla \Phi}{\|\nabla \Phi\|} \right) + \alpha_2 \mathcal{J}_2 - \alpha_1 \mathcal{J}_1 \right).
 \end{aligned} \tag{6.12}$$

Fixing Φ , we can obtain u_1 and u_2 by

$$u_1(\mathbf{x}) = \frac{(G_\sigma * I H(\Phi))(\mathbf{x})}{(G_\sigma * H(\Phi))(\mathbf{x})}, \quad u_2(\mathbf{x}) = \frac{(G_\sigma * I H(-\Phi))(\mathbf{x})}{(G_\sigma * H(-\Phi))(\mathbf{x})}, \quad (6.13)$$

by minimizing (6.7).

6.2.4 Pairwise Region-based Active Contours Energy

The pairwise active contours model was first introduced by [Sumengen and Manjunath \(2006\)](#) based on the dissimilarity measurement between pixels in different regions. ([Bertelli et al., 2008](#); [Dubrovina-Karni et al., 2015](#)) extended this model to deal with the multi-region image segmentation problem. [Jung et al. \(2012\)](#) introduced a non-local active contours model by computing the distance between a pair of patches. This model extended the pixel-based dissimilarity measurement ([Sumengen and Manjunath, 2006](#)) to a nonlocal patch-based similarity measurement.

For simplicity, we introduce the following notations:

$$\mathcal{D}_x(B) = \int_B D(\mathbf{x}, \mathbf{y}) d\mathbf{y}, \quad \mathcal{H}_x(B) = \int_B G_\sigma(\mathbf{x}, \mathbf{y}) d\mathbf{y}, \quad (6.14)$$

where D is the pairwise interaction kernel ([Jung et al., 2012](#)) defined by

$$D(\mathbf{x}, \mathbf{y}) = G_\sigma(\mathbf{x}, \mathbf{y}) d(p_x, p_y), \quad (6.15)$$

where $d(p_x, p_y)$ denotes the distance between two patches centred at \mathbf{x} and \mathbf{y} . A patch is defined by

$$p_x(t) = I(\mathbf{x} + t), \quad t \in \varpi_p := \left[-\frac{\varsigma}{2}, \frac{\varsigma}{2}\right]^2, \quad (6.16)$$

where ς^2 is the size of the patch. A typical definition for $d(\cdot, \cdot)$ is the weighted L^2 patch distance ([Jung et al., 2012](#)):

$$d(p_x, p_y) = \int_{\varpi_p} G_a(t) \|p_x(t) - p_y(t)\|^2 dt, \quad (6.17)$$

where G_a is a Gaussian kernel with variance a obeying that

$$\int_{\mathbb{R}^2} G_a(t) dt = 1.$$

The patch-based non-local active contours energy can be expressed as

$$E^{\text{PW}}(\gamma) = \int_B \frac{\mathcal{D}_{\mathbf{x}}(B)}{\mathcal{H}_{\mathbf{x}}(B)} d\mathbf{x} + \int_{B^c} \frac{\mathcal{D}_{\mathbf{x}}(B^c)}{\mathcal{H}_{\mathbf{x}}(B^c)} d\mathbf{x} + \lambda \int_0^1 \|\gamma'(t)\| dt, \quad (6.18)$$

The shape gradient of the energy

$$\mathcal{E}^{\text{PW}} := \int_B \frac{\mathcal{D}_{\mathbf{x}}(B)}{\mathcal{H}_{\mathbf{x}}(B)} d\mathbf{x}, \quad (6.19)$$

at shape $B \subset \Omega$ can be expressed for all $\mathbf{z} \in \partial B$ as

$$\nabla \mathcal{E}^{\text{PW}}(B)(\mathbf{z}) = \frac{\mathcal{D}_{\mathbf{z}}(B)}{\mathcal{H}_{\mathbf{z}}(B)} + \int_B \frac{D(\mathbf{x}, \mathbf{z})\mathcal{H}_{\mathbf{x}}(B) - G_{\sigma}(\mathbf{x}, \mathbf{z})\mathcal{D}_{\mathbf{x}}(B)}{\mathcal{H}_{\mathbf{x}}^2(B)} d\mathbf{x}. \quad (6.20)$$

6.3 Region-based Energy Minimization Problem

In this section, we proposed a new region-based active contours model combining with the Eikonal PDE-inspired minimal paths framework.

6.3.1 Linear Approximation of the Region-based Energy

Let $\Omega \subset \mathbb{R}^2$ be a bounded image domain. Within this chapter, a shape is an arbitrary measurable subset $A \subset \Omega$ with a rectifiable boundary ∂A . We denote by χ_A characteristic function of shape A :

$$\chi_A(\mathbf{x}) := \begin{cases} 1, & \mathbf{x} \in A, \\ 0, & \text{otherwise.} \end{cases} \quad (6.21)$$

We fix an exponent $p \in (1, 2)$ and denote by $q \in (2, \infty)$ the conjugate exponent of p , defined by

$$\frac{1}{p} + \frac{1}{q} = 1.$$

For any shape $B \subset \Omega$, the characteristic function obeys that $\chi_B \in L^p(\Omega)$.

A region-based functional $F : L^p(\Omega) \rightarrow \mathbb{R}$ is differentiable at $\chi_{B_0} \in L^p(\Omega)$ iff there exists $c \in \mathbb{R}$ and a functional $f \in L^q(\Omega)$ such that for all $\chi_B \in L^p(\Omega)$:

$$\begin{aligned} F(\chi_B) &= c + \int_{\Omega} \chi_B(\mathbf{x}) f(\mathbf{x}) d\mathbf{x} + o(\|\chi_{B_0} - \chi_B\|_p) \\ &= c + \int_B f(\mathbf{x}) d\mathbf{x} + o(\|\chi_{B_0} - \chi_B\|_p). \end{aligned} \quad (6.22)$$

In that case, c and f are uniquely determined and independent to χ_B . Scalar function f is the first variation of F with respect to χ_{B_0} :

$$f := F'(\chi_{B_0}). \tag{6.23}$$

For the sake of simplicity, in the following, we make use of the following notation

$$F'_B := F'(\chi_B).$$

By (6.22), for any $B \in \Omega$ close to $B_0 \in \Omega$, we have

$$F(\chi_B) = \underbrace{\int_B F'_{\chi_{B_0}}(\mathbf{x})d\mathbf{x}}_{\dagger} + c, \tag{6.24}$$

which means that the functional $F(\chi_B)$ can be naturally approximated by a linear region term \dagger in (6.24).

The most popular functional appearing in shape optimization or curve evolution are the sum of a linear region term, and a penalization of the Euclidean curve length $\ell(\partial A)$ of the boundary ∂A :

$$\mathcal{E}(A) = \alpha F(\chi_A) + \ell(\partial A). \tag{6.25}$$

The energy functional (6.25) can be minimized by *shape or curve evolution method*, providing an initial shape A_0 is given. Using (6.24), $\mathcal{E}(A)$ can be expressed as

$$\mathcal{E}(A) = \alpha \int_A F'_{\chi_{A_0}}(\mathbf{x})d\mathbf{x} + \ell(\partial A) \tag{6.26}$$

$$= \alpha \int_A f(\mathbf{x})d\mathbf{x} + \ell(\partial A), \tag{6.27}$$

where α is a positive constant and $f = F'_{\chi_{A_0}}$ is the first variation of F with respect to χ_{A_0} . Quantity $\ell(\partial A)$ denotes the standard Euclidean curve length ∂A , which is also the 1-dimensional Hausssdoff measure.

6.3.2 Time-Dependent Gradient Descent Method for Energy Minimization

Classical shape or curve evolution approaches optimize the energy functional \mathcal{E} (6.26) by using the corresponding linear Euler-Lagrange equations and the time-dependent gradient descent method (Jung et al., 2012; Tsai et al., 2001; Zhu and Yuille, 1996). In other words, these approaches make use of the gradient descent flows as the energy minimization way.

Let $\tau \geq 0$ denotes the time and \mathcal{N} denote the outward normal of a parametric active curve $\Gamma : [0, \infty) \times [0, 1] \rightarrow \Omega$, where $\Gamma(0, \cdot) = \partial A_0(\cdot)$. The curve evolution equation in terms of the gradient descent flow of the energy functional \mathcal{E} is

$$\frac{\partial}{\partial \tau} \Gamma = \left(-\alpha f(\Gamma) + \kappa \right) \mathcal{N}, \tag{6.28}$$

where κ is the curvature of the curve Γ . The gradient descent flow-based minimization scheme is known to be sensitive to the local minima and costs expensive computation time.

Level Set Curve Evolution Scheme

The level set method (Osher and Sethian, 1988) is one of the most popular tools for curve evolution, where the curves can be denoted by the zero-level set. Letting $\beta : \Omega \rightarrow \mathbb{R}$ denote the front propagation speed, the respective level set evolution equation (Osher and Sethian, 1988) can be expressed as

$$\frac{\partial \phi}{\partial \tau} = \beta \|\nabla \phi\|. \tag{6.29}$$

Corresponding to the gradient descent flow (6.28), the level set curve evolution equation is

$$\frac{\partial \phi}{\partial \tau} = -\alpha f \|\nabla \phi\| + \nabla \cdot \left(\frac{\nabla \phi}{\|\nabla \phi\|} \right) \|\nabla \phi\|, \tag{6.30}$$

where the curvature κ is expressed by

$$\kappa = \nabla \cdot \left(\frac{\nabla \phi}{\|\nabla \phi\|} \right).$$

Zhao et al. (1996) proposed a variational level set approach, which was adopted by (Chan and Vese, 2001; Chan et al., 2000; Li and Acton, 2007; Vese and Chan, 2002) for active contours and image segmentation. The details for this popular numerical tool can be found in Section 6.2.2.

In the course of the level set evolution, sometimes the level set function ϕ should be reinitialized as signed distance map, as discussed in Section 2.2.1. Moreover, the level set evolution scheme requires a small step for stability, which leads to high computation time. In this chapter, we solve the same region-based energy minimization problem in a different way, which is based on a geodesic energy minimization scheme and non-linear Eikonal PDE. The first step of the proposed method is to interpret the region-based energy functional by a Finsler geodesic curve energy via the divergence theorem and a Finsler metric, as discussed in Section 6.4.

6.4 Finsler Geodesic Energy Interpretation of the Region-based Energy

We consider the minimization of \mathcal{E} in (6.26) in the manner of shape evolution: for a given shape A_0 with boundary ∂A_0 , we aim to finding a contour ∂A^* as the boundary of shape A^* minimizing \mathcal{E} , where A^* is close to A . We make use of a tubular neighbourhood domain $U \subset \Omega$ of the contour ∂A_0 to restrict the searching space for the contour ∂A^* such that the expected contour obeys $\partial A^* : [0, \ell_{\partial A^*}] \rightarrow U$, where $\ell_{\partial A^*}$ is the Euclidean curve length of ∂A^* . For this purpose, we firstly define a vector field $\mathcal{V}_\perp \in L^2(U, \mathbb{R}^2)$ such that

$$\nabla \cdot \mathcal{V}_\perp(\cdot) = \alpha f(\cdot) \chi_U(\cdot), \tag{6.31}$$

where $\nabla \cdot$ is the classical divergence operator: for any $\mathbf{x} = (x, y)$ one has

$$\nabla \cdot \mathcal{V}_\perp(\mathbf{x}) = \frac{\partial}{\partial x} \mathcal{V}_\perp(\mathbf{x}) + \frac{\partial}{\partial y} \mathcal{V}_\perp(\mathbf{x}).$$

where χ_U is the characteristic function of tubular neighbourhood region U .

Tubular Neighbourhood-Constrained Region-based Energy

We consider a collection \mathcal{B}_U of all U -constrained paths γ where

$$\gamma : [0, 1] \rightarrow U, \tag{6.32}$$

The energy value $\mathcal{E}(A)$ for a shape A with boundary involved in \mathcal{B}_U can be rewritten as

$$\mathcal{E}(A) = \alpha \int_A F'_{\chi_{A_0}}(\mathbf{x}) \chi_U(\mathbf{x}) d\mathbf{x} + \alpha \int_{A_0 \setminus \{A_0 \cap U\}} F'_{\chi_{A_0}}(\mathbf{x}) d\mathbf{x} + \ell(\gamma) \tag{6.33}$$

$$= \alpha \int_A F'_{\chi_{A_0}}(\mathbf{x}) \chi_U(\mathbf{x}) d\mathbf{x} + \ell(\gamma) + Constant \tag{6.34}$$

$$= \alpha \int_{A \cap U} f(\mathbf{x}) \chi_U(\mathbf{x}) d\mathbf{x} + \ell(\gamma) + Constant, \tag{6.35}$$

where A_0 is the given initial shape and U is the tubular neighbourhood region of the boundary ∂A_0 . The scalar function f is the shape gradient of F at χ_{A_0} . Since A_0 is a fixed shape, the term

$$\alpha \int_{A_0 \setminus A_0 \cap U} F'_{\chi_{A_0}}(\mathbf{x}) d\mathbf{x},$$

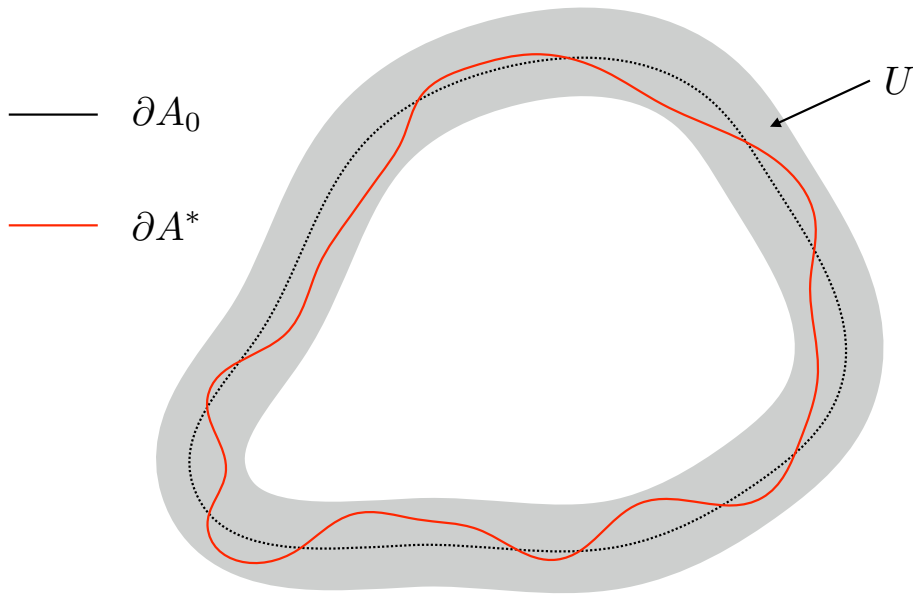


FIGURE 6.2: Illustration for the U-constrained shape evolution. Dash curve denotes the boundary ∂A_0 of the original shape A_0 and red curve is the expect boundary ∂A^* of the desired shape A^* .

is a constant. In Fig. 6.2, we illustrate the boundaries ∂A_0 of the original shape A_0 and the tubular neighbourhood region U of ∂A_0 . The goal is to search for an optimal shape A^* with boundary ∂A^* under the constraint:

$$\partial A^* \in \mathcal{B}_U,$$

to minimize \mathcal{E} formulated in (6.35). For this purpose, we define an energy \mathcal{E}_U such that $\mathcal{E}_U(A) = \infty$ if $\partial A \notin \mathcal{B}_U$, otherwise one has

$$\mathcal{E}_U(A) = \alpha \int_{A \cap U} f(\mathbf{x}) \chi_U(\mathbf{x}) d\mathbf{x} + \ell(\gamma) \tag{6.36}$$

$$= \int_{A \cap U} \nabla \cdot \mathcal{V}_\perp(\mathbf{x}) d\mathbf{x} + \ell(\gamma) \tag{6.37}$$

$$= \int_0^1 \langle \mathcal{V}_\perp(\gamma(t)), \mathcal{N}(t) \rangle \|\gamma'(t)\| dt + \ell(\gamma), \tag{6.38}$$

where \mathcal{N} is the outward normal of the curve $\gamma := \partial A \in \mathcal{B}_U$.

Equation (6.36) is obtained by (6.31) and equation (6.37) is obtained by the divergence theorem. We express \mathcal{E}_U in (6.38) by

$$\begin{aligned} \mathcal{E}_U(A) &= \int_0^1 \langle M \mathcal{V}_\perp(\gamma(t)), M \mathcal{N}(t) \|\gamma'(t)\| \rangle dt + \ell(\gamma) \\ &= \int_0^1 \left(\|\gamma'(t)\| + \langle \mathcal{V}(\gamma(t)), \gamma'(t) \rangle \right) dt, \end{aligned} \tag{6.39}$$

where M is a **clockwise** rotation matrix with rotation angle $\theta = \pi/2$, $\mathcal{V}(\cdot) = M \mathcal{V}_\perp(\cdot)$, and $ds = \|\gamma'(t)\| dt$, $t \in [0, 1]$. γ' is the tangent vector of γ in **clockwise** order. Indeed, $\mathcal{T} = M \mathcal{N}$ is the tangent vector and

$$\begin{aligned} \gamma'(t) &= \|\gamma'(t)\| \mathcal{T}(t) \\ &= \|\gamma'(t)\| M \mathcal{N}(t), \quad \forall t \in [0, 1]. \end{aligned}$$

We consider a function $K : \Omega \times \mathbb{R}^2 \rightarrow \mathbb{R}^+$ as follows:

$$K(\mathbf{x}, \mathbf{u}) = \begin{cases} \|\mathbf{u}\| + \langle \mathcal{V}(\mathbf{x}), \mathbf{u} \rangle, & \forall \mathbf{x} \in U, \\ \infty, & \text{otherwise,} \end{cases} \tag{6.40}$$

The term $\|\mathbf{u}\| + \langle \mathcal{V}(\mathbf{x}), \mathbf{u} \rangle$ will be a Finsler metric if it obeys the smallness condition formulated in (2.73), i.e.,

$$\|\mathcal{V}(\mathbf{x})\| < 1, \quad \forall \mathbf{x} \in U. \tag{6.41}$$

6.4.1 Computation of Vector Field \mathcal{V} Over a Subdomain U

We start the discussion of the computation of vector field \mathcal{V} from the Proposition 6.1 below.

Proposition 6.1. *Let $\Omega \subset \mathbb{R}^2$ be a bounded domain. Let $1 \leq p < 2$ and let $f \in L^q(\Omega)$ with*

$$\frac{1}{p} + \frac{1}{q} = 1.$$

Let $U \in \Omega$ be subdomain, and let $\omega \in L^2(\mathbb{R}^2, \mathbb{R}^2)$ solve:

$$\text{minimize} \quad \int_{\mathbb{R}^2} \|\omega(\mathbf{x})\|^2 d\mathbf{x}, \tag{6.42}$$

$$\text{s.t.} \quad \nabla \cdot \omega(\mathbf{x}) = \alpha f(\mathbf{x}) \chi_U(\mathbf{x}), \quad \forall \mathbf{x} \in \Omega. \tag{6.43}$$

Then one has

$$\|\omega\|_{L^\infty} \leq C_* \|f\|_{L^q(U)} (\text{Leb}(U))^e,$$

where $\varrho = \frac{1}{p} - \frac{1}{2}$ and

$$C_* := \frac{2^{\frac{1}{p}-1}}{\sqrt{\pi}(2-p)^{\frac{1}{p}}}.$$

Proof. The solution to the divergence equation (6.43) is known to be $\omega = \nabla\rho$, where ρ solves the Poisson equation

$$\Delta \rho(\mathbf{x}) = f(\mathbf{x}) \chi_U(\mathbf{x}), \quad \forall \mathbf{x} \in \mathbb{R}^2,$$

where Δ denotes the Laplacian operator.

Expressing ρ in terms of the Green kernel we obtain for all $\mathbf{x} \in \mathbb{R}^2$:

$$\rho(\mathbf{x}) = \frac{1}{2\pi} \int_U \ln \|\mathbf{x} - \mathbf{y}\| f(\mathbf{y}) d\mathbf{y}.$$

Therefore, one has

$$\begin{aligned} \omega(\mathbf{x}) &= \nabla \rho(\mathbf{x}) \\ &= \frac{1}{2\pi} \int_U \frac{\mathbf{x} - \mathbf{y}}{\|\mathbf{x} - \mathbf{y}\|} f(\mathbf{y}) d\mathbf{y}, \quad \forall \mathbf{x} \in U. \end{aligned}$$

Let $R_U > 0$ be the radius defined by $\pi R_U^2 = \text{Leb}(U)$, so that the disk $D(0, R_U)$ has the same area as U . Holder's inequality and a rearrangement inequality yield

$$\begin{aligned} 2\pi \|\omega(\mathbf{x})\| &\leq \|f\|_{L^q(U)} \left(\int_U \frac{1}{\|\mathbf{x} - \mathbf{y}\|^p} d\mathbf{y} \right)^{\frac{1}{p}} \\ &\leq \|f\|_{L^q(U)} \left(\int_{D(0, R_U)} \frac{1}{\|\mathbf{z}\|^p} d\mathbf{z} \right)^{\frac{1}{p}}. \end{aligned}$$

Evaluating the right hand side, we conclude the proof: for all $\mathbf{x} \in U$:

$$\begin{aligned} 2\pi \|\omega(\mathbf{x})\| &\leq \left(\int_0^{R_U} \frac{2\pi r}{r^p} dr \right)^{\frac{1}{p}} \|f\|_{L^q(U)} \\ &= \left(\frac{2\pi}{2-p} R_U^{2-p} \right)^{\frac{1}{p}} \|f\|_{L^q(U)} \\ &= \frac{2^{\frac{1}{p}}}{\sqrt{\pi}(2-p)^{\frac{1}{p}}} \text{Leb}(U)^{\varrho} \|f\|_{L^q(U)}. \end{aligned}$$

□

According to Proposition 6.1, the value $\|\omega\|_{L^\infty}$ depends only on the area of subdomain U providing that f is fixed. In other words, $\|\omega\|_{L^\infty} < 1$ holds if U is sufficiently small. Therefore, we can define the vector field $\mathcal{V} = M\omega$, where M is

the clockwise rotation matrix with rotation angle $\theta = \pi/2$. Given a suitable U , one can obtain that $\|\mathcal{V}\|_{L^\infty} < 1$.

In practice, it is difficult to solve the minimization problem (6.42) over \mathbb{R}^2 . Instead, we solve that problem over the tubular neighbourhood region U , i.e.,

$$\text{minimize } \int_U \|\mathcal{V}_\perp(\mathbf{x})\|^2 d\mathbf{x}, \tag{6.44}$$

$$\text{s.t. } \nabla \cdot \mathcal{V}_\perp(\mathbf{x}) = \alpha f(\mathbf{x}), \quad \forall \mathbf{x} \in U, \tag{6.45}$$

which gives good results.

The solution \mathcal{V}_\perp to the minimization problem (6.44) with linear constraint (6.45) admits the variational formulation: find $(\mathcal{V}_\perp, p) \in L^2(U, \mathbb{R}^2) \times H^1(U)$ such that for all (\mathcal{W}, q) in the same spaces one has

$$\begin{cases} \int_U \langle \mathcal{V}_\perp(\mathbf{x}), \mathcal{W}(\mathbf{x}) \rangle d\mathbf{x} + \int_U \langle \nabla p(\mathbf{x}), \mathcal{W}(\mathbf{x}) \rangle d\mathbf{x} = 0, \\ \int_U \langle \mathcal{V}_\perp(\mathbf{x}), \nabla q(\mathbf{x}) \rangle - \int_U f(\mathbf{x})q(\mathbf{x}) d\mathbf{x} = 0. \end{cases} \tag{6.46}$$

We use a finite differences discretization on the pixel grid $h\mathbb{Z}^2 \cap U$, where $h > 0$ is the pixel size. We also store the values of the potentials p and q on a staggered grid so as to improve the accuracy of the gradient operator. The numerical solution to (6.46) can be found in Appendix 6.46.

Recalling that $\gamma : [0, 1] \rightarrow \Omega$ denotes the boundary of shape A . Based on the computed vector field $\mathcal{V} = M \mathcal{V}_\perp$ (M is the clockwise rotation matrix with rotation angle $\theta = \pi/2$), the regional energy $\mathcal{E}_U(A)$ (6.39) is equivalent to a geodesic energy $\mathcal{L}(\gamma)$:

$$\mathcal{L}(\gamma) = \int_0^1 K(\gamma(t), \gamma'(t)) dt. \tag{6.47}$$

In the sense of shape evolution, a shape A_0 is given as initialization. In this case, the domain U is the minimal geodesic searching space and should be a tubular neighbourhood region of curve ∂A_0 . By reducing the width of the tubular neighbourhood U of ∂A_0 , we can limit its area as well, and thus obtain $\|\mathcal{V}\|_{L^\infty} = \|\mathcal{V}_\perp\|_{L^\infty} < 1$ by Proposition 6.1 as desired. However this also limits the search region for the expected path ∂A^* , which may ultimately lead to the algorithm failure if the tubular neighbourhood width is less than the pixel size. We use two methods to mitigate these issues. The first method is to make the parameter $\alpha = 1/\|\mathcal{V}\|_{L^\infty} + \epsilon$ (see (6.43)) where ϵ is a small positive constant. Thus $\|\mathcal{V}\|_{L^\infty} < 1$ will always hold for any searching space U .

We make use of the second way in this chapter for extending the size of the search region U , which is to replace the vector field \mathcal{V} with $\tilde{\mathcal{V}}$ defined by

$$\tilde{\mathcal{V}}(\mathbf{x}) := T(\|\mathcal{V}(\mathbf{x})\|) \frac{\mathcal{V}(\mathbf{x})}{\|\mathcal{V}(\mathbf{x})\|}, \quad \forall \mathbf{x} \in U, \quad (6.48)$$

where T is a nonlinear map which is a decreasing function defined as

$$T(\zeta) := 1 - e^{-\mu\zeta}, \quad \forall \zeta \in [0, \infty), \quad (6.49)$$

When ζ is small, we have the approximation

$$T(\zeta) \approx \zeta.$$

Clearly the smallness condition $\|\tilde{\mathcal{V}}\|_{L^\infty} < 1$ is automatically satisfied, and $\tilde{\mathcal{V}}(\mathbf{x})$ approximates well $\mathcal{V}(\mathbf{x})$ where its norm $\|\mathcal{V}(\mathbf{x})\|$ is small, $\forall \mathbf{x} \in U$.

Based on the vector field $\tilde{\mathcal{V}}$, a Finsler metric $\mathcal{K} : \Omega \times \mathbb{R}^2 \rightarrow \mathbb{R}^+$ can be constructed by

$$\mathcal{K}(\mathbf{x}, \mathbf{u}) := \begin{cases} \|\mathbf{u}\| + \langle \tilde{\mathcal{V}}_U(\mathbf{x}), \mathbf{u} \rangle, & \text{if } \mathbf{x} \in U, \forall \mathbf{u} \in \mathbb{R}^2 \\ \infty, & \text{otherwise,} \end{cases} \quad (6.50)$$

Therefore, the geodesic energy $\tilde{\mathcal{L}}$ (6.47) is defined by letting $K := \mathcal{K}$

$$\tilde{\mathcal{L}} := \int_0^1 \mathcal{K}(\gamma(t), \gamma'(t)) dt. \quad (6.51)$$

Hybrid Finsler Metric \mathcal{G}

In the expression of the U shape-constrained energy \mathcal{E}_U (6.36), the regularity term for contour γ is the standard Euclidean curve length $\ell(\gamma)$. [Kimmel \(2003\)](#) and [Kimmel and Bruckstein \(2003\)](#) proposed a geodesic curve length regularity term $\ell_g(\gamma)$ combining with an edge indicator function $g : \Omega \rightarrow [1, \infty)$:

$$\ell_g(\gamma) = \int_0^1 g(\gamma(t)) \|\gamma'(t)\| dt, \quad (6.52)$$

to replace the Euclidean curve length regularization term.

The edge indicator g has small values around the desired image features such as edges. Based on (6.52), we have the hybrid Finsler metric \mathcal{G} :

$$\mathcal{G}(\mathbf{x}, \mathbf{u}) = \begin{cases} g(\mathbf{x}) \|\mathbf{u}\| + \langle \tilde{\mathcal{V}}_U(\mathbf{x}), \mathbf{u} \rangle, & \text{if } \mathbf{x} \in U \text{ and } \forall \mathbf{u} \in \mathbb{R}^2 \\ \infty, & \text{otherwise.} \end{cases} \quad (6.53)$$

Since we restrict the lower bound of $g(\mathbf{x}) \geq 1$, the smallness condition for the Finsler metric \mathcal{G}

$$\tilde{\mathcal{V}}(\mathbf{x}) < g(\mathbf{x}), \quad \forall \mathbf{x} \in U,$$

will always hold.

Overview of the Proposed Shape Evolution Algorithm

The minimization of \mathcal{L} (6.47) is transferred to the minimization of $\tilde{\mathcal{L}}$. Note that since in general we induce $\tilde{\mathcal{L}}$ with a nonlinear mapping T (6.49), there is in fact slight difference in the minimization problems and the results show that our geodesic method is very efficient and robust. Two points guarantee that using the non-linear mapping T is reasonable:

- The minimization of \mathcal{L} in (6.47) is relevant to both the directions of the curve and the norm of \mathcal{V} , i.e., minimizing \mathcal{E}_U is to find a shape A^* with boundary $\mathcal{C} : [0, 1] \rightarrow U$, for which the direction $\mathcal{C}'(t)$ for each $t \in [0, 1]$ should be as opposite to $\mathcal{V}(\mathcal{C}(t))$ as possible and the norm $\|\mathcal{V}(\mathcal{C}(t))\|$ should be as large as possible, giving the relevance between the minimization problems of \mathcal{E}_U and $\tilde{\mathcal{L}}$. Introducing the nonlinear mapping T will not modify both goals of the minimization problems.
- When the Finsler geodesic evolution scheme as discussed in Algorithm 8 tends to stabilize, one can reduce the width of tubular neighbourhood U . Thus $T(\|\mathcal{V}(\mathbf{x})\|) \approx \|\mathcal{V}(\mathbf{x})\|$, $\forall \mathbf{x} \in U$ as $\|\mathcal{V}(\mathbf{x})\|$ is small. Moreover, We experimentally observe that near the centreline of U , the values of $\|\mathcal{V}\|$ will become very small, leading to a good approximation of \mathcal{V} by $\tilde{\mathcal{V}}$.

The rest part of this chapter will be devoted to minimize the geodesic energy $\tilde{\mathcal{L}}$ (6.51) by a iterative shape evolution method. The basic idea is to seek a family of clockwise contours \mathcal{C}_τ with $\tau \in \{1, 2, 3, \dots\}$ which converge to the expected object boundary as $\tau \rightarrow \infty$, where \mathcal{C}_0 is the boundary of an initial shape. In each iteration τ , this shape evolution procedure involves two steps:

1. Find a closed contour \mathcal{C}^* by a Finsler geodesics extraction strategy to minimize $\tilde{\mathcal{L}}$ with respect to the metric \mathcal{K} and the tubular neighbourhood U . This is described in Line 2 of the Alogrithm 8.
2. Update the Finsler metric \mathcal{K} in Line 7 of the Alogrithm 8, relying on the computation of first variation f (6.23) and tubular neighbourhood U .

In the following sections, we give the details to the construction of the neighbourhood U and the Finsler geodesics extraction strategy.

Algorithm 8 Summary algorithm of the entire shape evolution procedure

Input: Initial shape A_0 with boundary \mathcal{C}_0 .

Output: Final contour \mathcal{C}_∞ .

Initialization:

- Compute the first variation f_0 and tubular neighbourhood U_0 in terms of \mathcal{C}_0 .
- Compute the Finsler metric \mathcal{K}_0 using eqn. (6.50).
- $\tau \leftarrow 0$.

1: **while** ($d_H > \epsilon$) **do**

2: Find a closed contour \mathcal{C}^* minimizing $\tilde{\mathcal{L}}$ with respect to the metric \mathcal{K}_τ (6.50) and U_τ by a Finsler minimal paths extraction strategy.

3: Compute the Hausdorff distance d_H of paths \mathcal{C}^* and \mathcal{C}_τ .

4: $\tau \leftarrow \tau + 1$.

5: $\mathcal{C}_\tau \leftarrow \mathcal{C}^*$.

6: Update the first variation f_τ (6.23) and the tubular neighbourhood U_τ in terms of \mathcal{C}_τ .

7: Update the Finsler metric \mathcal{K}_τ using eqn. (6.50).

8: **end while**

6.5 Tubular Neighbourhood Construction

A tubular neighbourhood U of γ as the boundary of shape A is constructed as the set of points within a given geodesic distance d of γ :

$$U := \{\mathbf{x} \in \Omega; \mathcal{D}_\gamma(\mathbf{x}) < d\}, . \quad (6.54)$$

The geodesic distance map or minimal action map $\mathcal{D}_\gamma(\mathbf{x})$ from point $\mathbf{x} \in \Omega$ to the curve γ obeys the following isotropic Eikonal PDE:

$$\begin{cases} \|\nabla \mathcal{D}_\gamma(\mathbf{x})\| = P(\mathbf{x}), & \forall \mathbf{x} \in \Omega, \\ \mathcal{D}_\gamma(\gamma(t)) = 0, & \forall t \in [0, 1]. \end{cases} \quad (6.55)$$

This isotropic Eikonal equation can be efficiently solved using fast marching algorithm (Sethian, 1999).

If one sets $P \equiv 1$ identically, then U is a standard tubular neighbourhood of width d centred on the path γ . However, the algorithm efficiency can be improved by using non-cantered tubular neighbourhoods, based on a guess of the likely evolution of the boundary, and obtained using the following potential:

$$P(\mathbf{x}) := \begin{cases} \delta, & \text{if } \mathbf{x} \in A \text{ and } f(\mathbf{x}) > 0, \\ \delta, & \text{if } \mathbf{x} \in A^c \text{ and } f(\mathbf{x}) < 0, \\ \frac{1}{\delta}, & \text{otherwise,} \end{cases} \quad (6.56)$$

where $\delta > 1$ is a given constant, and $A^c := \Omega \setminus A$ is the complement of the shape $A \subset \Omega$.

6.6 Finsler Minimal Paths Extraction Strategy for the Minimization of $\tilde{\mathcal{L}}$

Let τ denote the iteration order. We present two Finsler geodesics extraction methods to minimize $\tilde{\mathcal{L}}$ providing that the metric \mathcal{K}_τ the tubular neighbourhood region U_τ , and a shape A_τ is given, with boundary $\mathcal{C}_\tau : [0, 1] \rightarrow \Omega$. The first method is named **contour initialization**, where the initial guess is a closed contour. The second method is called **fixed points initialization**. For the contour initialization method, we need to sample a set vertices from the current closed contour, where the vertices set involves N_s vertices.

6.6.1 Contour Initialization

6.6.1.1 In Case $N_s = 2$

We present a method to minimize the geodesic energy $\tilde{\mathcal{L}}$ by sampling two vertices \mathbf{s} and \mathbf{z} from the contour \mathcal{C}_τ . The closed contour \mathcal{C}_τ is decomposed into two curves: $\Upsilon_\curvearrowright, \Upsilon_\curvearrowleft : [0, 1] \rightarrow U_\tau$ with common end points $\Upsilon_\curvearrowright(0) = \Upsilon_\curvearrowleft(0) = \mathbf{s}$ and $\Upsilon_\curvearrowright(1) = \Upsilon_\curvearrowleft(1) = \mathbf{z}$, where $\Upsilon_\curvearrowright$ is in clockwise order and Υ_\curvearrowleft is in counter-clockwise order such that

$$\mathcal{C}_\tau(u) = \begin{cases} \Upsilon_\curvearrowright(2u), & \text{if } 0 \leq u \leq \frac{1}{2} \\ \Upsilon_\curvearrowleft(2 - 2u), & \text{if } \frac{1}{2} < u \leq 1. \end{cases} \quad (6.57)$$

We introduce a new path $\Upsilon_\epsilon := [\Upsilon_\curvearrowright(0 \rightarrow \epsilon)] \cup [\Upsilon_\curvearrowleft(0 \rightarrow \epsilon)]$ with $\epsilon < 1$, where a path $\gamma_\epsilon := [\Upsilon_\curvearrowleft(0 \rightarrow \epsilon)]$ is defined as a part of Υ_\curvearrowleft such that

$$\gamma_\epsilon(t) : [0, \epsilon] \rightarrow U_\tau, \text{ and } \gamma_\epsilon(t) = \Upsilon_\curvearrowleft(t), t \in [0, \epsilon].$$

In Fig. 6.3(a), $\Upsilon_\curvearrowright$ and Υ_\curvearrowleft are denoted by red curve and cyan curve respectively.

By Eqn. (6.55), we define the tubular neighbourhood regions $\Theta_\epsilon, \Theta_\curvearrowright$ and Θ_\curvearrowleft for the the paths $\Upsilon_\epsilon, \Upsilon_\curvearrowright \cup [\Upsilon_\curvearrowleft(0 \rightarrow \epsilon)]$ and $\Upsilon_\curvearrowleft \cup [\Upsilon_\curvearrowright(0 \rightarrow \epsilon)] \subset U_\tau$ respectively. This is done by computing the geodesic distance maps based on the potential P (6.56) from each paths respectively. In Figs. 6.3(a) to (d), we demonstrate the tubular neighbourhood regions $U_\tau|_{\tau=0}, \Theta_\epsilon, \Theta_\curvearrowright$ and Θ_\curvearrowleft respectively. Based on these definitions, we compute the minimal action map $\mathcal{U}_\curvearrowright$ with respect to

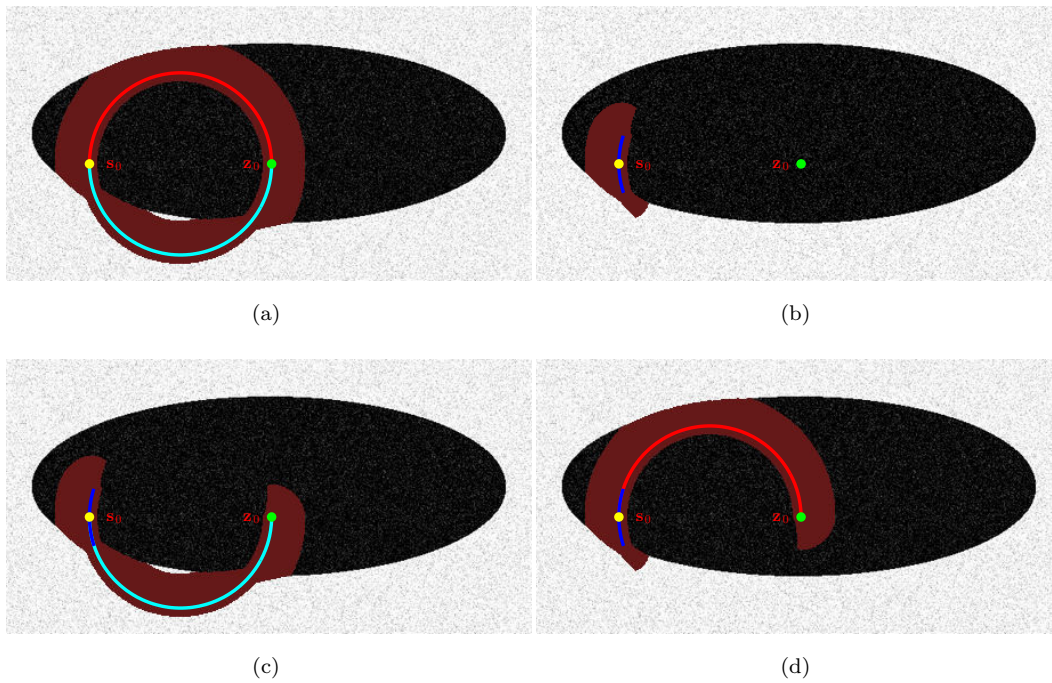


FIGURE 6.3: Tubular neighbourhood regions for $\tau = 0$, where we denote the neighbourhood regions by red shadow. **(a)** Neighbourhood region U_0 for contour \mathcal{C}_0 , which consists of two paths Υ_1 (cyan curve) and Υ_2 (red curve). **(b)** Neighbourhood region Θ_0 for curve Υ_0 (blue curve). **(c)** Neighbourhood region Θ_1 for path $\Upsilon_1 \cup [\Upsilon_2(0 \rightarrow \epsilon)]$. **(d)** Neighbourhood region Θ_2 for path $\Upsilon_2 \cup [\Upsilon_1(0 \rightarrow \epsilon)]$.

Finsler metric \mathcal{K}_τ (6.50) from the initial source point \mathbf{s} by the Θ_\curvearrowright -constrained fast marching algorithm (Mirebeau, 2014b). Similarly, we can compute the minimal action map $\mathcal{U}_\curvearrowright$ with respect to Θ_\curvearrowright with the same initial source point and the inverse Finsler metric computed by vector field $-\tilde{\mathcal{V}}$ using (6.50). We define a saddle point \mathbf{z}^* by

$$\mathbf{z}^* = \arg \min_{\mathbf{x} \in \Theta_0} \{\mathcal{U}_\curvearrowright(\mathbf{x}) + \mathcal{U}_\curvearrowleft(\mathbf{x})\}. \quad (6.58)$$

Using the saddle point \mathbf{z}^* , the geodesics $\mathcal{C}_\curvearrowright$ (resp. $\mathcal{C}_\curvearrowleft$) can be tracked by solving the ODE in (2.76) with respect to minimal action map $\mathcal{U}_\curvearrowright$ (resp. $\mathcal{U}_\curvearrowleft$). Thus, geodesics $\mathcal{C}_\curvearrowright$ and $\mathcal{C}_\curvearrowleft$ have the common end points \mathbf{s} and \mathbf{z}^* .

The value of $\mathcal{U}_\curvearrowright(\mathbf{z}^*) + \mathcal{U}_\curvearrowleft(\mathbf{z}^*)$ is a minimum of the following energy:

$$L(\gamma_\curvearrowright, \gamma_\curvearrowleft) = \int_0^1 \left(\mathcal{K}(\gamma_\curvearrowright(t), \gamma_\curvearrowright'(t)) + \mathcal{K}(\gamma_\curvearrowleft(t), -\gamma_\curvearrowleft'(t)) \right) dt,$$

for any regular curves $\gamma_\curvearrowright : [0, 1] \rightarrow \Theta_\curvearrowright$ and $\gamma_\curvearrowleft : [0, 1] \rightarrow \Theta_\curvearrowleft$ with common end point $\gamma_\curvearrowright(0) = \gamma_\curvearrowleft(0) = \mathbf{s}$. Since $\mathcal{C}_\curvearrowright$ and $\mathcal{C}_\curvearrowleft$ are geodesics, one has $L(\mathcal{C}_\curvearrowright, \mathcal{C}_\curvearrowleft) \leq$

$L(\Upsilon_{\curvearrowright}, \Upsilon_{\curvearrowleft})$. The desired closed geodesic $\mathcal{C}_{\tau+1} : [0, 1] \rightarrow U_{\tau}$ can be constructed by

$$\mathcal{C}_{\tau+1}(u) := \begin{cases} \mathcal{C}_{\curvearrowright}(2u), & \text{if } 0 \leq u \leq \frac{1}{2} \\ \mathcal{C}_{\curvearrowleft}(2-2u), & \text{if } \frac{1}{2} < u \leq 1. \end{cases} \quad (6.59)$$

In the course of shape evolution algorithm (see Algorithm 8), if the iteration order $\tau = 0$, then \mathbf{s} can be chosen randomly from the initial contour \mathcal{C}_0 . Otherwise, we set \mathbf{s} for the $(\tau + 1)$ -th iteration to be the saddle point \mathbf{z}^* at the τ -th iteration. In any iteration step, the vertex \mathbf{z} is selected such that the two splitted curves have the same Euclidean curve length.

6.6.1.2 In Case $N_s \geq 3$

We sample a collection of successive vertices from the given closed contour \mathcal{C}_{τ} in clockwise order such that \mathcal{C}_{τ} can be decomposed into a set of paths $\Upsilon_{\tau,i}$, where $i \in \{1, 2, \dots, N_s\}$ with $N_s \geq 3$ by these vertices. Let us denote the collection of the successive vertices by $\Lambda^{\tau} := \{\mathbf{p}_i^{\tau}, i \in \{1, 2, \dots, N_s\}\}$, by which the geodesic energy $\tilde{\mathcal{L}}$ can be expressed by:

$$\tilde{\mathcal{L}}(\mathcal{C}_{\tau}) = \sum_{i=1}^{N_s} \tilde{\mathcal{L}}(\Upsilon_{\tau,i}) = \sum_{i=1}^{N_s} \int_0^1 \mathcal{K}_{\tau}(\Upsilon_{\tau,i}(t), \Upsilon'_{\tau,i}(t)) dt. \quad (6.60)$$

Similarly to the procedure for $N_s = 2$ above, for each path $\Upsilon_{\tau,i}$ we can construct a tubular neighbourhood region $\Theta_i \subset U_{\tau}$. The two end points of path $\Upsilon_{\tau,i}$ are $\mathbf{p}_i^{\tau}, \mathbf{p}_{i+1}^{\tau} \in \Lambda^{\tau}$. Taking \mathbf{p}_i^{τ} as initial source point and \mathbf{p}_{i+1}^{τ} as end point, we perform the $\Theta_{\tau,i}$ constrained fast marching method to obtained the minimal action map with respect to the Finsler metric \mathcal{K}_{τ} . The geodesic $\Upsilon_{\tau,i}^*$ can be obtained by solving the ODE in (2.76). The expected closed contour \mathcal{C}_{τ} can be obtained by

$$\mathcal{C}_{\tau+1} = \Upsilon_{\tau,1}^* \cup \Upsilon_{\tau,2}^* \cup \dots \cup \Upsilon_{\tau,N_s}^*.$$

Since $\Upsilon_{\tau,i}^*$ are geodesics, we have $\mathcal{C}_{\tau+1} \leq \mathcal{C}_{\tau}$. In the course of shape evolution algorithm described in Algorithm 8:

1. If the iteration order $\tau = 0$, the vertices in Λ^0 are sampled such that the values of the Euclidean curve length for each path $\Upsilon_{0,i}$ are identical.
2. If the iteration order $\tau > 0$, each vertex \mathbf{p}_i^{τ} is identified as the middle point of the path $\Upsilon_{\tau-1,i}$, i.e., $\mathbf{p}_i^{\tau} = \Upsilon_{\tau-1,i}(\frac{1}{2})$.

6.6.2 Fixed Points Initialization

Suppose that the vertices collection $\Lambda^0 := \{\mathbf{p}_i, i \in \{1, 2, \dots, N_s\}\}$ in the procedure of contour initialization with $N_s \geq 3$ (see Section 6.6.1.2) is given by the user, where the vertices \mathbf{p}_i are distributed at the desired boundary in a clockwise order. At the $\tau = 0$ iteration, we link these vertices by straight lines to form a closed contour and construct the tubular neighbourhood region U_0 and Finsler metric \mathcal{K}_0 . The geodesics $\Upsilon_{\tau,i}^*$ is extracted in the same way as discussed in Section 6.6.1.2 can be used to identify the geodesics, except that we do not resample the vertices \mathbf{p}_i since they are fixed in each iteration τ .

This fixed points initialization incorporate the user constrained information and thus can obtain better results than the traditional active contours models based on local region information.

6.6.3 Computation of f for various types of Region-based Active Contours Energies

In this section, we give the first variation f (6.23) of the regional terms F in (6.25) of various types of active contours energy functionals presented in Sections 6.2.2 to 6.2.4. Note that for the regional terms of the Chan-Vese energy E^{CV} (6.2), we get rid of the ballon force term.

The first variation (or shape gradient) f^{CV} of the region-based term of the Chan-Vese energy E^{CV} (6.2) can be expressed as

$$f^{CV}(\mathbf{x}) = \alpha_1(I(\mathbf{x}) - c_1)^2 - \alpha_2(I(\mathbf{x}) - c_2)^2, \quad \forall \mathbf{x} \in \Omega, \quad (6.61)$$

where c_1 and c_2 are defined in (6.5). Constants α_1 and α_2 are two positive weighted parameters.

Similarly, we can compute the first variation f^{LBF} (6.7) for the region-based term of the locally binary fitting energy E^{LBF} , which can be denoted by

$$f^{LBF}(\mathbf{x}) = \mathcal{J}_1(\mathbf{x}) - \mathcal{J}_2(\mathbf{x}), \quad \forall \mathbf{x} \in \Omega, \quad (6.62)$$

where \mathcal{J}_1 and \mathcal{J}_2 are defined in (6.9) and (6.10) respectively.

Finally, we present the first variation f for region-based term of the pairwise energy E^{PW} (6.18):

$$f^{PW}(\mathbf{x}) = \nabla \mathcal{E}^{PW}(B)(\mathbf{x}) - \nabla \mathcal{E}^{PW}(B^c)(\mathbf{x}), \quad (6.63)$$

where $\nabla \mathcal{E}^{PW}(B)$ is defined in (6.63).

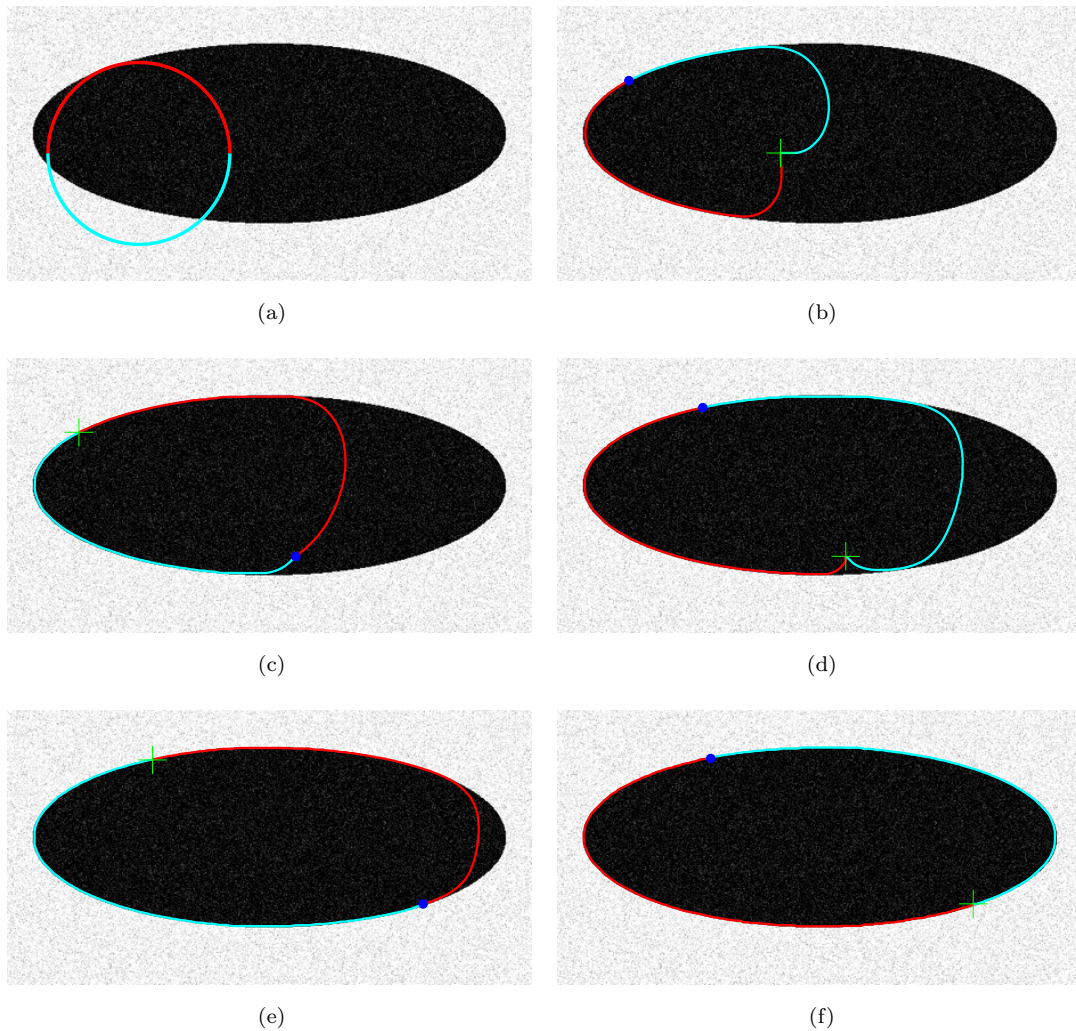


FIGURE 6.4: Shape evolution results of the proposed model with contour initialization and two sampled vertices. **(a)** Original image and initial contour. **(b-e)** Intermediate results. **(f)** Final segmentation results. The green crosses in each figure denote the saddle points. Blue dots denote the saddle points in the last step. Cyan curves denote the counter-clockwise paths and red curves

6.7 Numerical Experiments

In this section, we demonstrate the experimental results of the proposed method.

The numerical solver for the Finsler metric based Eikonal equation is the fast marching algorithm with adaptive stencils proposed by Mirebeau (2014b). We apply a region constraint to this fast marching algorithm, where the details can be seen in Algorithm 5.

In Fig. 6.4, we demonstrate the course of the shape evolution using the proposed model with contour initialization (two vertices are sampled). Fig. 6.4a shows the original image with initial contour. Figs. 6.4b to 6.4e are the intermediate

TABLE 6.1: Computation time and evolution steps (ES) required by the proposed method with regional term f^{CV} under different pairs of (δ, d) in equations (6.54) and (6.56).

(δ, d)	(3, 5)	(3, 10)	(3, 15)	(3, 20)	(3, 25)	(3, 30)	(1, 20)	(3.5, 20)
f^{CV} CPU	11.8s	7.1s	5.6s	5.1s	4.6s	4.6s	17.91s	4.6s
ES	29	15	10	8	6	5	22	7

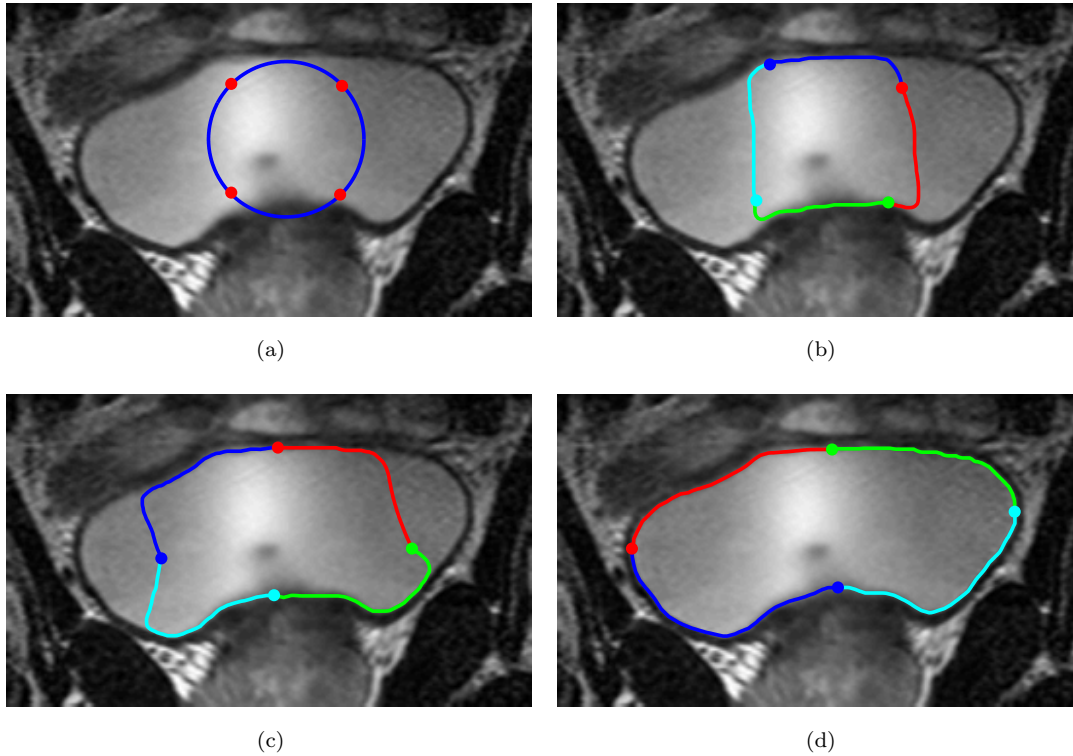


FIGURE 6.5: Shape evolution results of the proposed model with contour initialization and four sampled vertices. **(a)** Original image and initial contour with four sampled vertices. **(b)-(c)** Intermediate segmentation results. **(d)** Final segmentation result.

results and Fig. 6.4f is the final results. In this experiment, the proposed method requires only five steps to converge to the object boundaries. In this experiment, we use the f^{CV} (6.61) to construct the Finsler metric \mathcal{K} (6.50). We also investigate the respective computation time and evolution steps for the proposed model to converge to the boundaries with respect to different sizes and shapes of tubular neighbourhood regions U as demonstrated in Table 6.1. The sizes and shapes of U are controlled by (δ, d) in equations (6.54) and (6.56). From Table 6.1, we can see that a suitable pair of (δ, d) will reduce the computation time and evolution steps required by the proposed model.

In Fig. 6.5, we show the course of the shape evolution using the proposed model with four vertices based contour initialization. In this experiment, the Finsler

metric \mathcal{K} is constructed by the locally binary fitting based regional term f^{LBF} (6.62). In Fig. 6.5a is the original image with initial contour. Figs. 6.5b and 6.5c are intermediate segmentation results. 6.5d is the final segmentation results.

In Fig. 6.6, we show the segmentation results using the fixed points initialization way. In this experiment, we use the hybrid Finsler metric \mathcal{G} (6.53) constructed by the first variation f^{CV} of the Chan-Vese regional term. The reason for using the the hybrid Finsler metric \mathcal{G} is that the Chan-Vese regional term adopts the global region information such that for fixed points initialization, we need local image information like the image gradient magnitude values. Figs. 6.6a to 6.6d demonstrates the course of the shape evolution. The fixed points are denoted by dots. In this experiments, we need only four steps to obtain the final contour as shown in Fig. 6.6d.

In Fig. 6.8 we show the comparative segmentation results obtained by the nonlocal active contours model Jung et al. (2012) and the proposed shape evolution model with contour initialization. Column 1 shows the original images and the initial contours. Columns 2 and 3 show the segmentation results from the nonlocal active contours model and the proposed model respectively. One can claim that the proposed shape evolution model is more robust that local minimas compared to gradient descent method.

In Fig. 6.8, we show the comparative segmentation results obtained by the locally binary fitting model (Li et al., 2008) and the proposed shape evolution model with fixed points initialization. Column 1 shows the original images and the initial contours. Columns 2 and 3 show the segmentation results from the locally binary fitting model and the proposed model respectively. Again, with the proposed model, unexpected local minima suffered by the locally binary fitting model sometimes can be avoided.

6.8 Conclusion

In this chapter, a new framework of Finsler geodesics evolution model is proposed for region-based active contours and image segmentation. The proposed framework presents the first method that provides the connection between the geodesic curve energy and the general region-based active contour energy via a Finsler metric. This Finsler metric is induced from the region-based image data term of the active contour energy by solving a minimization problem with linear constraint. With the Finsler metric, the geodesic energy incorporated region information can be efficiently minimized by fast marching algorithm. Comparing to the popular level set approach, our model requires lower computational cost and can avoid unexpected local minima in case that the image data term invokes a local similarity

measurement. On the other hand, the proposed Finsler geodesics evolution can be naturally incorporated user intervention. By the user provided fixed points, the curve evolution results are more robust with low computation burden.

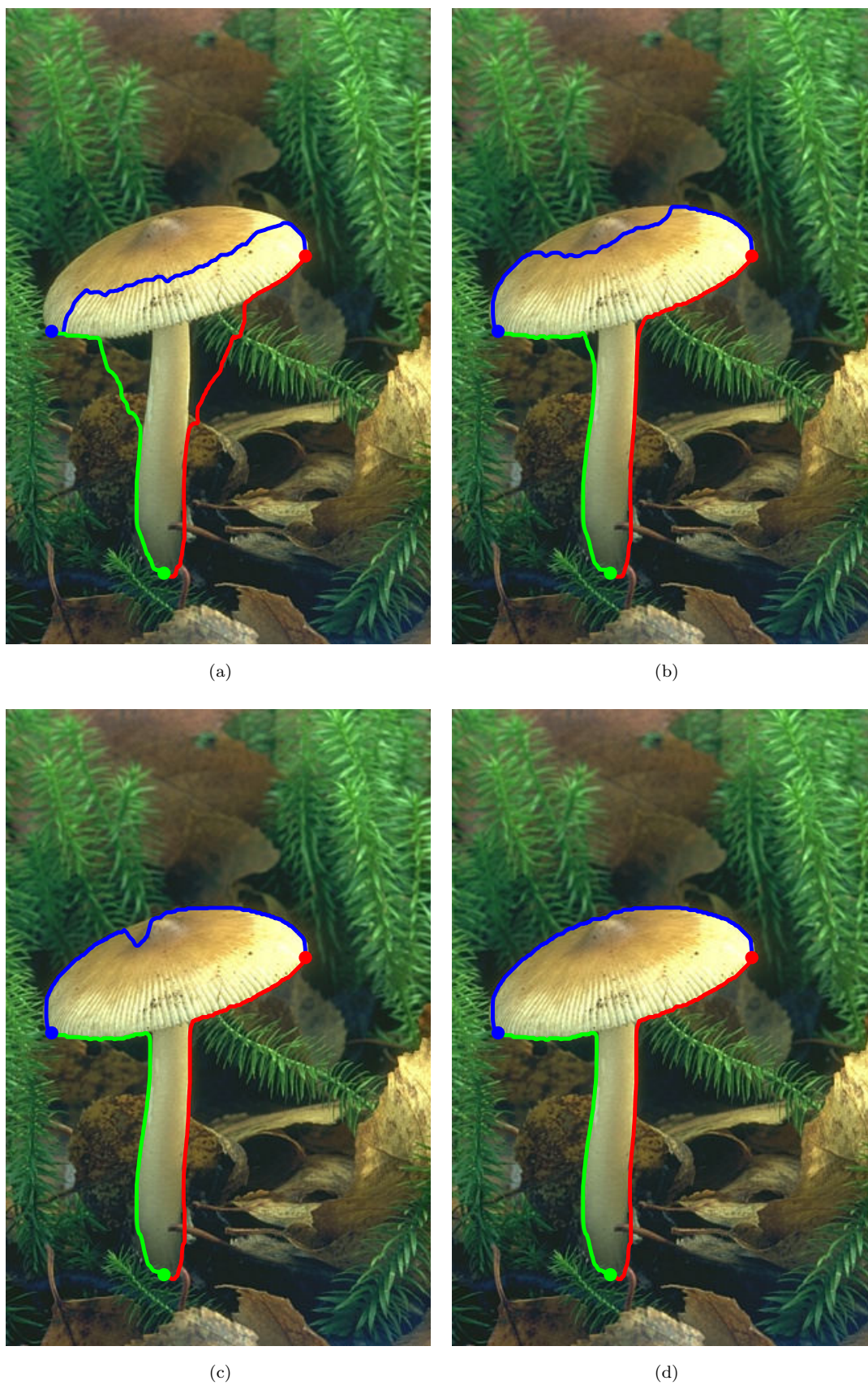


FIGURE 6.6: Shape evolution results of the proposed model with three fixed points initialization. Dots denote the fixed vertices.

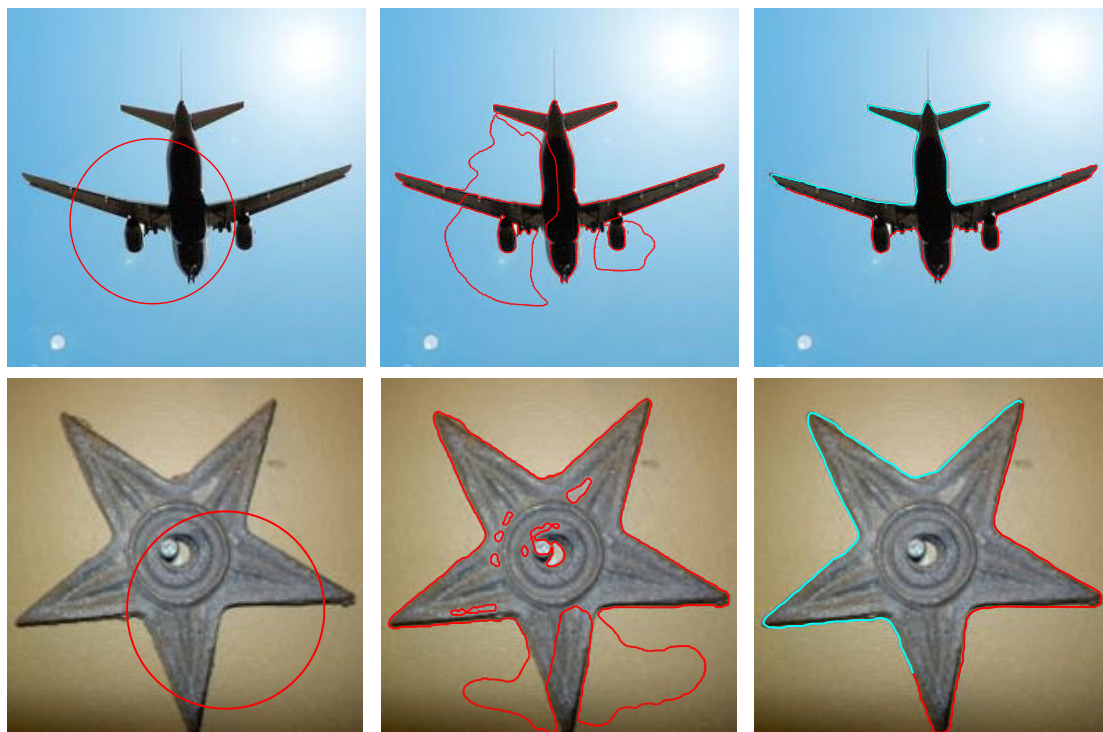


FIGURE 6.7: Comparative segmentation results by the level set based nonlocal active contours model (Jung et al., 2012) and the proposed model with contour initialization. Both models are based on the same regional terms. **Column 1** shows the original images and the initial contours. **Columns 2 and 3** show the segmentation results from the nonlocal active contours model and the proposed model respectively.

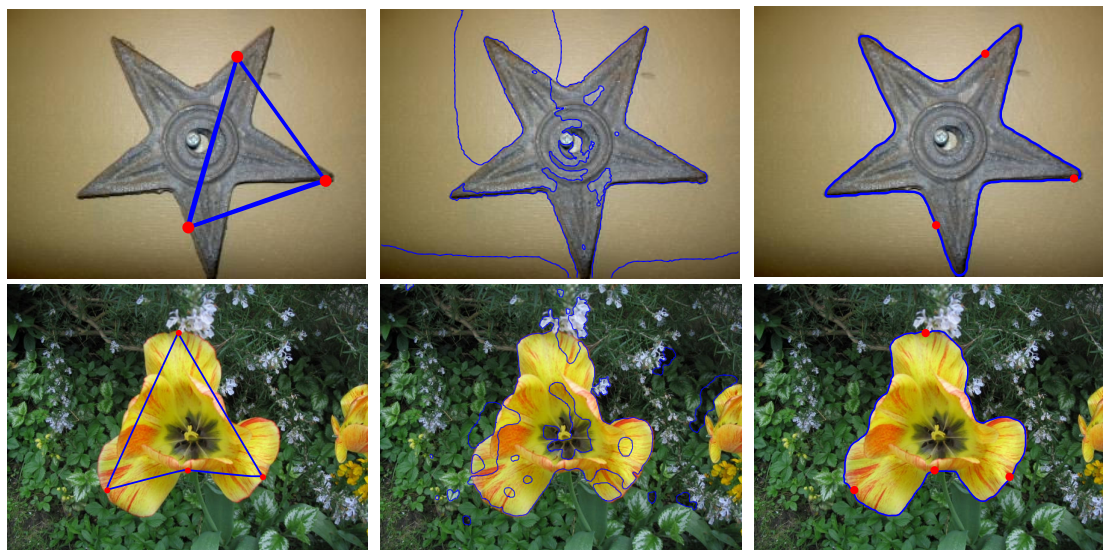


FIGURE 6.8: Comparative segmentation results by the level set based locally binary fitting model (Li et al., 2008) and the proposed model with fixed points initialization. Both models are based on the same regional terms. **Column 1** shows the original images and the initial contours. **Columns 2 and 3** show the segmentation results from the locally binary fitting model and the proposed model respectively.

Chapter 7

Summary of the Contributions and the Future Work

This thesis was devoted to the Eikonal equation based minimal path model and its applications. We have designed several new geodesic metrics and explored some applications according to these metrics.

We summarize the main contributions and discuss the possible future work.

- **Dynamic Riemannian Metric**

The dynamic Riemannian metric is designed to add penalty with respect to the image feature consistency property to the computation of the minimal paths. For the traditional isotropic or anisotropic Riemannian metrics, they only contain local pixel-based image feature information like tubular structure geometry and image gradient. In contrast, the proposed dynamic metric can incorporate non-local geodesic-based image feature. Thus this model is more robust and accurate in the task of vessel network extraction such as the retinal vein-artery vessel extraction.

- **Curvature-Penalized Finsler Elastica Metric**

Traditional minimal path models are first-order models. They are unable to penalize curvature property of the geodesics. We introduce in this thesis a curvature-penalized Finsler metric, namely Finsler elastica metric, to the framework of Eikonal equation, by an idea of orientation lifting. The proposed Finsler elastica metric establishes the equivalence between the Euler elastica bending energy and geodesic length energy. By solving the anisotropic Eikonal equation associated to the Finsler elastica metric, the globally minimizing Euler elastica curves or Finsler geodesics can be obtained efficiently. These geodesics blend the benefits from the smoothness

and asymmetry properties, which have important effects in tubular structure extraction and closed contour detection.

- **Region-based Information Embedded Finsler Metric**

We transfer the region-based active contours energy to the curve-based energy by divergence theorem. The crucial point is the construction of a Finsler metric induced from the shape gradient of the region-based active contour energy, which is done by solving a minimization problem with linear constraint. By the Eikonal framework and the constructed Finsler metric, the geodesic energy associated to the constructed Finsler metric can be minimized efficiently. In each iteration, the curve evolution-based minimization scheme of the traditional active contours models are tuned to extract a collection of geodesics. The regional information embedded Finsler metric bridges the two distinguished frameworks: the region-based active contours energy and the Eikonal framework.

- **Mask-based Keypoints Detection Method**

We designed a new keypoints detection method by invoking a set of masks. This model is able to iteratively add new initial source points in the course of the fast marching front propagation. These new initial source points, known as keypoints, are constrained by a set of computed masks such that we assume each detected keypoint must be inside the mask. Thanks to the mask constraint, the proposed keypoints search scheme is very robust and can avoid leaking problem in vessel tree extraction task.

- **Vessel Tracking via Region-Constrained Minimal Paths**

We take into account the pre-segmented binary vessel map to produce prior constrained regions. We restrict that the minimal paths should pass these constrained regions, to make the extraction of the minimal paths be very efficient, and to avoid the overlapping extraction problem. The constrained region is considered as a tubular neighbourhood of a curve that can be produced from a minimal path or a vessel skeleton curve. The expected minimal paths can be defined in the radius-lifted space. In this case, the obtained minimal paths can be used to represent the vessels including both the centerlines and radii.

- **Anisotropic Front Propagation for Image Segmentation**

We add anisotropy enhancement to the front propagation-based image segmentation scheme. This is done by invoking an anisotropic Riemannian metric for the fast marching method. Compared to the isotropic front propagation-based segmentation method, the anisotropy enhanced method can avoid leaking problem. We also design a method for anisotropy-preserving dynamic Riemannian metric construction, which makes use of the local gray

level information. This strategy can reduce the influence introduced by the intensity inhomogeneities.

Future Work

- **Finsler Elastica Metric for Keypoints Detection**

In this thesis, we proposed the Finsler elastica metric for globally minimizing Euler elastica curve detection between two given points. However, in some cases, a globally minimal curve is not the expected one. For example, to extract a long retinal artery vessel, a piecewise smooth path might be the desired one. This piecewise smooth curve can be decomposed into a set of Finsler elastica geodesics linking a set of ordered keypoints.

- **Dynamic Riemannian Metrics for Interactive Vessel Extraction with Simultaneously partially fast marching method**

The introduction of the dynamic Riemannian metric is motivated by the Retinal artery and vein vessel extraction task. In this thesis, we only perform the fast marching methods from one point. Since the dynamic metric makes use of local intensity consistency property, compute the geodesic distance from both points may return a better extracted path.

- **Edge-based Finsler Geodesics Evolution Model**

We introduced the Finsler geodesics evolution for region-based active contours and image segmentation. Along the same research line, we could extend this idea to pure edge-based active contours model by using the alignment term proposed by [Kimmel and Bruckstein \(2003\)](#). This work can benefit from the orientation enhancement of the object edges.

- **Piecewise Geodesics for Automatic Retinal Vessels Extraction**

We designed a new algorithm for retinal network vessel extraction by using region-constrained minimal paths model. The essential step is the Retinal vessels segmentation procedure. We used the optimally oriented flux filter for vessels segmentation. In the future, we could use a more advanced retinal vessel segmentation method such as the state-of-art orientation score-based method ([Zhang et al., 2016](#)) or the active contours-based model ([Zhao et al., 2015](#)).

Appendix A

Proof of Finsler Elastica Minimal Paths Convergence

This proof was obtained from a joint work (Chen et al., 2016a) with Dr. Jean-Marie Mirebeau.

Let $X \subset \mathbb{R}^d$ be a compact domain and \mathfrak{S} be the collection of compact convex sets of \mathbb{R}^d . We will later on specialize to $d = 3$ for the application to the Euler elastica curves. The set \mathfrak{S} is a metric space, equipped with the Hausdorff distance which is defined as follows.

Definition A.1. The Euclidean distance map from a set $A \subseteq \mathbb{R}^3$ is

$$d(A, \mathbf{x}) := \inf_{\mathbf{y} \in A} \|\mathbf{x} - \mathbf{y}\|. \quad (\text{A.0.1})$$

The Hausdorff distance between sets $A_1, A_2 \subseteq \mathbb{R}^d$ is

$$H(A_1, A_2) := \sup_{\mathbf{x} \in \mathbb{R}^d} |d(A_1, \mathbf{x}) - d(A_2, \mathbf{x})|. \quad (\text{A.0.2})$$

Definition A.2. Let $\gamma \in C^0([0, 1], X)$ be a path and $\mathcal{B} \in C^0(X, \mathfrak{S})$ be a collection of controls on X . The path γ is said \mathcal{B} -admissible iff it is locally Lipschitz and $\gamma'(t) \in \mathcal{B}(\gamma(t))$ for a.e. $t \in [0, 1]$.

Definition A.3. A collection of controls on X is a map $\mathcal{B} \in C^0(X, \mathfrak{S})$. Its diameter $\text{diam}(\mathcal{B})$ and modulus¹ of continuity $\Xi(\mathcal{B}, \epsilon)$ are defined by $\Xi(\mathcal{B}, 0) = 0$

¹ We actually use a slight variant of the classical modulus of continuity because the latter one, obtained with the hard cutoff function $\mathfrak{C}(t) = 1$ if $t \leq 1$, 0 otherwise, lacks continuity in general.

and for $\epsilon > 0$

$$\text{diam}(\mathcal{B}) := \sup\{\|\mathbf{u}\|; \mathbf{u} \in \mathcal{B}(\mathbf{x}), \forall \mathbf{x} \in X\}, \quad (\text{A.0.3})$$

$$\Xi(\mathcal{B}, \epsilon) := \sup_{\mathbf{x}, \mathbf{y} \in X} H(\mathcal{B}(\mathbf{x}), \mathcal{B}(\mathbf{y})) \mathfrak{C}(\|\mathbf{x} - \mathbf{y}\|/\epsilon), \quad (\text{A.0.4})$$

where \mathfrak{C} is the continuous cutoff function defined by

$$\mathfrak{C}(t) = \begin{cases} 1 & \text{if } t \leq 1 \\ 2 - t & \text{if } 1 \leq t \leq 2 \\ 0 & \text{if } t \geq 2. \end{cases}$$

Clearly $\mathcal{B} \mapsto \text{diam}(\mathcal{B})$ and $(\mathcal{B}, \epsilon) \mapsto \Xi(\mathcal{B}, \epsilon)$ are continuous functions of $\mathcal{B} \in C^0(X, \mathfrak{S})$ and $\epsilon \in \mathbb{R}^+$. In addition $\Xi(\mathcal{B}, \epsilon)$ is increasing w.r.t. ϵ . Here and below, if A_1, A_2 are metric spaces, and A_1 is compact, then $C^0(A_1, A_2)$ is equipped with the topology of uniform convergence. This applies in particular to the space of paths $C^0([0, 1], X)$ and of controls $C^0(X, \mathfrak{S})$.

Lemma A.4. *If γ is \mathcal{B} -admissible, then its Lipschitz constant is at most $\text{diam}(\mathcal{B})$. A necessary and sufficient condition for γ to be \mathcal{B} -admissible is: for all $0 \leq p \leq q \leq 1$,*

$$d\left(\mathcal{B}(\gamma(p)), \frac{\gamma(q) - \gamma(p)}{q - p}\right) \leq \Xi(\mathcal{B}, (q - p) \text{diam}(\mathcal{B})), \quad (\text{A.0.5})$$

Proof. Assume that γ is \mathcal{B} -admissible. Then for any $0 \leq p \leq q \leq 1$ one has

$$\|\gamma(p) - \gamma(q)\| \leq \int_p^q \|\gamma'(\varrho)\| d\varrho \leq |p - q| \text{diam}(\mathcal{B}),$$

hence γ is $\text{diam}(\mathcal{B})$ -Lipschitz as announced. Denoting $w_\varrho = p + (q - p)\varrho$, for all $\varrho \in [0, 1]$, one obtains

$$\frac{\gamma(q) - \gamma(p)}{q - p} = \int_0^1 \gamma'(w_\varrho) d\varrho. \quad (\text{A.0.6})$$

Hence by Jensen's inequality and the convexity of $d(\mathcal{B}(\gamma(p)), \cdot)$, which follows the convexity of $\mathcal{B}(\gamma(p))$, we obtain

$$d\left(\mathcal{B}(\gamma(p)), \frac{\gamma(q) - \gamma(p)}{q - p}\right) \leq \int_0^1 d(\mathcal{B}(\gamma(p)), \gamma'(w_\varrho)) d\varrho \quad (\text{A.0.7})$$

$$\leq \int_0^1 H(\mathcal{B}(\gamma(p)), \mathcal{B}(\gamma(w_\varrho))) d\varrho \quad (\text{A.0.8})$$

$$\leq \Xi(\mathcal{B}, (q - p) \text{diam}(\mathcal{B})). \quad (\text{A.0.9})$$

which establishes half of the announced characterization. The inequality (A.0.8) follows from the admissibility property $\gamma'(w_\varrho) \in \mathcal{B}(\gamma(w_\varrho))$ and the definition of

the Hausdorff distance (A.0.2). The inequality (A.0.9) follows from the above established Lipschitz regularity of γ and the definition of the modulus of continuity (A.0.4).

Conversely, assume that γ and \mathcal{B} obey (A.0.5). Then

$$\left\| \frac{\gamma(q) - \gamma(p)}{q - p} \right\| \leq \text{diam}(\mathcal{B}) + \Xi(\mathcal{B}, \text{diam}(\mathcal{B})),$$

for any $0 \leq p \leq q \leq 1$. Thus γ is a Lipschitz path as announced, and therefore it is almost everywhere differentiable. If $p \in [0, 1]$ is a point of differentiability, then letting $q \rightarrow p$ we obtain

$$d(\mathcal{B}(\gamma(p)), \gamma'(p)) \leq \Xi(\mathcal{B}, 0) = 0,$$

which is the announced admissibility property $\gamma'(p) \in \mathcal{B}(\gamma(p))$. \square

The characterization (A.0.5) is written in terms of continuous functions of the path γ and control set \mathcal{B} , hence it is a closed condition, which implies the following two corollaries.

We denote

$$T\mathcal{B}(\mathbf{x}) := \{T\mathbf{u}; \mathbf{u} \in \mathcal{B}(\mathbf{x}), \forall \mathbf{x} \in X\}.$$

Corollary A.5. *The set*

$$\left\{ (\gamma, \mathcal{B}) \in C^0([0, 1], X) \times C^0(X, \mathfrak{S}); \gamma \text{ is } \mathcal{B}\text{-admissible} \right\}$$

is closed.

Corollary A.6. *Let $\mathbf{x}_n, \mathbf{y}_n, \mathcal{B}_n$ and T_n be converging sequences in $X, X, C^0(X, \mathfrak{S})$ and \mathbb{R}^+ , with limits $\mathbf{x}_\infty, \mathbf{y}_\infty, \mathcal{B}_\infty$, and T_∞ , respectively. Let $\gamma_n \in C^0([0, 1], X)$ be a $(T_n + 1/n)\mathcal{B}_n$ -admissible path with endpoints \mathbf{x}_n and \mathbf{y}_n . Then the sequence of paths (γ_n) is equip continuous, and the limit γ_∞ of any converging subsequence is a $T_\infty\mathcal{B}_\infty$ -admissible path $\gamma \in C^0([0, 1], X)$ with endpoints \mathbf{x}_∞ and \mathbf{y}_∞ .*

Proof. Note that the map $(T, \mathcal{B}) \mapsto T\mathcal{B}$ is continuous on $\mathbb{R}^+ \times C^0(X, \mathfrak{S})$, hence the controls $\tilde{\mathcal{B}}_n := (T_n + 1/n)\mathcal{B}_n$ converge to $\tilde{\mathcal{B}}_\infty := T_\infty\mathcal{B}_\infty$. Defining $E := \sup\{\text{diam}(\mathcal{B}_n); n > 0\}$ which is finite by continuity of $\text{diam}(\cdot)$ (A.0.3) and convergence of $\tilde{\mathcal{B}}_n$, we find that the paths $(\gamma_n)_{n>0}$ are simultaneously E -Lipschitz, hence that a subsequence uniformly converges to some path γ_∞ . The $\tilde{\mathcal{B}}_\infty$ -admissibility of γ_∞ then follows from Corollary A.5. \square

We next introduce the minimum-time optimal control problems. The minimum of (A.0.10) is attained by Corollary A.6, which also immediately implies the Corollary A.8.

Definition A.7. For all $\mathbf{x}, \mathbf{y} \in X$, and $\mathcal{B} \in C^0(X, \mathfrak{S})$, we let

$$\begin{aligned} \mathcal{T}_{\mathcal{B}}(\mathbf{x}, \mathbf{y}) := \min\{T > 0; \exists \gamma \in C^0([0, 1], X), \\ \gamma(0) = \mathbf{x}, \gamma(1) = \mathbf{y}, \gamma \text{ is } T\mathcal{B}\text{-admissible}\}. \end{aligned} \quad (\text{A.0.10})$$

Corollary A.8. *The map $(\mathbf{x}, \mathbf{y}, \mathcal{B}) \mapsto \mathcal{T}_{\mathcal{B}}(\mathbf{x}, \mathbf{y})$ is lower semi-continuous on $X \times X \times C^0(X, \mathfrak{S})$. In other words, whenever $(\mathbf{x}_n, \mathbf{y}_n, \mathcal{B}_n) \rightarrow (\mathbf{x}_\infty, \mathbf{y}_\infty, \mathcal{B}_\infty)$ as $n \rightarrow \infty$ one has*

$$\liminf \mathcal{T}_{\mathcal{B}_n}(\mathbf{x}_n, \mathbf{y}_n) \geq \mathcal{T}_{\mathcal{B}_\infty}(\mathbf{x}_\infty, \mathbf{y}_\infty). \quad (\text{A.0.11})$$

Proof. For each $n > 0$ let $T_n = \mathcal{T}_{\mathcal{B}_n}(\mathbf{x}_n, \mathbf{y}_n)$ and let $T_\infty = \liminf T_n$ as $n \rightarrow \infty$. Up to extracting a subsequence, we can assume that $T_\infty = \lim T_n$ as $n \rightarrow \infty$. Denoting by γ_n a path as in Corollary A.6 for all $n > 0$, we find that there is a converging subsequence which limit γ_∞ is $T_\infty \mathcal{B}_\infty$ admissible and obeys $\gamma_\infty(0) = x_\infty$ and $\gamma_\infty(1) = y_\infty$. This shows that $T_\infty \geq \mathcal{T}_{\mathcal{B}_\infty}(\mathbf{x}_\infty, \mathbf{y}_\infty)$ as announced. \square

Definition A.9. Let $\mathcal{B}_1, \mathcal{B}_2 \in C^0(X, \mathfrak{S})$. These collections of controls are said included $\mathcal{B}_1 \subseteq \mathcal{B}_2$ iff $\mathcal{B}_1(\mathbf{x}) \subseteq \mathcal{B}_2(\mathbf{x})$ for all $\mathbf{x} \in X$.

The property $\mathcal{B}_1 \subseteq \mathcal{B}_2$ clearly implies, for all $\mathbf{x}, \mathbf{y} \in X$

$$\mathcal{T}_{\mathcal{B}_1}(\mathbf{x}, \mathbf{y}) \geq \mathcal{T}_{\mathcal{B}_2}(\mathbf{x}, \mathbf{y}). \quad (\text{A.0.12})$$

Corollary A.10. *Assume that one has a converging sequence of controls $\mathcal{B}_n \rightarrow \mathcal{B}_\infty$ obeying the inclusions $\mathcal{B}_n \subseteq \mathcal{B}_\infty$ for all $n > 0$. Then*

$$\lim \mathcal{T}_{\mathcal{B}_n}(\mathbf{x}, \mathbf{y}) = \mathcal{T}_{\mathcal{B}_\infty}(\mathbf{x}, \mathbf{y}). \quad (\text{A.0.13})$$

for all $\mathbf{x}, \mathbf{y} \in X$. Let $T_n := \mathcal{T}_{\mathcal{B}_n}$ for all $n \in \mathbb{N} \cup \{\infty\}$, and let γ_n be an arbitrary $(T_n + 1/n)\mathcal{B}_n$ -admissible path from \mathbf{x} to \mathbf{y} . If there exists a unique $T_\infty \mathcal{B}_\infty$ -admissible path γ_∞ from \mathbf{x} to \mathbf{y} , then $\gamma_n \rightarrow \gamma_\infty$ as $n \rightarrow \infty$.

Proof. The identity (A.0.13) follows from the inequalities (A.0.11) and (A.0.12). By Corollary A.6 the sequence of paths γ_n is equi-continuous, and any converging subsequence tends to a $T_* \mathcal{B}_\infty$ γ_* from \mathbf{x} to \mathbf{y} , with $T_* := \lim T_n$. Since $T_* = T_\infty$ and by uniqueness we have $\gamma_* = \gamma_\infty$ hence $\gamma_n \rightarrow \gamma_\infty$ as announced. \square

Application to Finsler Elastica Geodesics Convergence Problem

Consider an orientation-lifted Finsler metric $\mathcal{F} : X \times \mathbb{R}^3 \rightarrow \mathbb{R}^+$ where $X := \bar{\Omega} \subset \mathbb{R}^3$. For any orientation-lifted point $\bar{\mathbf{x}} \in X$, let $\mathcal{B}(\bar{\mathbf{x}}) := \{\bar{\mathbf{u}} \in \mathbb{R}^3; \mathcal{F}(\bar{\mathbf{x}}, \bar{\mathbf{u}}) \leq 1\}$ be the unit ball of the Finsler metric \mathcal{F} . $\mathcal{B}(\bar{\mathbf{x}})$ is compact and convex, due to the positivity, continuity and convexity of the metric \mathcal{F} and the map $\mathcal{B} : X \rightarrow \mathfrak{S}$ is

continuous. Furthermore, using the homogeneity of the metric \mathcal{F} , one obtains for all $\bar{\mathbf{x}}, \bar{\mathbf{y}} \in X$:

$$\mathcal{L}_{\mathcal{F}}^*(\bar{\mathbf{x}}, \bar{\mathbf{y}}) = \mathcal{T}_{\mathcal{B}}(\bar{\mathbf{x}}, \bar{\mathbf{y}}),$$

where $\mathcal{L}^*(\bar{\mathbf{x}}, \bar{\mathbf{y}})$ is the minimal geodesic curve length between $\bar{\mathbf{x}}$ and $\bar{\mathbf{y}}$ with respect to the Finsler metric \mathcal{F} .

In the case of Finsler elastica problem, one has $\mathcal{B}_{\infty}(\bar{\mathbf{x}}) := B_{\bar{\mathbf{x}}}^{\infty}$ and $\mathcal{B}_{\lambda}(\bar{\mathbf{x}}) := B_{\bar{\mathbf{x}}}^{\lambda}$, $\forall \bar{\mathbf{x}} \in X$, where $B_{\bar{\mathbf{x}}}^{\infty}$ and $B_{\bar{\mathbf{x}}}^{\lambda}$ are defined in equations (5.17) and (5.18), respectively. The Finsler elastica metrics \mathcal{F}^{λ} on X pointwisely tend to the metric \mathcal{F}^{∞} as $\lambda \rightarrow \infty$. Fortunately, the associated control sets $\mathcal{B}_{\lambda}(\bar{\mathbf{x}}) \rightarrow \mathcal{B}_{\infty}(\bar{\mathbf{x}})$ uniformly in $C^0(\Omega, \mathfrak{S})$, as can be seen from (5.21). Hence one has

$$\begin{aligned} \liminf \mathcal{L}_{\mathcal{F}^{\lambda}}^*(\bar{\mathbf{x}}, \bar{\mathbf{y}}) &= \liminf \mathcal{T}_{\mathcal{B}_{\lambda}}(\bar{\mathbf{x}}, \bar{\mathbf{y}}) \\ &\geq \mathcal{T}_{\mathcal{B}_{\infty}}(\bar{\mathbf{x}}, \bar{\mathbf{y}}) = \mathcal{L}_{\mathcal{F}^{\infty}}^*(\bar{\mathbf{x}}, \bar{\mathbf{y}}), \end{aligned}$$

as $\lambda \rightarrow \infty$ for all $\bar{\mathbf{x}}, \bar{\mathbf{y}} \in X$. To show that equality holds, it suffices to prove that sequence \mathcal{B}_{λ} obeys $\mathcal{B}^{\lambda} \supseteq \mathcal{B}^{\infty}$, equivalently to prove that $\mathcal{F}^{\lambda}(\bar{\mathbf{x}}, \bar{\mathbf{u}}) \leq \mathcal{F}^{\infty}(\bar{\mathbf{x}}, \bar{\mathbf{u}})$ for all $\bar{\mathbf{x}} \in X$ and any vector $\bar{\mathbf{u}} \in \mathbb{R}^3$. Indeed, let $\bar{\mathbf{x}} = (\mathbf{x}, \theta) \in X$, and $\bar{\mathbf{u}} = (\mathbf{u}, \nu) \in \mathbb{R}^2 \times \mathbb{R}$:

$$\mathcal{F}^{\lambda}(\bar{\mathbf{x}}, \bar{\mathbf{u}}) = \sqrt{\lambda^2 \|\mathbf{u}\|^2 + 2\lambda |\nu|^2} - (\lambda - 1) \langle \mathbf{u}, \mathbf{v}_{\theta} \rangle \quad (\text{A.0.14})$$

$$= \lambda \|\mathbf{u}\| \left(-1 + \sqrt{1 + \frac{2|\nu|^2}{\lambda \|\mathbf{u}\|^2}} \right) + \lambda \|\mathbf{u}\| - (\lambda - 1) \langle \mathbf{u}, \mathbf{v}_{\theta} \rangle. \quad (\text{A.0.15})$$

$$= \|\mathbf{u}\| + \frac{|\nu|^2}{\|\mathbf{u}\|} \left(\frac{2}{1 + \sqrt{1 + \frac{2|\nu|^2}{\lambda \|\mathbf{u}\|^2}}} \right) + (\lambda - 1) (\|\mathbf{u}\| - \langle \mathbf{u}, \mathbf{v}_{\theta} \rangle). \quad (\text{A.0.16})$$

$$\leq \mathcal{F}^{\infty}(\bar{\mathbf{x}}, \bar{\mathbf{u}}). \quad (\text{A.0.17})$$

The last inequality holds because the denominator in (A.0.17) is greater than 2, and $\|\mathbf{u}\| \geq \langle \mathbf{u}, \mathbf{v}_{\theta} \rangle$ for any vector \mathbf{u} and angle θ .

By Corollary A.6, minimal paths \mathcal{C}^{λ} with endpoints $\bar{\mathbf{x}}$ and $\bar{\mathbf{y}}$ for geodesic distance $\mathcal{L}_{\mathcal{F}^{\lambda}}^*(\bar{\mathbf{x}}, \bar{\mathbf{y}})$ converges as $\lambda \rightarrow \infty$ to a minimal path \mathcal{C}^{∞} for $\mathcal{L}_{\mathcal{F}^{\infty}}^*(\bar{\mathbf{x}}, \bar{\mathbf{y}})$. We finally point out that $\mathcal{L}_{\mathcal{F}^{\infty}}^*(\bar{\mathbf{x}}, \bar{\mathbf{y}}) < \infty$ for all $\bar{\mathbf{x}}, \bar{\mathbf{y}}$ in the interior of X , provided this interior is connected, due to a classical controllability result for the Euler elastica problem.

Appendix B

Numerical Solution to the Minimization Problem with Linear Constraint

We recall the minimization problem formulated in (6.44) and (6.45). Let $U \in \Omega$ be subdomain of the image domain Ω . We solve

$$\text{minimize } \int_U \|\mathcal{V}_\perp(\mathbf{x})\|^2 d\mathbf{x}, \quad (\text{B.0.1})$$

$$\text{s.t. } \nabla \cdot \mathcal{V}_\perp(\mathbf{x}) = \alpha f(\mathbf{x}) \chi_U(\mathbf{x}), \quad \forall \mathbf{x} \in U, \quad (\text{B.0.2})$$

where operator $\nabla \cdot \mathbf{u}$ denotes the divergence value of vector \mathbf{u} . The solution \mathcal{V}_\perp to the minimization problem (B.0.1) with linear constraint (B.0.2) admits the variational formulation: find $(\mathcal{V}_\perp, p) \in L^2(U, \mathbb{R}^2) \times H^1(U)$ such that for all (\mathcal{W}, q) in the same spaces one has

$$\begin{cases} \int_U \langle \mathcal{V}_\perp(\mathbf{x}), \mathcal{W}(\mathbf{x}) \rangle d\mathbf{x} + \int_U \langle \nabla p(\mathbf{x}), \mathcal{W}(\mathbf{x}) \rangle d\mathbf{x} = 0, \\ \int_U \langle \mathcal{V}_\perp(\mathbf{x}), \nabla q(\mathbf{x}) \rangle - \int_U f(\mathbf{x})q(\mathbf{x}) d\mathbf{x} = 0. \end{cases}$$

We use a finite differences discretization on the pixel grid $Z_U = h\mathbb{Z}^2 \cap U$, where $h > 0$ is the pixel size. We also store the values of the potentials p and q on a staggered grid so as to improve the accuracy of the gradient operator. The first step is to express (B.0.1) to the discrete forms. Specifically, one has

$$\int_U \|\mathcal{V}_\perp(\mathbf{x})\|^2 d\mathbf{x} \approx \vec{r}^\top \mathcal{Q} \vec{r}, \quad (\text{B.0.3})$$

where \mathcal{Q} is identity matrix with size $2N \times 2N$. Letting $\mathcal{V}_\perp = (u, v)$, \vec{r} is a vector of size $2N \times 1$

$$\vec{r} = \left(u(\mathbf{x}_1) \cdots u(\mathbf{x}_N), v(\mathbf{x}_1) \cdots v(\mathbf{x}_N) \right)^T, \quad \mathbf{x}_1, \dots, \mathbf{x}_N \in Z_U,$$

where N is the number of grid points in the discrete domain Z_U of U .

We denote the divergence operator as

$$\begin{aligned} & (\vec{q}_1, \dots, \vec{q}_N)^T \cdot \vec{r} \\ &= \left(f(\mathbf{x}_1)\chi_U(\mathbf{x}_1), \dots, f(\mathbf{x}_N)\chi_U(\mathbf{x}_N) \right)^T, \quad \mathbf{x}_1, \dots, \mathbf{x}_N \in Z_U, \end{aligned} \quad (\text{B.0.4})$$

\vec{q}_i is a divergence vector with size $2N \times 1$ such that

$$\vec{q}_i^T \vec{r} = f_{\chi_U}(\mathbf{x}_i) = \vec{p}(\mathbf{x}_i).$$

where \vec{p} is a vector column with size $2N \times 1$. Letting $A = (\vec{q}_1, \dots, \vec{q}_N)$, then the minimization problem (B.0.1) with linear constraint can be formulated as

$$\min_{\vec{r}} \{ \vec{r}^T \mathcal{Q} \vec{r} \}, \quad s.t. \quad A^T \vec{r} = \vec{p}.$$

The solution \vec{r}^* can be given by

$$\begin{pmatrix} \mathcal{Q} & A^T \\ A & \mathbf{0} \end{pmatrix} \begin{pmatrix} \vec{r}^* \\ \vec{\lambda} \end{pmatrix} = \begin{pmatrix} \mathbf{0} \\ \vec{p} \end{pmatrix}. \quad (\text{B.0.5})$$

where $\vec{\lambda}$ is a collection of Lagrange multipliers which come out of the solution alongside \vec{r}^* . Then using the solution \vec{r}^* , we can obtain the vector field \mathcal{V}_\perp .

Bibliography

- B. Al-Diri, A. Hunter, and D. Steel. An active contour model for segmenting and measuring retinal vessels. *IEEE Transactions on Medical Imaging*, 28(9):1488–1497, 2009.
- S. Alpert, M. Galun, A. Brandt, and R. Basri. Image segmentation by probabilistic bottom-up aggregation and cue integration. *IEEE Transactions on Pattern Analysis and Machine Intelligence*, 34(2):315–327, 2012.
- K. Alton and I. M. Mitchell. An ordered upwind method with precomputed stencil and monotone node acceptance for solving static convex hamilton-jacobi equations. *Journal of Scientific Computing*, 51(2):313–348, 2012.
- V. Appia and A. Yezzi. Active geodesics: Region-based active contour segmentation with a global edge-based constraint. In *Proceedings of IEEE International Conference on Computer Vision (ICCV 2011)*, pages 1975–1980, 2011.
- B. Appleton and H. Talbot. Globally optimal geodesic active contours. *Journal of Mathematical Imaging and Vision*, 23(1):67–86, 2005.
- P. Arbelaez, M. Maire, C. Fowlkes, and J. Malik. Contour detection and hierarchical image segmentation. *IEEE Transactions on Pattern Analysis and Machine Intelligence*, 33(5):898–916, 2011.
- E. Bekkers, R. Duits, T. Berendschot, and B. ter Haar Romeny. A multi-orientation analysis approach to retinal vessel tracking. *Journal of Mathematical Imaging and Vision*, 49(3):583–610, 2014.
- E. J. Bekkers, R. Duits, A. Mashtakov, and G. R. Sanguinetti. Data-Driven Sub-Riemannian Geodesics in SE(2). In *Proceedings of Scale Space and Variational Methods in Computer Vision (SSVM 2015)*, pages 613–625, 2015a.
- E. J. Bekkers, R. Duits, A. Mashtakov, and G. R. Sanguinetti. A PDE Approach to Data-driven Sub-Riemannian Geodesics in SE (2). *SIAM Journal on Imaging Sciences*, 8(4):2740–2770, 2015b.
- F. Benmansour and L. D. Cohen. Fast object segmentation by growing minimal paths from a single point on 2D or 3D images. *Journal of Mathematical Imaging and Vision*, 33(2):209–221, 2009.

- F. Benmansour and L. D. Cohen. Tubular Structure Segmentation Based on Minimal Path Method and Anisotropic Enhancement. *International Journal of Computer Vision*, 92(2):192–210, 2011.
- L. Bertelli, B. Sumengen, B. Manjunath, and F. Gibou. A variational framework for multiregion pairwise-similarity-based image segmentation. *IEEE Transactions on Pattern Analysis and Machine Intelligence*, 30(8):1400–1414, 2008.
- F. Bornemann and C. Rasch. Finite-element discretization of static hamilton-jacobi equations based on a local variational principle. *Computing and Visualization in Science*, 9(2):57–69, 2006.
- U. Boscain, G. Charlot, and F. Rossi. Existence of planar curves minimizing length and curvature. *Proceedings of the Steklov Institute of Mathematics*, 270(1):43–56, 2010.
- S. Bougleux, G. Peyré, and L. Cohen. Anisotropic Geodesics for Perceptual Grouping and Domain Meshing. In *Proceedings of European Conference on Computer Vision (ECCV 2008)*. Springer Berlin Heidelberg, pages 129–142, 2008.
- Y. Boykov and G. Funka-Lea. Graph cuts and efficient ND image segmentation. *International Journal of Computer Vision*, 70(2):109–131, 2006.
- Y. Boykov and V. Kolmogorov. An experimental comparison of min-cut/max-flow algorithms for energy minimization in vision. *IEEE Transactions on Pattern Analysis and Machine Intelligence*, 26(9):1124–1137, 2004.
- T. Brox and D. Cremers. On local region models and a statistical interpretation of the piecewise smooth Mumford-Shah functional. *International Journal of Computer Vision*, 84(2):184–193, 2009.
- J. Canny. A computational approach to edge detection. *IEEE Transactions on Pattern Analysis and Machine Intelligence*, (6):679–698, 1986.
- V. Caselles, F. Catté, T. Coll, and F. Dibos. A geometric model for active contours in image processing. *Numerische Mathematik*, 66(1):1–31, 1993.
- V. Caselles, R. Kimmel, and G. Sapiro. Geodesic active contours. *International Journal of Computer Vision*, 22(1):61–79, 1997.
- T. F. Chan and L. A. Vese. Active contours without edges. *IEEE Transactions on Image Processing*, 10(2):266–277, 2001.
- T. F. Chan, B. Y. Sandberg, and L. A. Vese. Active contours without edges for vector-valued images. *Journal of Visual Communication and Image Representation*, 11(2):130–141, 2000.

- S. Chaudhuri, S. Chatterjee, N. Katz, M. Nelson, and M. Goldbaum. Detection of blood vessels in retinal images using two-dimensional matched filters. *IEEE Transactions on Medical Imaging*, 8(3):263–269, 1989.
- D. Chen and L. D. Cohen. Interactive retinal vessel centreline extraction and boundary delineation using anisotropic fast marching and intensities consistency. In *Proceedings of 37th Annual International Conference of IEEE Engineering in Medicine and Biology Society (EMBC 2015)*, pages 4347–4350, 2015a.
- D. Chen and L. D. Cohen. Piecewise Geodesics for Vessel Centreline Extraction and Boundary Delineation with Application to Retina Segmentation. In *Proceedings of Scale Space and Variational Methods in Computer Vision (SSVM 2015)*, pages 270–281, 2015b.
- D. Chen and L. D. Cohen. Vessel Tree Segmentation via Front Propagation and Dynamic Anisotropic Riemannian Metric. In *IEEE International Symposium on Biomedical Imaging (ISBI 2016)*, 2016.
- D. Chen, L. D. Cohen, and J.-M. Mirebeau. Vessel extraction using anisotropic minimal paths and path score. In *Proceedings of IEEE International Conference on Image Processing (ICIP 2014)*, pages 1570–1574, 2014.
- D. Chen, J.-M. Mirebeau, and L. D. Cohen. Global Minimum for Curvature Penalized Minimal Path Method. In *Proceedings of the British Machine Vision Conference (BMVC 2015)*, pages 86.1–86.12, 2015.
- D. Chen, J.-M. Mirebeau, and L. D. Cohen. Global Minimum for a Finsler Elastica Minimal Path Approach. *International Journal of Computer Vision*, 2016a.
- D. Chen, J.-M. Mirebeau, and L. D. Cohen. A new finsler minimal path model with curvature penalization for image segmentation and closed contour detection. In *Proceedings of IEEE Conference on Computer Vision and Pattern Recognition (CVPR 2016)*, pages 355–363, 2016b.
- Y. Chen, Y. Zhang, J. Yang, Q. Cao, G. Yang, J. Chen, H. Shu, L. Luo, J.-L. Coatrieux, and Q. Feng. Curve-like structure extraction using minimal path propagation with backtracking. *IEEE Transactions on Image Processing*, 25(2): 988–1003, 2016c.
- D. L. Chopp. Replacing iterative algorithms with single-pass algorithms. *Proceedings of the National Academy of Sciences*, 98(20):10992–10993, 2001.
- O. Chutatape, L. Zheng, and S. Krishnan. Retinal blood vessel detection and tracking by matched Gaussian and Kalman filters. In *Proceedings of 20th Annual International Conference of the IEEE Engineering in Medicine and Biology Society (EMBC 1998)*, volume 6, pages 3144–3149, 1998.

- G. Citti and A. Sarti. A cortical based model of perceptual completion in the roto-translation space. *Journal of Mathematical Imaging and Vision*, 24(3):307–326, 2006.
- L. D. Cohen. On active contour models and balloons. *CVGIP: Image understanding*, 53(2):211–218, 1991.
- L. D. Cohen. Avoiding local minima for deformable curves in image analysis. *Curves and Surfaces with Applications in CAGD*, pages 77–84, 1997.
- L. D. Cohen. Multiple contour finding and perceptual grouping using minimal paths. *Journal of Mathematical Imaging and Vision*, 14(3):225–236, 2001.
- L. D. Cohen and I. Cohen. Finite-element methods for active contour models and balloons for 2-D and 3-D images. *IEEE Transactions on Pattern Analysis and Machine Intelligence*, 15(11):1131–1147, 1993.
- L. D. Cohen and T. Deschamps. Segmentation of 3D tubular objects with adaptive front propagation and minimal tree extraction for 3D medical imaging. *Computer Methods in Biomechanics and Biomedical Engineering*, 10(4):289–305, 2007.
- L. D. Cohen and R. Kimmel. Global minimum for active contour models: A minimal path approach. *International Journal of Computer Vision*, 24(1):57–78, 1997.
- T. Deschamps and L. D. Cohen. Fast extraction of minimal paths in 3D images and applications to virtual endoscopy. *Medical image analysis*, 5(4):281–299, 2001.
- T. Deschamps and L. D. Cohen. Fast extraction of tubular and tree 3D surfaces with front propagation methods. In *Proceedings of International Conference on Pattern Recognition (ICPR 2002)*, volume 1, pages 731–734, 2002.
- S. Di Zenzo. A note on the Gradient of a Multi-Image. *Computer vision, graphics, and image processing*, 33(1):116–125, 1986.
- E. W. Dijkstra. A note on two problems in connexion with graphs. *Numerische Mathematik*, 1(1):269–271, 1959.
- E. Dominguez, W. Raoul, B. Calippe, J.-A. Sahel, X. Guillonnet, M. Paques, and F. Sennlaub. Experimental Branch Retinal Vein Occlusion Induces Upstream Pericyte Loss and Vascular Destabilization. *PloS one*, 10(7):e0132644, 2015.
- A. Dubrovina-Karni, G. Rosman, and R. Kimmel. Multi-region active contours with a single level set function. *IEEE Transactions on Pattern Analysis and Machine Intelligence*, 37(8):1585–1601, 2015.

- R. Duits, M. Felsberg, G. Granlund, and B. ter Haar Romeny. Image analysis and reconstruction using a wavelet transform constructed from a reducible representation of the euclidean motion group. *International Journal of Computer Vision*, 72(1):79–102, 2007.
- R. Duits, A. Ghosh, T. D. Haije, and A. Mashtakov. On sub-Riemannian geodesics in $SE(3)$ whose spatial projections do not have cusps. *arXiv preprint arXiv:1305.6061*, 2013.
- R. Duits, U. Boscaïn, F. Rossi, and Y. Sachkov. Association fields via cusplless sub-Riemannian geodesics in $SE(2)$. *Journal of mathematical imaging and vision*, 49(2):384–417, 2014.
- N. Y. El-Zehiry and L. Grady. Fast global optimization of curvature. In *Proceedings of IEEE Conference on Computer Vision and Pattern Recognition (CVPR 2010)*, pages 3257–3264, 2010.
- A. F. Frangi, W. J. Niessen, K. L. Vincken, and M. A. Viergever. Multiscale vessel enhancement filtering. In *Proceedings of Medical Image Computing and Computer-Assisted Intervention (MICCAI 1998)*, pages 407–433, 1998.
- M. M. Fraz, P. Remagnino, A. Hoppe, B. Uyyanonvara, A. R. Rudnicka, C. G. Owen, and S. A. Barman. Blood vessel segmentation methodologies in retinal images—a survey. *Computer methods and programs in biomedicine*, 108(1):407–433, 2012.
- W. T. Freeman and E. H. Adelson. The design and use of steerable filters. *IEEE Transactions on Pattern Analysis and Machine Intelligence*, (9):891–906, 1991.
- L. Grady. Random walks for image segmentation. *IEEE Transactions on Pattern Analysis and Machine Intelligence*, 28(11):1768–1783, 2006.
- J. Hannink, R. Duits, and E. Bekkers. Crossing-preserving multi-scale vesselness. In *Proceedings of Medical Image Computing and Computer-Assisted Intervention (MICCAI 2014)*, pages 603–610. 2014.
- A. Hoover, V. Kouznetsova, and M. Goldbaum. Locating blood vessels in retinal images by piecewise threshold probing of a matched filter response. *IEEE Transactions on Medical imaging*, 19(3):203–210, 2000.
- M. Jacob and M. Unser. Design of steerable filters for feature detection using canny-like criteria. *IEEE Transactions on Pattern Analysis and Machine Intelligence*, 26(8):1007–1019, 2004.
- A. C. Jalba, M. H. Wilkinson, and J. B. Roerdink. CPM: A deformable model for shape recovery and segmentation based on charged particles. *IEEE Transactions on Pattern Analysis and Machine Intelligence*, 26(10):1320–1335, 2004.

- S. Jbabdi, P. Bellec, R. Toro, J. Daunizeau, M. Péligrini-Issac, and H. Benali. Accurate anisotropic fast marching for diffusion-based geodesic tractography. *Journal of Biomedical Imaging*, 2008:2, 2008.
- X. Jiang and D. Mojon. Adaptive local thresholding by verification-based multi-threshold probing with application to vessel detection in retinal images. *IEEE Transactions on Pattern Analysis and Machine Intelligence*, 25(1):131–137, 2003.
- J. P. Jones and L. A. Palmer. An evaluation of the two-dimensional Gabor filter model of simple receptive fields in cat striate cortex. *Journal of neurophysiology*, 58(6):1233–1258, 1987.
- M. Jung, G. Peyré, and L. D. Cohen. Nonlocal active contours. *SIAM Journal on Imaging Sciences*, 5(3):1022–1054, 2012.
- M. Kass, A. Witkin, and D. Terzopoulos. Snakes: Active contour models. *International Journal of Computer Vision*, 1(4):321–331, 1988.
- V. Kaul, A. Yezzi, and Y. Tsai. Detecting curves with unknown endpoints and arbitrary topology using minimal paths. *IEEE Transactions on Pattern Analysis and Machine Intelligence*, 34(10):1952–1965, 2012.
- S. Kichenassamy, A. Kumar, P. Olver, A. Tannenbaum, and A. Yezzi. Gradient flows and geometric active contour models. In *Proceedings of International Conference on Computer Vision (ICCV 1995)*, pages 810–815, 1995.
- R. Kimmel. Fast edge integration. In *Geometric Level Set Methods in Imaging, Vision, and Graphics*, pages 59–77. 2003.
- R. Kimmel and A. M. Bruckstein. Regularized laplacian zero crossings as optimal edge integrators. *International Journal of Computer Vision*, 53(3):225–243, 2003.
- R. Kimmel and J. Sethian. Optimal algorithm for shape from shading and path planning. *Journal of Mathematical Imaging and Vision*, 14(3):237–244, 2001.
- C. Kirbas and F. Quek. A review of vessel extraction techniques and algorithms. *ACM Computing Surveys*, 36(2):81–121, 2004.
- E. Koch, D. Rosenbaum, A. Brolly, J.-A. Sahel, P. Chaumet-Riffaud, X. Girerd, F. Rossant, and M. Paques. Morphometric analysis of small arteries in the human retina using adaptive optics imaging: relationship with blood pressure and focal vascular changes. *Journal of hypertension*, 32(4):890, 2014.
- V. Kolmogorov and R. Zabini. What energy functions can be minimized via graph cuts? *IEEE Transactions on Pattern Analysis and Machine Intelligence*, 26(2):147–159, 2004.

- H. J. Kushner. Numerical methods for stochastic control problems in continuous time. *SIAM Journal on Control and Optimization*, 28(5):999–1048, 1990.
- L. Lam, S.-W. Lee, and C. Y. Suen. Thinning methodologies—a comprehensive survey. *IEEE Transactions on pattern analysis and machine intelligence*, 14(9):869–885, 1992.
- S. Lankton and A. Tannenbaum. Localizing region-based active contours. *IEEE Transactions on Image Processing*, 17(11):2029–2039, 2008.
- M. W. Law and A. Chung. Efficient implementation for spherical flux computation and its application to vascular segmentation. *IEEE Transactions on Image Processing*, 18(3):596–612, 2009.
- M. W. Law and A. C. Chung. An oriented flux symmetry based active contour model for three dimensional vessel segmentation. In *Proceedings of European Conference on Computer Vision (ECCV 2010)*, pages 720–734. 2010.
- M. W. K. Law and A. C. S. Chung. Three Dimensional Curvilinear Structure Detection Using Optimally Oriented Flux. In *Proceedings of European Conference on Computer Vision (ECCV 2008)*. Springer Berlin Heidelberg, pages 368–382, 2008.
- D. Lesage, E. D. Angelini, I. Bloch, and G. Funka-Lea. A review of 3D vessel lumen segmentation techniques: Models, features and extraction schemes. *Medical image analysis*, 13(6):819–845, 2009.
- B. Li and S. T. Acton. Active contour external force using vector field convolution for image segmentation. *IEEE Transactions on Image Processing*, 16(8):2096–2106, 2007.
- C. Li, C.-Y. Kao, J. C. Gore, and Z. Ding. Minimization of region-scalable fitting energy for image segmentation. *IEEE Transactions on Image Processing*, 17(10):1940–1949, 2008.
- C. Li, C. Xu, C. Gui, and M. D. Fox. Distance regularized level set evolution and its application to image segmentation. *IEEE Transactions on Image Processing*, 19(12):3243–3254, 2010.
- H. Li and A. Yezzi. Vessels as 4-D curves: Global minimal 4-D paths to extract 3-D tubular surfaces and centrelines. *IEEE Transactions on Medical Imaging*, 26(9):1213–1223, 2007.
- H. Li, A. Yezzi, and L. Cohen. 3D multi-branch tubular surface and centerline extraction with 4D iterative key points. In *Medical Image Computing and Computer-Assisted Intervention (MICCAI 2009)*, pages 1042–1050. 2009.

- W. Liao, S. Wörz, and K. Rohr. Globally minimal path method using dynamic speed functions based on progressive wave propagation. In *Proceedings of Asian Conference on Computer Vision (ACCV2012)*, pages 25–37, 2012.
- W. Liao, K. Rohr, and S. Wörz. Globally optimal curvature-regularized fast marching for vessel segmentation. In *Proceeding of International Conference on Medical Image Computing and Computer-Assisted Intervention (MICCAI 2013)*, pages 550–557, 2013.
- P.-L. Lions. *Generalized solutions of Hamilton-Jacobi equations*, volume 69. Pitman Publishing, 1982.
- J. Lowell, A. Hunter, D. Steel, A. Basu, R. Ryder, and R. L. Kennedy. Measurement of retinal vessel widths from fundus images based on 2-d modeling. *IEEE Transactions. on Medical Imaging*, 23(10):1196–1204, 2004.
- R. Malladi and J. A. Sethian. A real-time algorithm for medical shape recovery. In *Proceedings of IEEE International Conference on Computer Vision*, pages 304–310, 1998.
- R. Malladi, J. A. Sethian, and B. C. Vemuri. Evolutionary fronts for topology-independent shape modeling and recovery. In *Proceedings of European Conference on Computer Vision (ECCV 1994)*. Springer Berlin Heidelberg, pages 1–13, 1994.
- R. Malladi, J. Sethian, and B. C. Vemuri. Shape modeling with front propagation: A level set approach. *IEEE Transactions on Pattern Analysis and Machine Intelligence*, 17(2):158–175, 1995.
- C. Mariño, M. G. Penedo, M. Penas, M. J. Carreira, and F. Gonzalez. Personal authentication using digital retinal images. *Pattern Analysis and Applications*, 9(1):21–33, 2006.
- A. Mashtakov, R. Duits, Y. Sachkov, E. Bekkers, and I. Beschastnyi. Tracking of Lines in Spherical Images via Sub-Riemannian Geodesics on $SO(3)$. *arXiv preprint*, 2016.
- J. Mille and L. D. Cohen. Geodesically linked active contours: evolution strategy based on minimal paths. In *Proceedings of International Conference on Scale Space and Variational Methods in Computer Vision (SSVM 2009)*, pages 163–174, 2009.
- J. Mille, S. Bougleux, and L. D. Cohen. Combination of piecewise-geodesic paths for interactive segmentation. *International Journal of Computer Vision*, 112(1): 1–22, 2014.
- J.-M. Mirebeau. Anisotropic Fast-Marching on Cartesian Grids Using Lattice Basis Reduction. *SIAM Journal on Numerical Analysis*, 52(4):1573–1599, 2014a.

- J.-M. Mirebeau. Efficient fast marching with Finsler metrics. *Numerische Mathematik*, 126(3):515–557, 2014b.
- D. Mumford. Elastica and computer vision. in *Algebraic Geometry and Its Applications* (C. L. Bajaj, Ed.), Springer-Verlag, New York, pages 491-506, 1994.
- D. Mumford and J. Shah. Optimal approximations by piecewise smooth functions and associated variational problems. *Communications on pure and applied mathematics*, 42(5):577–685, 1989.
- M. Nitzberg and D. Mumford. The 2.1-D sketch. In *Proceedings of IEEE International Conference on Computer Vision (ICCV 1990)*, pages 138–144, 1990.
- S. Osher and J. A. Sethian. Fronts propagating with curvature-dependent speed: algorithms based on Hamilton-Jacobi formulations. *Journal of computational physics*, 79(1):12–49, 1988.
- N. Paragios and R. Deriche. Geodesic active regions: A new framework to deal with frame partition problems in computer vision. *Journal of Visual Communication and Image Representation*, 13(1):249–268, 2002.
- N. Paragios, O. Mellina-Gottardo, and V. Ramesh. Gradient vector flow fast geodesic active contours. In *Proceedings of IEEE International Conference on Computer Vision (ICCV 2001)*, volume 1, pages 67–73, 2001.
- M. Péchaud, R. Keriven, and G. Peyré. Extraction of tubular structures over an orientation domain. In *Proceedings of IEEE Conference on Computer Vision and Pattern Recognition (CVPR 2009)*, pages 336–342, 2009.
- J. Petitot. The neurogeometry of pinwheels as a sub-Riemannian contact structure. *Journal of Physiology-Paris*, 97(2-3):265–309, 2003.
- G. Peyré, M. Péchaud, R. Keriven, and L. D. Cohen. Geodesic Methods in Computer Vision and Graphics. *Foundations and Trends in Computer Graphics and Vision*, pages 197–397, 2010.
- G. Randers. On an asymmetrical metric in the four-space of general relativity. *Physical Review*, 59(2):195, 1941.
- Y. Rouchdy and L. D. Cohen. Geodesic voting for the automatic extraction of tree structures. Methods and applications. *Computer Vision and Image Understanding*, 117(10):1453–1467, 2013.
- E. Rouy and A. Tourin. A viscosity solutions approach to shape-from-shading. *SIAM Journal on Numerical Analysis*, 29(3):867–884, 1992.
- C. Sagiv, N. A. Sochen, and Y. Y. Zeevi. Integrated active contours for texture segmentation. *IEEE Transactions on Image Processing*, 15(6):1633–1646, 2006.

- G. Sanguinetti, E. Bekkers, R. Duits, M. H. Janssen, A. Mashtakov, and J.-M. Mirebeau. Sub-Riemannian Fast Marching in SE (2). In *Proceedings of Iberoamerican Congress on Pattern Recognition*, pages 366–374, 2015.
- Y. Sato, S. Nakajima, N. Shiraga, H. Atsumi, S. Yoshida, T. Koller, G. Gerig, and R. Kikinis. Three-dimensional multi-scale line filter for segmentation and visualization of curvilinear structures in medical images. *Medical image analysis*, 2(2):143–168, 1998.
- T. Schoenemann, F. Kahl, and D. Cremers. Curvature regularity for region-based image segmentation and inpainting: A linear programming relaxation. In *IEEE 12th International Conference on Computer Vision*, pages 17–23, 2009.
- T. Schoenemann, S. Masnou, and D. Cremers. The Elastic Ratio: Introducing Curvature Into Ratio-Based Image Segmentation. *IEEE Transactions on Image Processing*, 20(9):2565–2581, 2011.
- T. Schoenemann, F. Kahl, S. Masnou, and D. Cremers. A linear framework for region-based image segmentation and inpainting involving curvature penalization. *International Journal of Computer Vision*, 99(1):53–68, 2012.
- J. Sethian and A. Vladimirsky. Ordered upwind methods for static Hamilton–Jacobi equations. *Proceedings of the National Academy of Science of the USA*, 98(20):11069–11074 (electronic), 2001.
- J. A. Sethian. A fast marching level set method for monotonically advancing fronts. *Proceedings of the National Academy of Sciences*, 93(4):1591–1595, 1996.
- J. A. Sethian. Fast marching methods. *SIAM Review*, 41(2):199–235, 1999.
- J. A. Sethian and A. Vladimirsky. Ordered upwind methods for static Hamilton–Jacobi equations: Theory and algorithms. *SIAM Journal on Numerical Analysis*, 41(1):325–363, 2003.
- J. Shen, S. H. Kang, and T. F. Chan. Euler’s elastica and curvature-based inpainting. *SIAM Journal on Applied Mathematics*, 63(2):564–592, 2003.
- J. Shi and J. Malik. Normalized cuts and image segmentation. *IEEE Transactions on Pattern Analysis and Machine Intelligence*, 22(8):888–905, 2000.
- J. Staal, M. D. Abràmoff, M. Niemeijer, M. A. Viergever, and B. Van Ginneken. Ridge-based vessel segmentation in color images of the retina. *IEEE Transactions on Medical Imaging*, 23(4):501–509, 2004.
- B. Sumengen and B. Manjunath. Graph partitioning active contours (GPAC) for image segmentation. *IEEE Transactions on Pattern Analysis and Machine Intelligence*, 28(4):509–521, 2006.

- M. Sussman, P. Smereka, and S. Osher. A level set approach for computing solutions to incompressible two-phase flow. *Journal of computational physics*, 114(1):146–159, 1994.
- X.-C. Tai, J. Hahn, and G. J. Chung. A fast algorithm for Euler’s elastica model using augmented Lagrangian method. *SIAM Journal on Imaging Sciences*, 4(1):313–344, 2011.
- A. Tsai, A. Yezzi Jr, and A. S. Willsky. Curve evolution implementation of the Mumford-Shah functional for image segmentation, denoising, interpolation, and magnification. *IEEE Transactions on Image Processing*, 10(8):1169–1186, 2001.
- J. N. Tsitsiklis. Efficient algorithms for globally optimal trajectories. *IEEE Transactions on Automatic Control*, 40(9):1528–1538, 1995.
- J. Ulen, P. Strandmark, and F. Kahl. Shortest Paths with Higher-Order Regularization. *IEEE Transactions on Pattern Analysis and Machine Intelligence*, 37(12):2588–2600, 2015.
- A. Vasilevskiy and K. Siddiqi. Flux maximizing geometric flows. *IEEE Transactions on Pattern Analysis and Machine Intelligence*, 24(12):1565–1578, 2002.
- L. A. Vese and T. F. Chan. A multiphase level set framework for image segmentation using the Mumford and Shah model. *International Journal of Computer Vision*, 50(3):271–293, 2002.
- O. Weber, Y. S. Devir, A. M. Bronstein, M. M. Bronstein, and R. Kimmel. Parallel algorithms for approximation of distance maps on parametric surfaces. *ACM Transactions on Graphics*, 27(4):104, 2008.
- C. Xiao, M. Staring, Y. Wang, D. P. Shamonin, and B. C. Stoel. Multiscale bi-Gaussian filter for adjacent curvilinear structures detection with application to vasculature images. *IEEE Transactions on Image Processing*, 22(1):174–188, 2013.
- X. Xie and M. Mirmehdi. MAC: Magnetostatic active contour model. *IEEE Transactions on Pattern Analysis and Machine Intelligence*, 30(4):632–646, 2008.
- C. Xu and J. L. Prince. Snakes, shapes, and gradient vector flow. *IEEE Transactions on Image Processing*, 7(3):359–369, 1998.
- X. Xu, M. Niemeijer, Q. Song, M. Sonka, M. K. Garvin, J. M. Reinhardt, and M. D. Abràmoff. Vessel boundary delineation on fundus images using graph-based approach. *IEEE Transactions on Medical Imaging*, 30(6):1184–1191, 2011.
- A. Yezzi, S. Kichenassamy, A. Kumar, P. Olver, and A. Tannenbaum. A geometric snake model for segmentation of medical imagery. *IEEE Transactions on Medical Imaging*, 16(2):199–209.

- Y. Yin, M. Adel, and S. Bourennane. Retinal vessel segmentation using a probabilistic tracking method. *Pattern Recognition*, 45(4):1235–1244, 2012.
- J. Zhang, B. Dashtbozorg, E. Bekkers, J. Pluim, R. Duits, and B. ter Haar Romeny. Robust retinal vessel segmentation via locally adaptive derivative frames in orientation scores. *IEEE Transactions on Medical Imaging*, 2016.
- H.-K. Zhao, T. Chan, B. Merriman, and S. Osher. A variational level set approach to multiphase motion. *Journal of computational physics*, 127(1):179–195, 1996.
- Y. Zhao, L. Rada, K. Chen, S. P. Harding, and Y. Zheng. Automated vessel segmentation using infinite perimeter active contour model with hybrid region information with application to retinal images. *IEEE Transactions on Medical Imaging*, 34(9):1797–1807, 2015.
- S. C. Zhu and A. Yuille. Region competition: Unifying snakes, region growing, and Bayes/MDL for multiband image segmentation. *IEEE Transactions on Pattern Analysis and Machine Intelligence*, 18(9):884–900, 1996.
- W. Zhu, X.-C. Tai, and T. Chan. Image segmentation using Euler’s elastica as the regularization. *Journal of scientific computing*, 57(2):414–438, 2013.

Résumé

Dans les domaines de l'imagerie médicale et de la vision par ordinateur, la segmentation joue un rôle crucial dans le but d'extraire les composantes intéressantes d'une image ou d'une séquence d'images. Elle est à l'intermédiaire entre le traitement d'images de bas niveau et les applications cliniques et celles de la vision par ordinateur de haut niveau. Ces applications de haut niveau peuvent inclure le diagnostic, la planification de la thérapie, la détection et la reconnaissance d'objet, etc. Parmi les méthodes de segmentation existantes, les courbes géodésiques minimales possèdent des avantages théoriques et pratiques importants tels que le minimum global de l'énergie géodésique et la méthode bien connue de Fast Marching pour obtenir une solution numérique. Dans cette thèse, nous nous concentrons sur les méthodes géodésiques basées sur l'équation aux dérivées partielles, l'équation Eikonale, afin d'étudier des méthodes précises, rapides et robustes, pour l'extraction de structures tubulaires et la segmentation d'image, en développant diverses métriques géodésiques locales pour des applications cliniques et la segmentation d'images en général. Cette thèse contribue principalement à l'étude approfondie des diverses métriques géodésiques et leurs applications en imagerie médicale et segmentation d'images. Des expériences ont été réalisées sur des images médicales et des images naturelles pour montrer l'efficacité des contributions présentées.

Mots Clés

Chemin minimal, géodésique, équation aux dérivées partielles, équation Eikonale, segmentation d'images, segmentation de structure tubulaire, contours actifs, courbe Elastica d'Euler, métrique de Riemann, métrique de Finsler, pénalité de courbure, méthode de Fast Marching.

Abstract

In the fields of medical imaging and computer vision, segmentation plays a crucial role with the goal of separating the interesting components from one image or a sequence of image frames. It bridges the gaps between the low-level image processing and high level clinical and computer vision applications. Among the existing segmentation methods, minimal geodesics have important theoretical and practical advantages such as the global minimum of the geodesic energy and the well-established fast marching method for numerical solution. In this thesis, we focus on the Eikonal partial differential equation based geodesic methods to investigate accurate, fast and robust tubular structure extraction and image segmentation methods, by developing various local geodesic metrics for types of clinical and segmentation tasks. The main contributions of this thesis lie at the deep study of the various geodesic metrics and their applications in medical imaging and image segmentation. Experiments on medical images and nature images show the effectiveness of the presented contributions.

Keywords

minimal path, geodesic, Eikonal partial differential equation, image segmentation, tubular structure segmentation, active contours, Euler elastica curve, Riemannian metric, Finsler metric, curvature penalty, fast marching method.